UNIVERSITY OF CALIFORNIA

SANTA CRUZ

**Manipulation of Catalyst Fine Structures for Fuel Conversion and Antimicrobial Applications**

A dissertation submitted in partial satisfaction

of the requirements for the degree of

DOCTOR OF PHILOSOPHY

in

CHEMISTRY

by

**Forrest Nichols**

June 2022

The Dissertation of Forrest Nichols is

approved:

_____
Professor Shaowei Chen, chair

_____
Professor Ilan Benjamin

_____
Professor Alex Ayzner

_____
Peter Biehl

Vice Provost and Dean of Graduate Studies

## Table of Contents

LIST OF FIGURES ..... v

LIST OF TABLES ..... xviii

ABSTRACT ..... xix

ACKNOWLEDGEMENT ..... xxii

Chapter 1 Introduction ..... 1

1.1 hydrogen as a sustainable fuel ..... 1

1.2 Electrochemistry of the hydrogen evolution reaction (HER) ..... 3

1.3 Nanomaterial design methods ..... 5

1.4 Electrochemistry for reactive species generation ..... 8

1.5 Photocatalysis for the generation of reactive oxygen species ..... 10

1.6 Reactive species interaction with microorganisms ..... 11

1.6.1 Introducing reactive species interactions with microorganisms ..... 11

1.6.2 Oxidative homeostasis regulated within microorganisms ..... 12

1.6.3 Damaging effects caused by reactive species ..... 15

1.7 References ..... 18

Chapter 2 Platinum Oxide Nanoparticles for Electrochemical Hydrogen Evolution: Influence of Platinum Valence State ..... 29

2.1 Abstract ..... 30

2.2 Introduction ..... 30

2.3 Results and Discussion ..... 32

2.4 Experimental Section ..... 51

2.5 Conclusions ..... 52

2.6 References ..... 53

Chapter 3 Platinum-complexed phosphorous-doped carbon nitride for electrocatalytic hydrogen evolution ..... 59

3.1 Abstract ..... 60

3.2 Introduction ..... 60

3.3 Results and Discussion ..... 64

3.4 Experimental Section ..... 86

3.5 Conclusions ..... 89

3.6 References ..... 89

Chapter 4 Electrocatalytic Generation of Reactive Species and Implications in Microbial Inactivation ..... 97
4.1 Abstract ..... 98
4.2 Introduction ..... 98
4.3 Electrocatalytic generation of reactive species ..... 100
4.3.1 Reactive oxygen species ..... 100
4.3.2 Reactive chlorine species ..... 116
4.3.3 Other reactive species ..... 122
4.3.4 Homogeneous electrocatalysis for RS generation ..... 124
4.4 Interactions of Reactive Species with Microorganisms ..... 124
4.4.1 Oxidative homeostasis regulated within microorganisms ..... 125
4.4.2 Damaging effects caused by reactive species ..... 128
4.5 Electrogenerated Reactive Species for Microbial Inactivation ..... 131
4.6 Conclusions and perspectives ..... 137
4.7 References ..... 139
Chapter 5 Graphene Oxide Quantum Dot-Based Functional Nanomaterials for Effective Antimicrobial Applications ..... 166
5.1 Abstract ..... 167
5.2 Introduction ..... 167
5.3 Graphene Oxide Quantum Dots ..... 171
5.4 Graphene Oxide Quantum Dots/Metal Oxide Nanocomposites ..... 180
5.5 Summaries and Perspectives ..... 190
5.6 References ..... 191
Chapter 6 Antibacterial Activity of Nitrogen-Doped Carbon Dots Enhanced by Atomic Dispersion of Copper ..... 199
6.1 Abstract ..... 200
6.2 Introduction ..... 200
6.3 Results and Discussion ..... 203
6.4 Experimental ..... 225
6.5 Conclusions ..... 229
6.6 References ..... 230
Chapter 7 Summary ..... 237

# LIST OF FIGURES

## Chapter 1

**Figure 1.** schematic representation of a proton exchange membrane (PEM) water electrolysis device. Reproduced with permission © Elsevier 2022.

**Figure 2.** HER volcano plot for various bulk metal materials. Reproduced with permission © AAAS 2017

**Figure 3.** Abundance (atomic fraction) of elements on earth as a function of atomic number (Z).

**Figure 4.** Particle geometry, electronic structure, and surface free energy as a function of particle size. Reproduced with permission from © 2021 American Chemical Society.

**Figure 5.** Reactive oxygen species generated by photocatalytic reduction and oxidation of water and molecular oxygen by photoinduced electron and hole.

**Fig. 6.** Regulation of reactive oxygen species within the cell by enzymes superoxidase dismutase (SOD), Catalase (Cat), and other peroxidase enzymes (GPx, and Prx). Red spheres represent oxygen and grey spheres denote hydrogen.

**Fig. 7.** (a) spectrum of cellular response to RS ranging from cellular homeostasis, left, to cell death, right. (b) Schematic representation of glutathione (GSH) oxidation to glutathione disulphide (GSSG) by reactive species (RS). (c) UV-vis absorption spectrum for the Ellman's reagent. Panels (a) copyright 2013, Springer Nature. Panel (c) copyright 2020, Royal chemistry society.

**Fig. 8.** (a) An example of lipid peroxidation using linoleate as the starting substrate. copyright 2005, Elsevier. (b) Results of protein damage caused by increased levels of oxidation. copyright 2003, Elsevier.

**Chapter 2**

**Figure 1.** TEM images of (a) Pt2+90C and (b) Pt4+90C. Scale bars 10 nm. Insets are the corresponding high-resolution TEM images, with the scale bars of 5 nm.

**Figure 2.** TEM images of (a,b) Pt2+90C and (c,d) Pt4+90C samples. Scale bars are (a) 100 nm, (b) 5 nm, (c) 40 nm, and (d) 5 nm.

**Figure 3.** Representative TEM images of as-prepared C3N4. Scale bars are (a) 50 nm and (b) 5 nm.

**Figure 4.** Core size histograms of Pt2+90C and Pt4+90C.

**Figure 5.** Powder X-ray Diffraction spectra. Tick lines represent expected patterns from that of $PtO_2$ (Grey) (Ref. Code: 01-075-0978) and PtO (Green) (Ref. Code: 00-027-1331).

**Figure 6.** (a) XPS survey spectra and (b) the corresponding high-resolution scans for the Pt4f electrons of as-prepared C3N4 (Black), Pt2+90C (Red), and Pt4+90C (Blue). Solid curves are experimental data and shaded peaks are deconvolution fits.

**Figure 7.** High resolution XPS spectra of the (a) C 1s and (b) N 1s regions for samples C3N4 (black), Pt2+90C (red), and Pt4+90C (blue).

**Figure 8.** (a) Pt L3 edge XANES data for Pt2+90C and Pt4+90C (Pt foil and commercial $\alpha$-$PtO_2$ as references). All edge steps are normalized to an edge step height of 1. The

energy range selected to normalize the edge is 11700 to 12000 eV. Measurements are performed at the temperature of 10 K. (b) Pt L3 edge r-space data for Pt2+90C (red), Pt4+90C (blue) and commercial α-$PtO_2$ (black). The Fourier transform (FT) window is from 3.0 to 10.8 $Å^{-1}$, rounded using a Gaussian function of width, 0.2 $Å^{-1}$. The fast oscillating function is the real part R of the FT while the amplitude is the $\sqrt{R^2 + I^2}$ where $I$ is the imaginary part of the FT. Pt4+90C has been shifted vertically by 0.4 while α-$PtO_2$ has been shifted vertically by 0.8.

**Figure 9.** Pt L3 edge k-space data at 10 K of various samples.

**Figure 10.** Fittings to the hexagonal structure of α-$PtO_2$, as a sum of Pt-O and Pt-Pt, for (a) Pt2+90C and (b) Pt4+90C. Pt-O bond length decreases from 2.07 to 2.03 Å.

**Figure 11.** Nyquist plots of C3N4 (black), Pt2+90C (red), and Pt4+90C (blue). Symbols are experimental data and solid curves are fits by using the Randles equivalent circuit in the figure inset. All measurements are carried out at the potential of -10 mV vs RHE in a nitrogen-purged 0.5 M H2SO4 solution.

**Figure 12.** (a) Polarization curves of HER in 0.5M $H_2SO_4$ for as prepared C3N4 (black), Pt2+90C (red), Pt4+90C (blue), and commercial platinum on carbon (magenta). (b) Tafel Plots derived from polarization curves in panel (a). (c) Oxidized cycling and recovery tests.

**Figure 13.** High resolution XPS scans of Pt 4f electrons of the Pt2+90C sample after 50 potential cycling between +0.9 and +1.2 V vs RHE.

**Figure 14.** Polarization curves of Pt4+90C prepared at reduced $PtCl_4$ loading (1/2 and 1/10 of that described in the main text) in 0.5 M $H_2SO_4$.

**Chapter 3**

**Figure 1.** (a) SEM image of the $PtCNP_2$ sample, with the EDS elemental maps shown at the bottom for C, N, P, Pt, Cl, and O. (b) High-magnification SEM image for the red box area in panel (a). (c, d) TEM images of $PtCNP_2$. Scale bars are (a) 5 μm, (b) 1 μm, (c) 50 nm and (d) 10 nm.

**Figure 2.** SEM images of (a) PtCNP1, (b) PtCNP2, (c) PtCNP3, and (d) PtCNP4. The corresponding EDS spectra are included below the respective panel, where Pt signals can be readily identified in all samples.

**Figure 3.** TEM images of (a, b) PtCN, (c, d) PtCNP1, (e, f) PtCNP3, (g, h) PtCNP4. Scale bars are (a, c, e, g) 50 nm and (b, d, f, h) 20 nm.

**Figure 4.** XRD patterns of the sample series deposited onto an aluminum plate. Reference lines are provided at the bottom of the plot and refer to cubic Pt with space group fm-3m (JCPDS: 00-001-1190 (cyan), tetragonal PtO with space group p42/mmc JCPDS: 00-027-1331 (black), and orthorhombic $PtO_2$ with space group pnnm JCPDS: 00-023-1306 (red).

**Figure 5.** (a) XPS survey spectra of PtCN, PtCNP1, PtCNP2, PtCNP3, and PtCNP4. (b) High-resolution Cl 2p spectra of the sample series.

**Figure 6.** High resolution XPS spectra of the (a) C 1s, (b) N 1s, (c) Pt 4f, and (d) P 2p electrons of the PtCN, $PtCNP_1$, $PtCNP_2$, $PtCNP_3$, and $PtCNP_4$ samples.

**Figure 7.** Pt L3 edge k-space data for the sample series collected at 10 K. Plots are produced by averaging 3 traces from each sample.

**Figure 8.** (a) Normalized Pt L3 edge XANES for the sample series in comparison to Pt Zeise's salt precursor (orange) and Pt foil (cyan). All edge steps are normalized to an

edge height of 1. The energy range selected to normalize the edge is 11.7-12.0 keV. Measurements were performed at a temperature of 10K to reduce thermal disorder within samples. Inset is the zoom in of the white line region. (b) Pt L3 edge r-space EXAFS data for the sample series and two reference samples, Pt Zeise's salt (orange) and Pt Foil (cyan). The FT window is from 3.5 to 12.0 $Å^{-1}$, rounded using a Gaussian function of width, 0.2 $Å^{-1}$. The fast-oscillating function is the real part R of the FT, and the amplitude is $(R^2+I^2)^{1/2}$, whereas I is the imaginary part of the FT. Samples have been shifted vertically for better comparison.

**Figure 9.** Ball and stick model representations of the fitting structures for (a) PtCN and (b) $PtCNP_2$. Coordination to the centre Pt atom indicates first and second shell atoms used for fitting. Atoms are colour coded with carbon (brown), nitrogen (gray), platinum (cyan), chlorine (green), and phosphorous (light red). EXAFS fitting results shown in R-space for (c) PtCN and (d) $PtCNP_2$. Raw R-space data is shown in solid with fits shown in gray circles. Fittings are performed in the R range of 1.3 to 2.5 Å.

**Figure 10.** Cyclic voltammogram of the PtCNP2 sample performed in $N_2$ saturated $H_2SO_4$ at a scan rate of 10 mV $s^{-1}$. Current density is obtained by normalizing the current to the electrode geometrical surface area.

**Figure 11.** (a) HER polarization curves on various electrocatalysts in 0.5M $H_2SO_4$ at the rotation rate of 1600 rpm, potential sweep rate of 10 mV/s and 85% iR compensation. (b) Corresponding $\eta_{10}$ from the HER polarization curves in panel (a). (c) Mass activity at -0.07 V vs RHE per µg of Pt calculated from ICP-OES measurements. (d) Tafel plots derived from panel (a). Note the overlapping data points between the Pt/C and $PtCNP_2$ samples.

**Figure 12.** (a) Nyquist plots for the sample series produced from electrochemical impedance measurements at -10 mV overpotential. Inset is the Randle's equivalent circuit where $R_1$ is the solution resistance, $R_{ct}$ is the charge-transfer resistance, C is the double-layer capacitance, and $W_d$ is the Warburg diffusion term. (b) Mott-Schottky measurements for the sample series performed in 0.1 M $Na_2SO_4$. Potentials are vs an Ag/AgCl reference electrode. Regression taken within the linear portion of each sample is shown as a black solid line. Y-axis on the left correspond to samples PtCN, $PtCNP_1$, and $PtCNP_4$ while y-axis on the right corresponds to $PtCNP_2$ and $PtCNP_3$.

**Chapter 4**

**Fig. 1.** Schematic representation of the electrosynthesis of RS and corresponding targets for microbial damage. Spheres represent oxygen (red), hydrogen (grey), chlorine (green), sulfur (yellow), and nitrogen (blue) atoms.

**Fig. 2.** (a) Pseudo-color surface plot created from HAADF-STEM image of $Mo_1$/OSG-H. (b) FT-EXAFS curves at Mo K edge. (c) Free energy diagram of $2e^-$ ORR on three substrates at equilibrium potential. Panels (a-c) reproduced with permission from ref. [63], copyright 2020, Wiley-VCH. (d) Volcano plots for ORR producing water (blue) and $H_2O_2$ (red). Solid lines are created from the calculations of various M-$N_4$ species (M = Co, Ni, Fe, and Ag). (e) Polarization curves for NG(O) (black), $Co_1$-NG(O) (red), and $Co_1$-NG(R) (blue) with currents from the disk (solid) and ring (dashed) electrodes. (f) $H_2O_2$ selectivity % measured for $Co_1$-NG(O) (red) and $Co_1$-NG(R) (blue) over the potential range of 0.1 V – 0.8 V vs RHE. Measurements performed at 1600 rpm rotation rate in 0.1M KOH. Panels (d-f) reproduced with permission from ref. [64], copyright 2020, Springer Nature.

**Fig. 3.** (a) Volcano plot of electrocatalytic activity corresponding to limiting potential vs $OH^*$ adsorption energy for $2e^-$ (black) and $4e^-$ (blue) WOR. Equilibrium potentials are shown in dashed lines. (b) Polarization curves for four select metal oxides toward $2e^-$ WOR. Panels (a,b) reproduced with permission from ref. [66], Springer Nature. (c) Free energy diagram for the stepwise $O_2$ evolution reaction (blue) and $H_2O_2$ evolution reaction (green) with 4 intermediate steps. (d) Volcano plots produced from calculated limiting potential ($U_L$) as a function of OH* binding free energy ($\Delta G_{OH*}$) for the four-electron water oxidation (blue dashed line) and two electron water oxidation to $H_2O_2$ (black line). Three favorable reaction pathways are highlighted by shading $O_2$ evolution (blue), $H_2O_2$ evolution (green), and $OH^\bullet$ production (red). (e) SEM images of ZnO($10\bar{1}0$) nanorods. (f) Catalytic activity of $2e^-$ WOR in 2M potassium bicarbonate of ZnO($10\bar{1}0$), Zn(0001) and other metal oxides. Inset depicts model representations of the ZnO(0001) and ZnO($10\bar{1}0$) crystal structures. (g) Faraday Efficiency (FE) at 3.0 V vs RHE for ZnO($10\bar{1}0$), as compared to various other metal oxide materials with error bars taken from 5 independent measurements. Panels (c-g) reproduced with permission from ref. [67], copyright 2019, American Chemical Society.

**Fig. 4.** (a) Calculated free energy diagrams of $2e^-$ and $4e^-$ ORR for c-$CoS_2$ (100) (blue), c-$CoSe_2$ (100) (green), and o-$CoSe_2$ (101) (red). (b) Kinetic current density for $H_2O_2$ normalized to geometric surface area and compared to previously reported $2e^-$ ORR catalysts. Panels (a,b) reproduced with permission from ref. [74], copyright 2020, Royal Chemistry Society. (c) Linear sweep voltammetry (LSV) with 1200 rpm rotation and 10 mV $s^{-1}$ scan rate in 0.05 M $Na_2SO_4$ (pH = 6) for fresh electrolyte (green), 10 mM NaF poisoning agent (purple), and repeated with fresh electrolyte after poisoning measurements (red). (d) Schematic representation of $O_2$ stepwise reduction to $H_2O_2$ and $OH^\bullet$. (e) $OH^\bullet$ yield with increased levels of poisoning agent, NaF. (f) Spin trapping ESR

spectra with DMPO (3mM). (g) degradation of nitrobenzene (blue), phenol (green), and benzoic acid (purple) with calculated kinetic constants normalized to Fe mass ($K_M$). Panels (c-g) reproduced with permission from ref. [76] copyright 2020, Springer Science.

**Fig. 5.** (a) Polarization curves for chlorine evolution reaction (CER) for various cobalt containing materials. (b) In situ XANES at Co K edge for $Co_3O_4$ nanoparticles under CER and OER conditions in 0.6 M NaCl and 0.5 M phosphate buffered species (Pi), respectively. (c) In situ Raman measurements under increasing oxidative potentials from 0.4 V to 1.3 V in 4M NaCl. Broad peak occurs near 500 $cm^{-1}$ ascribed to Co-Cl, with deconvolution (d) in $H_2O$, $D_2O$, and $H_2{}^{18}O$. Reproduced with permission from ref. [84], copyright 2019, American Chemical Society.

**Fig. 6.** Regulation of reactive oxygen species within the cell by enzymes superoxidase dismutase (SOD), Catalase (Cat), and other peroxidase enzymes (GPx, and Prx). Red spheres represent oxygen and grey spheres denote hydrogen.

**Fig. 7.** (a) spectrum of cellular response to RS ranging from cellular homeostasis, left, to cell death, right. (b) Schematic representation of glutathione (GSH) oxidation to glutathione disulphide (GSSG) by reactive species (RS). (c) UV-vis absorption spectrum for the Ellman's reagent. Panels (a) reproduced with permission from ref. [147] copyright 2013, Springer Nature. Panel (c) reproduced with permission from ref. [163] copyright 2020, Royal chemistry society.

**Fig. 8.** (a) An example of lipid peroxidation using linoleate as the starting substrate. Reproduced with permission from ref. [167] copyright 2005, Elsevier. (b) Results of protein damage caused by increased levels of oxidation. Reproduced with permission from ref. [170] copyright 2003, Elsevier.

**Fig. 9.** (a) HAADF-STEM image of Fe-CNT composites. (b) FT-EXAFS R real-space plot of Fe foil (black), Fe-CNT (red), and $Fe_3O_4$ (blue). (c) Calculated $H_2O_2$ selectivity and electron transfer number for Fe-CNT (black), Pd-CNT (red), Co-CNT (blue), and Mn-CNT (green). (d) Calculated $H_2O_2$ selectivity and electron transfer number for Fe-CNT (black), nitrogen doped Fe-N-CNT (red), and gas reduced Red. Fe-CNT (blue). (e) CCD Photos of overnight cultured *E. coli* plates taken from different electrolysis timepoints. Reproduced with permission from ref. [211] copyright 2019, Springer Nature.

**Chapter 5**

**Figure 1.** Schematic representation of graphene-based material preparation by top-down and bottom-up approaches.

**Figure 2.** (a) TEM image of GOQD. Scale bar 20 nm. (b) UV-Vis spectra of GOQD (black) and rGOQD (red). Inset are the photographs of the two solutions upon irradiation at 365 nm. (c) Time-resolved photoluminescence (TRPL) emission spectra for GOQD (black) and rGOQD (red) with an excitation wavelength of 400 nm. Inset depicts the steady-state fluorescence spectra. Yellow lines depict exponential decay fittings to TRPL spectra. (d) X-ray Photoelectron Spectroscopy (XPS) survey spectra for GOQD (black) and rGOQD (red). High resolution XPS spectra of the carbon 1s orbitals for (e) GOQD and (f) rGOQD. Reproduced with permission from ref. 27, copyright 2020, the authors.

**Figure 3**. (a) Photodynamic experiment results depicting the photoinactivation % for GOQD and rGOQD toward *Staphylococcus Epidermitis*. (b) Fluorescence microscopy micrographs imaging fluorescence of CellROX green. (c) EPR spectra of GOQD (black) and rGOQD (red) upon light irradiation (400 nm) for 1 minute in the presence of the

spin-trapping reagent, DMPO. Reproduced with permission from ref. 27, copyright 2020, the authors.

**Figure 4.** (a) UV-vis and steady state photoluminescence spectra for ZnO (black), GOQD (red), and ZnO/GOQD composite (green). Inset depicts the color of the ZnO/GOQD solution under UV (365 nm) and visible light photoirradiation. (b) EPR spectra for water control (black) and ZnO/GOQD nanocomposite (red) upon photoexcitation for 1 min. (c) Bacterial growth at varying concentrations of ZnO/GOQD composite from 0 mg/mL (black) to 4.0 mg/mL (red square) performed in the dark for 24 h. Measurements are taken from light absorption at 600 nm for each timepoint. (d) Results from photodynamic experiments plotting colony forming units (CFU) versus irradiation time (min). Reproduced with permission from ref. 17, copyright 2018, the Royal Society of Chemistry.

**Figure 5.** Schematic representation of ZnO/GOQD-PEI antibacterial mechanism (a). (b) Measured ζ-potentials for E. coli (black), ZnO/GOQD (red), and ZnO/GOQD-PEI (blue). (c) EPR results in water with addition of DMPO spin-trapping reagent after light irradiation for 1 min. Reproduced with permission from re. 28, copyright 2019, the American Chemical Society.

**Figure 6**. *E. coli* growth assays performed under dark conditions for (a) ZnO/GOQD and (b) ZnO/GOQD-PEI over a 24 h period at varying nanoparticle concentrations ranging from 0.8 – 4.0 mg/mL. Photodynamic experiment performed under UV irradiation for ZnO/GOQD (red circles) and ZnO/GOQD-PEI (blue triangles) over a 5 min period. Reproduced with permission from ref. 28, copyright 2019, the American Chemical Society.

**Chapter 6**

**Figure 1.** Representative TEM images of (a) NCD and (b) Cu/NCD-3. Scale bars are both 50 nm. (c) XRD patterns of (black) NCD, (red) Cu/NCD-1, (blue) Cu/NCD-2, and (magenta) Cu/NCD-3. Reference XRD patterns are provided along the X-axis for copper (orange, 00-001-1241), CuO (dark red, 00-002-1040), and $Cu_2O$ (green, 00-003-0892).

**Figure 2.** Core size histogram of the NCD (black) and Cu/NCD-3 (magenta) samples.

**Figure 3.** High-resolution TEM images of (a) NCD and (b) Cu/NCD-3. Scale bars are (a) 5 nm and (b) 10 nm.

**Figure 4.** (a) STEM image of the Cu/NCD-3 sample, where the red box marks the region for elemental mapping analysis. (b) EELS spectrum acquired from the red box region in panel (a) with signals originating primarily from carbon and nitrogen and virtually no detectable copper signal (ca. 930 eV), as the Cu content (Table S2) is below the sensitivity limitation of STEM (ca. 1 at%). The fact that no particulate forms of Cu are detected is also consistent with the atomic dispersion of Cu in the carbon dots. The corresponding elemental maps are shown in (c) C, (d) N and (e) Cu.

**Figure 5.** XPS survey scans of NCD (black), Cu/NC-1 (red), Cu/NC-2 (blue), and Cu/NC-3 (magenta).

**Figure 6.** High-resolution XPS spectra of the (a) C 1s, (b) N 1s and (c) Cu 2p electrons of the NCD and Cu/NCD samples Solid curves are experimental data and shaded peaks are deconvolution fits.

**Figure 7.** Comparison of copper wt% from the XPS (green) and ICP-OES (orange) measurements.

**Figure 8.** (a) UV-vis and SSPL spectra of (black) NCD, (red) Cu/CND-1, (blue) Cu/CND-2, and (magenta) Cu/CND-3. The UV-vis spectra are normalized to the respective absorbance at 203 nm and the fluorescence spectra are normalized to the corresponding optical absorbance at the excitation wavelength and then normalized to the emission intensity of the NCD sample. All measurements are performed in PBS 1×. (b) TRPL emission spectra at the excitation of 365 nm for the NCD and Cu/NCD-3 samples. Symbols are experimental data and solid curves are exponential fits.

**Figure 9.** UV-vis difference spectra by normalizing the spectra to the absorbance at 250 nm and then subtracting the absorbance from the NCD spectrum.

**Figure 10.** (a) Antibacterial studies under photoirradiation at the peak wavelength at 365 nm. Two control samples are included: (light green) *E. coli* alone in PBS 1×, and (orange) $CuCl_2$ in PBS 1× at a concentration equivalent to that of Cu/NCD-3 (12.8 ppm). A second sample of Cu/NCD-3 is tested in the presence of a hydroxyl radical quencher, TBA at 10 mg $L^{-1}$ (dark green). All samples have been tested in triplicate and the data points display the corresponding average and standard deviation. (b) Photographs depicting *E. coli* grown on LB agar plates at different photoirradiation time points (0, 1, 2, 4, and 7 min) in the (bottom) absence and (top) presence of Cu/NCD-3. SEM images of (c) the *E. coli* control, (d) *E. coli* with Cu/NCD-3 after photo irradiation, for 7 min, and (e) *E. coli* with Cu/NCD-3 in the dark. The scale bars, indicated in red are 1 μm, 1μm, and 2μm, respectively.

**Figure 11.** Digital photographs of incubated LB agar plates: from top to bottom for the samples of Cu/NCD-2, Cu/NCD-1, NCD, and Cu/NCD-3 + TBA. The columns from left to right are images acquired at the 0, 2, 4, and 7 min time points of photo irradiation at 356 nm.

**Figure 12.** Gram positive antibacterial studies under photoirradiation with the peak wavelength at 365 nm. Two control samples are included: (light green) S. epidermidis alone in PBS 1×, and (orange) CuCl2 in PBS 1× at a concentration equivalent to that of Cu/NCD-3 (12.8 ppm). Data for Cu/NCD-3 is shown in magenta.

**Figure 13.** Bacterial growth curves in the dark. Each measurement is repeated in triplicate, with PBS 1× as the solvent. Sample concentrations are all 600 μg $mL^{-1}$, identical to those in photodynamic experiments in Figure 10.

**Figure 14.** Representative fluorescence micrographs of *E. coli* cells stained with CellROX™ green after 1 min of photoirradiation at a peak wavelength between 395-400 nm in the presence of (a) PBS only, (b) NCD (600 μg/mL in PBS), and Cu/NCD-3 (600 μg/mL in PBS). (d) Bar charts of the average fluorescence intensity of the bacterial cells after photoirradiation.

**Figure 15.** *E. coli* growth curves in the dark in the presence of Cu/NCD-3 at varying concentrations from 400 to 1100 μg/mL.

# LIST OF TABLES

**Chapter 2**

**Table 1.** EXAFS fitting results to Hexagonal α-$PtO_2$.

**Table 2.** Comparison of HER performance by platinum oxide nanoparticles reported in recent literature

**Chapter 3**

**Table 1.** Elemental compositions (at%) of the sample series from XPS measurements

**Table 2.** Pt 4f binding energy and atomic ratio of the sample series

**Table 3.** Binding energy of the P and Cl 2p3/2 electrons in the sample series

**Table 4.** Bond length (r (Å)), coordination number (CN) and the Debye-Waller parameter ($\sigma^2$) from fitting of the EXAFS data in Figure 4.

**Chapter 6**

**Table 1.** XPS Binding energy (BE, eV) of the various elements in the series of samples

**Table 2.** Atomic percentage (at%) of the various elements in the series of samples

**Manipulation of Catalyst Fine Structures for Fuel Conversion and Antimicrobial Applications**

**Forrest Nichols**

## ABSTRACT

Humans are becoming more connected through world trade, aviation, the internet, and social media. Through this connection we are beginning to identify shared problems facing humanity that have the potential to threaten human existence including climate change and infectious disease. There remains time and hope that humans have the potential to understand these threats and find collaborative solutions through innovation. Electric and fuel cell vehicles can reduce human dependency on fossil fuels and reduce global $CO_2$ emissions. Renewable electricity is on the horizon with innovations in electricity generation by wind and solar devices. Water electrolysis devices can complete the renewable energy economy by using renewable electricity to produce hydrogen fuel for fuel cell vehicles. Additional innovations are necessary to improve economics and performance of such devices for large scale adoption. On the front of infectious disease, alternative antibiotics are necessary to combat the rise of antibiotic resistant microorganisms. Generation of reactive species through electrocatalysis or photocatalysis for microbial inactivation are promising solutions to reduce human dependence on traditional β-lactam antibiotics. Additional study is necessary to understand the catalytic generation of these species and their resulting interactions with microorganisms. My thesis has focused on the design and synthesis of nanomaterial catalysts with applications in renewable fuel and microbial inactivation technologies.

More specifically, **chapter 1** provides background on hydrogen as an alternative and renewable fuel, a mechanistic understanding of hydrogen electrocatalysis, catalyst synthesis methods, methods of material characterization. Furthermore, background on reactive species generation by electrocatalysis and photocatalysis is provided with additional understanding of reactive oxygen species interactions with microorganisms.

**Chapters 2** and **chapter 3** cover two pieces of work focused on the optimization of platinum based electrocatalysts for the hydrogen evolution reaction. Comparison to a commercially available platinum on carbon electrocatalyst is provided. In **chapter 2**, platinum oxide nanoparticles are deposited on a carbon nitride support material. The influence of platinum valence state is systematically studied revealing the preferential hydrogen generation on platinum oxide in a higher valence state. Utilizing this principle, further studies are carried out to demonstrate electrochemical generation of active $Pt^{4+}$ species and electrocatalyst recyclability. **Chapter 3** manipulates the synthetic parameters from **chapter 2** to prevent platinum oxide nanoparticle deposition and promote platinum chelation on pyridinic nitrogen groups within the carbon nitride support material. Phosphorous doping is utilized to improve conductivity of the support material and decrease charge transfer resistance during hydrogen evolution. The mass activity of the material is found to nearly triple compared to platinum nanoparticles on carbon suggesting three times less platinum can be used to generate an equivalent amount of hydrogen gas.

**Chapter 4**, **chapter 5**, and **chapter 6** explore routes toward microbial inactivation through the design of nanomaterials capable of catalyzing reactive species. Specifically, **chapter 4** summarizes research utilizing electrocatalysis for the generation of reactive species. Details are provided on targeted reactive species generation including reactive oxygen, chlorine, sulfur, phosphorous, and nitrogen containing species. Interactions of

these species with microorganism components including proteins, lipids, and DNA are discussed. The state of the field and requirements to move the field forward are discussed. **Chapter 5** summarizes the use of graphene-based nanomaterials for microbial inactivation through physical and photocatalytic mechanisms. Top-down and bottom-up approaches are considered and the transformation of optical properties due to quantum confinement are discussed as a route to generate reactive oxygen species by photocatalysis. Copper doped carbon quantum dots are developed in **chapter 6** and are shown to photo catalyze hydroxyl radicals from water. The material is demonstrated to have broad spectrum activity for both gram-positive and gram-negative bacteria strains. Such a material could be implemented in wound care or medical devices to prevent microbial growth.

**Chapter 7** summarizes the work completed and its possible impact on the future of renewable energy devices and antimicrobial control.

## ACKNOWLEDGEMENT

I want to thank my advisor, Professor Shaowei Chen for his support throughout my time at UCSC. As an undergraduate I began work in Professor Chen's lab where I quickly felt accepted as part of the research team. I thank Professor Chen for his kindness and for motivating my research interests. I gave my first literature review presentation in Professor Chen's group meeting as an undergraduate. I remember I was very nervous but was reassured by Professor Chen's interest in the presentation and constructive feedback. This is one of the memories I look back on as a catalyst for my interest in graduate schooling. I would likely have not gone to graduate school without my involvement in Professor Chen's research group. I also want to thank Professor Chen for his commitment to each student in his group. Weekly one-on-one meetings and group meetings provided an environment where I could constantly assess my work and formulate plans for next steps in the research process. Professor Chen was always available to discuss any looming questions about any topic. I especially want to thank Professor Chen for his understanding during difficult times in my life. There were times during graduate school where I was in the hospital for long periods of time, up to 2 weeks at one time and unable to get up or walk. Professor Chen was always supportive during these times. I am truly grateful to have met and been mentored by Professor Shaowei Chen.

I thank Professor Bud Bridges for introducing me to XANES and EXAFS interpretation, teaching me how to operate the beamline at SLAC, and how to use the Linux based software necessary for data reduction and structure fitting analysis. I also thank

Professor Bridges for his patience in this process. It took me a long time to learn the software and operate the beamline. Professor Bridges would be at the beamline nearly 24 hours a day during our time at SLAC to ensure proper operation of the equipment. I would also like to thank Professor Bridges for being my outside committee member for my oral qualifications.

I would like to thank Professor Chad Saltikov for teaching me the microbiology fundamentals necessary for my work and answering all my questions about biology. Professor Saltikov helped me a lot with designing antimicrobial experiments and how I could adjust the experiments to make my time more efficient.

I would like to thank Professor Ilan Benjamin for being my committee Chair and Professor Alex Ayzner for being my committee member. Their interest and questions during my second-year seminar, orals, and yearly reviews were very helpful in my learning process. I also want to thank Professor Alex Ayzner for teaching advanced physical chemistry lab and statistical mechanics courses I took as an undergraduate. Thank you, Professor Ilan Benjamin, for teaching statistical mechanics during my graduate studies.

I also thank Dr. Peter Weiss and Dr. Randa Roland for their guidance when working as a teaching assistant. I worked as a grader for Dr. Weiss' class as an undergraduate and was a student in his chemistry 1C course. I was also a student of Dr. Roland before working as a teaching assistant for her. I thank my graduate advisor Karen Meece and Katie Cramton for helping navigate all the deadlines and requirements during graduate school.

I thank all the professors in the department who helped throughout the years. I thank Professor Gene Switkes and Professor Jin Zhang who taught chemistry 1B and 1A my first year as an undergraduate. The exciting topics I learned in their courses motivated me to change my proposed major from biochemistry to chemistry.

I would like to thank all the lab members I got to meet and collaborate with in Professor Chen's lab. Thanks to Dr. Bruce Phebus, Dr. Chris Deming, Dr. Peiguang Hu, Dr. Limei Chen, Dr. Samantha Sweeney, Dr. Yi Peng, Dr. Gabby Lu, Dr. Bingzhang Lu, Dr. John Diniz, Dr. Gustavo Chata, Dr. Rene Mercado, Carolin wahl, and Qiming Liu. I want to thank Dr. Mauricio D. Rojas-Andrade for being my graduate student mentor when I was an undergraduate. Dr. Mauricio was my TA for chemistry 1N and invited me to help him do research in Professor Chen's lab. Dr. Mauricio introduced me to research and taught me all about the projects he worked on in the group. I would not be writing this without Dr. Mauricio's kindness and friendship.

Thank you to visiting Professor Zhang and Qiming for taking my wife and I to lunch at Noodle Talk in San Jose before the pandemic began. Professor Zhang paid for the lunch, and we planned to pay for the next lunch, but were unable to once the pandemic began.

I would like to thank our newer lab members John Tressel, Bingzhe Yu, Denner Pan, Davida Simpson, and visiting scholar Warisha Naseeb for their kindness and help in the lab. I want to thank all the work performed by my undergraduate students Jasleen Sandhu, Zahra Azhar, Rafael Cazares, and Edgar Olivar. Their contributions to this work were significant and being a mentor for them helped me grow as a researcher and a person.

Thank you to those in my cohort in the physical sciences building including Anna Johnston, Jerah Barnett, Beatriz Ehlke, Melissa Guarino-Hotz, Vivien Chenrrette, Mingpeng Chen, Megan Freyman, Shanwen Wang, and Stephanie Grace Pitch. Thank you to others in the department including Dr. A'lester Allen, Dr. Sarah Lindley, Dr. Eaindar Soe, Dr. Gregory Pitch, Pamela Schleissner, Levi Matsushima, Heng Zhang, Dr. Gabriella Amberchan, Dr. Jocelyn Macho, and Dr. Angel Resendez.

Thank you to my wife, Kimberly Pérez, for joining me through the entirety of this journey, your daily support helped me survive. Multiple times throughout the last 5 years I lost sight of the light at the end of the tunnel, and you helped me back every time. You made me a better person and catalyzed the motivation I needed to complete my PhD. I look back on the last 7 years and am thankful for having the opportunity to spend it with you and our beautiful son, Bobby Meowman Flay. I am excited to complete this chapter in my life and look forward to spending the rest of my life with you.

Thank you to my family for your endless support. To my mom, Jerilynn Ice, I thank you for supporting me through my bachelor's degree and graduate school, working multiple jobs, and loving me no matter what. You taught me tenacity and empathy. I hope to provide love and support to my children the way you provide it to me. Thank you to my sister, Hope Nichols, for always being available to talk during difficult times. Thank you to my stepdad, Allen Ice, for being with my mom and loving me like a son. Thank you to my dad, Matt Nichols, for believing in me.

I would like to thank the surgeons, nurses, medical workers, and doctors at UCSF who have helped me throughout my life, especially during my visits as a graduate student. I

was born in Santa Rosa, CA with bladder exstrophy in 1994 and immediately taken to UCSF medical hospital where I spent the first 8 weeks of my life. I have had several surgeries to reconstruct my bladder throughout my life. Part of my small intestine was cut to help with the bladder reconstruction. With this condition I get regular bladder infections and catheterize every three hours from a stoma created at the entrance to my belly button. During the beginning of the second year in graduate school I ruptured my bladder and was sick in the hospital for several weeks. In June 2020 and September 2021, I had two operations to bisect a section of my small intestine which was closing due to scar tissue from my bladder reconstruction operations. The scar tissue was causing small bowel obstructions which required regular visits to an emergency room where the nurses and doctors would place a tube through my nose into my stomach to help relieve built up pressure. These episodes occurred from 2018 to my last surgery in September 2021. I have received phenomenal medical care at UCSF my whole life and I owe the people working there a great thank you.

I am also thankful for the funding sources for my research, including UCSC chancellors' dissertation year fellowship, the John and Grace Wang award, and the National Science Foundation. Thank you to the molecular foundry, Lawrence Berkeley national laboratory and SLAC National accelerator laboratory. Thank you to the scientist who provided training on the equipment used at these facilities including Dr. Liana Klivansky and Dr. Chengyu Song.

The text of this dissertation includes reprints of the following previously published material:

Forrest Nichols, Jia En Lu, Rene Mercado, Ryan Dudschus, Frank Bridges, Shaowei Chen, "Platinum Oxide Nanoparticles for Electrochemical Hydrogen Evolution: Influence of Platinum Valence State", Chem. Eur. J., 2020, 26, 4136.

Forrest Nichols, Shaowei Chen, "Graphene Oxide Quantum Dot-Based Functional Nanomaterials for Effective Antimicrobial Applications", Chem. Rec., 2020, 20, 1505.

Forrest Nichols, Jia En Lu, Rene Mercado, Mauricio D. Rojas-Andrade, Shunlian Ning, Zahra Azhar, Jasleen Sandhu, Rafael Cazares, Chad Saltikov, Shaowei Chen, "Antibacterial Activity of Nitrogen-Doped Carbon Dots Enhanced by Atomic Dispersion of Copper", Langmuir, 2020, 36, 11629.

Forrest Nichols, Kenneth I. Ozoemena, and Shaowei Chen, "Electrocatalytic Generation of Reactive Species and Implications in Microbial Inactivation", Chin. J. Catal., 2021, accepted.

Forrest Nichols, Qiming Liu, Jasleen Sandhu, Zahra Azhar, Rafael Cazares, Rene Mercado, Frank Bridges, Shaowei Chen, "Platinum-complexed phosphorous-doped carbon nitride for electrocatalytic hydrogen evolution", J. Mater. Chem. A, 2022, 10, 5962.

The corresponding author, Professor Shaowei Chen, listed in the publications, directed and supervised the research which forms the basis for the dissertation.

# Chapter 1 Introduction

## 1.1 hydrogen as a sustainable fuel

Fossil fuels are a limited resource, and the burning of these fuels are the cause of anthropogenic climate change. Future energy production and consumption must be performed in a sustainable manner while preventing the release of detrimental greenhouse gases. Extensive research has been dedicated to new forms of energy generation technologies including hydro, wind, solar, and nuclear.[1-4] The combination of these technologies has the potential to produce renewable electricity at a scale far exceeding human demand. Additional technologies are necessary to store the produced renewable electricity to be used at peak times and locations. Battery technologies and renewable fuel research, including the generation of hydrogen fuel by electrocatalysis, serve as two highly studied solutions.[5-10] $H_2$ is an attractive fuel as its combustion produces water as a sole byproduct and $H_2$ generation can be carried out on an appropriate electrocatalyst via water electrolysis.

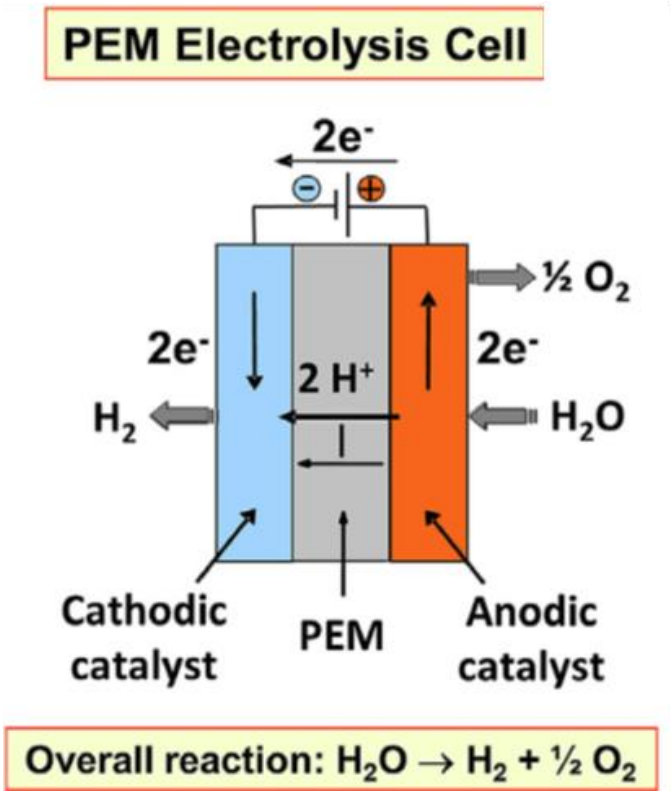


**Figure 1.** schematic representation of a proton exchange membrane (PEM) water electrolysis device. Reproduced with permission © Elsevier 2022.[11]

Figure 1 depicts a proposed water electrolysis device composed of three components, an anodic catalyst material responsible for oxidizing water to form oxygen ($O_2$) known as the oxygen evolution reaction (OER), a proton exchange membrane (PEM) which acts as a barrier between the cathode and anode compartment, shuttling protons produced during OER toward the cathodic compartment of the electrolysis device, and a cathodic catalyst material responsible for reducing protons forming $H_2$ known as the hydrogen evolution reaction (HER). These components complete the overall water electrolysis reaction converting water to molecular oxygen and hydrogen. The produced hydrogen can be collected and used as fuel to power devices including proton exchange membrane fuel cells. A device like the one described here could theoretically be installed in every gas station around the world allowing for onsite fuel production and significantly reducing

the current cost of fuel transportation. One can begin to imagine the many benefits of hydrogen fuel over the current fossil fuel economy.

### 1.2 Electrochemistry of the hydrogen evolution reaction (HER)

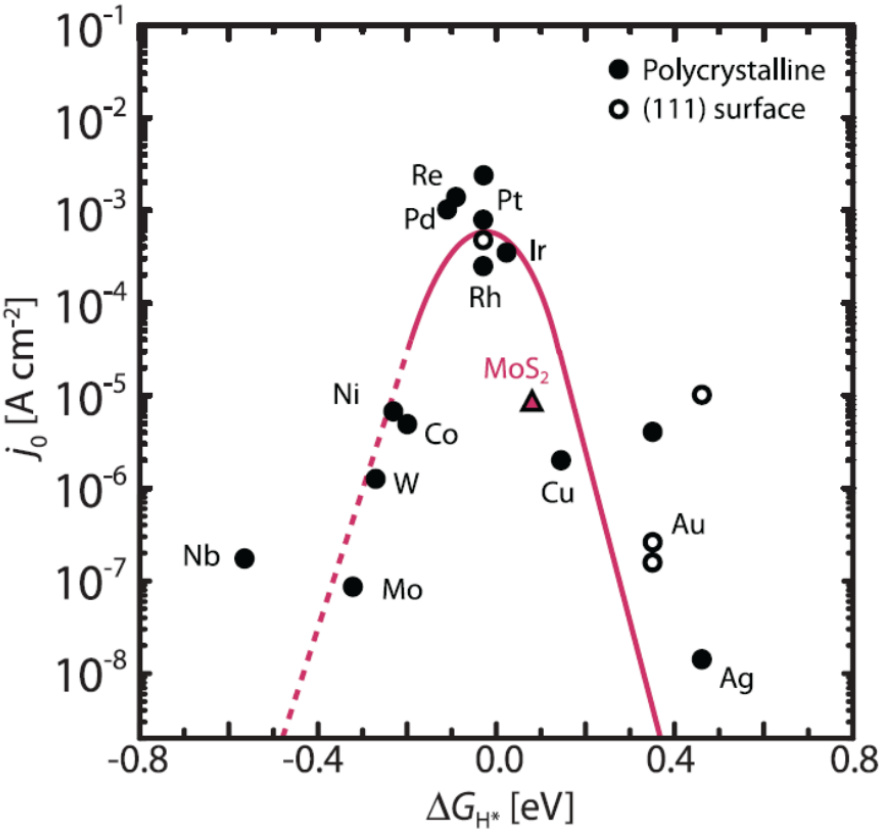


**Figure 2.** HER volcano plot for various bulk metal materials. Reproduced with permission © AAAS 2017.[12]

Platinum based catalysts remain the leading material for hydrogen evolution due to their low overpotential required for HER attributed to an ideal hydrogen adsorption free energy. Figure 2 depicts a volcano shaped relationship between experimentally measured exchange current density ($j_0$) versus theoretically calculated hydrogen adsorption free energy ($\Delta G_{H^*}$) for several bulk metallic materials. One can identify platinum at the top of the volcano plot in figure 2 resulting from its high exchange current density and $\Delta G_{H^*}$

near 0 eV. This relationship follows from the Sabatier principle of heterogeneous catalysis which states an interaction between a catalyst material and its substrate should be balanced to optimize product formation. In the example of HER, materials such as Niobium and Molybdenum have negative $\Delta G_{H^*}$ suggesting a strong hydrogen adsorption energy. In this case HER is limited by the catalyst's ability to release the adsorbed hydrogen and continue the catalytic process. Relatively inert metals like gold and silver on the other hand have positive $\Delta G_{H^*}$ suggesting hydrogen struggles to adsorb on the catalyst surface. Electrocatalysis is a surface science and cannot proceed without adsorption.

$$2H^+_{(aq)} + 2e^- \rightarrow H_{2\,(g)} \qquad \text{eq. 1}$$

Volmer Step $\quad H^+ + e^- \rightarrow H_{ads}$ eq. 2

Tafel Step $\quad 2H_{ads} \rightarrow H_2$ eq. 3

Heyrovsky Step $\quad H^+{}_{(aq)} + H_{ads} + e^- \rightarrow H_2$ eq. 4

HER proceeds in an acidic electrolyte following equation 1 where two aqueous protons combine with two electrons to form hydrogen gas. Equation 1 can be broken down into a two-step process with two possible second step reaction pathways. The first step must involve hydrogen adsorption, referred to as the Volmer step. The second step can follow either a Tafel or Heyrovsky step. The Tafel step, energetically more favorable compared to the Heyrovsky step, occurs when two protons adsorbed at a catalyst surface combine and release to form hydrogen gas. The Heyrovsky step occurs when one adsorbed proton combines with one non-adsorbed aqueous proton and an electron to form hydrogen gas. These two possible routes are then referred to as Volmer-Tafel and Volmer-Heyrovsky mechanisms. Distinguishing between these two pathways is

important in assessing an HER catalyst and can be done through Tafel plots of the resulting polarization curves. Details for these calculations and interpretations are provided within the discussion of chapters 2 and 3.

### 1.3 Nanomaterial design methods

In section 1.2 we discussed the benefits of platinum based electrocatalysts for HER. However, this emerging technology has additional constraints for real world applications. The hydrogen generation must be efficient in its use of electricity, but also the materials used for such a device needs to be economical. This constraint is the primary driving force limiting large scale incorporation of HER technologies as platinum is low in earth abundance, seen by figure 3, resulting in high costs.

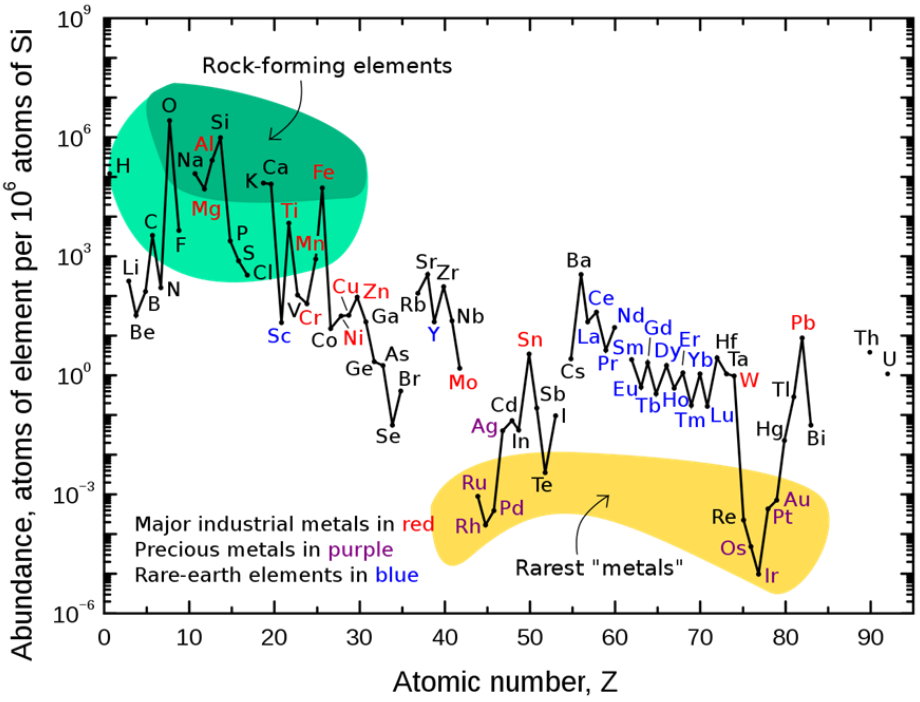


**Figure 3.** Abundance (atomic fraction) of elements on earth as a function of atomic number (Z).[13]

Due to the economics surrounding platinum-based catalysts a major question to answer becomes; “how can we decrease the amount of platinum used while retaining or improving the electrochemical performance of the catalyst for HER?” Two solutions are explored in chapters 2 and 3. Chapter 2 utilizes a bottom-up method for synthesizing carbon nitride through the polymerization of urea. The alkaline nature of carbon nitride with thermal refluxing is utilized for $PtO_x$ nanoparticle deposition. Synthetic parameters are changed in chapter 3 to prevent $PtO_x$ deposition, namely, an aqueous solvent is replaced with a non-aqueous acetone solvent and reaction temperature is reduced using an ice bath. Furthermore, selection of an alternative platinum salt is implemented to prevent nanoparticle deposition and promote platinum chelation to pyridinic nitrogen centers on the carbon nitride support material.

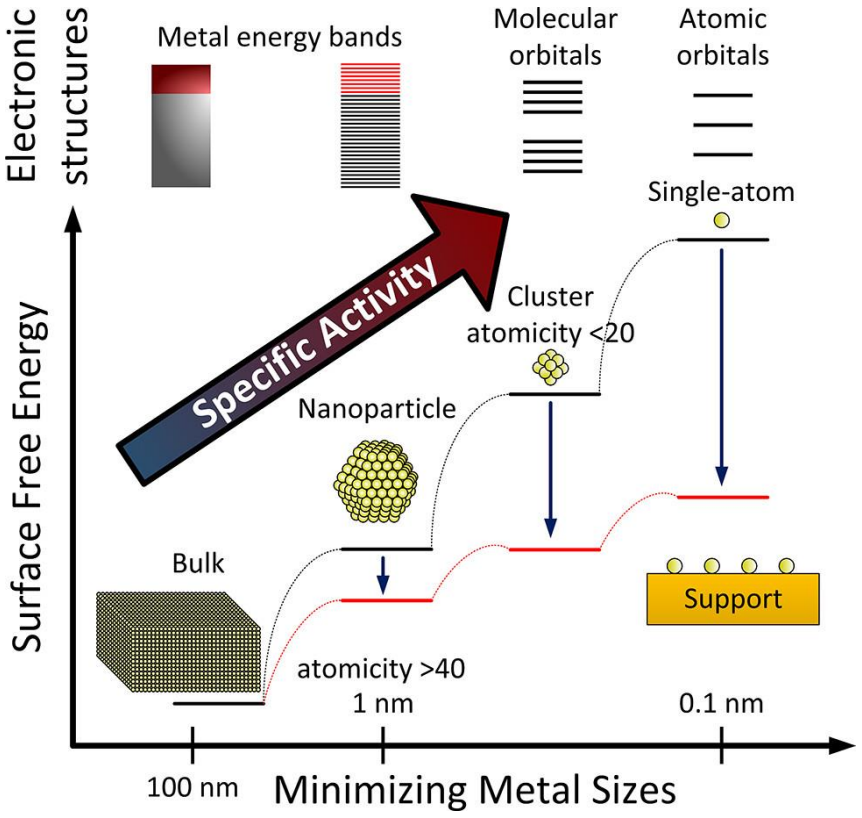


**Figure 4.** Particle geometry, electronic structure, and surface free energy as a function of particle size. Reproduced with permission from © 2021 American Chemical Society.[14]

Electrocatalysis is a surface science meaning only atoms at the surface of an electrode participate in the catalytic process. Increasing a particle's surface area (S) to volume (V) ratio (S/V) will increase the percentage of atoms participating in a catalytic process and reduce the amount of material required to produce a given amount of hydrogen. As particle size decreases S/V increases due to the relationship between S/V and a particle's radius (R) given by S/V = 3/R. For this reason, decreasing the particle size of a material is one strategy for improving the mass activity for HER and other electrocatalytic processes.

One can see from figure 4 that decreasing particle size results in material property changes related to electronic and surface energy properties. Smaller particle size leads to an increase in surface free energy which means smaller particles are less stable and want to aggregate together to minimize this surface energy. Under this condition particle-support interactions become important to stabilize the small particles as illustrated by red lines in figure 4. For this reason, one must select an appropriate support material as described in chapters 2 and 3. Furthermore, electronic structure of the material begins to change from metallic energy bands in bulk materials to atomic orbitals in the case of a single atom catalyst material. This implies bulk platinum will behave different from single atom isolated platinum likely resulting in changes to $\Delta G_{H^*}$ as described previously. However, through control of single atom / support interactions one can tailor hydrogen binding and therefore tune the HER capability of the material. This will be further discussed in chapter 3.

Other catalyst synthetic methods are described in further detail in chapter 4 and chapter 5. Both bottom-up and top-down strategies are considered and compared. A bottom-up strategy is utilized in chapter 6 to produce copper doped carbon quantum dots from the solid-state polymerization of citric acid and copper acetylacetonate. Copper

acetylacetonate is implemented due to its relative thermal stability among other copper containing salts to prevent decomposition and formation of toxic copper containing nanoparticles.

### 1.4 Electrochemistry for reactive species generation

Assurance of safe and healthy water is critical for progress of life on earth. Many methods for water disinfection have been implemented, including physical, biological, and chemical pathways [15]. A chemical route toward water disinfection typically involves the use of advanced processes to remove contaminants through oxidation. Several advanced oxidative processes (AOP) have already been implemented into water treatment, including ozonation and UV light [16]. The field of electrochemistry provides another viable pathway toward efficient water disinfection, which also poses a sustainable pathway as electricity supply becomes increasingly renewable [17]. Water treatment by AOP primarily focusses on production of highly oxidizing substances, such as hydroxyl radicals ($HO^{\bullet}$); however, significant research has been dedicated in recent literature to the electrochemical generation of many other reactive species (RS), including reactive oxygen species (ROS) like superoxide ($O_2^{\bullet -}$) and hydrogen peroxide ($H_2O_2$), reactive chlorine species (RCS), reactive nitrogen species (RNS), as well as reactive sulfur species (RSS), which can also be used in the water treatment process [18-21]. Numerous microorganisms have been found to transmit diseases through water systems, including bacteria, viruses, protozoa, and helminths [22]. It is essential for humans to treat these threats during the water disinfection process. Bacteria are particularly susceptible to the presence of RS with damage to proteins, DNA, and lipid membranes leading to cell death [18-21]. This makes electrochemical generation of RS an attractive pathway toward microbial inactivation during water treatment. There are several distinct

advantages of electrochemical RS generation over other methods such as photocatalysis. One major advantage is the ability for an electrochemical device to disinfect a wide variety of contaminated water including particularly cloudy or murky water that would otherwise prevent the transmittance of light through the water medium necessary for photocatalytic treatment. Another distinct advantage is the ability to have fine control over the input energy source, electricity, during the decontamination process.

Like the oxygen reduction reaction (ORR) in fuel cell electrocatalysis, the conversion of molecular oxygen to water in a biological cell is not without error and can lead to toxic oxygen by-products, such as superoxide ($O_2^{\bullet-}$) and hydrogen peroxide ($H_2O_2$) [23-31]. Production of these species during electrocatalysis is often categorized as an undesirable effect; however, production of such ROS can be advantageous under controlled conditions. From the electrochemistry perspective, researchers are beginning to design electrocatalysts capable of efficiently producing ROS for many applications, including industrial hydrogen peroxide production, organic molecule synthesis, microbial inactivation, water disinfection, electrocoagulation, and other contaminant disinfection (e.g., organic dye degradation) [18-21, 32-39].

Electrochemical ROS generation can occur on the cathode by reduction of molecules, including molecular oxygen, or at the anode through oxidation of adsorbates, such as water. A proposed stepwise mechanism for generating such ROS is depicted in reaction (1), flowing from left to right for the reduction processes and right to left for the oxidation processes [40].

$$O_2 \leftrightarrows O_2^{\bullet-} \leftrightarrows H_2O_2 \leftrightarrows HO^{\bullet} \leftrightarrows H_2O \qquad (1)$$

From reaction (1), we can see that there are three primary ROS products, superoxide, hydrogen peroxide, and hydroxyl radical. In Chapter 4, we will explore in further detail

the relationship between these species, their chemical reactivity, and relevant electrocatalysts reported recently for the synthesis of these species.

### 1.5 Photocatalysis for the generation of reactive oxygen species

The work discussed thus far has focused on the use of electricity as the driving force for catalytic product generation. Chapter 5 and chapter 6 will discuss work focused on designing light sensitive materials for photocatalytic generation of reactive oxygen species. Photocatalysis is particularly attractive because the excitation light source can be produced using renewable electricity, as discussed previously, or directly from sunlight. Current research has focused on an array of nanomaterials capable of producing various photocatalytic products including hydrogen, carbon fuels, and reactive species.[41-46]

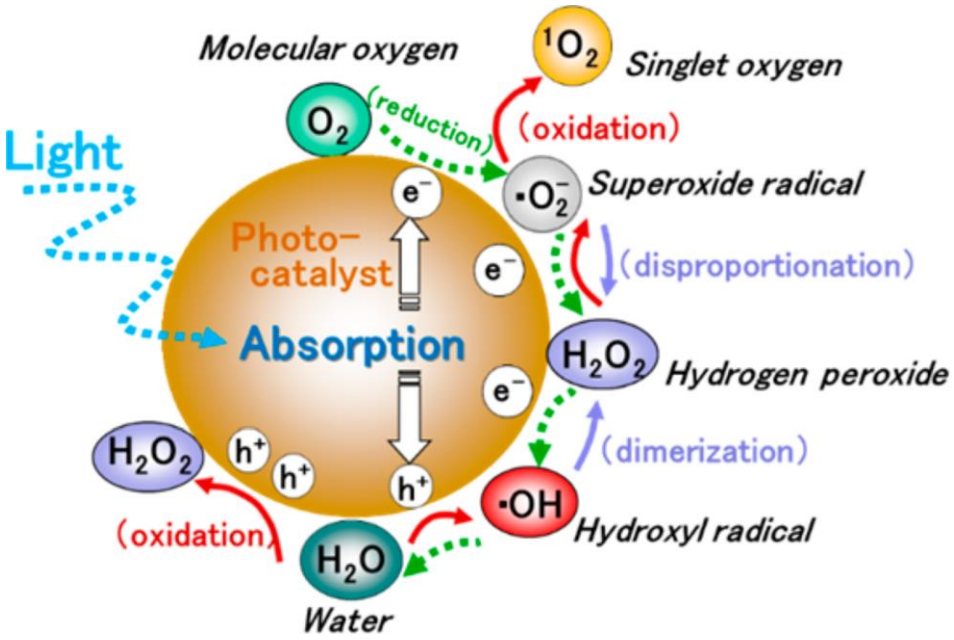


**Figure 5.** Reactive oxygen species generated by photocatalytic reduction and oxidation of water and molecular oxygen by photoinduced electron and hole.[47]

The photocatalytic effect is carried out using light sensitive, typically semiconductor, nanoparticles capable of absorbing a photon of light to excite electrons from a ground

state to an excited state producing a photoinduced electrons ($e^-$) and holes ($h^+$) on the nanoparticle surface. Possessing sufficient energy, the photo induced electron acting as a reducing agent and hole acting as an oxidizing agent can react through redox reactions with surface adsorbed $H_2O$ or $O_2$ to produce the same ROS as described in equation 1 of section 1.4. Figure 5 depicts this process on the photocatalyst surface.

## 1.6 Reactive species interaction with microorganisms

### 1.6.1 Introducing reactive species interactions with microorganisms

Reactive species (RS) can cause severe damage within a microorganism at high enough levels and in the absence of remediation pathways [35, 48-51]. For instance, RS can oxidize amino acids within proteins and nucleic acids within DNA, leading to protein and DNA inactivation [52-56]. Oxidation of polyunsaturated lipids within the microorganism's lipid membrane can cause structural damage with apoptosis and cell death after prolonged lipid membrane degradation [57-61]. Outer lipid membrane degradation is of particular importance since RS does not need to penetrate the cell to cause microorganism inactivation, considering the limited lifespan of the generated RS and difficulties penetrating microbial membranes [62, 63]. If the RS can contact the surface lipid layer of the microorganism, microbial inactivation can occur [64, 65]. Notably, microorganisms produce small levels of RS on their own, which has led to the development of specific enzymes used to break down RS, as shown in Fig. 6. The following section will explore the regulation of these RS within the cell.

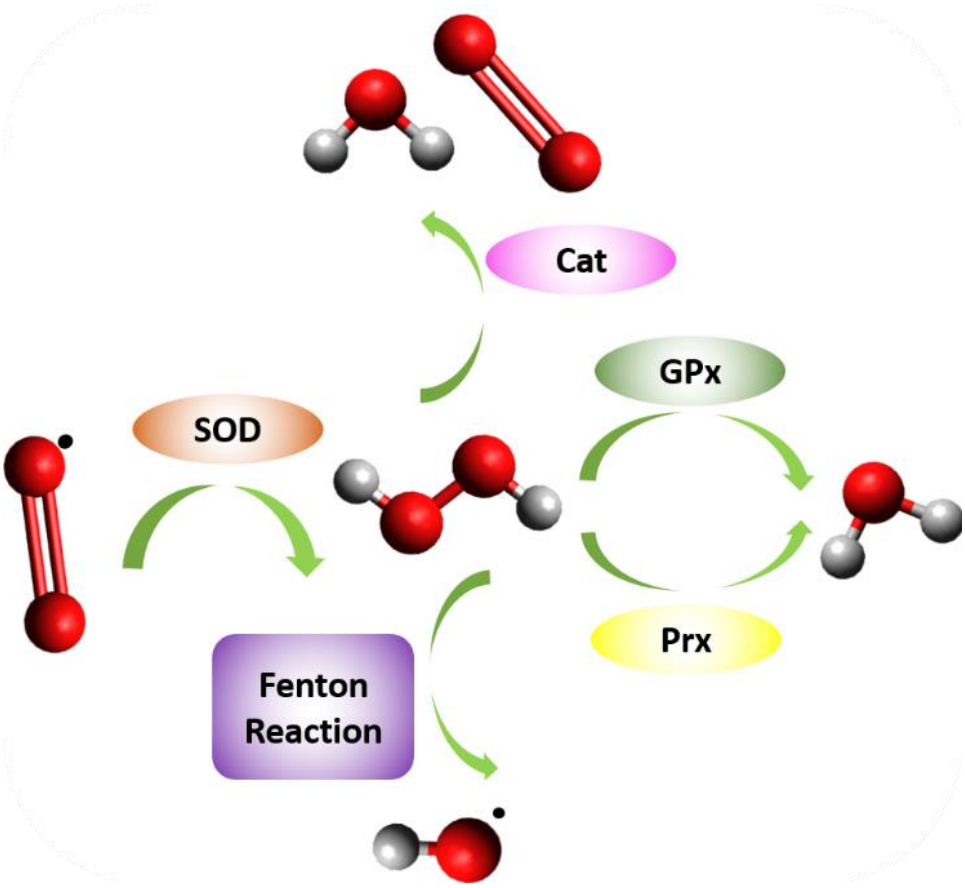


**Fig. 6.** Regulation of reactive oxygen species within the cell by enzymes superoxidase dismutase (SOD), Catalase (Cat), and other peroxidase enzymes (GPx, and Prx). Red spheres represent oxygen and grey spheres denote hydrogen.

### 1.6.2 Oxidative homeostasis regulated within microorganisms

It is also important to note that microorganisms encounter some level of RS regularly with response pathways designed to circumvent the damaging effects of RS [66, 67]. Toxic RS can be removed by antioxidant enzymes within a microorganism. These enzymes include superoxidase dismutase (SOD), catalase (Cat) and glutathione peroxidase (GPx) (Fig. 6) [68]. SOD was first discovered by Fridovich and McCord in 1969 [69]. The most common RS found natively within the cell is $O_2^{\bullet-}$ produced within the electron transport chain of mitochondria [70, 71]. SOD has been found to catalyze the

conversion of $O_2^{\bullet-}$ to $H_2O_2$. Working alone, the conversion of one RS to another is not ideal; however, Loew identified an antioxidant enzyme, Cat, in 1900 which catalyzed the conversion of $H_2O_2$ to $H_2O$ and $O_2$ [72]. In 1957, Mills discovered another enzyme, GPx, that was responsible for breaking down hydroperoxides, including lipid hydroperoxides, which were formed during radical reactions with lipid membranes found in microorganisms [73]. There have been several other peroxidase (Prx)-like enzymes discovered thereafter [18, 74-77]. A schematic summary of RS conversion within the cell is shown in Fig. 6. It is important to note the familiarity that microorganisms have with RS, such as $O_2^{\bullet-}$ and $H_2O_2$, due to their production within mitochondria and their evolved methods for controlling damage from these species. RS including $HO^{\bullet}$ and HClO are not directly produced within the cell, providing less pathways for damage prevention by the microorganism's stress response. Under increased levels of oxidative stress, microorganisms are unable to prevent damage caused by their interaction with RS. In these cases, there are some measures that the microorganism can take to repair damage to the cell. In-depth studies of these pathways can be found in the literature [77-80].

Microorganisms exist under a spectrum of RS exposure (Fig. 7a). This is because microorganisms naturally produce some level of RS, most often within mitochondria, through aerobic respiration processes. Normal levels of RS are handled by various cellular processes and minor damage caused by RS can be repaired. When a certain RS threshold is surpassed, cellular processes cannot keep up with RS removal and the microorganism enters a state of oxidative stress. Under these conditions, microbes increase the production of glutathione (GSH), which is limited by the availability of the precursor amino acid, cysteine, and the expression of the gene *gshA* [81]. GSH will become oxidized to glutathione disulfide (GSSG) upon contact with RS (Fig. 7b). Oxidation of GSH prevents oxidation of other nearby species that may result in long-

lasting damage to the microbial organism. Many research reports have used this as a method of determining effective antimicrobial catalysts through quantifying GSH interactions [82, 83]. Electrocatalysts must produce enough RS to overcome the presence of glutathione before moving on to degrade the microorganism's cellular components. One frequently used method for quantifying GSH and thiol oxidation is known as the Ellman's assay [84, 85]. In this process the Ellman reagent, 5,5′-dithio-bis(2-nitrobenzoic acid) (DTNB), is added and light absorption near 430 nm is measured over time (Fig. 7c). As shown in Fig. 7a, there is a point at which the microorganism cannot properly function in the presence of RS, and experience damaging effects, as detailed below.

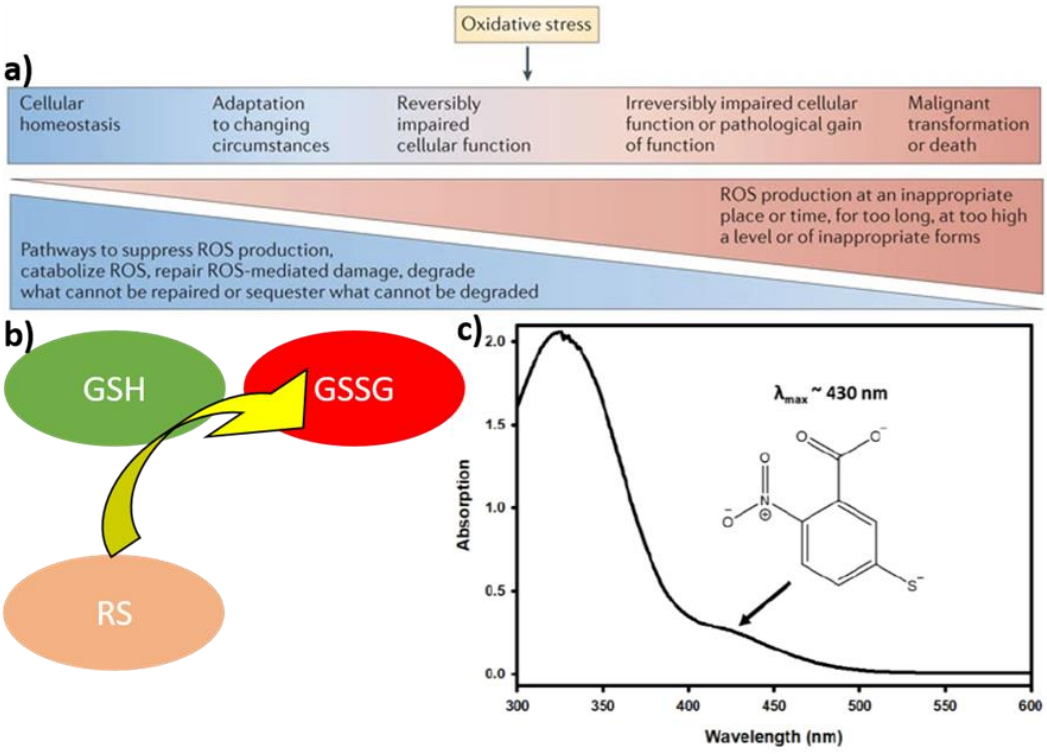


**Fig. 7.** (a) spectrum of cellular response to RS ranging from cellular homeostasis, left, to cell death, right. (b) Schematic representation of glutathione (GSH) oxidation to glutathione disulphide (GSSG) by reactive species (RS). (c) UV-vis absorption spectrum

for the Ellman's reagent. Panels (a) copyright 2013, Springer Nature. Panel (c) copyright 2020, Royal chemistry society.

### 1.6.3 Damaging effects caused by reactive species

#### Lipids

Exogenous RS first encounter the lipid membrane of the cell, and this must be breached to further interact with organelle and other cell components, such as proteins and DNA. In eukaryotes, this lipid membrane is composed of glycerophospholipids with >50% of these phospholipids comprised of phosphatidylcholine [86]. These lipids self-organize to form a bilayer exposing polar groups toward the surface of the membrane. Nonpolar groups within the membrane are comprised of saturated and cis-unsaturated fatty acyl chains. Both the polar groups at the surface of the membrane and the unsaturated acyl chains are vulnerable to RS oxidation. The oxidation of the unsaturated nonpolar fatty acyl chains by RS is known as lipid peroxidation and results in the oxidative degradation [64, 65, 87-89]. Fig. 8a depicts the lipid peroxidation of linoleate resulting in structural changes to the lipid and addition of polar oxygen-containing functional groups. This reaction follows a free radical chain reaction mechanism resulting in proliferation of membrane damage and incorporation of oxygen functional groups within the nonpolar chains. The oxygen functional groups at this site are polar in nature and leads to increased hydrophilicity and ultimately decomposition of the membrane barrier and exposure of endogenous cellular components.

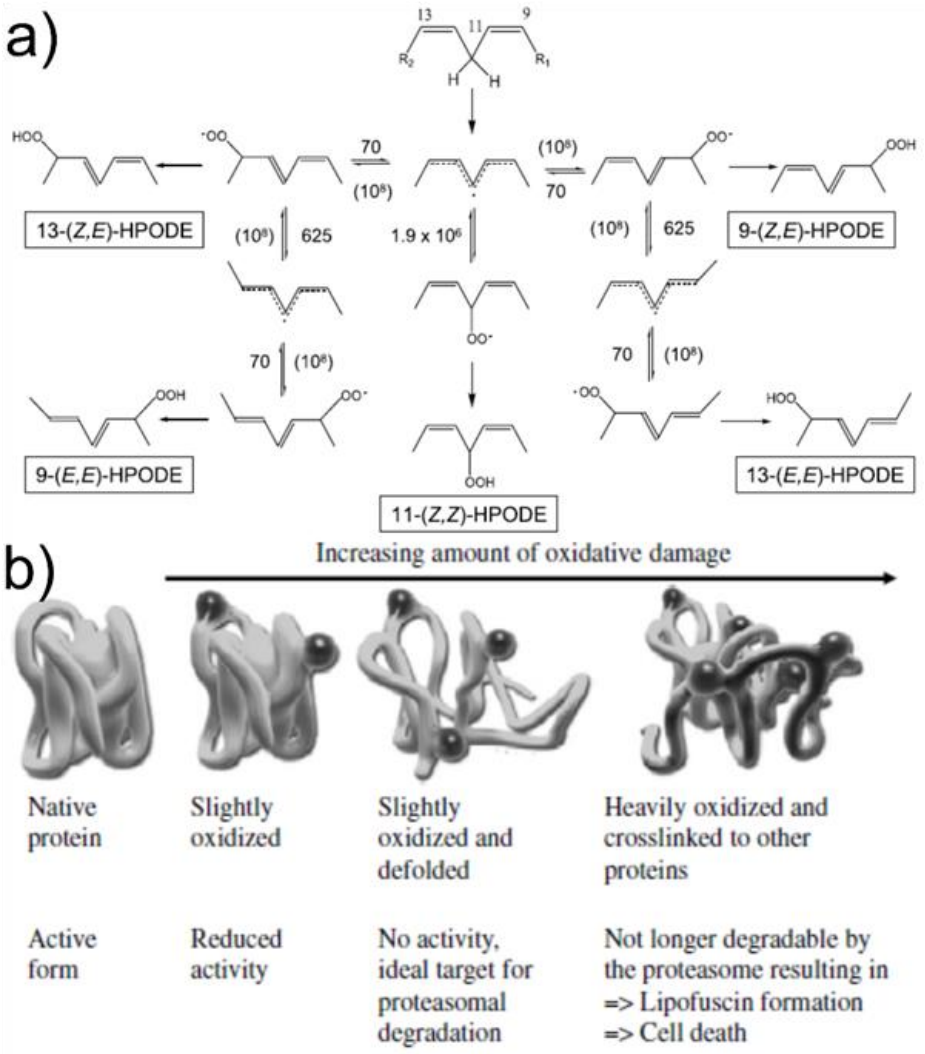


**Fig. 8.** (a) An example of lipid peroxidation using linoleate as the starting substrate. copyright 2005, Elsevier. (b) Results of protein damage caused by increased levels of oxidation. copyright 2003, Elsevier.

**Proteins**

Once the lipid membrane of the organism is compromised, further RS damage may be accrued to inner cellular components, including proteins and DNA. Exposure of RS to a protein leads to modifications of amino acid side chains by protein oxidation. These changes can prevent protein function or make the protein increasingly susceptible to

proteolytic degradation by the proteosome, a catalytic ATP-independent enzyme complex designed to degrade proteins tagged by ubiquitin [90]. This is part of the cell's evolved methods for self-preservation by removing damaged cellular components.

The ability for the proteosome to track and remove damaged protein has been shown to correlate with oxidant concentration [91]. At mild oxidant concentrations the proteosome can keep up with proper removal of damaged proteins. Under conditions of high oxidant concentrations, damaged proteins are less likely to be captured and removed from the cell matrix resulting in an increased opportunity for these proteins to become further damaged or interact with undamaged cell components. These protein-protein interactions can lead to protein cross-linkage where two proteins become attached to one another either by hydrophobic, electrostatic, or covalent interactions. Left unchecked, the cross-linking can continue and create a protein aggregate. Such aggregates can overwhelm the proteolytic system making basic cell function increasingly difficult. Fig. 8b depicts the progression of protein damage with increased oxidation from left to right. Heavily oxidized and crosslinked proteins cannot be degraded by the proteosome and establish cell signals related to programmed cell death. For antimicrobial purposes, this creates a circumstance in which increased RS production only improves bacterial inactivation efficiency.

**DNA**

A third vital component susceptible to RS interactions is DNA. The central dogma of biology states that DNA holds the code necessary for producing cellular components critical for survival. DNA is converted to RNA through transcription within the nucleus and RNA produces the final product including proteins and enzymes through translation [92]. Thus, cell function relies on the preservation of DNA and any deletions, mutations, or other structural damage can lead to devastating effects during the transcription or translation processes.

Structurally DNA is comprised of a sugar phosphate backbone connected in a double helix through hydrogen bonding between 4 unique nucleotide bases, adenine, thymine, guanine, and cytosine. Damage to the DNA can occur in many ways including deletion of one or more nucleotide base pair, mutation of one or more base pairs replaced by another, or by breaks in the DNA chain either through single (SSB) or double strand breaks (DSB) [93, 94]. This type of damage to DNA is so frequent that multiple recovery pathways have evolved within the cell to correct such damage and prevent mutant RNA or protein from being produced. With this reasoning, DNA damage does not directly result in cell death, but prolonged exposure to RS and further DNA damage can result in irreversible DNA damage and contribute to cell inactivation.

$OH^{\bullet}$ has been shown to interact with DNA nucleotide base pairs through addition to the pyrimidine region of thymine and cytosine and to the purine region of adenine and guanine [95]. This interaction can lead to separation of the double stranded structure and prevent transcription from occurring. HClO has also been shown to cause nucleotide chlorination leading to similar damaging effects [96]. With sufficient RS concentration the microorganism exhibits an increase in devastating effects including lipid peroxidation, protein degradation, and irreversible DNA damage culminating to prevent necessary cell functions and ultimately results in cell inactivation.

## 1.7 References


1. Kougias, I., et al., *Analysis of emerging technologies in the hydropower sector.* Renewable and Sustainable Energy Reviews, 2019. **113**: p. 109257.
2. Vargas, S.A., et al., *Wind power generation: A review and a research agenda.* Journal of Cleaner Production, 2019. **218**: p. 850-870.

3. Kabir, E., et al., *Solar energy: Potential and future prospects.* Renewable and Sustainable Energy Reviews, 2018. **82**: p. 894-900.

4. Wang, Q., R. Li, and G. He, *Research status of nuclear power: A review.* Renewable and Sustainable Energy Reviews, 2018. **90**: p. 90-96.

5. Ue, M., K. Sakaushi, and K. Uosaki, *Basic knowledge in battery research bridging the gap between academia and industry.* Materials Horizons, 2020. **7**(8): p. 1937-1954.

6. Carmo, M., et al., *A comprehensive review on PEM water electrolysis.* International Journal of Hydrogen Energy, 2013. **38**(12): p. 4901-4934.

7. Nocera, D.G., *The Artificial Leaf.* Accounts of Chemical Research, 2012. **45**(5): p. 767-776.

8. Seh, Z.W., et al., *Combining theory and experiment in electrocatalysis: Insights into materials design.* Science, 2017. **355**(6321).

9. Zheng, Y., et al., *Advancing the Electrochemistry of the Hydrogen-Evolution Reaction through Combining Experiment and Theory.* Angewandte Chemie-International Edition, 2015. **54**(1): p. 52-65.

10. Zou, X.X. and Y. Zhang, *Noble metal-free hydrogen evolution catalysts for water splitting.* Chemical Society Reviews, 2015. **44**(15): p. 5148-5180.

11. Falcão, D. and A. Pinto, *A review on PEM electrolyzer modelling: Guidelines for beginners.* Journal of Cleaner Production, 2020. **261**: p. 121184.

12. Seh, Z.W., et al., *Combining theory and experiment in electrocatalysis: Insights into materials design.* Science, 2017. **355**(6321): p. eaad4998.

13. Haxel, G., *Rare earth elements: critical resources for high technology*. Vol. 87. 2002: US Department of the Interior, US Geological Survey.

14. Fonseca, J. and J. Lu, *Single-Atom Catalysts Designed and Prepared by the Atomic Layer Deposition Technique.* Acs Catalysis, 2021. **11**(12): p. 7018-7059.

15. Miklos, D.B., et al., *Evaluation of advanced oxidation processes for water and wastewater treatment–A critical review.* Water Res., 2018. **139**: p. 118-131.

16. Vallejo, M., et al., *Overview of the PCDD/Fs degradation potential and formation risk in the application of advanced oxidation processes (AOPs) to wastewater treatment.* Chemosphere, 2015. **118**: p. 44-56.

17. Hand, M.M. and S.D. Baldwin, E.; Reilly, J.M.; Mai, T.; Arent, D.; Porro, G.; Meshek, M.; Sandor, D. eds, *Renewable Electricity Futures Study.* NREL, 2012. **1-4**.

18. Imlay, J.A., *Pathways of oxidative damage.* Annu. Rev. Microbiol., 2003. **57**(1): p. 395-418.

19. Nosaka, Y. and A.Y. Nosaka, *Generation and Detection of Reactive Oxygen Species in Photocatalysis.* Chem. Rev., 2017. **117**(17): p. 11302-11336.

20. Krumova, K. and G. Cosa, *Chapter 1 Overview of Reactive Oxygen Species*, in *Singlet Oxygen: Applications in Biosciences and Nanosciences, Volume 1*. 2016, The Royal Society of Chemistry. p. 1-21.

21. Gerschman, R., *Oxygen poisoning and x-irradiation: a mechanism in common*, in *Glutathione*. 1954, Elsevier. p. 288-291.

22. Lugo, J.L., E.R. Lugo, and M. Puente, *A systematic review of microorganisms as indicators of recreational water quality in natural and drinking water systems.* J. Water Health, 2020. **19**(1): p. 20-28.

23. Mercado, R., et al., *Nitrogen-Doped Porous Carbon Cages for Electrocatalytic Reduction of Oxygen: Enhanced Performance with Iron and Cobalt Dual Metal Centers.* ChemCatChem, 2020. **12**(12): p. 3230-3239.

24. Lu, B., et al., *Oxygen Reduction Reaction Catalyzed by Carbon-Supported Platinum Few-Atom Clusters: Significant Enhancement by Doping of Atomic Cobalt.* Research, 2020. **2020**: p. 9167829.

25. Jiang, H., et al., *Defect-rich and ultrathin N doped carbon nanosheets as advanced trifunctional metal-free electrocatalysts for the ORR, OER and HER.* Energy Environ. Sci., 2019. **12**(1): p. 322-333.

26. Li, J.Z., et al., *Atomically dispersed manganese catalysts for oxygen reduction in proton-exchange membrane fuel cells.* Nat. Catal., 2018. **1**(12): p. 935-945.

27. Jiang, K., J. Zhao, and H. Wang, *Catalyst design for electrochemical oxygen reduction toward hydrogen peroxide.* Adv. Funct. Mater., 2020. **30**(35): p. 2003321.

28. Tian, X., et al., *Understanding the Promotion Effect of Mn on CuO/Al2O3 for Catalyzed HCl Oxidation to Cl2.* ChemCatChem, 2020. **12**(12): p. 3240-3248.

29. He, D., et al., *Hydrogen peroxide electrosynthesis via regulating the oxygen reduction reaction pathway on Pt noble metal with ion poisoning.* Electrochim. Acta, 2021. **371**: p. 137721.

30. Dong, K., et al., *Noble-metal-free electrocatalysts toward H 2 O 2 production.* J. Mater. Chem. A, 2020. **8**(44): p. 23123-23141.

31. Jung, E., et al., *Recent Advances on Electrochemical Oxygen Reduction to H2O2: Catalyst and Cell Design.* ACS Energy Lett., 2020. **5**(6): p. 1881-1892.

32. Pelaez, M., et al., *A review on the visible light active titanium dioxide photocatalysts for environmental applications.* Appl. Catal. B . 2012. **125**: p. 331-349.

33. Fu, P.P., et al., *Mechanisms of nanotoxicity: Generation of reactive oxygen species.* J. Food Drug Anal., 2014. **22**(1): p. 64-75.

34. Graves, D.B., *The emerging role of reactive oxygen and nitrogen species in redox biology and some implications for plasma applications to medicine and biology.* J. Phys. D Appl. Phys., 2012. **45**(26): p. 263001.

35. Sirelkhatim, A., et al., *Review on Zinc Oxide Nanoparticles: Antibacterial Activity and Toxicity Mechanism.* Nanomicro Lett., 2015. **7**(3): p. 219-242.

36. Li, Q.L., et al., *Antimicrobial nanomaterials for water disinfection and microbial control: Potential applications and implications.* Water Res., 2008. **42**(18): p. 4591-4602.

37. Barrera-Díaz, C., et al., *Electrochemical advanced oxidation processes: an overview of the current applications to actual industrial effluents.* J. Mex. Chem., 2014. **58**(3): p. 256-275.

38. Gonzalez-Rivas, N., H. Reyes-Perez, and C.E. Barrera-Diaz, *Recent Advances in Water and Wastewater Electrodisinfection.* Chemelectrochem, 2019. **6**(7): p. 1978-1983.

39. Linares-Hernández, I., et al., *A combined electrocoagulation–electrooxidation treatment for industrial wastewater.* J. Hazard. Mater., 2010. **175**(1-3): p. 688-694.

40. Song, C. and J. Zhang, *Electrocatalytic oxygen reduction reaction*, in *PEM Fuel Cell Electrocatalysts and Catalyst Layers*. 2008, Springer. p. 89-134.

41. Beydoun, D., et al., *Role of nanoparticles in photocatalysis.* Journal of Nanoparticle Research, 1999. **1**(4): p. 439-458.

42. Kashef, N., Y.Y. Huang, and M.R. Hamblin, *Advances in antimicrobial photodynamic inactivation at the nanoscale.* Nanophotonics, 2017. **6**(5): p. 853-879.

43. Rawalekar, S. and T. Mokari, *Rational Design of Hybrid Nanostructures for Advanced Photocatalysis.* Advanced Energy Materials, 2013. **3**(1): p. 12-27.

44. Vivero-Escoto, J.L., et al., *Recent progress in mesoporous titania materials: adjusting morphology for innovative applications.* Science and Technology of Advanced Materials, 2012. **13**(1).

45. Wen, M.C., et al., *Design and architecture of metal organic frameworks for visible light enhanced hydrogen production.* Applied Catalysis B-Environmental, 2017. **218**: p. 555-569.

46. Yahya, N., et al., *A review of integrated photocatalyst adsorbents for wastewater treatment.* Journal of Environmental Chemical Engineering, 2018. **6**(6): p. 7411-7425.

47. Nosaka, Y. and A.Y. Nosaka, *Generation and Detection of Reactive Oxygen Species in Photocatalysis.* Chemical Reviews, 2017. **117**(17): p. 11302-11336.

48. Chen, G.Y. and G. Nunez, *Sterile inflammation: sensing and reacting to damage.* Nat. Rev. Immunol., 2010. **10**(12): p. 826-837.

49. Holmstrom, K.M. and T. Finkel, *Cellular mechanisms and physiological consequences of redox-dependent signalling.* Nat. Rev. Mol., 2014. **15**(6): p. 411-421.

50. Hou, J., et al., *Toxicity and mechanisms of action of titanium dioxide nanoparticles in living organisms.* J. Environ. Sci., 2019. **75**: p. 40-53.

51. Liao, X.W., et al., *Enhanced Electrocatalysis via Boosted Separation of Hot Charge Carriers of Plasmonic Gold Nanoparticles Deposited on Reduced Graphene Oxide.* Chemelectrochem, 2019. **6**(5): p. 1419-1426.

52. Singh, A., et al., *Oxidative Stress: A Key Modulator in Neurodegenerative Diseases.* Molecules, 2019. **24**(8): p. 1583.

53. Kryston, T.B., et al., *Role of oxidative stress and DNA damage in human carcinogenesis.* Mutat. Res. Fund. Mol. M., 2011. **711**(1-2): p. 193-201.

54. Dizdaroglu, M. and P. Jaruga, *Mechanisms of free radical-induced damage to DNA.* Free Radic. Res., 2012. **46**(4): p. 382-419.

55. Cadet, J., T. Douki, and J.L. Ravanat, *Oxidatively generated base damage to cellular DNA.* Free Radic. Biol. Med., 2010. **49**(1): p. 9-21.

56. Cadet, J. and K.J.A. Davies, *Oxidative DNA damage & repair: An introduction.* Free Radic. Biol. Med., 2017. **107**: p. 2-12.

57. Prochazkova, D., I. Bousova, and N. Wilhelmova, *Antioxidant and prooxidant properties of flavonoids.* Fitoterapia, 2011. **82**(4): p. 513-523.

58. Mateen, S., et al., *Increased Reactive Oxygen Species Formation and Oxidative Stress in Rheumatoid Arthritis.* PloS One, 2016. **11**(4): p. 0152925.

59. Garcia, J.J., et al., *Protective effects of melatonin in reducing oxidative stress and in preserving the fluidity of biological membranes: a review.* J. Pineal Res., 2014. **56**(3): p. 225-237.

60. Bains, M. and E.D. Hall, *Antioxidant therapies in traumatic brain and spinal cord injury.* Biochim. Biophys. Acta. Mol. Basis Dis., 2012. **1822**(5): p. 675-684.

61. Skouta, R., et al., *Ferrostatins Inhibit Oxidative Lipid Damage and Cell Death in Diverse Disease Models.* J. Am. Chem. Soc., 2014. **136**(12): p. 4551-4556.

62. Shi, X.L., N.S. Dalal, and K.S. Kasprzak, *GENERATION OF FREE-RADICALS FROM HYDROGEN-PEROXIDE AND LIPID HYDROPEROXIDES IN THE PRESENCE OF CR(III).* Arch. Biochem. Biophys., 1993. **302**(1): p. 294-299.

63. Torreggiani, A., M. Tamba, and C. Ferreri, *Radical damage involving sulfur-containing enzymes and membrane lipids.* Protein Pept. Lett., 2007. **14**(7): p. 716-722.

64. Pre, J., *FREE-RADICALS AND LIPID-PEROXIDATION .1. GENERAL BIOLOGICAL ASPECTS.* Sem. Hop. Inf., 1992. **68**(41): p. 1430-1437.

65. Cheeseman, K.H., *MECHANISMS AND EFFECTS OF LIPID-PEROXIDATION.* Mol. Asp. Med., 1993. **14**(3): p. 191-197.

66. Nathan, C. and A. Cunningham-Bussel, *Beyond oxidative stress: an immunologist's guide to reactive oxygen species.* Nat. Rev. Immunol., 2013. **13**(5): p. 349-361.

67. Staerck, C., et al., *Microbial antioxidant defense enzymes.* Microb. Pathog., 2017. **110**: p. 56-65.

68. Marín-García, J., *Post-genomic cardiology*. 2011: Academic Press.

69. McCord, J.M. and I. Fridovich, *Superoxide Dismutase: AN ENZYMIC FUNCTION FOR ERYTHROCUPREIN (HEMOCUPREIN).* J. Biol. Chem., 1969. **244**(22): p. 6049-6055.

70. Zhao, R.Z., et al., *Mitochondrial electron transport chain, ROS generation and uncoupling (Review).* Int. J. Mol. Med., 2019. **44**(1): p. 3-15.

71. Lambert, A.J. and M.D. Brand, *Reactive oxygen species production by mitochondria.* Methods Mol. Biol., 2009. **554**: p. 165-81.

72. Loew, O., *A new enzyme of general occurrence in organismis.* Science, 1900. **11**(279): p. 701-702.

73. Mills, G.C., *Hemoglobin catabolism: I. Glutathione peroxidase, an erythrocyte enzyme which protects hemoglobin from oxidative breakdown.* J. Biol. Chem., 1957. **229**(1): p. 189-197.

74. Sies, H., *Oxidative stress: Oxidants and antioxidants.* Exp. Physiol., 1997. **82**(2): p. 291-295.

75. Rodriguez, C., et al., *Regulation of antioxidant enzymes: a significant role for melatonin.* J. Pineal Res., 2004. **36**(1): p. 1-9.

76. Blokhina, O., E. Virolainen, and K.V. Fagerstedt, *Antioxidants, oxidative damage and oxygen deprivation stress: a review.* Ann. Bot., 2003. **91**(2): p. 179-194.

77. Imlay, J.A., *Cellular defenses against superoxide and hydrogen peroxide.* Annu. Rev. Biochem., 2008. **77**: p. 755-776.

78. Marnett, L.J., *Oxyradicals and DNA damage.* Carcinogenesis, 2000. **21**(3): p. 361-370.

79. Chapman, J.R., M.R.G. Taylor, and S.J. Boulton, *Playing the End Game: DNA Double-Strand Break Repair Pathway Choice.* Mol. Cell, 2012. **47**(4): p. 497-510.

80. Ciccia, A. and S.J. Elledge, *The DNA Damage Response: Making It Safe to Play with Knives.* Mol. Cell, 2010. **40**(2): p. 179-204.

81. Masip, L., K. Veeravalli, and G. Georgiou, *The many faces of glutathione in bacteria.* Antioxidants, 2006. **8**(5-6): p. 753-762.

82. Gong, N., et al., *Carbon-dot-supported atomically dispersed gold as a mitochondrial oxidative stress amplifier for cancer treatment.* Nat. Nanotechnol., 2019. **14**(4): p. 379.

83. Chaudhary, R.G., et al., *Graphene-based Materials and their Nanocomposites with Metal Oxides: Biosynthesis, Electrochemical, Photocatalytic and Antimicrobial Applications*. Magnetic Oxides and Composites II. Vol. 83. 2020. 79-116.

84. Rojas-Andrade, M.D., et al., *Antimicrobial activity of graphene oxide quantum dots: impacts of chemical reduction.* Nanoscale Adv., 2020. **2**(3): p. 1074-1083.

85. Riener, C.K., G. Kada, and H.J. Gruber, *Quick measurement of protein sulfhydryls with Ellman's reagent and with 4, 4'-dithiodipyridine.* Anal. Bioanal. Chem., 2002. **373**(4): p. 266-276.

86. Van Meer, G., D.R. Voelker, and G.W. Feigenson, *Membrane lipids: where they are and how they behave.* Nat. Rev. Mol. Cell Biol., 2008. **9**(2): p. 112-124.

87. El-Beltagi, H.S. and H.I. Mohamed, *Reactive Oxygen Species, Lipid Peroxidation and Antioxidative Defense Mechanism.* Not. Bot. Horti. Agrobo., 2013. **41**(1): p. 44-57.

88. Niki, E., et al., *Lipid peroxidation: Mechanisms, inhibition, and biological effects.* Biochem Bioph Res Co, 2005. **338**(1): p. 668-676.

89. Svingen, B.A., et al., *MECHANISM OF NADPH-DEPENDENT LIPID PEROXIDATION - PROPAGATION OF LIPID PEROXIDATION.* J. Biol. Chem., 1979. **254**(13): p. 5892-5899.

90. Cabiscol Català, E., J. Tamarit Sumalla, and J. Ros Salvador, *Oxidative stress in bacteria and protein damage by reactive oxygen species.* Int. J. Microbiol., 2000. **3**(1): p. 3-8.

91. Grune, T., et al., *Selective degradation of oxidatively modified protein substrates by the proteasome.* Biochem Bioph Res Co, 2003. **305**(3): p. 709-718.

92. Tansey, J.T., *Biochemistry*. 2020, John Wiley & Sons,: Hoboken, NJ. p. 1 online resource.

93. Yamaza, T., et al., *Oxidative stress-induced DNA damage in the synovial cells of the temporomandibular joint in the rat.* Journal of Dental Research, 2004. **83**(8): p. 619-624.

94. Limoli, C.L., et al., *Attenuation of radiation-induced genomic instability by free radical scavengers and cellular proliferation.* Free Radical Biology and Medicine, 2001. **31**(1): p. 10-19.

95. Cadet, J. and J.R. Wagner, *DNA base damage by reactive oxygen species, oxidizing agents, and UV radiation.* Cold Spring Harb. Perspect. Biol., 2013. **5**(2): p. a012559.

96. Badouard, C., et al., *Detection of chlorinated DNA and RNA nucleosides by HPLC coupled to tandem mass spectrometry as potential biomarkers of inflammation.* J. Chromatogr. B. J. Chromatogr. B., 2005. **827**(1): p. 26-31.

## Chapter 2 Platinum Oxide Nanoparticles for Electrochemical Hydrogen Evolution: Influence of Platinum Valence State

## 2.1 Abstract

Electrochemical hydrogen generation is a rising prospect for future renewable energy storage and conversion. Platinum remains a leading choice of catalysts. Because of high cost and low Earth abundance, it is critical to improve the use of platinum. In the present study, platinum oxide nanoparticles of ca. 2 nm in diameter are deposited on carbon nitride (C3N4) nanosheets by thermal refluxing of C3N4 and $PtCl_2$ or $PtCl_4$ in water, and exhibit apparent electrocatalytic activity towards hydrogen evolution reaction (HER) in acid. Interestingly the HER activity increases with increasing concentration of $Pt^{4+}$ species in the nanoparticles, and the optimized catalyst even outperforms commercial Pt/C, exhibiting an overpotential of only −7.7 mV to reach the current density of 10 mA $cm^{-2}$ and a Tafel slope of −26.3 mV $dec^{-1}$. Results from this study suggest that future design of platinum oxide catalysts should strive to maximize the $Pt^{4+}$ sites while minimizing the formation of the less active $Pt^{2+}$ species.

## 2.2 Introduction

It has been proposed that 80% of electricity generated in the United States has the potential to be made renewable by 2050.[1] With the prospect of completely renewable electricity on the rise, electrochemical water splitting for hydrogen generation poses a promising technology for sustainable energy storage and conversion.[2, 3] Implementation of this technology will require improved catalyst design.[4] Platinum has remained a leading electrocatalyst for the multi-electron transfer process of hydrogen evolution reaction (HER), with a high exchange-current density and ideal Tafel slope.[5] However, due to the high cost and low natural abundance of platinum, future catalysts must optimize the use of platinum within the material.[6, 7] To achieve this goal researchers have developed various methods to limit the amount of platinum through reducing particle size and the use of platinum oxide rather than platinum metal particles.

For instance, Yang et al. used platinum oxide nanoparticles for HER catalysis and found that decreasing particle size from 2 to 0.2 nm resulted in increased catalytic activity, which was attributed to size-dependent proton adsorption properties.[8] More recently, Sarno and colleagues showed that decreasing particle size as well as strong metal oxide-support interactions can help reduce platinum loading and improve hydrogen evolution rates by using a composite material containing platinum metal, platinum(IV) oxide, and iron oxide.[9] Strong metal-support interactions were also reported by Cheng et al. using platinum oxide clusters containing $Pt^{2+}$ and $Pt^{4+}$ species supported on $TiO_2$.[10] It is widely believed that hydrogen adsorption onto the catalyst surface, known as the Volmer step, is often the rate determining step for HER in both acidic and basic media.[11, 12] Thus, to better understand the reaction rates, Cheng and colleagues used density functional theory (DFT) to calculate changes in Gibbs free energy ($\Delta G_H$) for hydrogen adsorption. It was found that platinum in a highly oxidized state resulted in a $\Delta G_H$ close to zero (–0.06 eV) that is ideal for HER. This improved hydrogen binding was attributed to the presence of $Pt^{4+}$ sites in Pt-O-Ti bonding. This result suggests that highly oxidized platinum sites can efficiently adsorb hydrogen onto the surface while minimizing the adsorption energy to allow for hydrogen gas formation and release from the catalyst surface. However, the material under study[10] contained a large portion of platinum in a lower oxidation state ($Pt^{2+}$ and $Pt^0$) and the HER performance remained subpar as compared to that of commercial Pt/C. In addition, the catalytic contributions and importance of the portion of low-valence platinum were not distinguished. Therefore, further study is required to understand how the platinum's oxidation state can be controlled to tailor the hydrogen evolution performance. With this in mind, controlling platinum oxidation state within the oxide material poses a useful route to effective catalyst design.

The selection of an ideal catalyst support is also critical as this plays a key role in the manipulation of the resulting particle size, stability and other key factors influencing the catalytic performance.[13-15] Graphitic carbon nitride (C3N4) represents a promising support for its surface functionality, ease and low cost of production, and inherent ability to control nanoparticle size. Zhu and colleagues have shown how manipulation of C3N4 condensation rate and temperature can be used to control the size of the resulting gold and platinum nanoparticles in a C3N4-mesoporous silica (SBA-15) composite material.[16] It was shown that incorporation of the C3N4 resulted in small, homogeneously dispersed nanoparticles and prevented nanoparticle agglomeration, which was attributed to strong support interactions, in comparison to SBA-15 alone. Vinu and coworkers demonstrated the inherent ability of C3N4 to act as a stabilizing agent to produce ultra-small, highly dispersed Au nanoparticles anchored firmly on the functional moieties on the C3N4 surface. This can be attributed to the pyridinic nitrogen on the C3N4 surface that act as a strong Lewis base and π-bond planar layers able to anchor the substrate.[17] For these reasons, C3N4 is an ideal candidate for the fabrication of small metal oxide nanoparticle composites.

Herein we report a facile, effective approach to properly distinguish contributions from different platinum oxide species toward HER utilizing C3N4 as a unique support material. C3N4 nanosheets are first prepared through condensation of urea by a two-step route. Platinum oxide nanoparticles of about 1.4 nm in diameter are then deposited onto the C3N4 surface by a thermal refluxing method in water with platinum chloride.[18-20] Electrochemical measurements show that $Pt^{4+}$ species is primarily responsible for the remarkable HER activity, which even surpasses that of commercial Pt/C; and the HER activity increases with increasing $Pt^{4+}$ content.

## 2.3 Results and Discussion

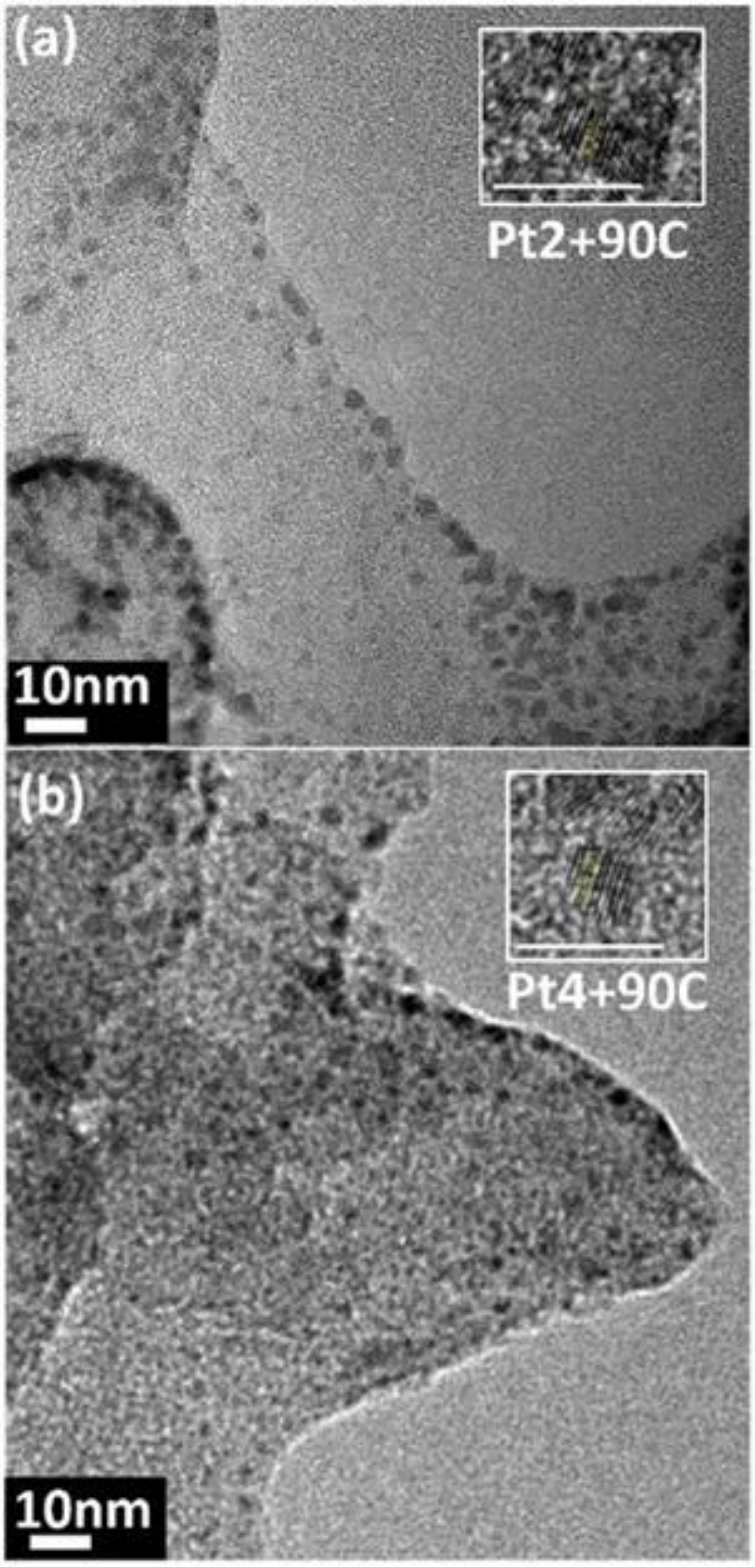


Figure 1. TEM images of (a) Pt2+90C and (b) Pt4+90C. Scale bars 10 nm. Insets are the corresponding high-resolution TEM images, with the scale bars of 5 nm.

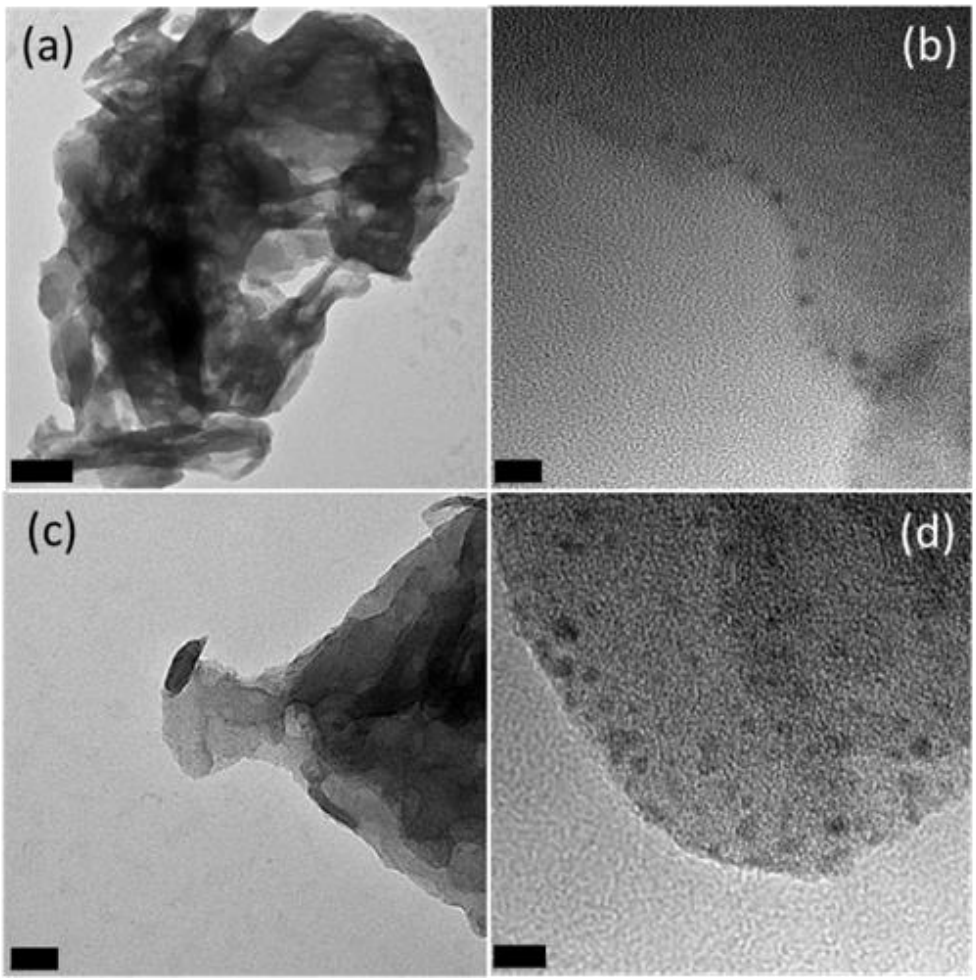


Figure 2. TEM images of (a,b) Pt2+90C and (c,d) Pt4+90C samples. Scale bars are (a) 100 nm, (b) 5 nm, (c) 40 nm, and (d) 5 nm.

Experimentally, C3N4 nanosheets were prepared by thermal treatment of urea, onto which were then deposited platinum oxide nanoparticles by thermal refluxing of C3N4 and $PtCl_2$ or $PtCl_4$ in water at 90 ºC. The resulting samples were referred to as Pt2+90C and Pt4+90C (synthetic details in the Experimental Section). Figures 1 and 2 depict representative TEM images of Pt2+90C and Pt4+90C. The overall morphologies are consistent with those of the as-prepared C3N4 (Figure 3), displaying a layered, sheet-like structure. In addition, both Pt2+90C and Pt4+90C samples can be seen to contain a

number of dark-contrast nanoparticles deposited on the C3N4 surface (note that no such nanoparticulate objects were observed in the C3N4 sample, Figure 3).

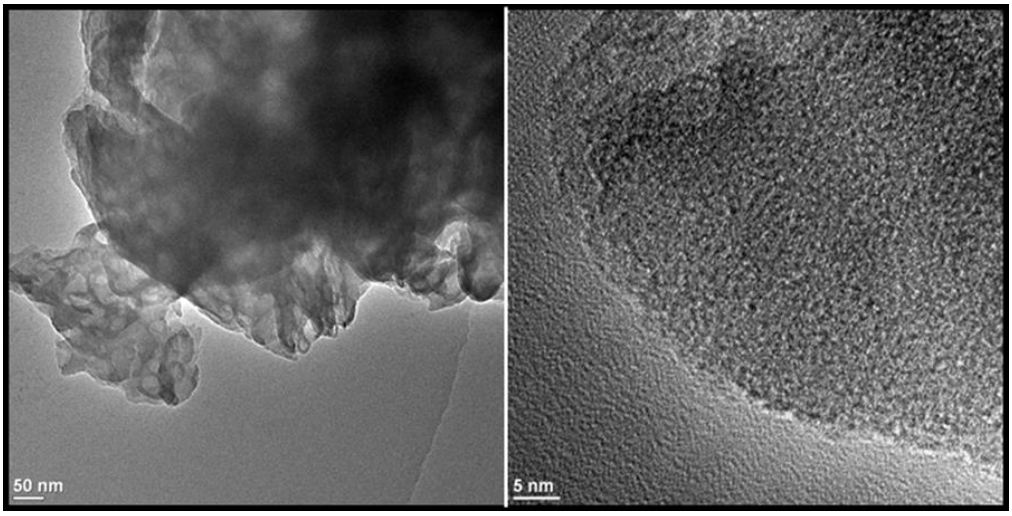


Figure 3. Representative TEM images of as-prepared C3N4. Scale bars are (a) 50 nm and (b) 5 nm.

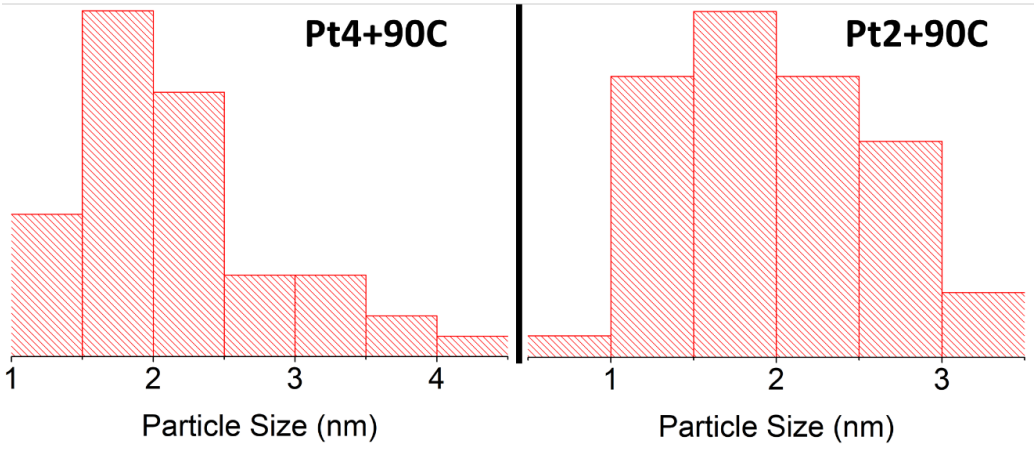


Figure 4. Core size histograms of Pt2+90C and Pt4+90C.

From the core histograms in Figure 4, the nanoparticles can be seen to mostly fall within the narrow range of 1.0 to 4.4 nm, with the average particle diameter at 2.0 ± 0.6 nm for Pt2+90C and 2.1 ± 0.7 nm for Pt4+90C. Furthermore, high resolution TEM images reveal clearly-defined lattice fringes of the nanoparticles (insets to Figure 1), with an interplanar

spacing of 0.23 nm for Pt2+90C and 0.24 nm for Pt4+90C, which are consistent with several crystalline facets, such as PtO(110), $PtO_2$(011), and Pt(111).[21, 22] Yet, further characterizations below suggest that these are actually due to the formation of platinum oxide $PtO_x$ (vide infra).

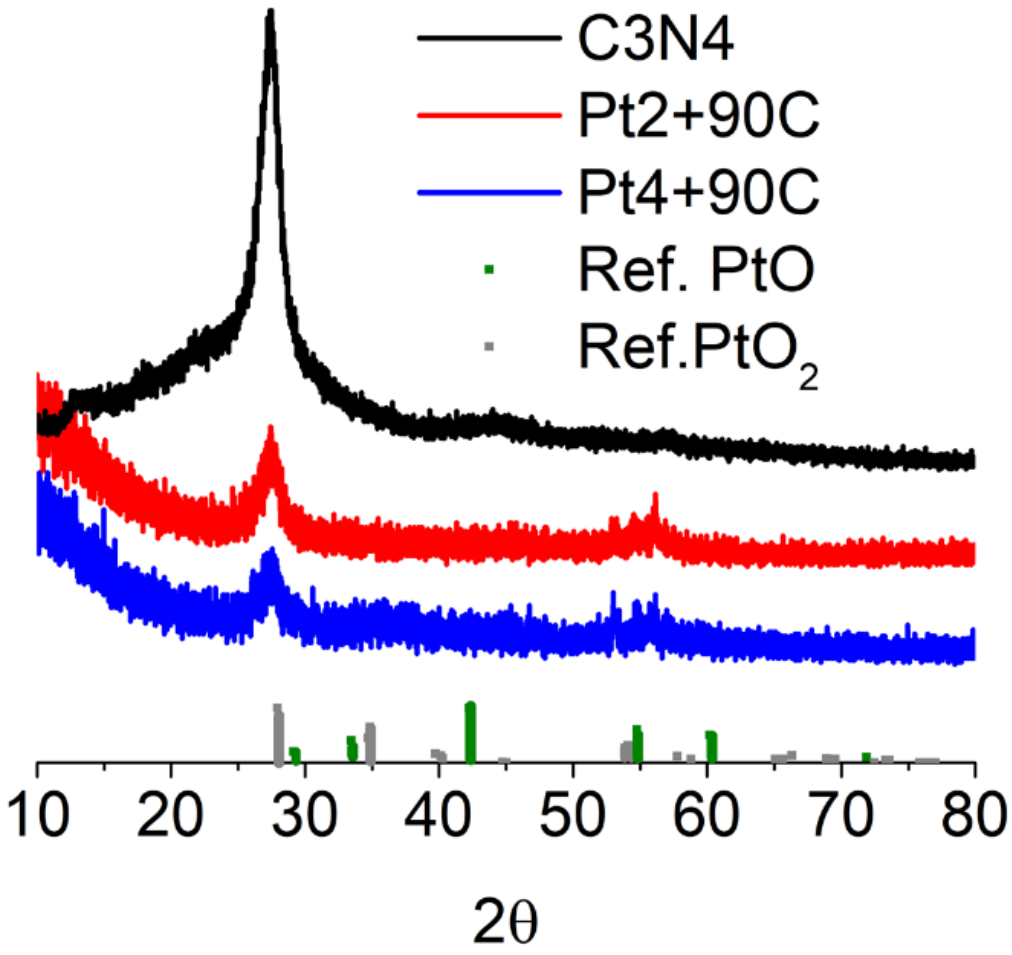


Figure 5. Powder X-ray Diffraction spectra. Tick lines represent expected patterns from that of $PtO_2$ (Grey) (Ref. Code: 01-075-0978) and PtO (Green) (Ref. Code: 00-027-1331).

Further structural insights were obtained in X-ray diffraction (XRD) measurements. From Figure 5, one can see that Pt4+90C, Pt2+90C, and C3N4 all exhibit a single, major diffraction peak centered at $2\theta = 27°$, which can be assigned to the (002) crystalline

facets of carbon nitride, as observed previously.[23] In the Pt4+90C and Pt2+90C samples, the diffraction patterns of platinum oxide cannot be resolved, in comparison to the standard references of PtO (reference code 00-027-1331) and $PtO_2$ (reference code 01-075-0978), most likely due to the small nanoparticle size, as seen in TEM measurements (Figure 1).

XPS measurements were then carried out to probe the chemical composition and electronic environment of the material. From the survey spectra in Figure 6a, two major peaks can be seen at 288 and 399 eV, due to C 1s and N 1s of C3N4, respectively; and for Pt2+90C and Pt4+90C, two additional species can be identified at ca. 75 eV for Pt 4f,[24] and 532 eV for O 1s, indicating the successful deposition of platinum species onto the C3N4 surface (the small peaks at 199 eV and 270 eV can be assigned to Cl 2p and Cl 2s, respectively, due to residual chloride in the samples);[25] and based on the integrated peak areas, the Pt loading was found to be very comparable at 32 wt% for Pt4+90C and 28 wt% for Pt2+90C. Figure 6b depicts the corresponding high-resolution XPS scans of the Pt 4f electrons. The Pt2+90C sample (red curve) can be seen to exhibit two doublets. The first pair at 76.3 and 73.0 eV corresponds to the $4f_{5/2}$ and $4f_{7/2}$ electrons of $Pt^{2+}$, whereas the other at 78.0 and 74.7 eV to those of $Pt^{4+}$ and a peak splitting of 3.3 eV is consistent with Pt 4f spin-orbit coupling (note that no metallic Pt can be resolved).[9, 20, 24, 26, 27] Additionally, based on the integrated peak areas, the atomic ratio of $Pt^{4+}$:$Pt^{2+}$ in Pt2+90C is estimated to be 0.45:1. Similar behaviors can be seen with the Pt4+90C sample, where the two doublets appear at 76.2/72.9 eV and 78.0/74.7 eV, respectively. However, the ratio of $Pt^{4+}$:$Pt^{2+}$ is significantly higher at 1.66:1, more than 3.5 times that in Pt2+90C. Regardless, this suggests that thermal refluxing of platinum chloride and C3N4 effectively led to the deposition of $PtO_x$ nanoparticles onto the C3N4 surface (Figure 1).

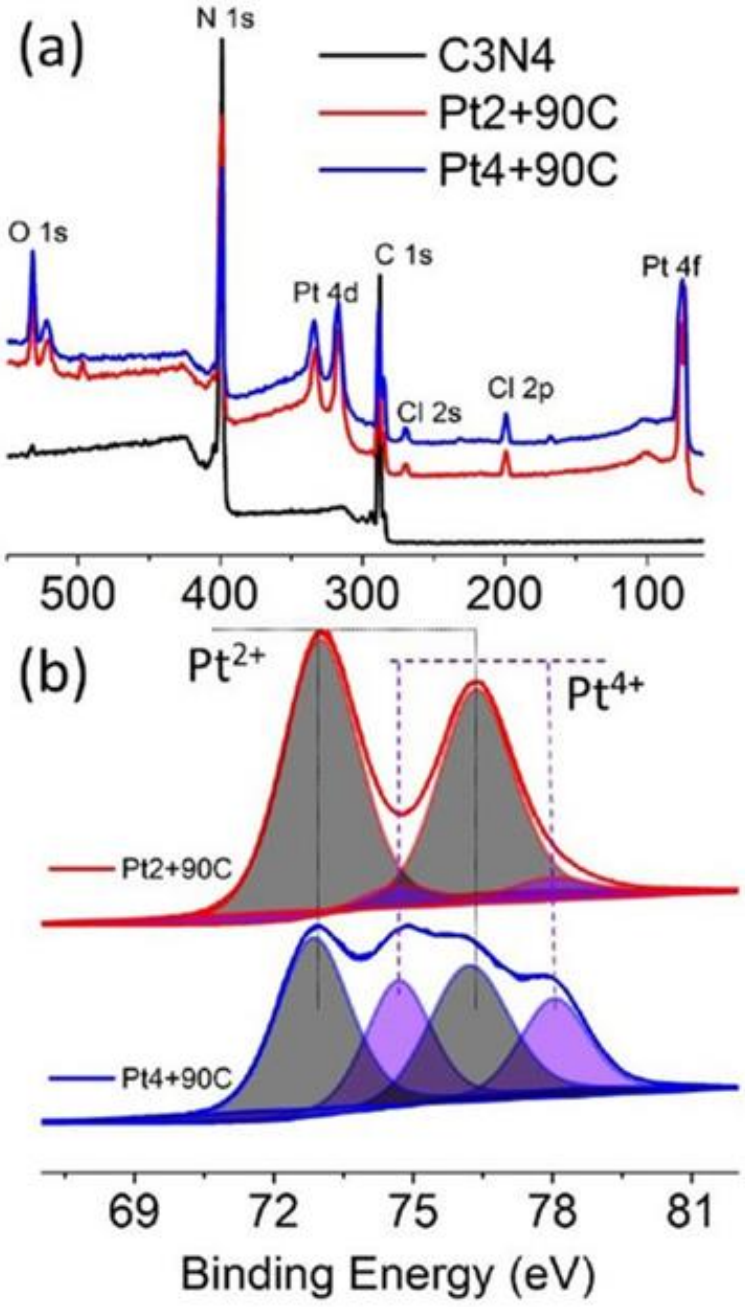


Figure 6. (a) XPS survey spectra and (b) the corresponding high-resolution scans for the Pt4f electrons of as-prepared C3N4 (Black), Pt2+90C (Red), and Pt4+90C (Blue). Solid curves are experimental data and shaded peaks are deconvolution fits.

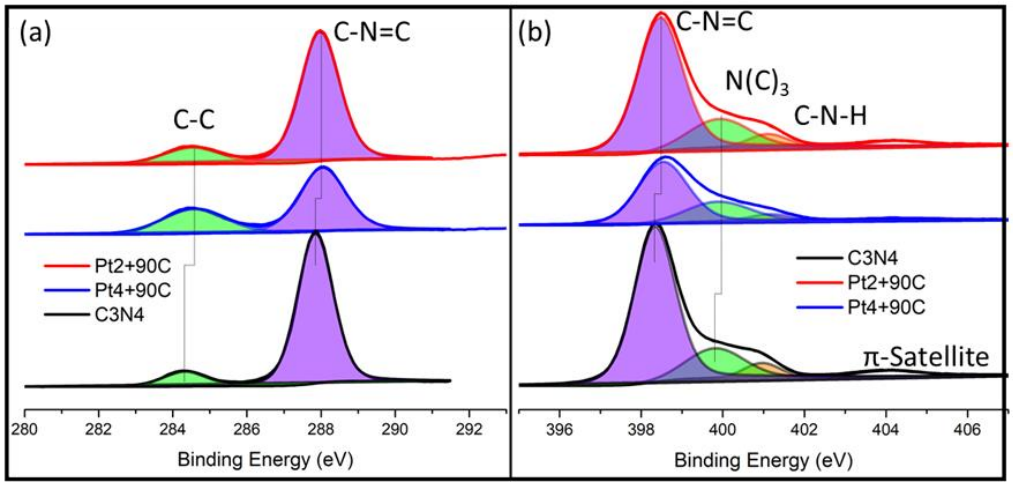


Figure 7. High resolution XPS spectra of the (a) C 1s and (b) N 1s regions for samples C3N4 (black), Pt2+90C (red), and Pt4+90C (blue).

The high-resolution scans of the C 1s and N 1s electrons are depicted in Figure 7. Deconvolution reveals two distinct peaks at 287.85 and 284.33 eV for the C3N4 sample, which are attributed to the $sp^2$ hybridized carbon within the C3N4 network (C-N=C) and $sp^3$ carbon due to defect moieties (C-C), respectively.[23, 28-30] The N 1s region of C3N4 was deconvoluted into four components centered at 398.34 eV, 399.81 eV, 400.96 eV, and a weak one at 404.10 eV. These individual components can be attributed to the $sp^2$ hybridized pyridinic nitrogen (C-N=C), $sp^3$ hybridized tertiary nitrogen ($N-(C)_3$), quaternary nitrogen (C-N-H), and a π-satellite excitation, respectively.[23, 28-30] Upon thermal refluxing with platinum salts, the nitrogen and carbon peaks associated with the C3N4 matrix exhibit an increase in binding energy. The primary carbon peak shifts to 287.97 and 288.04 eV (C-N=C), and the defect carbon to 284.53 and 284.57 eV (C-C) for Pt2+90C and Pt4+90C, respectively. The N 1s electrons also experience a similar increase in binding energy with the three primary peaks centered at 398.47 eV and 398.54 eV (C-N=C), 399.92 eV and 399.88 eV ($N-(C)_3$), 401.10 eV and 401.18 eV (C-N-H), corresponding again to Pt2+90C and Pt4+90C, respectively. This slight increase in

binding energy can be attributed to electron donation from the C3N4 support to the Pt centers suggesting a strong interaction between the nanoparticles and C3N4.[31, 32]

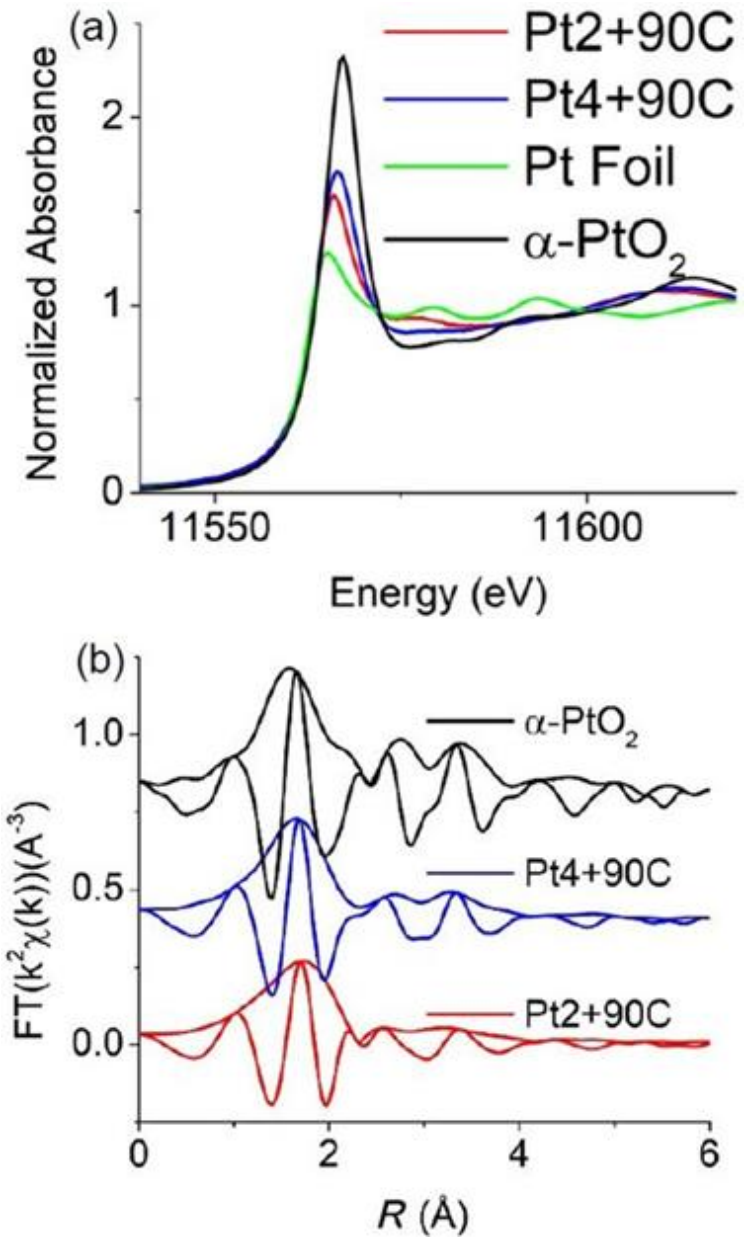


Figure 8. (a) Pt L3 edge XANES data for Pt2+90C and Pt4+90C (Pt foil and commercial α-$PtO_2$ as references). All edge steps are normalized to an edge step height of 1. The energy range selected to normalize the edge is 11700 to 12000 eV. Measurements are performed at the temperature of 10 K. (b) Pt L3 edge r-space data for Pt2+90C (red),

Pt4+90C (blue) and commercial α-$PtO_2$ (black). The Fourier transform (FT) window is from 3.0 to 10.8 $Å^{-1}$, rounded using a Gaussian function of width, 0.2 $Å^{-1}$. The fast oscillating function is the real part R of the FT while the amplitude is the $\sqrt{R^2 + I^2}$ where $I$ is the imaginary part of the FT. Pt4+90C has been shifted vertically by 0.4 while α-$PtO_2$ has been shifted vertically by 0.8.

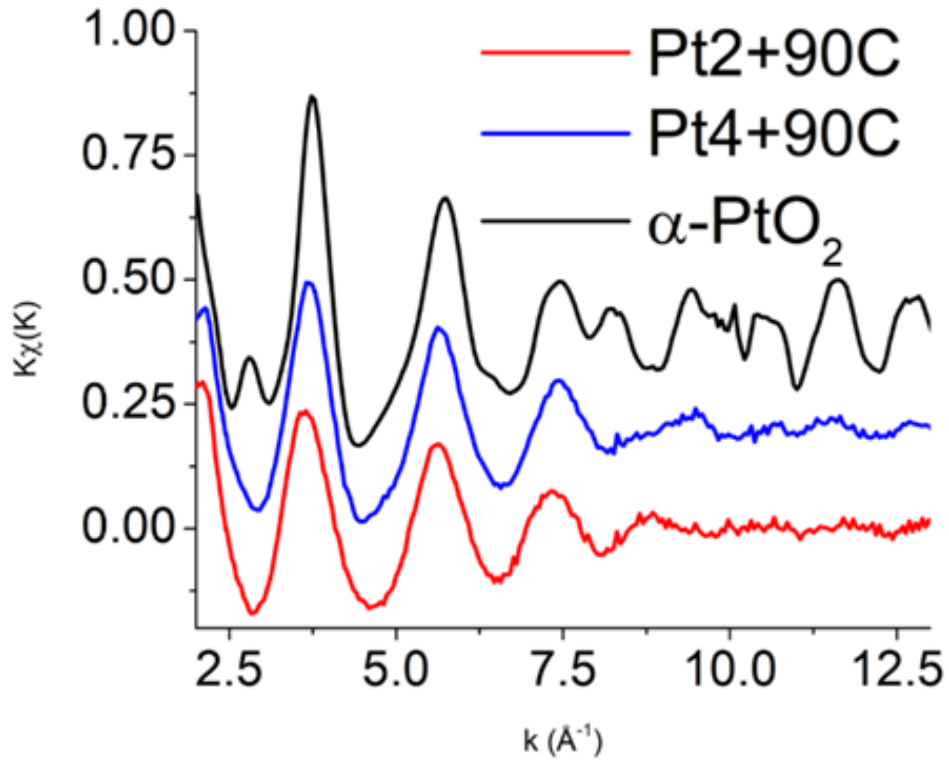


Figure 9. Pt L3 edge k-space data at 10 K of various samples.

Further structural insights were obtained in X-ray absorption spectroscopic (XAS) measurements, where data were collected at the Pt L3 edge to probe the Pt electronic states and investigate the local structures. The data were reduced and analyzed using the RSXAP package.[33] In Figure 8a, the Pt L3 XANES (X-ray absorption near edge spectroscopy) data for Pt2+90C and Pt4+90C are compared with those for a Pt foil and the α-$PtO_2$ reference sample. All samples are electrically conducting and there is no shift of the main edge as typically observed for different valences in insulating materials,

suggesting that the Fermi energies are nearly identical among the samples. A strong absorption in this region, referred to as the white line, is observed due to the Pt 2p → 5d transitions.[34, 35] Typically, the white line intensity increases with decreasing 5d orbital occupancy (i.e., increasing valence states).[35-37] The fact that the white line intensity increases in the order of Pt foil < Pt2+90C < Pt4+90C < $PtO_2$ indicates that the Pt charge state in Pt2+90C and Pt4+90C fell in the intermediate between Pt(0) and Pt(IV), and is higher in Pt4+90C than in Pt2+90C, in good agreement with results from XPS measurements (Figure 6). Consistent behaviors can be seen with the white line energy, which shifts positively in the order of Pt foil (11565.16 eV) < Pt2+90C (11566.00 eV) < Pt4+90C (11566.44 eV) < α-$PtO_2$ (11567.27 eV).

Table 1. EXAFS fitting results to Hexagonal α-$PtO_2$.

| Sample | Pt-O (Å) | Pt-Pt (Å) |
|---|---|---|
| Pt2+90C | 2.071 ± 0.01 | 3.204 ± 0.02 |
| Pt4+90C | 2.034 ± 0.01 | 3.154 ± 0.02 |

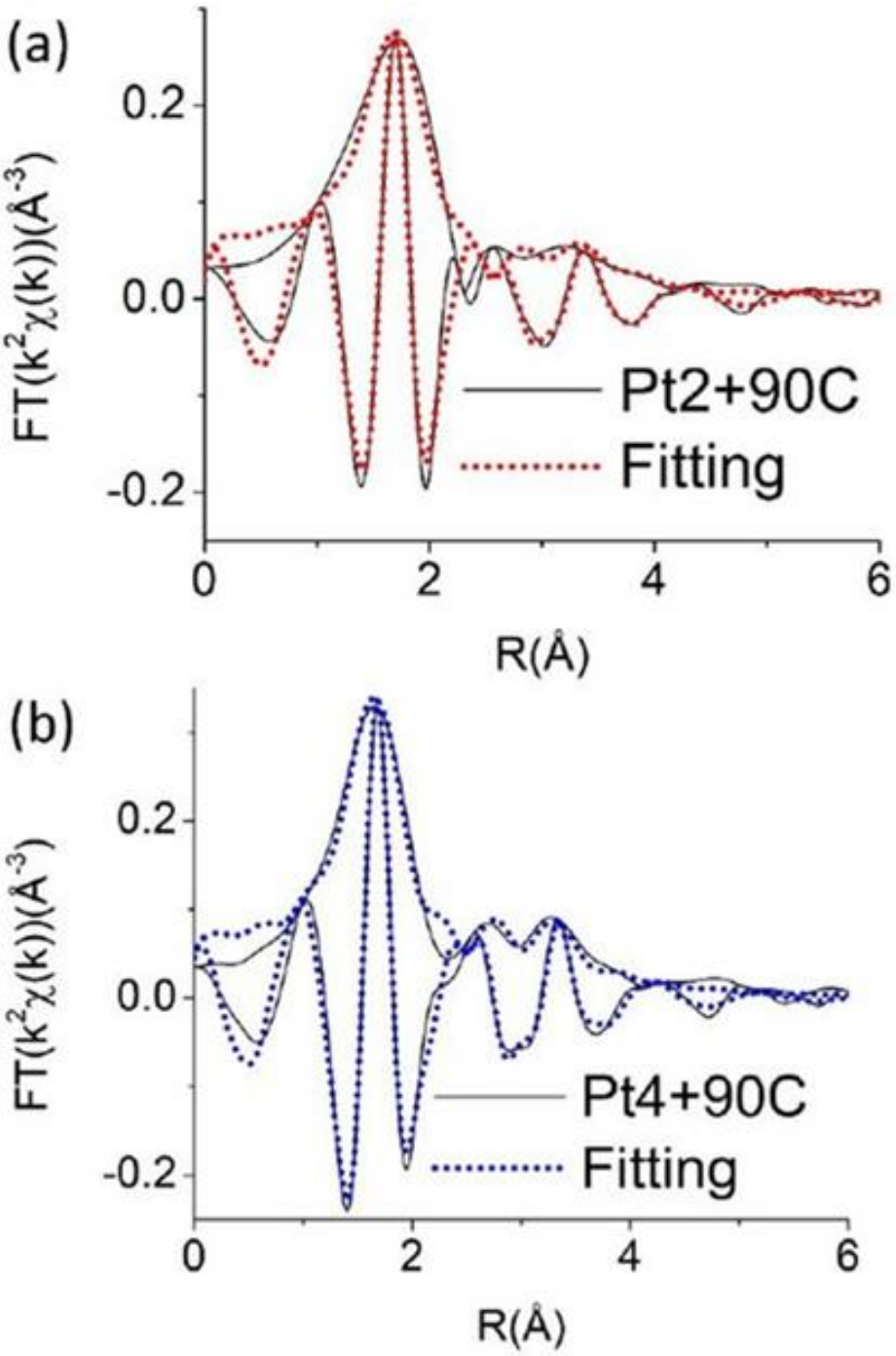


Figure 10. Fittings to the hexagonal structure of α-$PtO_2$, as a sum of Pt-O and Pt-Pt, for (a) Pt2+90C and (b) Pt4+90C. Pt-O bond length decreases from 2.07 to 2.03 Å.

EXAFS (extended X-ray absorption fine structure) analysis for Pt2+90C and Pt4+90C was then carried out and compared to that for α-$PtO_2$ in Figure 3b. The same FT range

(3.0 to 10.8 $Å^{-1}$) is used for each plot although the k-space data for α-$PtO_2$ extend to much higher k (Figure 9). The k-space plots show increasing disorder from the reference sample to Pt2+90C. Note that the double peak structure near 3 Å in Figure 8b, associated with Pt-Pt second neighbor pairs in α-$PtO_2$, is nearly washed out for the latter sample. α-$PtO_2$ has a hexagonal structure;[38, 39] and the environment about Pt consists of six nearest-neighbor O atoms, six second-neighbor Pt atoms and six third-neighbor O atoms. To fit the data, theoretical Pt-O and Pt-Pt functions were calculated for α-$PtO_2$ using FEFF7,[40] plus a weak multiscattering peak, as shown in Figure 10. The data were then fitted to a sum of such standards, allowing the pair distances and pair distribution widths, σ, to vary. Note that the third neighbor Pt-$O_2$ and the multiscattering peak amplitudes are very small and we only quote the results for the first two neighbors. As shown in Table 1, the Pt-O bond length is somewhat shorter for Pt4+90C than for Pt2+90C. A similar change is also observed for the second neighbors, again, consistent with a higher charge state of Pt in Pt4+90C than in Pt2+90C.

To assess the electrocatalytic performance of these materials toward HER, linear sweep voltammetry was performed under a nitrogen atmosphere in 0.5 M $H_2SO_4$ at the potential scan rate of 10 mV $s^{-1}$. Figure 12a displays the polarization curves of Pt2+90C, Pt4+90C, and commercial Pt/C, in comparison to that of C3N4. One can see that C3N4 exhibited essentially zero HER activity, whereas apparent catalytic activity appears with the other three Pt-containing samples. Remarkably, at equivalent platinum mass loadings, Pt4+90C stood out as the best among the series, even outperforming commercial Pt/C, with an ultralow overpotential ($\eta_{10}$) of only −7.7 mV to reach the current density of 10 mA $cm^{-2}$, in comparison to −26.1 mV for Pt/C and −214.6 mV for Pt2+90C, suggesting that $Pt^{4+}$ species played a critical role in the HER activity. In fact, to the best of our knowledge, the Pt4+90C sample outperforms most platinum oxide-based HER catalysts in acidic

media that have been reported in recent literature (Table 2). To further understand the reaction mechanisms of these materials, Tafel plots were derived from the polarization curves, as shown in Figure 12b, from which the Tafel slopes was estimated to be 21.0 mV $dec^{-1}$ for Pt4+90C, 26.3 mV $dec^{-1}$ for Pt/C and 55.4 mV $dec^{-1}$ for Pt2+90C[41]. This suggests that kinetically Pt4+90C behaved similarly to Pt/C where the Tafel reaction is the rate determining step, while for Pt2+90C, HER is likely limited by the slower Heyrovsky reaction.

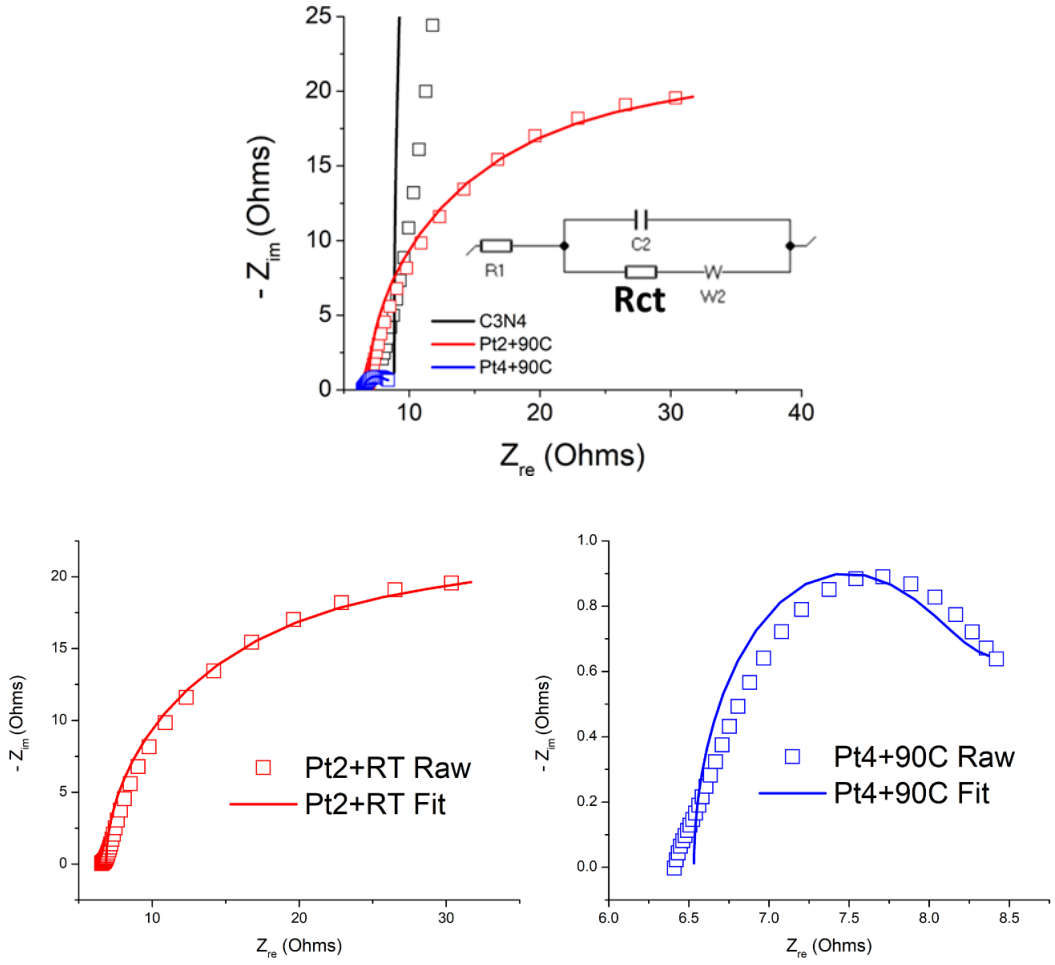


Figure 11. Nyquist plots of C3N4 (black), Pt2+90C (red), and Pt4+90C (blue). Symbols are experimental data and solid curves are fits by using the Randles equivalent circuit in

the figure inset. All measurements are carried out at the potential of -10 mV vs RHE in a nitrogen-purged 0.5 M H2SO4 solution.

Figure 11 depicts the Nyquist plots (squares) and the corresponding fits (solid lines) using a typical Randle's equivalent circuit modified with a Warburg diffusion term (W2). The charge-transfer resistances ($R_{CT}$) were estimated to be 2230 Ω for the as-prepared C3N4, and diminished markedly to 26.8 Ω for Pt2+90C, and only 1.6 Ω for Pt4+90C. That is, the charge-transfer kinetics of HER was dramatically improved with the deposition of platinum onto C3N4, and the Pt4+90C sample showed the lowest charge transfer resistance among the series of samples.

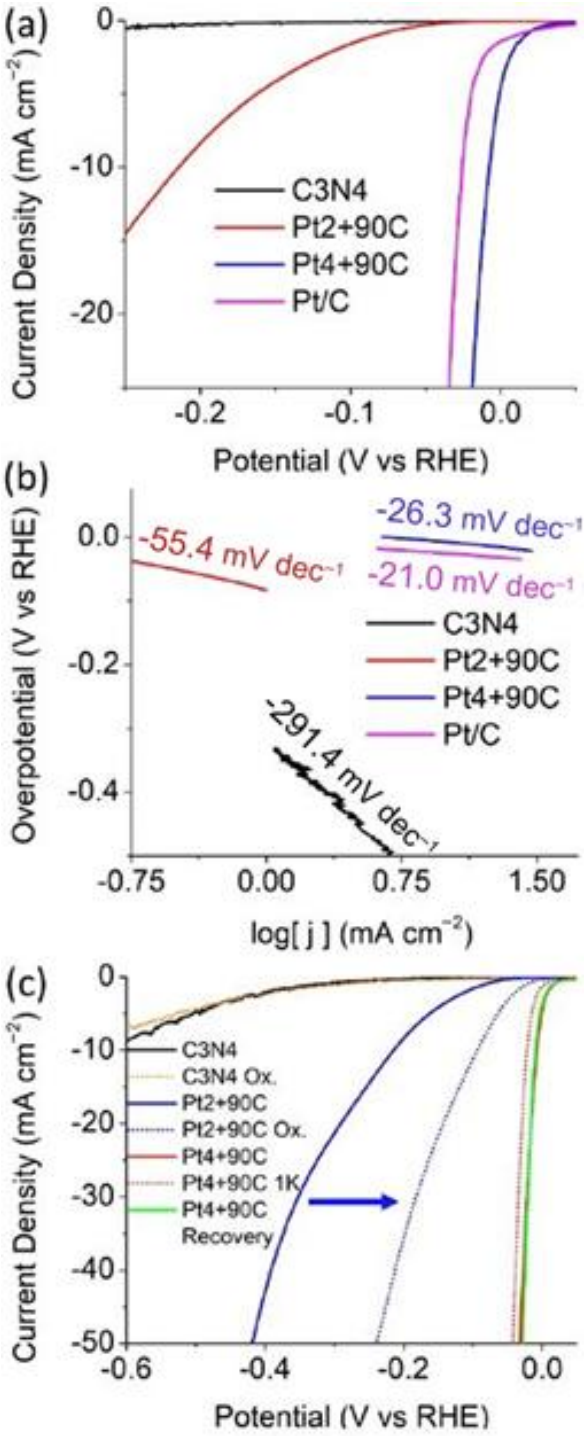


Figure 12. (a) Polarization curves of HER in 0.5M $H_2SO_4$ for as prepared C3N4 (black), Pt2+90C (red), Pt4+90C (blue), and commercial platinum on carbon (magenta). (b) Tafel Plots derived from polarization curves in panel (a). (c) Oxidized cycling and recovery tests.

To further examine the influence of the Pt oxidation state on the HER performance, several additional electrochemical measurements were performed. In the first test, the Pt2+90C sample was found to show a marked improvement of the HER performance after 50 cycles at high potentials between +0.9 and +1.2 V vs RHE (where $Pt^{2+}$ was electrochemically oxidized to $Pt^{4+}$) at the potential rate of 10 mV $s^{-1}$. From Figure 5c, one can see that $\eta_{10}$ diminished drastically by 120 mV to –93.8 mV (blue solid and dotted curves). XPS measurements (Figure 13) show that the primary peak appears at 73.9 eV, ca. 0.9 eV higher than that of the as-prepared sample, suggesting the formation of $Pt^{4+}$ species that led to the improved HER performance.[9, 20, 24, 26, 27] Additional tests were carried out with the Pt4+90C sample. When the catalyst was subject to potential cycling between 0 and +0.02 V vs RHE (where $Pt^{4+}$ was electrochemically reduced to lower valence states) for 1000 cycles at 10 mV $s^{-1}$, the $\eta_{10}$ in the subsequent HER measurement was found to deteriorate slightly, from –7.7 mV to –21.7 mV (red solid and dotted curves). However, after 50 potential cycles between +0.9 and +1.2 V to regenerate the $Pt^{4+}$ species, the HER performance was almost fully recovered, with $\eta_{10}$ = –9.8 mV (green solid curve). By sharp contrast, electrochemical treatment (reduction or oxidation, black solid and orange dotted curves) of C3N4 alone did not lead to any change of the electrochemical response, suggesting that it is the Pt species that is responsible for the HER activity and $Pt^{4+}$ is far more active than $Pt^{2+}$. In fact, the HER activity increases markedly with increasing $Pt^{4+}$ loading in the Pt4+90C sample (Figure 14).

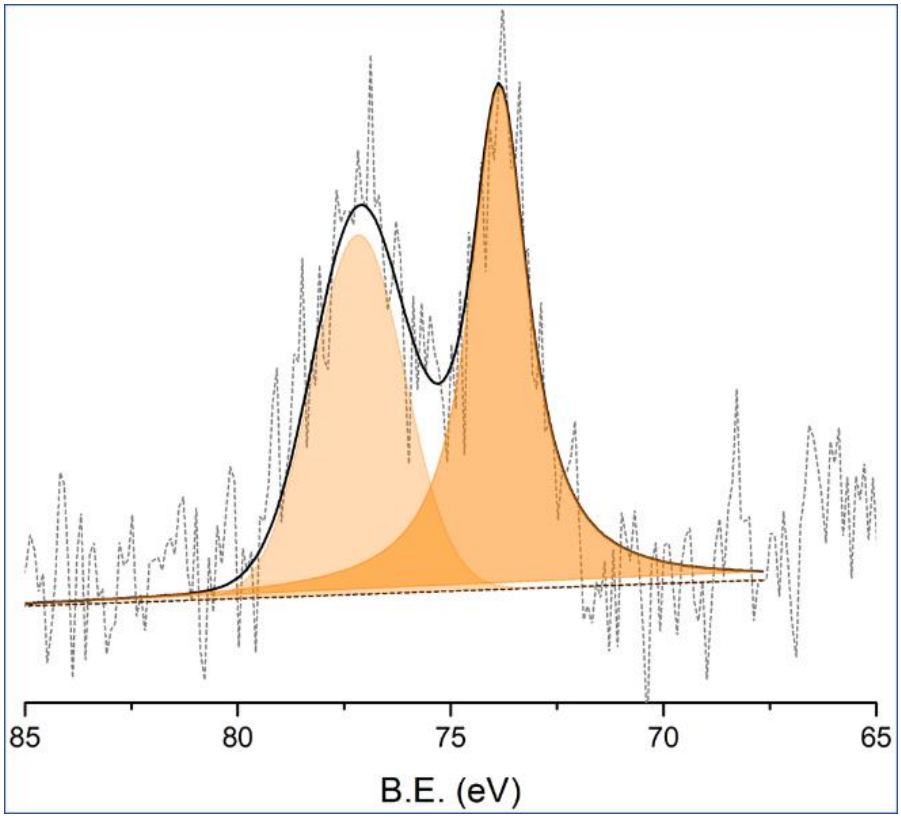


Figure 13. High resolution XPS scans of Pt 4f electrons of the Pt2+90C sample after 50 potential cycling between +0.9 and +1.2 V vs RHE.

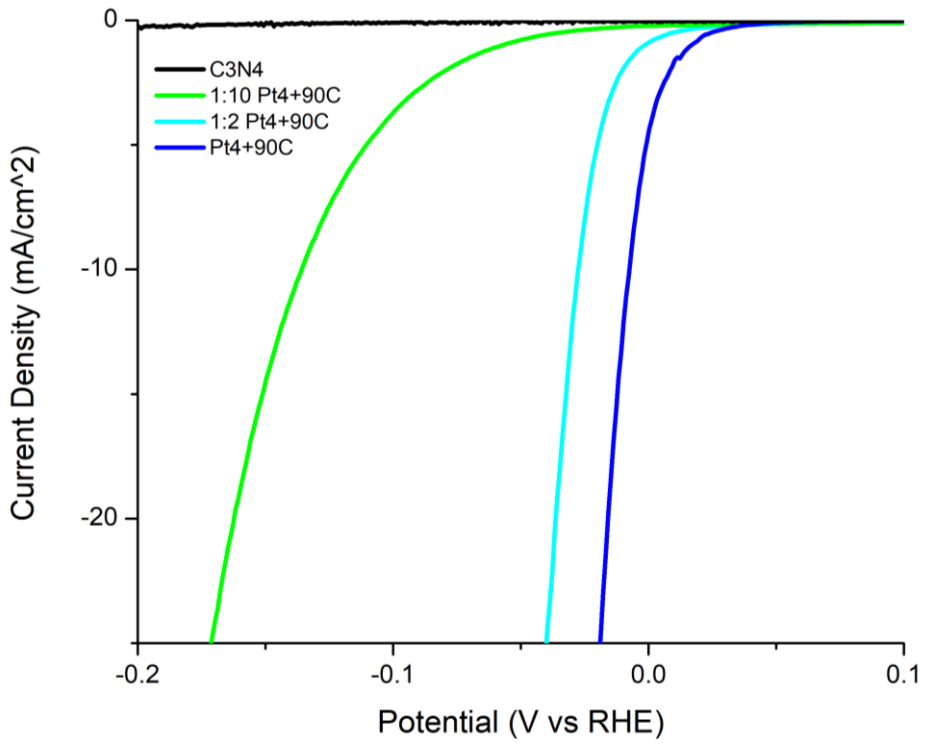


Figure 14. Polarization curves of Pt4+90C prepared at reduced $PtCl_4$ loading (1/2 and 1/10 of that described in the main text) in 0.5 M $H_2SO_4$.

Table 2. Comparison of HER performance by platinum oxide nanoparticles reported in recent literature.

| Catalyst | Platinum Composition | Catalyst Loading ($mg/cm^2$) | Electrolyte Solution | $\eta_{10}$ (mV) | Reference |
|---|---|---|---|---|---|
| Pt oxide $C_3N_4$ | $Pt^{2+}/Pt^{4+}$ | 0.24 | 0.5 M $H_2SO_4$ | -7.7 | This Work |
| Pt/PtO2/Fe3O4 | $Pt^0/Pt^{2+}/Pt^{4+}$/Fe | - | 1.0 M $H_2SO_4$ | > -10 | [9] |
| $PtO_x$ / $TiO_2$ | $Pt^{2+}$/ $Pt^{4+}$/Ti | - | 0.5 M $H_2SO_4$ | -150 | [10] |
| $MoS_x$-O-$PtO_x$ | $Pt^{2+}/Pt^{4+}/MoS_x$ | 0.45 | 0.5 M $H_2SO_4$ | -25 | [42] |
| Pt-($PtO_x$)-NSs/C | $Pt^0/Pt^{2+}/Pt^{4+}$ | 0.036 | 0.5 M $H_2SO_4$ | -5 | [43] |

## 2.4 Experimental Section

### Chemicals

Urea (Certified ACS, Fisher Chemicals), platinum(II) chloride ($PtCl_2$, 73% Pt, ACROS Organics), platinum(IV) chloride ($PtCl_4$, 99%, ACROS Organics), platinum on carbon (Pt/C, nominally 20 wt.%, Alfa Aesar), platinum(IV) oxide (□-$PtO_2$, Matheson Coleman & Bell), carbon black (Vulcan XC 72R), and Nafion 117 (Sigma-Aldrich) were used as received. All solvents were obtained through typical commercial sources and used as received. Water was supplied with a Barnstead Nanopure water system (18.3 MΩ cm).

### Synthesis of graphitic carbon nitride

Graphitic carbon nitride (C3N4) was prepared by adopting a method reported previously.[23, 28] Briefly, urea (15 g) was placed in a crucible, covered, heated in air to 300 °C at a rate of 2 °C $min^{-1}$ and held for 3 h. The resulting white solid was ground to a fine powder, heated again in air to 520 °C at a rate of 20 °C $min^{-1}$ and held for 4 h. The resulting light-yellow solid was collected and washed with Nanopure water, filtered, and dried in a vacuum furnace for 24 h at 60 °C, affording C3N4.

### Synthesis of platinum oxide on graphitic carbon nitride

Platinum oxide deposition was performed by following a method described previously.[8, 20] Briefly, 50 mg of C3N4 prepared above was dispersed in Nanopure water (50 mL) under ultrasonication for 1 h. The resulting dispersion was then placed onto a hot plate under stirring. $PtCl_2$ or $PtCl_4$ (0.27 mmol) was slowly added to the stirring solution and allowed to mix at 90 °C for 48 h. In the case of $PtCl_2$, the salt was first dissolved in HCl and neutralized with anhydrous sodium carbonate to achieve a neutral pH before addition. The products were collected by centrifugation at 4500 rpm for 10 min, washed with Nanopure water and acetone, and dried in a vacuum oven overnight, which were

named as Pt2+90C and Pt4+90C. It should be noted that the supernatant exhibited an orange color, indicative of an excess of platinum chloride in the solution, and became clear after washing, signifying effective removal of excess metal salts.

**Characterization**

TEM measurements were carried out on a JOEL JEM 2100F microscope. XRD patterns were acquired with a Bruker D8 Advance diffractometer with Cu $K_{\square}$ radiation ($\lambda$ = 0.15418 nm). XPS measurements were performed with a Phi 5400/XPS instrument equipped with an Al $K_{\alpha}$ source operated at 350 W and $10^{-9}$ Torr. XAS measurements were carried out at 10 K on beamline 4-1 at the Stanford Synchrotron Radiation Lightsource using an Oxford liquid helium cryostat.

**Electrochemistry**

Electrochemical measurements were performed with a CHI710 workstation, and electrochemical impedance measurements were carried out with a Gamry Reference 600 instrument. A glassy carbon electrode (5.60 mm in diameter, 0.246 $cm^2$) was used as the working electrode, while a Ag/AgCl (1.0 M KCl) electrode and graphite rod were used as the reference and counter electrodes, respectively. The Ag/AgCl electrode was calibrated versus a reversible hydrogen electrode (RHE) and all potentials in the present study were referenced to this RHE. In a typical experiment, 2 mg of a dry sample prepared above was mixed with 3 mg of carbon black and sonicated for 20 min in 1 mL of isopropanol followed by an addition of Nafion (40 µL) and sonicated for an additional 10 min. 30 µL of the prepared ink was dropped onto the surface of the glassy carbon electrode and dried at room temperature, corresponding to a catalyst mass loading of 0.244 mg $cm^{-2}$.

## 2.5 Conclusions

In summary, PtOx nanoparticles were deposited onto C3N4 surfaces by thermal refluxing of C3N4 nanosheets and platinum chloride in water. The nanocomposites displayed similar platinum loading and particle size but with stark differences in the platinum valence states. It was shown that the platinum oxidation state greatly influenced the hydrogen evolution performance under electrochemical conditions, and platinum oxide nanoparticles in primarily a $4^+$ charge state exhibited an HER performance even superior to that of commercial platinum on carbon in acid media. This catalyst showed excellent recoverability after recycling the material under oxidizing conditions. Results from the present study suggest that future design of platinum oxide catalysts should attempt to optimize the valence states of platinum by minimizing the formation of less oxidized, and less active species.

## 2.6 References


1. Hand, M.M. and S.D. Baldwin, E.; Reilly, J.M.; Mai, T.; Arent, D.; Porro, G.; Meshek, M.; Sandor, D. eds, *Renewable Electricity Futures Study.* National Renewable Energy Laboratory, 2012. **1-4**.
2. Greeley, J., et al., *Computational high-throughput screening of electrocatalytic materials for hydrogen evolution.* Nature Materials, 2006. **5**(11): p. 909-913.
3. Voiry, D., et al., *Enhanced catalytic activity in strained chemically exfoliated WS2 nanosheets for hydrogen evolution.* Nature Materials, 2013. **12**(9): p. 850-855.
4. Cabán-Acevedo, M., et al., *Efficient hydrogen evolution catalysis using ternary pyrite-type cobalt phosphosulphide.* Nature Materials, 2015. **14**: p. 1245.
5. Eftekhari, A., *Electrocatalysts for hydrogen evolution reaction.* International Journal of Hydrogen Energy, 2017. **42**(16): p. 11053-11077.
6. Sealy, C., *The problem with platinum.* Materials Today, 2008. **11**(12): p. 65-68.

7. Zhao, Z.P., et al., *Surface-Engineered PtNi-O Nanostructure with Record-High Performance for Electrocatalytic Hydrogen Evolution Reaction.* Journal of the American Chemical Society, 2018. **140**(29): p. 9046-9050.

8. Hui, L., et al., *Availability of the Basal Planes of Graphene Oxide Determines Whether It Is Antibacterial.* ACS Applied Materials & Interfaces, 2014. **6**(15): p. 13183-13190.

9. Sarno, M. and E. Ponticorvo, *Much enhanced electrocatalysis of Pt/PtO2 and low platinum loading Pt/PtO2-Fe3O4 dumbbell nanoparticles.* International Journal of Hydrogen Energy, 2017. **42**(37): p. 23631-23638.

10. Cheng, X., et al., *Highly active, stable oxidized platinum clusters as electrocatalysts for the hydrogen evolution reaction.* Energy & Environmental Science, 2017. **10**(11): p. 2450-2458.

11. Durst, J., et al., *New insights into the electrochemical hydrogen oxidation and evolution reaction mechanism.* Energy & Environmental Science, 2014. **7**(7): p. 2255-2260.

12. Subbaraman, R., et al., *Enhancing Hydrogen Evolution Activity in Water Splitting by Tailoring Li<sup>+</sup>-Ni(OH)<sub>2</sub>-Pt Interfaces.* Science, 2011. **334**(6060): p. 1256-1260.

13. Hui, L., et al., *Highly Efficient and Selective Generation of Ammonia and Hydrogen on a Graphdiyne-Based Catalyst.* Journal of the American Chemical Society, 2019. **141**(27): p. 10677-10683.

14. Xue, Y., et al., *Rationally engineered active sites for efficient and durable hydrogen generation.* Nature Communications, 2019. **10**(1): p. 2281.

15. Xue, Y., et al., *Anchoring zero valence single atoms of nickel and iron on graphdiyne for hydrogen evolution.* Nature Communications, 2018. **9**(1): p. 1460.

16. Xiao, P., et al., *Polymeric Carbon Nitride/Mesoporous Silica Composites as Catalyst Support for Au and Pt Nanoparticles.* Chemistry – A European Journal, 2014. **20**(10): p. 2872-2878.

17. Gong, Y., et al., *Graphitic carbon nitride polymers: promising catalysts or catalyst supports for heterogeneous oxidation and hydrogenation.* Green Chemistry, 2015. **17**(2): p. 715-736.

18. Spieker, W.A., et al., *An EXAFS study of the co-ordination chemistry of hydrogen hexachloroplatinate(IV) 1. Speciation in aqueous solution.* Applied Catalysis a-General, 2002. **232**(1-2): p. 219-235.

19. Hindmarsh, K., D.A. House, and R. van Eldik, *The redox kinetics of platinum(II)/(IV) complexes.* Inorganica Chimica Acta, 1998. **278**(1): p. 32-42.

20. He, B.L., et al., *Size control synthesis of polymer-stabilized water-soluble platinum oxide nanoparticles.* Journal of Colloid and Interface Science, 2007. **308**(1): p. 105-111.

21. Westwood, W. and C. Bennewitz, *Formation of PtO films by reactive sputtering.* Journal of Applied Physics, 1974. **45**(5): p. 2313-2315.

22. Hoekstra, H., S. Siegel, and G. FX. *REACTIONS OF PLATINUM DIOXIDE WITH SOME METAL OXIDES*. in *ABSTRACTS OF PAPERS OF THE AMERICAN CHEMICAL SOCIETY*. 1969. AMER CHEMICAL SOC 1155 16TH ST, NW, WASHINGTON, DC 20036.

23. Lazauskas, A., et al., *Characterization of urea derived polymeric carbon nitride and resultant thermally vacuum deposited amorphous thin films: Structural, chemical and photophysical properties.* Carbon, 2016. **107**: p. 415-425.

24. Peuckert, M., F.P. Coenen, and H.P. Bonzel, *XPS study of the electrochemical surface oxidation of Platinum in N H2SO4 acid electrolyte.* Electrochimica Acta, 1984. **29**(10): p. 1305-1314.

25. Karhu, H., et al., *XPS analysis of chlorine residues in supported Pt and Pd catalysts with low metal loading.* Applied Catalysis A: General, 2003. **247**(2): p. 283-294.

26. Wang, Z.Q., et al., *A platinum oxide decorated amorphous cobalt oxide hydroxide nanosheet array towards alkaline hydrogen evolution.* Journal of Materials Chemistry A, 2018. **6**(9): p. 3864-3868.

27. Svintsitskiy, D.A., et al., *Highly Oxidized Platinum Nanoparticles Prepared through Radio-Frequency Sputtering: Thermal Stability and Reaction Probability towards CO.* Chemphyschem, 2015. **16**(15): p. 3318-3324.

28. Thomas, A., et al., *Graphitic carbon nitride materials: variation of structure and morphology and their use as metal-free catalysts.* Journal of Materials Chemistry, 2008. **18**(41): p. 4893-4908.

29. Liu, J.H., et al., *Simple pyrolysis of urea into graphitic carbon nitride with recyclable adsorption and photocatalytic activity.* Journal of Materials Chemistry, 2011. **21**(38): p. 14398-14401.

30. Thurston, J.H., et al., *Urea-derived graphitic carbon nitride (u-g-C3N4) films with highly enhanced antimicrobial and sporicidal activity.* Journal of Colloid and Interface Science, 2017. **505**: p. 910-918.

31. Chen, L., et al., *Platinum nanoparticles encapsulated in nitrogen-doped graphene quantum dots: Enhanced electrocatalytic reduction of oxygen by nitrogen dopants.* International Journal of Hydrogen Energy, 2017. **42**(49): p. 29192-29200.

32. Ahmadi, M., H. Mistry, and B. Roldan Cuenya, *Tailoring the Catalytic Properties of Metal Nanoparticles via Support Interactions.* The Journal of Physical Chemistry Letters, 2016. **7**(17): p. 3519-3533.

33. Booth, C.H., *R-Space X-ray Absorption Package, 2010.* 2010.

34. Horsley, J.A., *RELATIONSHIP BETWEEN THE AREA OF L2,3 X-RAY ABSORPTION-EDGE RESONANCES AND THE D ORBITAL OCCUPANCY IN COMPOUNDS OF PLATINUM AND IRIDIUM.* Journal of Chemical Physics, 1982. **76**(3): p. 1451-1458.

35. Mansour, A.N., J.W. Cook, and D.E. Sayers, *QUANTITATIVE TECHNIQUE FOR THE DETERMINATION OF THE NUMBER OF UNOCCUPIED D-ELECTRON STATES IN A PLATINUM CATALYST USING THE L2,3 X-RAY ABSORPTION-EDGE SPECTRA.* Journal of Physical Chemistry, 1984. **88**(11): p. 2330-2334.

36. Friebel, D., et al., *In situ X-ray probing reveals fingerprints of surface platinum oxide.* Physical Chemistry Chemical Physics, 2011. **13**(1): p. 262-266.

37. Yoshida, H., et al., *Quantitative determination of platinum oxidation state by XANES analysis.* Physica Scripta, 2005. **T115**: p. 813-815.

38. Persson, K., *Materials Data on PtO2 (SG:186) by Materials Project.* 2014.

39. Gao, M.R., et al., *Completely Green Synthesis of Colloid Adams' Catalyst a-PtO2 Nanocrystals and Derivative Pt Nanocrystals with High Activity and Stability for Oxygen Reduction.* Chemistry-a European Journal, 2012. **18**(27): p. 8423-8429.

40. Ankudinov, A.L. and J.J. Rehr, *Relativistic calculations of spin-dependent x-ray-absorption spectra.* Physical Review B, 1997. **56**(4): p. R1712-R1716.

41. Peng, Y., et al., *Ruthenium Ion-Complexed Graphitic Carbon Nitride Nanosheets Supported on Reduced Graphene Oxide as High-Performance Catalysts for Electrochemical Hydrogen Evolution.* Chemsuschem, 2018. **11**(1): p. 130-136.

42. Zhan, Y.X., et al., *Synthesis of a MoSx-O-PtOx Electrocatalyst with High Hydrogen Evolution Activity Using a Sacrificial Counter-Electrode.* Advanced Science, 2019. **6**(5).

43. Kundu, M.K., et al., *Platinum Nanostructure/Nitrogen-Doped Carbon Hybrid: Enhancing its Base Media HER/HOR Activity through Bi-functionality of the Catalyst.* Chemsuschem, 2018. **11**(14): p. 2388-2401.

## Chapter 3 Platinum-complexed phosphorous-doped carbon nitride for electrocatalytic hydrogen evolution

## 3.1 Abstract

Sustainable hydrogen gas production is critical for future fuel infrastructure. Here, a series of phosphorous-doped carbon nitride materials were synthesized by thermal annealing of urea and ammonium hexafluorophosphate, and platinum was atomically dispersed within the structural scaffold by thermal refluxing with Zeise's salt forming Pt-N/P/Cl coordination interactions, as manifested in X-ray photoelectron and absorption spectroscopic measurements. The resulting materials were found to exhibit markedly enhanced electrocatalytic activity towards the hydrogen evolution reaction (HER) in acidic media, as compared to the P-free counterpart. This was accounted for by P doping that led to a significantly improved charge carrier density within $C_3N_4$, and the sample with the optimal P content showed an overpotential of only -22 mV to reach the current density of 10 mA $cm^{-2}$, lower than that of commercial Pt/C (-26 mV), and a mass activity (7.1 mA $\mu g_{Pt}^{-1}$ at -70 mV vs reversible hydrogen electrode) nearly triple that of the latter. Results from the present study highlight the significance of P doping in the manipulation of the electronic structures of metal/carbon nitride nanocomposites for high-performance HER electrocatalysis.

## 3.2 Introduction

Globally, renewable electricity is projected to reach 33% of the total installed power capacity by 2025, surpassing electricity produced by coal and becoming the largest segment of electricity generation around the world.[1] With renewable electricity on the rise, electrochemical water splitting for hydrogen generation provides a promising technology for sustainable energy storage and conversion.[2, 3] Currently, more than 95% of the world's hydrogen gas is produced through steam methane reforming, which produces a significant amount of carbon dioxide byproduct.[4] Acceptance of electrochemical water splitting as a viable means for hydrogen gas generation will require

improvements in electrocatalyst design and usage of platinum within the material to lower device costs and hydrogen gas conversion efficiencies, as platinum remains the catalyst of choice towards the hydrogen evolution reaction (HER), in particular, in acidic media.[5-7] Numerous routes have been taken to achieve this goal including the use of platinum oxide particles,[8, 9] manipulation of nanoparticle morphologies,[10, 11] and decreased particle size down to the single platinum atom regime.[12, 13]

Significant improvement in Pt mass efficiency can be achieved through the utilization of Pt single atom sites because of maximal surface exposure and utilization of Pt within the catalyst materials.[13-22] For instance, Cheng et al.[12] recently deposited Pt single atoms on nitrogen-doped carbon nanosheets by utilizing an atomic layer deposition (ALD) approach, and the resulting Pt single atom catalysts (SAC) showed a mass activity of 10.1 mA $\mu g_{Pt}^{-1}$ in a 0.5 M $H_2SO_4$ electrolyte, 37 times that of Pt/C (0.27 mA $\mu g_{Pt}^{-1}$), at the applied potential of -50 mV vs reversible hydrogen electrode (RHE). Fang and associates recently deposited Pt single atoms onto a nitrogen-doped carbon framework of approximately 300 nm in diameter also through an ALD process, and the catalyst exhibited a low overpotential ($\eta_{10}$) of -19 mV to reach the current density of 10 mA $cm^{-2}$ in a 0.5 M $H_2SO_4$ electrolyte. Operando synchrotron X-ray absorption spectroscopy studies revealed partial release of the Pt single atoms resulting in undercoordination. Further analysis by extended X-ray absorption fine structure (EXAFS) measurements and theoretical simulations suggested that a high 5d orbital occupancy, close to zero valency of Pt, was responsible for the high HER activity.

However, recent reports have shown Pt in a lower orbital occupancy, such as Pt oxide, can facilitate HER efficiently as well. For example, Yu and colleagues recently reported on Pt-O as a superior active site to $Pt^0$ for HER with the use of a platinum tungsten oxide ($PtW_6O_{24}$) spherical particles of ca. 20 nm in diameter.[23] The material was prepared

from a mixture of $Na_2Pt(OH)_6$ and $Na_2WO_4$ followed by collection of precipitates and washing. Electrochemical measurements revealed a mass activity of 20.175 mA $\mu g_{Pt}^{-1}$ for HER at the overpotential of -70 mV in 0.5 M $H_2SO_4$, significantly better than commercial Pt/C (20 wt%, 0.398 mA $\mu g_{Pt}^{-1}$). Cao and co-workers[10] employed a one-pot synthesis route using $Pt(acac)_2$ and $Ni(acac)_2$ metal precursors and produced Pt-Ni branched nanocages of approximately 200 nm in diameter with a thinner branching morphology spreading out from the center (50 nm), which exhibited a mass activity nearly 2.5-fold higher than commercial Pt/C. These findings confirm that Pt does not need to possess high orbital occupancy to efficiently catalyse HER. To this end, an array of interesting Pt-based catalysts can be devised for the efficient evolution of hydrogen through unique synthetic methods beyond the ALD process.

Note that ALD, used in these previous studies for the synthesis of Pt-based SAC, requires the use of sophisticated and expensive instrumentation. It would be of great significance to develop low-cost, effective procedures for the preparation of Pt SAC. A range of synthetic approaches toward Pt SAC have been studied and well documented in recent reviews.[24, 25] These synthetic approaches include wet-chemistry, ALD, pyrolysis of metal-organic frameworks, electrodeposition, high-temperature atom trapping from bulk particles, and vacancy/defect immobilization methods. For example, Wang and colleagues demonstrated an electro-filtration strategy to synthesize Pt single atom sites using a Pt foil and graphite carbon paper. In this electroplating strategy Pt single atoms were created through oxidation of the Pt foil counter electrode followed by Pt single atom deposition onto the carbon paper working electrode. A graphene oxide membrane was used as a filter between the counter and working electrodes to control the Pt single atom diffusion rate and prevent Pt particle formation. Scalability of this process is of somewhat

concern since production of the Pt SAC is limited by the size of the electrochemical cell and working electrode.

In recent studies,[16, 26] it was observed that ion complexation by simple thermal refluxing can be exploited to effectively embed isolated metal centers within the structural skeleton of graphitic carbon nitride ($C_3N_4$) by taking advantage of the pyridine-like nitrogen moieties, where the incorporation of metal centers was found to lead to charge redistribution and enhanced electrical conductivity of the semiconducting $C_3N_4$ matrix. For example, Zeng and colleagues reported on the synthesis of single-atom Pt confined by interlayer $C_3N_4$ for efficient photocatalytic hydrogen evolution.[27] The synthesis process involved mixing of potassium-intercalated $C_3N_4$ with $Pt(NH_3)_4Cl_2$ in deionized water under vigorous stirring at room temperature over a 24 h period. Incorporation of Pt single atoms into the $C_3N_4$ framework significantly improved the photocatalytic hydrogen evolution efficiency to 22.65 mmol($H_2$) $g^{-1}$ $h^{-1}$ with an 8.7 wt% Pt loading. The semiconductor properties of $C_3N_4$ are ideal for such photocatalytic processes; however, this leads to poor electron carrier capabilities when applied to electrocatalysis. Fortunately, deliberate modifications to the carbon nitride framework can be made to improve the electrocatalytic efficiency of $C_3N_4$. One such modification involves heteroatom doping within the $C_3N_4$ framework to improve electrical conductivity of the support material.[28-30] For example, Zhang and co-workers developed a phosphorous-doped $C_3N_4$ solid which demonstrated enhanced electrical conductivity.[29] Experimentally, 1-butyl-3-methylimidazolium hexafluorophosphate was added as a phosphorous source during the polycondensation of dicyandiamide (DCDA) forming P-doped $C_3N_4$, which was confirmed in spectroscopic and electrochemical measurements. Such P-doped $C_3N_4$ materials have been implemented for electrochemical applications. Qiu and co-workers reported on a three-dimensional P-

doped $C_3N_4$ for enhanced metal-free oxygen reduction reaction (ORR) applications, which was prepared by polycondensation of DCDA and nitrilotris(methylene)-triphosphoric acid as a phosphorous source at 600 °C. P-doping was seen to substantially improve the ORR half-wave potential and limiting current, likely due to improved electrical conductivity as found in electrochemical impedance measurements. Notably, heteroatom doping of semiconductor materials is well studied as a tool for tuning the band gap structure,[31-33] where doping of higher periodic elements typically leads to a narrower band gap and lower highest occupied molecular orbital (HOMO) levels.[34] Thus, the larger atomic size of phosphorous, versus carbon and nitrogen, is anticipated to lead to improved conformation and conductivity of $C_3N_4$. This is the primary motivation of the present study.

Herein, P-doped $C_3N_4$ was first prepared via a facile thermal annealing procedure using urea and ammonium hexafluorophosphate as the precursors, into which were then embedded Pt metal centers by thermal refluxing with Zeise's salt forming Pt-N/P/Cl coordination bonds, as attested in spectroscopic measurements. Mott-Schottky analysis showed that P doping led to a marked improvement of the charge carrier density and electrical conductivity. Electrochemical tests demonstrated that the resulting PtCNP nanocomposites outperformed the P-free counterparts, and the sample with the optimal P content showed an $\eta_{10}$ of only -22 mV, lower than that of commercial Pt/C (-26 mV), and a mass activity (7.1 mA $\mu g_{Pt}^{-1}$ at -70 mV vs RHE) nearly triple that of the latter. The results suggest that P-doped $C_3N_4$ may be used as a unique structural scaffold to optimize the use of Pt for HER electrocatalysis.

### 3.3 Results and Discussion

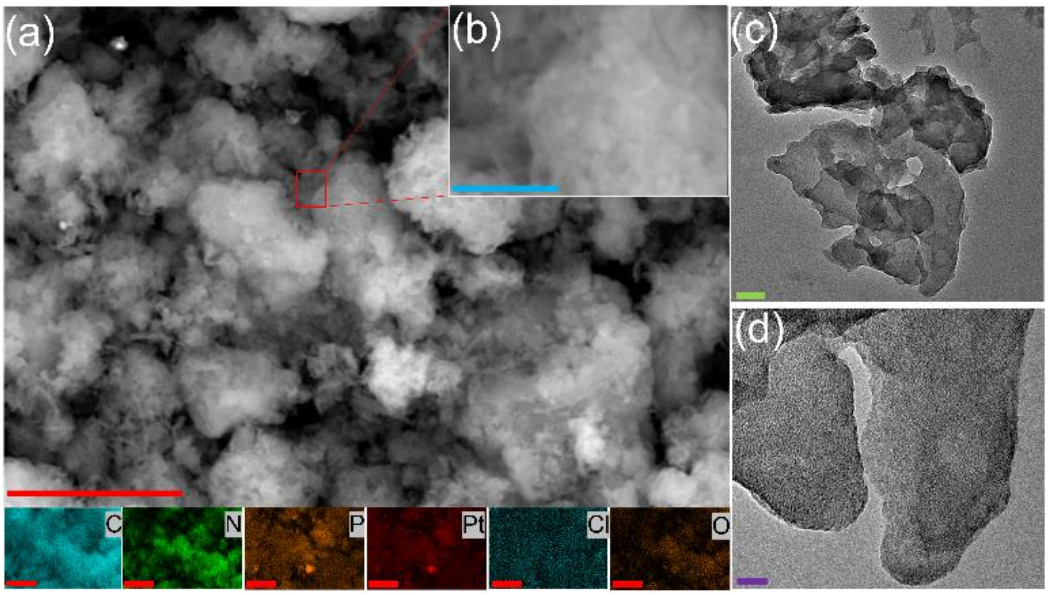


Figure 1. (a) SEM image of the $PtCNP_2$ sample, with the EDS elemental maps shown at the bottom for C, N, P, Pt, Cl, and O. (b) High-magnification SEM image for the red box area in panel (a). (c, d) TEM images of $PtCNP_2$. Scale bars are (a) 5 μm, (b) 1 μm, (c) 50 nm and (d) 10 nm.

The material structures were first characterized by electron microscopic measurements. From the SEM images in Figure 1a and 1b, one can see that $PtCNP_2$ exhibits a flaky morphology that closely resembles that of typical polymeric carbon nitride,[29, 35] and the wrinkled, porous nature of the material likely arose from oxygen-containing gases generated during the polymerization of the urea precursor resulting in punctures and holes in the material matrix. The corresponding EDS elemental maps are depicted directly below panel (a), where one can readily see an even distribution of all elements characterized including C, N, O, P, Pt, and Cl. The porous, layered structure of the composite is also evident in the TEM images shown in Figure 1c-1d. Notably, no particulates can be resolved in the TEM images of the sample, suggesting successful atomic dispersion of Pt within the $C_3N_4$ skeletons. Similar structural characteristics can

also be seen with other samples in the series, as manifested in both SEM (Figure 2) and TEM measurements (Figure 3).

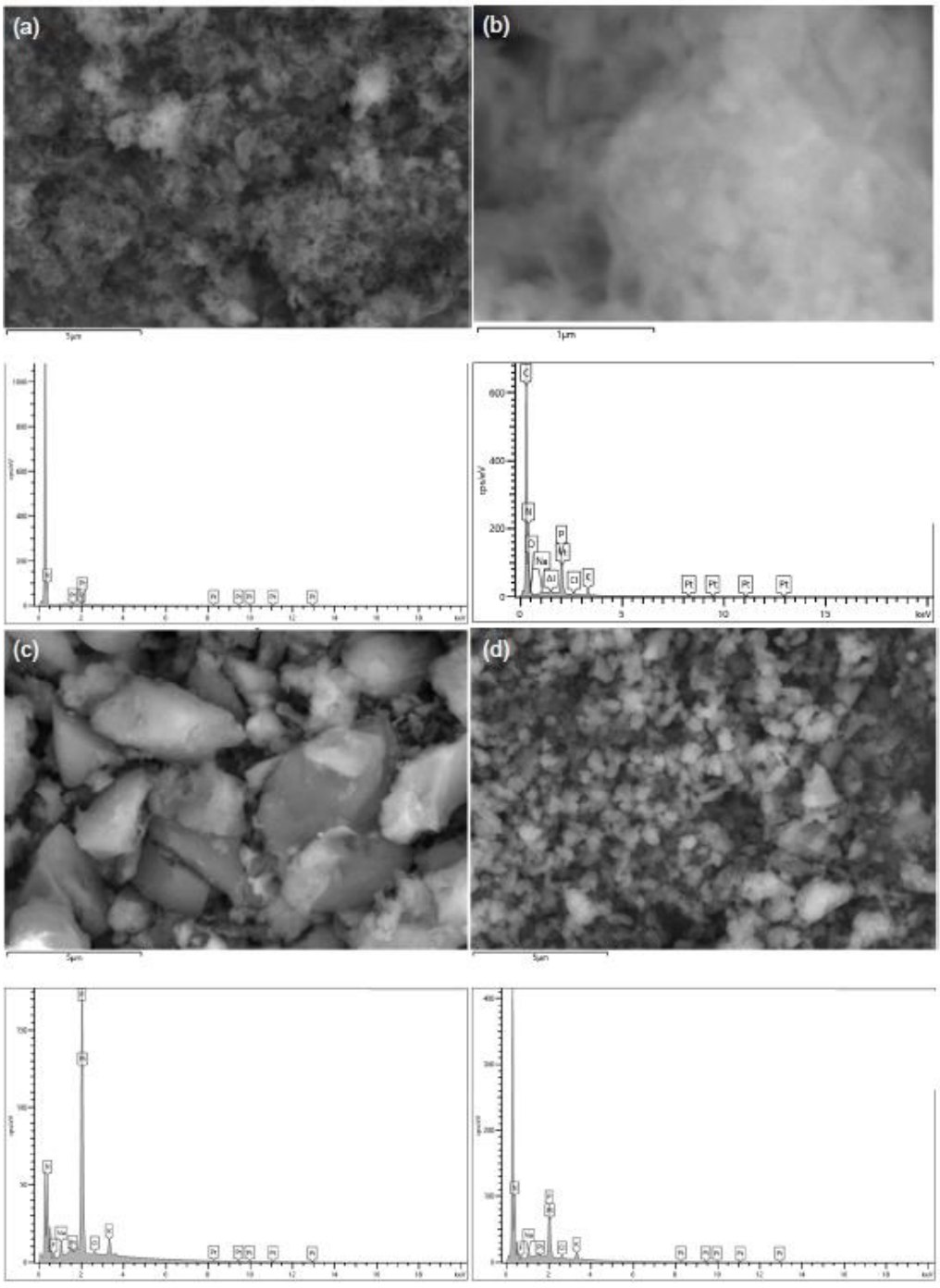


Figure 2. SEM images of (a) PtCNP1, (b) PtCNP2, (c) PtCNP3, and (d) PtCNP4. The corresponding EDS spectra

are included below the respective panel, where Pt signals can be readily identified in all samples.

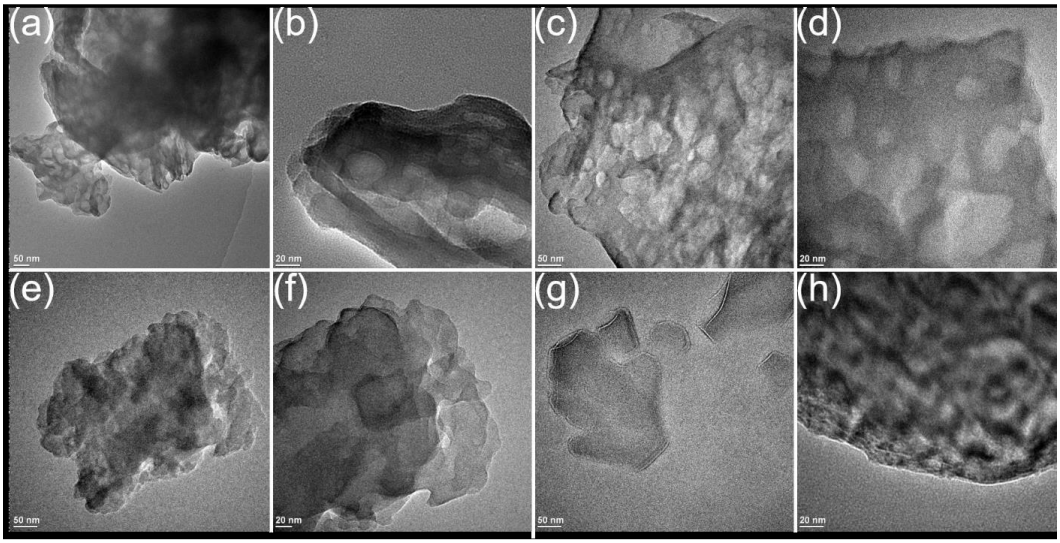


Figure 3. TEM images of (a, b) PtCN, (c, d) PtCNP1, (e, f) PtCNP3, (g, h) PtCNP4. Scale bars are (a, c, e, g) 50 nm and (b, d, f, h) 20 nm.

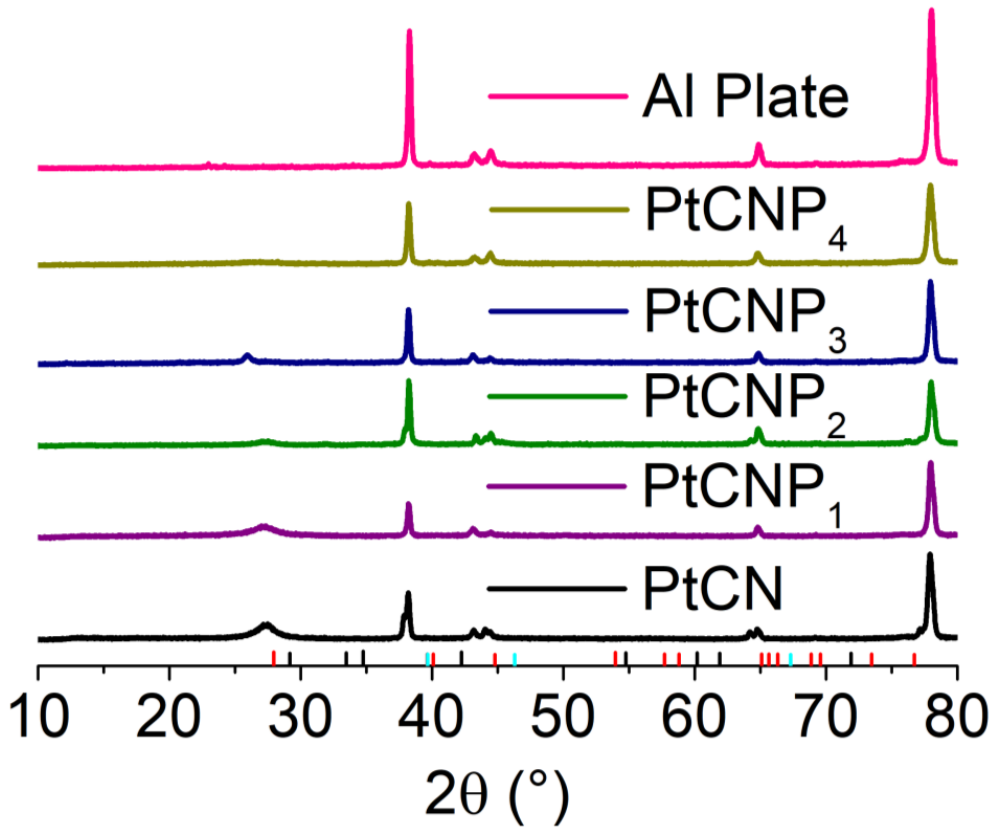


Figure 4. XRD patterns of the sample series deposited onto an aluminum plate. Reference lines are provided at the bottom of the plot and refer to cubic Pt with space group fm-3m (JCPDS: 00-001-1190 (cyan), tetragonal PtO with space group p42/mmc JCPDS: 00-027-1331 (black), and orthorhombic $PtO_2$ with space group pnnm JCPDS: 00-023-1306 (red).

The sample structures were then examined by XRD measurements. From Figure 4, one can see that in addition to the diffraction patterns of the Al plate (substrate), the PtCN, $PtPCN_1$ and $PtCNP_2$ composites all exhibited a small peak at $2\theta = 27°$, consistent with results reported previously for orthorhombic polymeric carbon nitride materials.[35] Notably, this peak shifted to a somewhat smaller angle of ca. 26° in $PtCNP_3$ and became significantly broadened in $PtCNP_4$, likely due to the doping of larger-sized P into the $C_3N_4$ framework which resulted in deterioration of the material crystallinity at high P concentration. Furthermore, no diffraction features of Pt, PtO, or $PtO_2$ can be resolved in

any of the samples, in agreement with the results from SEM and TEM measurements which suggested the absence of metal (oxide) nanoparticles.

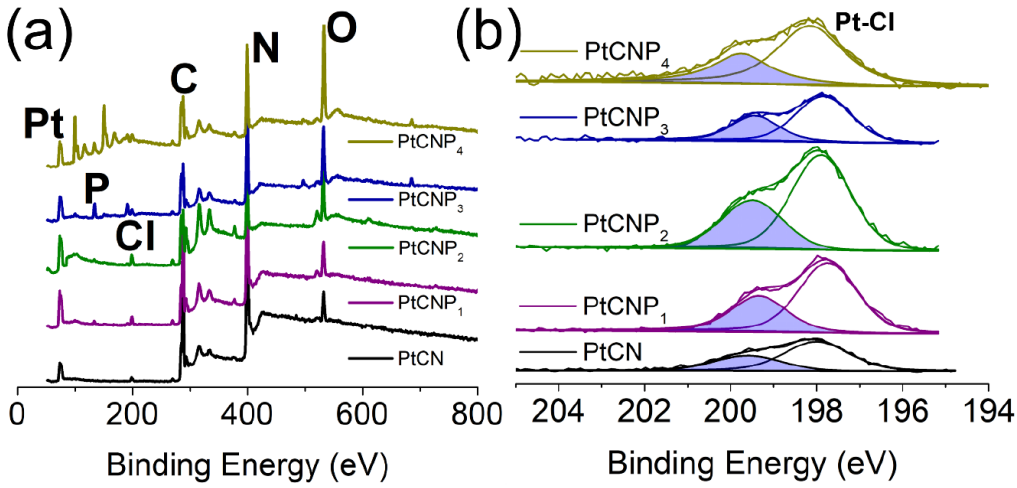


Figure 5. (a) XPS survey spectra of PtCN, PtCNP1, PtCNP2, PtCNP3, and PtCNP4. (b) High-resolution Cl 2p spectra of the sample series.

The elemental composition and valence state was then investigated by XPS measurements. From the survey spectra in Figure 5a, the PtCNP samples can be seen to entail a series of well-defined peaks, at ca. 75 eV for Pt 4f electrons, 133 eV for P 2p, 200 eV for Cl 2p, 285 eV for C 1s, 400 eV for N 1S, and 530 eV for O 1s. PtCN exhibited a similar profile except for the P 2p peak. Based on the integrated peak areas, the elemental compositions of the samples were then estimated and listed in Table 1. One can see that the C:N atomic ratios of the samples all deviated appreciably from the theoretical value of 0.75 for pristine $C_3N_4$, likely the result of a combined contribution of structural defects and heteroatom doping.[36, 37] Notably, with increasing P doping, the C:N ratio increases accordingly in the order of PtCN (0.86) < $PtCNP_1$ ≈ $PtCNP_2$ (0.96) < $PtCNP_3$ (1.04) < $PtCNP_4$ (2.75), likely due to the incorporation of oxygen and phosphorous into carbon nitride replacing nitrogen. In fact, one can see that the oxygen content increased from 3.71% for PtCN to 6.38%, 4.73%, 13.19%, and 55.53 % for $PtCNP_1$, $PtCNP_2$,

$PtCNP_3$, and $PtCNP_4$, respectively; and the corresponding phosphorous content was found to increase from 0% to 1.31%, 1.11%, 6.32%, and 11.03%. The corresponding Pt contents were estimated to be 0.73, 1.69, 1.69, 1.58 and 0.32 at% (or 9.72, 19.52, 19.59, 17.45, and 3.38 wt%), which were substantially higher than those obtained in ICP-OES measurements (1.8, 1.8, 5.1, 0.6, and 0.8 wt%). As XPS is a surface probing technique, this suggests enrichment of Pt on the carbon nitride surface. This follows reasonably from the catalyst preparation methods, where the Pt salt could only complex at the surface upon contact with the previously prepared $C_3N_4$. Note that preventing the incorporation of Pt toward the inside of the $C_3N_4$ support is beneficial for electrocatalysis as only the surface Pt will be involved in electrochemical processes, thereby improving mass activity of the electrocatalysts (vide infra). Furthermore, high doping levels of P appeared to hinder Pt incorporation, likely due to the highly defective scaffold, and $CNP_2$ represented the optimal structure for Pt complexation. Notably, the Cl:Pt ratios of all but $PtCNP_4$ were found to be close to 1:1, at 0.79 for PtCN, 0.95 for $PtCNP_1$, 1.02 for $PtCNP_2$, and 0.74 for $PtCNP_3$, suggesting that the incorporation of Pt into the nanocomposites was due to partial replacement of the original Cl ligands of the Zeise's salt precursor (which features a Cl:Pt ratio of 3) (Scheme 1).

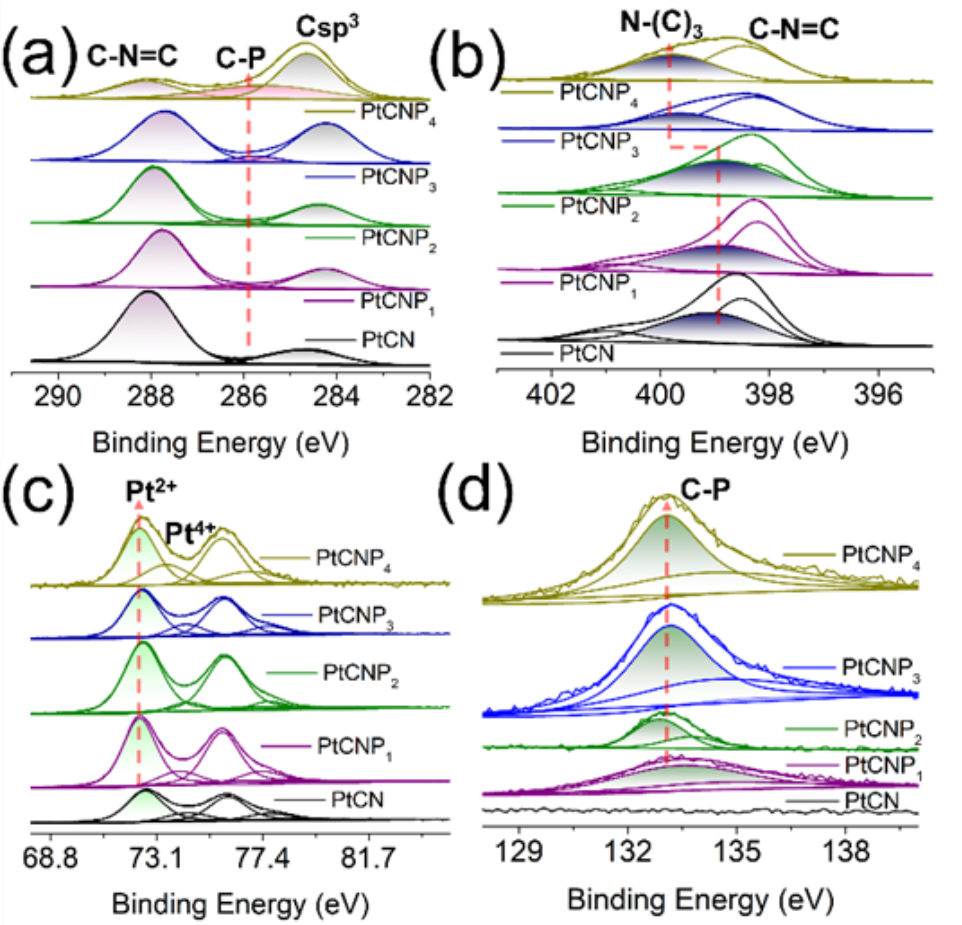


Figure 6. High resolution XPS spectra of the (a) C 1s, (b) N 1s, (c) Pt 4f, and (d) P 2p electrons of the PtCN, $PtCNP_1$, $PtCNP_2$, $PtCNP_3$, and $PtCNP_4$ samples.

Further structural insights were obtained in high-resolution XPS analysis. Figure 6a depicts the C 1s spectra of the sample series, where two major components can be deconvoluted for all samples at ca. 288.0 and 284.5 eV, due to the $sp^2$ hybridized carbon within the carbon nitride matrix (C-N=C) and defected carbon ($Csp^3$), respectively.[38-40] Interestingly, the ratio between the areas of these two peaks decreased from 4.14 for PtCN to 1.99 for $PtCNP_1$, 2.07 for $PtCNP_2$, 1.16 for $PtCNP_3$, and 0.3 for $PtCNP_4$, again, suggesting the formation of an increasingly defective $C_3N_4$ skeleton with increasing phosphorous doping. Additionally, for the PtCNP samples, a third peak can be resolved at

ca. 286 eV, which can be ascribed to C-P bond, signifying successful P doping of $C_3N_4$.[28, 41]

The corresponding N 1s spectra are shown in Figure 6b, where two major components can be resolved, C-N=C at ca. 398.4 eV and tertiary N-$(C)_3$ at ca. 399 eV.[38-40] The exact binding energy of C-N=C varied slightly, 398.49 eV for PtCN, 398.21 eV for $PtCNP_1$, 398.36 eV for $PtCNP_2$, 398.29 eV for $PtCNP_3$, and 398.47 eV for $PtCNP_4$. For tertiary N-$(C)_3$, the binding energy was very close among the P-free PtCN (399.05 eV), and low-P $PtCNP_1$ (398.86 eV) and $PtCNP_2$ (398.99 eV), whereas for $PtCNP_3$ and $PtCNP_4$ that contained a high P dopant concentration, the binding energy was substantially higher at 399.62 and 399.78 eV, respectively. This suggests that at low P doping, the $C_3N_4$ skeleton structure remained largely intact, whereas at high doping, the matrix became increasingly defective, as manifested in XRD measurements (Figure 4).

The high-resolution scans of the Pt 4f region are depicted in Figure 6c. In all samples, deconvolution yields two doublets, where the major one at ca. 72.5/75.8 can be ascribed to the $4f_{5/2}/4f_{7/2}$ electrons of Pt(II), whereas the minor one at 74.3/77.6 eV to those of Pt(IV) (Table 2).[9] One can see that the $4f_{7/2}$ binding energy of both Pt(II) and Pt(IV) in the PtCNP series diminished somewhat, as compared to those of P-free PtCN, implying that P doping led to electron enrichment of the Pt centres, and there appears a volcano variation of the binding energies with P dopant concentration, with $PtCNP_2$ at the maxima (72.54 and 74.34 eV). A reverse trend is observed in the binding energy of the P 2p electrons (Figure 6d), where $PtCNP_2$ exhibited the lowest binding energy (132.88 eV) of the $2p_{3/2}$ electrons (Table 3). This suggests a possible interaction between Pt and P within the P-doped samples, and such an interaction (charge transfer) was the strongest in $PtCNP_2$ among the series. Note that the binding energy of 132.88 eV is consistent with

that observed for P-C bond, again, confirming the successful doping of P into the $C_3N_4$ structure.[42]

Figure 5b depicts the corresponding high-resolution Cl 2p spectra, where the Cl $2p_{3/2}$ binding energy can be identified at 198.00, 197.74, 197.79, 197.83, and 198.15 eV for PtCN, $PtCNP_1$, $PtCNP_2$, $PtCNP_3$, and $PtCNP_4$ (Table 3), respectively. These binding energies are consistent with those observed for Pt-Cl containing complexes reported previously in the literature.[43, 44]

Table 1. Elemental compositions (at%) of the sample series from XPS measurements

| Sample | C | N | O | P | Cl | Pt |
|---|---|---|---|---|---|---|
| PtCN | 43.98 | 51.01 | 3.71 | 0.00 | 0.58 | 0.73 |
| $PtCNP_1$ | 43.66 | 45.35 | 6.38 | 1.31 | 1.60 | 1.69 |
| $PtCNP_2$ | 44.39 | 46.37 | 4.73 | 1.11 | 1.72 | 1.69 |
| $PtCNP_3$ | 39.63 | 38.11 | 13.19 | 6.32 | 1.17 | 1.58 |
| $PtCNP_4$ | 19.91 | 7.25 | 55.53 | 11.03 | 5.96 | 0.32 |

Table 2. Pt 4f binding energy and atomic ratio of the sample series

| Sample | Pt(II) | | Pt(IV) | | Pt(II)/Pt(IV) ratio |
|---|---|---|---|---|---|
| | $4f_{7/2}$ (eV) | $4f_{5/2}$ (eV) | $4f_{7/2}$ (eV) | $4f_{5/2}$ (eV) | |
| PtCN | 72.63 | 75.98 | 74.35 | 77.70 | 4.01 |
| $PtCNP_1$ | 72.40 | 75.75 | 74.02 | 77.37 | 5.12 |
| $PtCNP_2$ | 72.54 | 75.89 | 74.34 | 77.69 | 11.80 |
| $PtCNP_3$ | 72.49 | 75.84 | 74.29 | 77.64 | 4.70 |
| $PtCNP_4$ | 72.41 | 75.76 | 73.48 | 76.83 | 2.70 |

Table 3. Binding energy of the P and Cl 2p3/2 electrons in the sample series

| Sample | P | | Cl | |
|---|---|---|---|---|
| | $2p_{3/2}$ (eV) | $2p_{1/2}$ (eV) | $2p_{3/2}$ (eV) | $2p_{1/2}$ (eV) |
| PtCN | - | | 198.00 | 199.6 |
| $PtCNP_1$ | 133.39 | 134.26 | 197.74 | 199.34 |
| $PtCNP_2$ | 132.88 | 133.75 | 197.79 | 199.39 |
| $PtCNP_3$ | 133.12 | 133.99 | 197.83 | 199.43 |
| $PtCNP_4$ | 133.01 | 133.88 | 198.15 | 199.75 |

Further insights into the Pt electronic state and coordination structures were obtained through XAS measurements in the range of 11.5 to 12.0 keV corresponding to the Pt L3 edge. Figure 8a depicts the X-ray absorption near edge structures (XANES) for the sample series, the Zeise's salt precursor (orange curve), and a Pt foil (cyan curve). The obtained data were reduced and analysed using the RSXAP package.[45] The Pt foil (cyan curve) can be seen to exhibit a strong absorption peak at 11.566 keV, which is referred to as the white line and attributed to the Pt 2p → 5d transition (L3 edge).[46, 47] The white line peak position for the Zeise's salt occurs at 11.567 keV, and the remaining samples exhibit a peak position of 11.568 keV. The white line amplitude in this region typically increases with decreasing 5d orbital occupancy (i.e., increasing average valence state). One can see that the white line amplitude increases in the order of Pt foil < Zeise's salt < $PtCNP_1 \approx PtCNP_2 \approx PtCNP_3 \approx PtCNP_4$ < PtCN (inset to Figure 3a). This suggests (i) a non-metallic valence state of Pt in the PtCN and PtCNP samples, and (ii) a somewhat lower Pt valence state in PtCNP than in PtCN.[47-49] These findings are consistent with results from XPS measurements (Table 2). At higher energies, one can see that the PtCN and PtCNP samples exhibited a very similar extended X-ray absorption fine structure (EXAFS), which was very similar to that of the Zeise's salt but markedly different from that of the Pt foil. This can also be manifested in the corresponding R-space profiles in Figure 8b, where the same Fourier transform range (3.5-12 $Å^{-1}$) was used for the samples. A plot of the k space for the sample series can be seen in Figure 7. The R-space plots depict a clear change in the Pt environment in PtCN and PtCNP, with a smaller amplitude (increasing disorder), as compared to the two reference samples of Zeise's salt (orange curve) and Pt foil (cyan curve). Note that the peak structure near 2.4 Å, corresponding to the Pt-Pt pairs within the Pt foil (cyan curve), is not found in any of the other samples, whereas the primary peak near 1.9 Å in Zeise's salt (orange curve) corresponding to Pt-Cl pairs is shifted to a lower R position for the PtCN and PtCNP

samples and becomes broadened. Of note, the PtCN and PtCNP samples exhibit very similar R-space spectra with a broad peak near 1.7 Å, suggesting a consistent coordination environment around the Pt centres.

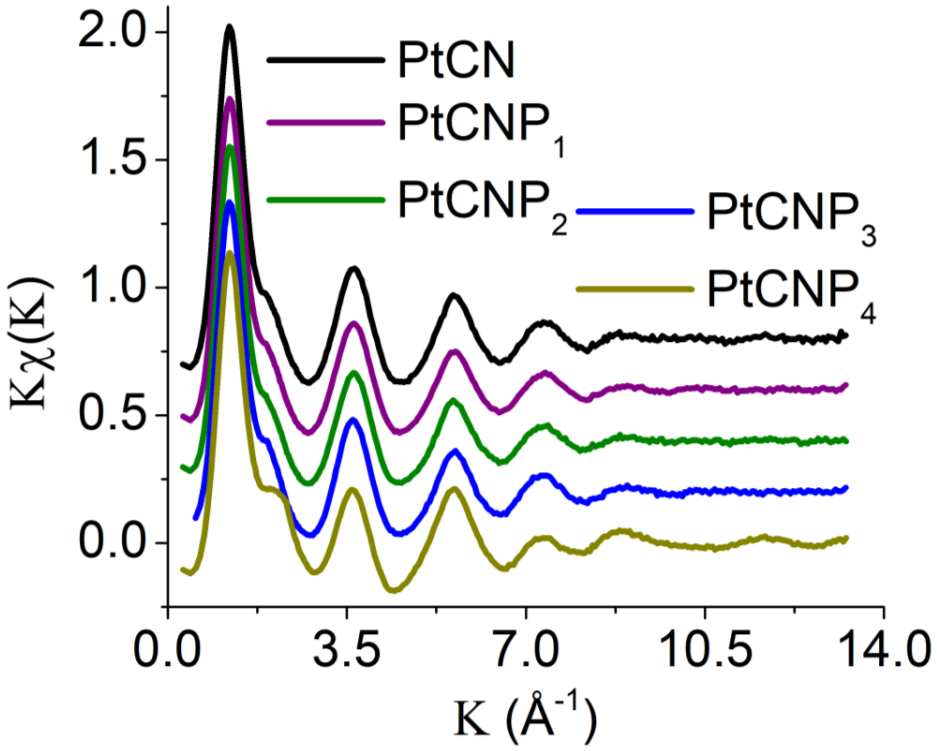


Figure 7. Pt L3 edge k-space data for the sample series collected at 10 K. Plots are produced by averaging 3 traces from each sample.

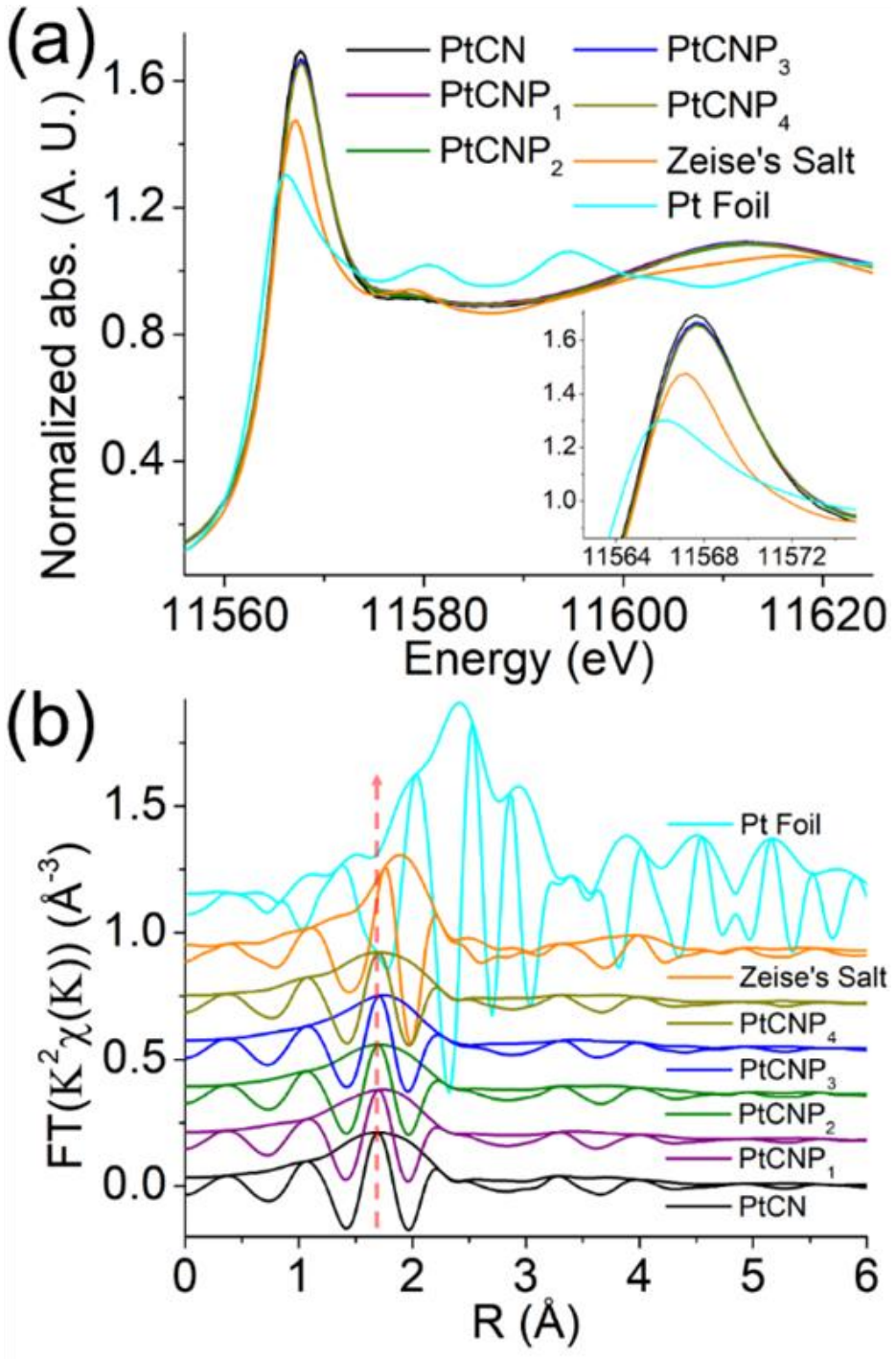


Figure 8. (a) Normalized Pt L3 edge XANES for the sample series in comparison to Pt Zeise's salt precursor (orange) and Pt foil (cyan). All edge steps are normalized to an edge height of 1. The energy range selected to normalize the edge is 11.7-12.0 keV. Measurements were performed at a temperature of 10K to reduce thermal disorder within

samples. Inset is the zoom in of the white line region. (b) Pt L3 edge r-space EXAFS data for the sample series and two reference samples, Pt Zeise's salt (orange) and Pt Foil (cyan). The FT window is from 3.5 to 12.0 $Å^{-1}$, rounded using a Gaussian function of width, 0.2 $Å^{-1}$. The fast-oscillating function is the real part R of the FT, and the amplitude is $(R^2+I^2)^{1/2}$, whereas I is the imaginary part of the FT. Samples have been shifted vertically for better comparison.

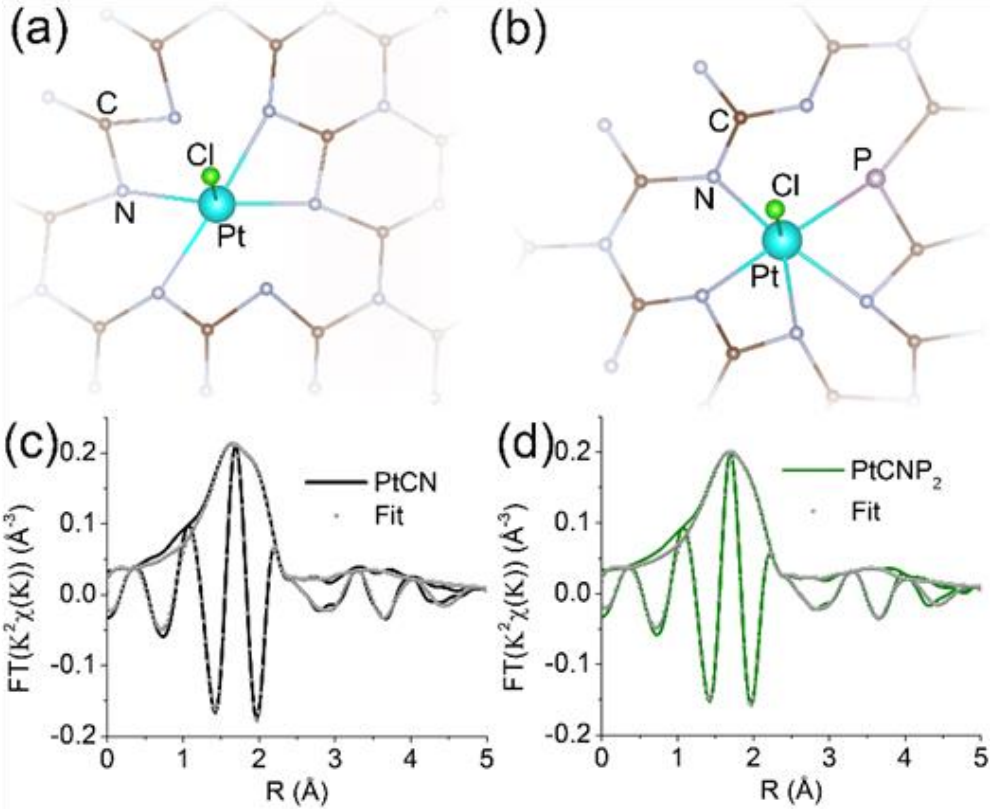


Figure 9. Ball and stick model representations of the fitting structures for (a) PtCN and (b) $PtCNP_2$. Coordination to the centre Pt atom indicates first and second shell atoms used for fitting. Atoms are colour coded with carbon (brown), nitrogen (gray), platinum (cyan), chlorine (green), and phosphorous (light red). EXAFS fitting results shown in R-space for (c) PtCN and (d) $PtCNP_2$. Raw R-space data is shown in solid with fits shown in gray circles. Fittings are performed in the R range of 1.3 to 2.5 Å.

Table 4. Bond length (r (Å)), coordination number (CN) and the Debye-Waller parameter ($\sigma^2$) from fitting of the EXAFS data in Figure 4.

| **Sample** | | **PtCN** | **PtCNP$_2$** |
|---|---|---|---|
| **Pt-N/C** | r (Å) | 2.01 | 2.03 |
| | CN | 4 | 4 |
| | $\sigma^2$ | 0.0066 | 0.0092 |
| **Pt-Cl/P** | r (Å) | 2.31 | 2.31 |
| | CN | 0.75 | 1.65 |
| | $\sigma^2$ | 0.0026 | 0.014 |
| **Pt-N/C** | r (Å) | 2.53 | 2.52 |
| | CN | 4 | 4 |
| | $\sigma^2$ | 0.0059 | 0.006 |
| **Pt-N/C** | r (Å) | 3.54 | 3.51 |
| | CN | 19.5 | 14.1 |
| | $\sigma^2$ | 0.04 | 0.035 |
| **Pt-N/C** | r (Å) | 4.14 | 4.15 |
| | CN | 12.7 | 9.02 |
| | $\sigma^2$ | 0.024 | 0.014 |

The EXAFS spectra were then fitted to quantify the bond lengths and coordination numbers using the rsFit function within the RSXAP software. The FEFF7 software was used to calculate the theoretical functions for each Pt pair (Pt-N/C, Pt-Cl/P).[52] The samples were fitted using four Pt-N/C paths and one Pt-Cl/P path created from the atomic positions in the structures depicted in Figure 4a and 4b with distances from Pt of 2.0 Å (Pt-N), 2.5 Å (Pt-N/C), 3.5 Å (Pt-N/C), 4.1 Å (Pt-N/C), and 2.3 Å (Pt-Cl/P), respectively.

The structure for fittings was created using a heptazine-based carbon nitride matrix. Pt was introduced into the gap between three tris-s-tiazine structures with the inclusion of one remaining Cl, and P was incorporated by replacement of a nearby N and bonded to C within the carbon nitride framework, as is consistent with the XPS findings (Figure 6). The structure was relaxed using density functional theory to minimize the geometric strain. The coordinates of each atom within the relaxed structure were used as input to FEFF7 to create the 5 Pt paths used for EXAFS fittings. The first path arises from the 4 nearest N neighbors to Pt, shown by direct bonds in Figure 9a and 9b. the second path arises from the next nearest neighbors to Pt, one Cl for structure 4a and one Cl and one P in structure 9b. As PtCN contained no P, P is absent in the structure used for PtCN fittings (Figure 9a). Paths 3, 4, and 5 arise from C and N atoms farther away from the central Pt atom, between 2.5 and 4.1 Å. These atoms are not directly bonded to Pt, but nonetheless are responsible for some structure in the raw spectra for each sample. At farther distances from Pt there will be more possible neighbors and therefore we see an increase in the coordination number at these distances. The number of neighbors in the first Pt-N/C path of both fittings was fixed at 4 to be consistent with the structures in Figure 9a and 9b. The number of neighbors in all other paths were allowed to vary. The Debye-Waller parameter ($\sigma^2$) for all paths remained low between 0.003 and 0.04. Fittings were performed in the R range of 1.3 to 3.7 Å for both samples, and the results are shown graphically in Figure 9c and 9d, respectively (also listed in Table 4). Due to the proximity of the atomic number of C (6), N (7), P (15), and Cl (17), a Pt-N and Pt-C paths are indistinguishable from one another through EXAFS fitting. Similarly, Pt-Cl and Pt-P paths are also indistinguishable. Therefore, the coordination number estimated from the fitting for a given path represents the sum of either Pt-C/Pt-N or Pt-Cl/Pt-P coordination. From the fitting results, the Pt-N/C bond length (r) for the first shell atoms was estimated to be 2.01 Å for PtCN and 2.03 Å for $PtCNP_2$, both with a coordination number of ca. 4,

suggesting a slightly stronger bonding interaction in the former, in agreement with the somewhat higher binding energy of the Pt 4f electrons in XPS measurements (Table 2). This bond length is consistent with the proposed structure and the expected bond length of a Pt-N coordination complex. Meanwhile, the Pt-Cl/P bond length showed identical bond lengths of 2.31 Å, with the respective coordination number of 0.75 and 1.65. As mentioned earlier in XPS measurements, the atomic ratio of Cl:Pt was ca. 0.79 for PtCN (Table 1), very consistent with the coordination number of 0.75, suggesting the formation of a single Pt-Cl bond in PtCN. In XPS measurements, $PtCNP_2$ showed a Cl:Pt ratio of 1.02, indicating also a single Pt-Cl coordination. Thus, the Pt-Cl/P coordination number of 1.65 in $PtCNP_2$ suggests that additional coordination most likely arose from a Pt-P environment.

Note that EXAFS fittings in Figure 9c and 9d were performed on the first primary peak beginning at 1.3 Å and extended to the structure near 3.7 Å using three additional Pt-N/C paths in 9-19 atom clusters, consistent with the structures depicted in Figure 9a and 9b. The results show no interaction between Pt-Pt neighbours and hence the absence of metallic Pt or $PtO_x$, which is consistent with atomic dispersion of Pt within the sample, as suggested in TEM measurements (Figure 1 and S2). Thus, based on the XPS and EXAFS fitting results, two structural models were constructed for PtCN and $PtCNP_2$, as depicted in Figure 9a and 9b, respectively, involving $PtN_4Cl$ and $PtN_4PCl$ nearest neighbours. Note there are several equivalent ways to place P on one of the nearby N/C sites.

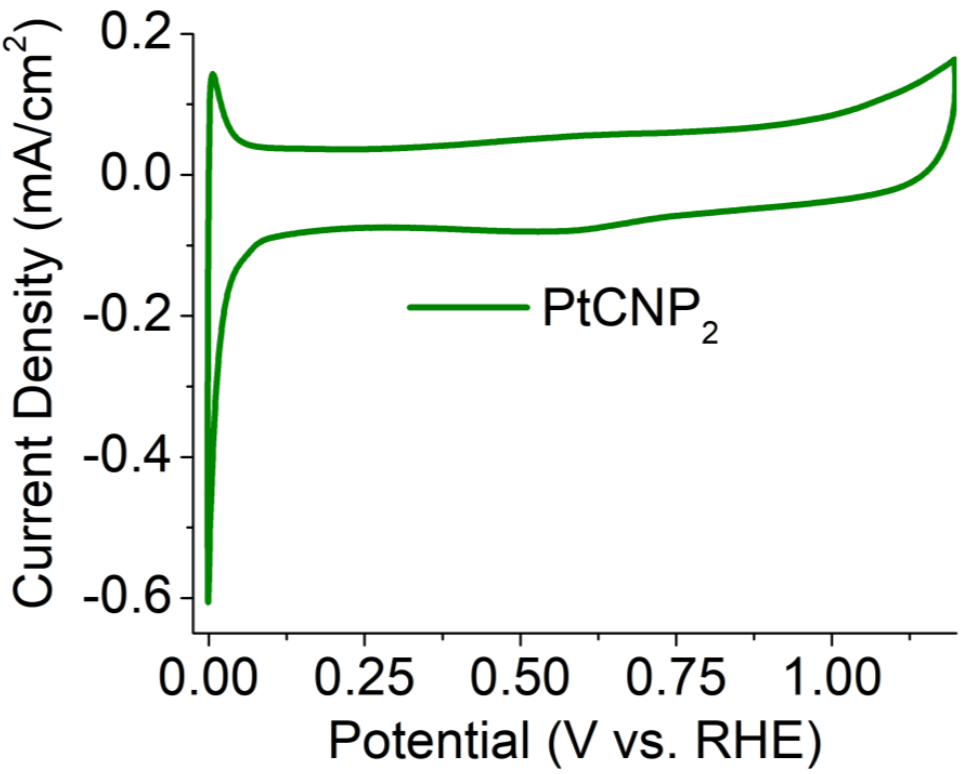


Figure 10. Cyclic voltammogram of the PtCNP2 sample performed in $N_2$ saturated $H_2SO_4$ at a scan rate of 10 mV $s^{-1}$. Current density is obtained by normalizing the current to the electrode geometrical surface area.

The electrocatalytic activity towards HER was then analysed and compared in acidic media. Note that cyclic voltametric measurements of $PtCNP_2$ within the potential range of 0 to +1.2 V in a $N_2$-saturated $H_2SO_4$ solution reveals no noticeable hydrogen adsorption-desorption feature (Figure 10), further confirming the absence of Pt and $PtO_x$ nanoparticles within the sample (vide ante). Figure 11a depicts the HER polarization curves in $N_2$-saturated 0.5 M $H_2SO_4$ of the various catalysts loaded onto a glassy carbon electrode. Notably, the metal-free $C_3N_4$ and $CNP_2$ exhibit only a minimal HER activity, which was then markedly improved with the incorporation of Pt forming PtCN and PtCNP. In fact, one can see that $PtCNP_2$ even outperformed commercial Pt/C catalyst. This can be readily seen in Figure 11b, where the $\eta_{10}$ was estimated to be -383 mV for

PtCN, -116 mV for $PtCNP_1$, -22 mV for $PtCNP_2$, -217 mV for $PtCNP_3$, -304 mV for $PtCNP_4$, and -26 mV for Pt/C. That is, P-doping significantly enhanced the HER activity of PtCN, and $PtCNP_2$ stood out as the best HER catalyst among the series, with a performance even better than that of Pt/C. Further contrast is observed in Figure 11c depicting the mass activity (MA, by normalizing the HER current to the Pt mass determined by ICP-OES measurements) obtained at -0.070 V vs RHE, which is 0.028 mA $\mu g_{Pt}^{-1}$ for PtCN, 0.771 mA $\mu g_{Pt}^{-1}$ for $PtCNP_1$, 7.1 mA $\mu g_{Pt}^{-1}$ for $PtCNP_2$, 0.226 mA $\mu g_{Pt}^{-1}$ for $PtCNP_3$, 0.05 mA $\mu g_{Pt}^{-1}$ for $PtCNP_4$, and 2.387 mA $\mu g_{Pt}^{-1}$ for Pt/C. Again, $PtCNP_2$ possessed the best performance, with the MA nearly triple that of Pt/C.

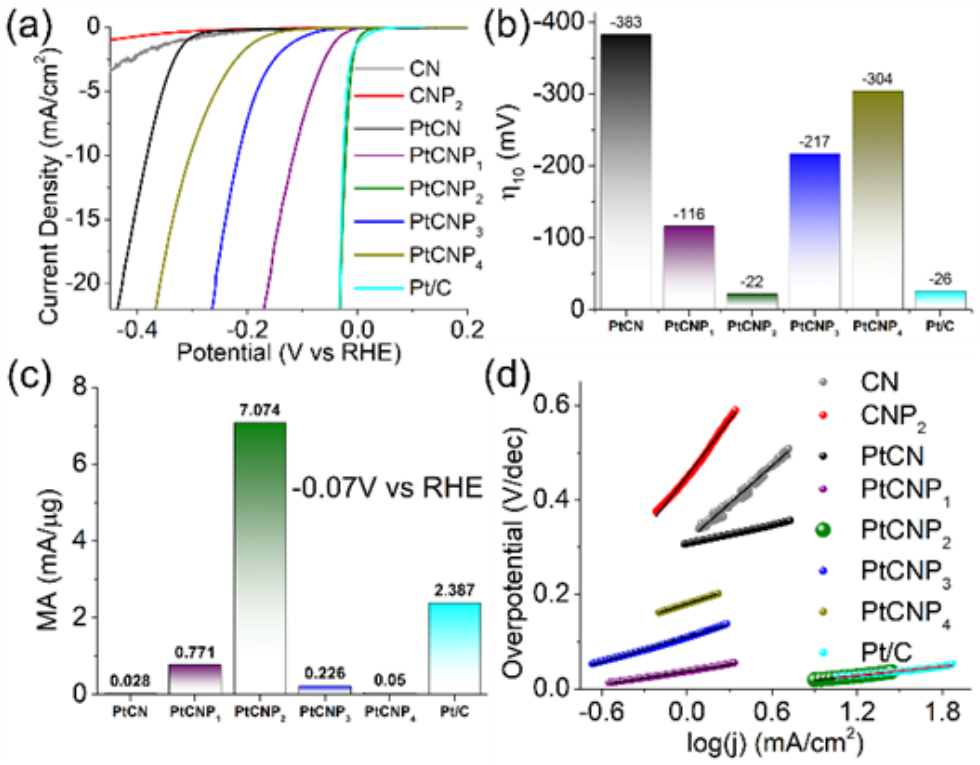


Figure 11. (a) HER polarization curves on various electrocatalysts in 0.5M $H_2SO_4$ at the rotation rate of 1600 rpm, potential sweep rate of 10 mV/s and 85% iR compensation. (b) Corresponding $\eta_{10}$ from the HER polarization curves in panel (a). (c) Mass activity at -0.07 V vs RHE per μg of Pt calculated from ICP-OES measurements. (d) Tafel plots

derived from panel (a). Note the overlapping data points between the Pt/C and $PtCNP_2$ samples.

Figure 11d depicts the Tafel plots for the various samples. Based on linear regression, the Pt-free samples can be seen to display a high Tafel slope of 265.4 mV $dec^{-1}$ for $C_3N_4$ (grey) and 390.8 mV $dec^{-1}$ for $CNP_2$ (red), which became substantially reduced for the PtCN and PtCNP samples, 65.7 mV $dec^{-1}$ for PtCN, 47.3 mV $dec^{-1}$ for $PtCNP_1$, 31.2 mV $dec^{-1}$ for $PtCNP_2$, 88.2 mV $dec^{-1}$ for $PtCNP_3$, 95.7 mV $dec^{-1}$ for $PtCNP_4$, and 31.5 mV $dec^{-1}$ for Pt/C. That is, $PtCNP_2$ exhibited the lowest Tafel slope (even slightly lower than that of Pt/C), suggesting most favorable electron-transfer kinetics. This also suggests that the Tafel or recombination reaction is the rate determining step,[50] as observed with commercial Pt/C, in which two adsorbed hydrogen join at the surface of the electrocatalyst and desorb to form molecular hydrogen.

Electrochemical impedance measurements were then carried out to evaluate the HER charge-transfer resistance ($R_{ct}$). Figure 12a depicts the Nyquist plots produced at the overpotential of -10 mV in 0.5 M $H_2SO_4$, which were fitted by using EC-Lab's software V11.10 with the equivalent circuit shown in the figure inset ($R_1$ is the solution resistance, $R_{ct}$ is the charge-transfer resistance, C is the double-layer capacitance, and $W_d$ is the Warburg diffusion term). At the selected overpotential, $R_{ct}$ was found to vary significantly among the samples, 2926 Ω for PtCN, 102.6 Ω for $PtCNP_1$, 19.3 Ω for $PtCNP_2$, 5862 Ω for $PtCNP_3$, and 6851 Ω for $PtCNP_4$, consistent with their HER activity as manifested in the HER polarization curves (Figure 11a).

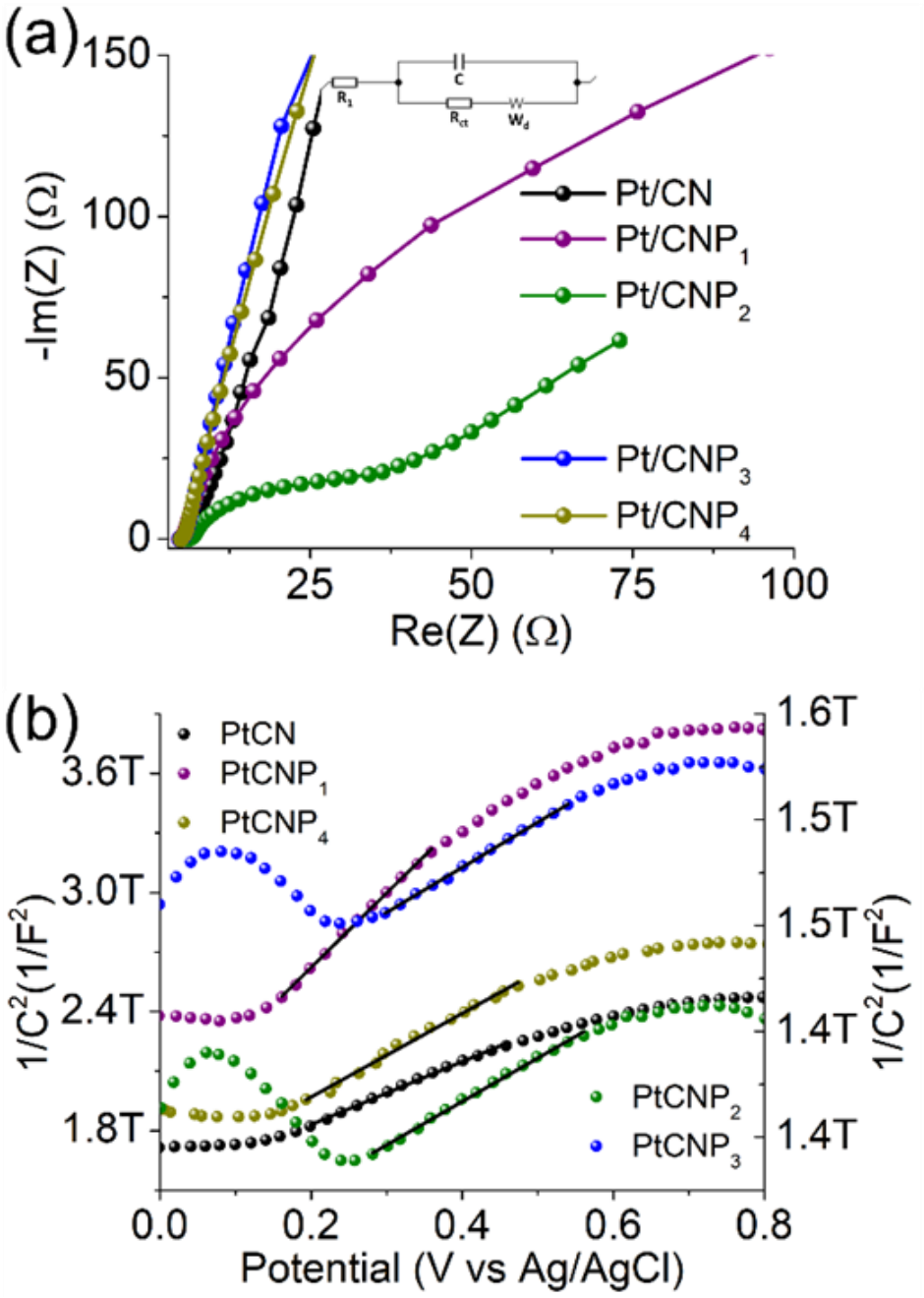


Figure 12. (a) Nyquist plots for the sample series produced from electrochemical impedance measurements at -10 mV overpotential. Inset is the Randle's equivalent circuit where $R_1$ is the solution resistance, $R_{ct}$ is the charge-transfer resistance, C is the double-layer capacitance, and $W_d$ is the Warburg diffusion term. (b) Mott-Schottky measurements for the sample series performed in 0.1 M $Na_2SO_4$. Potentials are vs an

Ag/AgCl reference electrode. Regression taken within the linear portion of each sample is shown as a black solid line. Y-axis on the left correspond to samples PtCN, $PtCNP_1$, and $PtCNP_4$ while y-axis on the right corresponds to $PtCNP_2$ and $PtCNP_3$.

To gain further insight into the charge-transfer capability of the samples, Mott-Schottky analysis was performed in 0.1 M $Na_2SO_4$. From Figure 12b, all samples can be seen to possess a positive slope along the linear region of each curve, suggesting n-type semiconductor behavior.[26] The flat band potential ($E_{fb}$) for PtCN was calculated to be -0.92 V vs Ag/AgCl and an anodic shift was observed upon phosphorous doping to -0.61 V for $PtCNP_1$ and -0.60 V for $PtCNP_2$, whereas a further increase of the phosphorous dopant concentration was found to result in a slight cathodic shift of $E_{fb}$ to -0.65 V for $PtCNP_3$ and -0.68 V for $PtCNP_4$. Note that the formal potential for hydrogen evolution ($H^+/H_2$) is -0.59 V vs Ag/AgCl in 0.1 M $Na_2SO_4$.[26] A positive shift toward -0.59 V found in the $PtCNP_1$ and $PtCNP_2$ samples suggests a narrowing of the energy barrier, while the slight negative shift in $PtNP_3$ and $PtCNP_4$ suggests a broadening of the energy barrier. These findings are consistent with the HER polarization curves in Figure 11a and the electrocatalytic activity trend observed. Furthermore, the charge carrier density ($N_d$) of the catalyst can be calculated by $N_d = \frac{2}{e\varepsilon\varepsilon_0 m}$, where e is the elementary charge of an electron ($1.602 \times 10^{-19}$ C), ε is the dielectric constant (10),[51] $\varepsilon_0$ is the permittivity in a vacuum ($8.85 \times 10^{-12}$ $Fm^{-1}$), and (m) is the slope of the Mott-Schottky linear regression. $N_d$ was calculated to be $8.66 \times 10^{16}$ for PtCN, $4.30 \times 10^{16}$ for $PtCNP_1$, $6.60 \times 10^{17}$ for $PtCNP_2$, $6.55 \times 10^{17}$ for $PtCNP_3$, and $6.32 \times 10^{16}$ for $PtCNP_4$. That is, $PtCNP_2$ possessed the highest charge carrier density (with $PtCNP_3$ being the close second) among the sample series, which is nearly 10 times that of PtCN. These results suggest phosphorous doping within the carbon nitride framework reaches an optimum level for charge carrier density for $PtCNP_2$, in coincidence with the best HER activity.

## 3.4 Experimental Section

### Chemicals

Urea ($CO(NH_2)_2$, certified ACS, Fisher Chemicals), potassium trichloro(ethylene)platinate(II) hydrate (Zeise's salt, $KPtCl_3(C_2H_4)$, Sigma Aldrich), ammonium hexafluorophosphate ($NH_4PF_6$, Acros Organics), potassium hydroxide (KOH, Fisher Chemicals), platinum on carbon (Pt/C, nominally 20 wt.%, Alfa Aesar), carbon black (Vulcan XC 72R), and Nafion 117 (Sigma Aldrich) were used as received. All solvents were obtained through typical commercial sources and used as received, too. Water was supplied with a Barnstead Nanopure water system (18.3 MΩ cm).

### Synthesis of (phosphorous-doped) polymeric carbon nitride

P-doped $C_3N_4$ was synthesized by a modified method from previous reports,[29] as illustrated in Scheme 1. Briefly, urea (10 g) was ground to a fine powder with a designated amount of $NH_4PF_6$ (i.e., 0.5, 1.0, 2.5, or 5 g), and the mixture was placed in a crucible, covered, heated in air to 300 °C at a rate of 2 °C $min^{-1}$ and held at 300 °C for 3 h. The resulting white solid was ground to a fine powder, heated again in air to 520 °C at a rate of 2 °C $min^{-1}$ and held at this temperature for 4 h. The produced yellow solid was collected, washed with Nanopure water, and dried in a vacuum oven overnight, affording P-doped $C_3N_4$ that was referred to as $CNP_1$, $CNP_2$, $CNP_3$, and $CNP_4$, respectively. Undoped $C_3N_4$ was produced in the same manner but without the addition of $NH_4PF_6$.[9, 35]

Scheme 1. Schematic of the synthetic procedure of PtCNP.

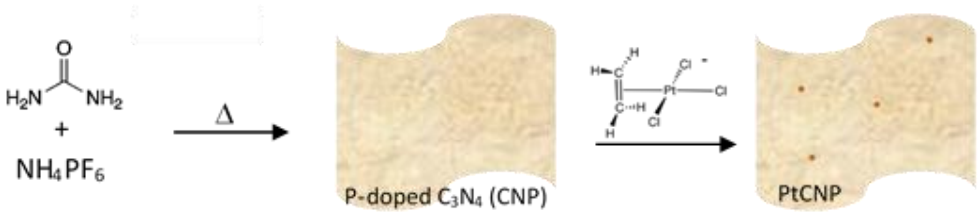


**Synthesis of platinum-carbon nitride nanocomposites**

Platinum was incorporated into the carbon nitride scaffold obtained above by following a procedure used for the synthesis of platinum bipyridine complexes (Scheme 1).[52] Briefly, the P-doped $C_3N_4$ prepared above (50 mg) was dispersed in a mixture of acetone (4 mL) and isopropanol (1 mL) by sonication for 1 h. In a separate vial, Zeise's salt (50 mg) was dissolved in acetone (5 mL) under magnetic stirring in an ice bath. KOH (20 mg) was dissolved in a minimum amount of water and added to the Zeise's salt solution under stirring for 40 min, where KCl salt precipitates could be seen accumulated on the walls of the glass vial. The carbon nitride dispersion was immersed into an ice bath under vigorous stirring for 10 min, into which was added the Zeise's salt solution. After magnetic stirring for 40 min, the resulting mixture was centrifuged at 6000 rpm for 10 min, and the precipitate was collected and washed 5 times with acetone to remove any unreacted platinum salts and contaminants. It should be noted that the colour of the supernatant changed from light yellow to clear after the subsequent washes, indicating a saturated loading of platinum into carbon nitride and the subsequent removal of unreacted metal salt upon washing. The material was dried in a vacuum oven overnight, affording platinum containing carbon nitrides, which were denoted as $PtCNP_1$, $PtCNP_2$, $PtCNP_3$, $PtCNP_4$, respectively. The P-free sample (PtCN) was prepared in the same manner except that undoped $C_3N_4$ was used instead of P-doped $C_3N_4$.

**Characterization**

Scanning electron microscopic (SEM) images were collected on a Thermo Scientific Apreo scanning electron microscope with high/low-vacuum compatibility and a 400 nA beam current equipped with an Oxford instruments energy dispersive X-ray spectroscopy (EDS) attachment. Transmission electron microscopy (TEM) and scanning transmission electron microscopy (STEM) measurements were carried out on a JOEL JEM 2100F microscope. X-ray diffraction (XRD) patterns were acquired with a Rigaku Smartlab Diffractometer, where the samples were deposited on an Al plate and the measurements were conducted at a step of 0.02° and a scan rate of 3° $min^{-1}$. X-ray photoelectron spectroscopy (XPS) measurements were performed with a Phi 5400/XPS instrument equipped with an Al $K_\alpha$ source operated at 350 W and $10^{-9}$ Torr. X-ray absorption spectroscopy (XAS) measurements were carried out at 10 K on beamline 4-1 at the Stanford Synchrotron Radiation Light source using an Oxford liquid helium cryostat. Inductively coupled plasma-optical emission spectrometry (ICP-OES) measurements were conducted with a SPECTROBLUE SOP instrument.

**Electrochemistry**

Electrochemical measurements were performed with a CHI 710 workstation, and electrochemical impedance measurements were carried out with a Gamry Reference 600 instrument. A glassy carbon electrode (5.60 mm in diameter, 0.246 $cm^2$) was used as the working electrode, while a Ag/AgCl (1.0 M KCl) electrode and graphite rod were used as the reference and counter electrodes, respectively. The Ag/AgCl electrode was calibrated versus a RHE and all potentials in the present study were referenced to this RHE, unless specified otherwise. To prepare the catalyst ink, 2 mg of the nanocomposites obtained above was mixed with carbon black (3 mg) and sonicated for 10 min in isopropanol (1 mL), followed by the addition of Nafion (40 μL) and sonicated for an additional 20 min. 30 μL of the prepared ink was dropcast onto the surface of the glassy carbon electrode

and dried at room temperature, corresponding to a catalyst mass loading of 0.244 mg $cm^{-2}$. Finally, 6 µL of Nafion (20 wt.%) in isopropanol was added to the prepared catalyst surface and allowed to dry, before the electrode was immersed into an electrolyte solution for data collection.

## 3.5 Conclusions

In summary, a series of phosphorous-doped carbon nitride materials were synthesized by thermal annealing of urea and $NH_4PF_6$. A facile chelation procedure was exploited for the complexation of isolated Pt centers into the carbon nitrile matrix using of an activated Pt(II) Zeise's salt as the precursor. XPS and XAS measurements confirmed the atomic dispersion of Pt into the structural scaffold with Pt-N/P/Cl coordination. The resulting materials were found to exhibit remarkable electrocatalytic activity towards HER in acidic media, and the results suggest that P doping was critical in enhancing the electrical conductivity and HER electron-transfer kinetics of the composite catalysts. Among the series, the $PtCNP_2$ sample was found to possess the best HER electrocatalytic performance, with a mass activity almost three-times that of commercial Pt/C benchmark. This was coincident with the highest charge carrier density and lowest charge-transfer resistance. Results from the present study highlight the unique advantage of P doping in manipulating the electronic properties and enhancing the electrocatalytic activity of metal-carbon nanocomposites for electrocatalysis in important electrochemical energy technologies.

## 3.6 References

1. Renewables, I.E.A., *Technical report, IEA, Paris, 2020b.* https://www.iea.org/reports/renewables-2020, 2020.

2. Greeley, J., et al., *Computational high-throughput screening of electrocatalytic materials for hydrogen evolution.* Nature materials, 2006. **5**(11): p. 909-913.

3. Voiry, D., et al., *Enhanced catalytic activity in strained chemically exfoliated WS 2 nanosheets for hydrogen evolution.* Nature materials, 2013. **12**(9): p. 850-855.

4. Liu, K., C. Song, and V. Subramani, *Hydrogen and syngas production and purification technologies*. 2010: John Wiley & Sons.

5. Eftekhari, A., *Electrocatalysts for hydrogen evolution reaction.* International Journal of Hydrogen Energy, 2017. **42**(16): p. 11053-11077.

6. Adams, B.D. and A.C. Chen, *The role of palladium in a hydrogen economy.* Materials today, 2011. **14**(6): p. 282-289.

7. Zhao, Z., et al., *Surface-engineered PtNi-O nanostructure with record-high performance for electrocatalytic hydrogen evolution reaction.* Journal of the American Chemical Society, 2018. **140**(29): p. 9046-9050.

8. Liu, J., et al., *Positively charged Pt-based cocatalysts: an orientation for achieving efficient photocatalytic water splitting.* Journal of Materials Chemistry A, 2020. **8**(1): p. 17-26.

9. Nichols, F., et al., *Platinum Oxide Nanoparticles for Electrochemical Hydrogen Evolution: Influence of Platinum Valence State.* Chemistry-A European Journal, 2020. **26**(18): p. 4136-4142.

10. Cao, Z.M., et al., *Monocrystalline platinum–nickel branched nanocages with enhanced catalytic performance towards the hydrogen evolution reaction.* Nanoscale, 2018. **10**(11): p. 5072-5077.

11. Tian, X., et al., *Engineering bunched Pt-Ni alloy nanocages for efficient oxygen reduction in practical fuel cells.* Science, 2019. **366**(6467): p. 850-856.

12. Cheng, N., et al., *Platinum single-atom and cluster catalysis of the hydrogen evolution reaction.* Nature communications, 2016. **7**(1): p. 13638.

13. Yin, X.P., et al., *Engineering the coordination environment of single-atom platinum anchored on graphdiyne for optimizing electrocatalytic hydrogen evolution.* Angewandte Chemie International Edition, 2018. **57**(30): p. 9382-9386.

14. Lu, B.Z., et al., *Ruthenium atomically dispersed in carbon outperforms platinum toward hydrogen evolution in alkaline media.* Nature Communications, 2019. **10**: p. 631.

15. Liu, Q.M., Q.X. Li, and S.W. Chen, *Metal-nitrogen coordination moieties in carbon for effective electrocatalytic reduction of oxygen.* Current Opinion in Electrochemistry, 2020. **21**: p. 46-54.

16. Peng, Y., et al., *Hydrogen evolution reaction catalyzed by ruthenium ion-complexed graphitic carbon nitride nanosheets (2017).* Journal of Materials Chemistry A, 2017. **5**(36): p. 19499-19499.

17. Wang, Y., et al., *Advanced Electrocatalysts with Single-Metal-Atom Active Sites.* Chemical Reviews, 2020. **120**(21): p. 12217-12314.

18. Lu, B., et al., *Oxygen Reduction Reaction Catalyzed by Carbon-Supported Platinum Few-Atom Clusters: Significant Enhancement by Doping of Atomic Cobalt.* Research, 2020. **2020**: p. 9167829.

19. Zhu, W.Y. and S.W. Chen, *Recent Progress of Single-atom Catalysts in the Electrocatalytic Reduction of Oxygen to Hydrogen Peroxide.* Electroanalysis, 2020. **32**(12): p. 2591-2602.

20. Peng, J., et al., *High-performance Ru-based electrocatalyst composed of Ru nanoparticles and Ru single atoms for hydrogen evolution reaction in alkaline solution.* International Journal of Hydrogen Energy, 2020. **45**(38): p. 18840-18849.

21. Lu, B., Q. Liu, and S.W. Chen, *Electrocatalysis of single-atom sites: impacts of atomic coordination.* ACS Catalysis, 2020. **10**(14): p. 7584-7618.

22. Liu, Q.M., et al., *Atomic dispersion and surface enrichment of palladium in nitrogen-doped porous carbon cages lead to high-performance electrocatalytic reduction of oxygen.* ACS Applied Materials & Interfaces, 2020. **12**(15): p. 17641-17650.

23. Yu, F.-Y., et al., *Pt-O bond as an active site superior to Pt 0 in hydrogen evolution reaction.* Nature communications, 2020. **11**(1): p. 490.

24. Pu, Z.H., et al., *Single-Atom Catalysts for Electrochemical Hydrogen Evolution Reaction: Recent Advances and Future Perspectives.* Nano-Micro Letters, 2020. **12**(1): p. 21.

25. Kim, J., H.E. Kim, and H. Lee, *Single-atom catalysts of precious metals for electrochemical reactions.* ChemSusChem, 2018. **11**(1): p. 104-113.

26. Peng, Y., et al., *Ruthenium Ion-Complexed Graphitic Carbon Nitride Nanosheets Supported on Reduced Graphene Oxide as High-Performance Catalysts for Electrochemical Hydrogen Evolution.* Chemsuschem, 2018. **11**(1): p. 130-136.

27. Zeng, Z., et al., *Single-atom platinum confined by the interlayer nanospace of carbon nitride for efficient photocatalytic hydrogen evolution.* Nano Energy, 2020. **69**: p. 104409.

28. Yan, H., et al., *Phosphorus-modified tungsten nitride/reduced graphene oxide as a high-performance, non-noble-metal electrocatalyst for the hydrogen evolution reaction.* Angewandte Chemie, 2015. **127**(21): p. 6423-6427.

29. Zhang, Y.J., et al., *Phosphorus-Doped Carbon Nitride Solid: Enhanced Electrical Conductivity and Photocurrent Generation.* Journal of the American Chemical Society, 2010. **132**(18): p. 6294-+.

30. Guo, S., et al., *Phosphorus-doped carbon nitride tubes with a layered micro-nanostructure for enhanced visible-light photocatalytic hydrogen evolution.* Angewandte Chemie, 2016. **128**(5): p. 1862-1866.

31. Paraknowitsch, J.P. and A. Thomas, *Doping carbons beyond nitrogen: an overview of advanced heteroatom doped carbons with boron, sulphur and phosphorus for energy applications.* Energy & Environmental Science, 2013. **6**(10): p. 2839-2855.

32. Wang, X.W., et al., *Heteroatom-doped graphene materials: syntheses, properties and applications.* Chemical Society Reviews, 2014. **43**(20): p. 7067-7098.

33. Yang, S.B., et al., *Efficient Synthesis of Heteroatom (N or S)-Doped Graphene Based on Ultrathin Graphene Oxide-Porous Silica Sheets for Oxygen Reduction Reactions.* Advanced Functional Materials, 2012. **22**(17): p. 3634-3640.

34. Hu, Z.F., Z.R. Shen, and J.C. Yu, *Phosphorus containing materials for photocatalytic hydrogen evolution.* Green Chemistry, 2017. **19**(3): p. 588-613.

35. Lazauskas, A., et al., *Characterization of urea derived polymeric carbon nitride and resultant thermally vacuum deposited amorphous thin films: Structural, chemical and photophysical properties.* Carbon, 2016. **107**: p. 415-425.

36. Han, H.-X. and B.J. Feldman, *Structural and optical properties of amorphous carbon nitride.* Solid State Communications, 1988. **65**(9): p. 921-923.

37. Ogata, K., J.F.D. Chubaci, and F. Fujimoto, *Properties of carbon nitride films with composition ratio C/N= 0.5–3.0 prepared by the ion and vapor deposition method.* Journal of applied physics, 1994. **76**(6): p. 3791-3796.

38. Khabashesku, V.N., J.L. Zimmerman, and J.L. Margrave, *Powder synthesis and characterization of amorphous carbon nitride.* Chemistry of Materials, 2000. **12**(11): p. 3264-3270.

39. Xiang, Q.J., J.G. Yu, and M. Jaroniec, *Preparation and Enhanced Visible-Light Photocatalytic H-2-Production Activity of Graphene/C3N4 Composites.* Journal of Physical Chemistry C, 2011. **115**(15): p. 7355-7363.

40. Yan, S.C., Z.S. Li, and Z.G. Zou, *Photodegradation of Rhodamine B and Methyl Orange over Boron-Doped g-C3N4 under Visible Light Irradiation.* Langmuir, 2010. **26**(6): p. 3894-3901.

41. Lv, C., et al., *Phosphorus doped single wall carbon nanotubes loaded with nanoparticles of iron phosphide and iron carbide for efficient hydrogen evolution.* Journal of Materials Chemistry A, 2016. **4**(34): p. 13336-13343.

42. Wu, H., et al., *Regulating the allocation of N and P in codoped graphene via supramolecular control to remarkably boost hydrogen evolution.* Energy & Environmental Science, 2019. **12**(9): p. 2697-2705.

43. Andersson, C. and R. Larsson, *X-Ray Photoelectron-Spectroscopy and Homogeneous Catalysis .4. Hydrido Phosphine Complexes of Platinum(Ii) Chloride Investigated by Ir-Methods and Esca-Methods.* Chemica Scripta, 1977. **11**(3): p. 140-144.

44. Clark, D.T., D. Briggs, and D.B. Adams, *Esca Studies of Square-Planar Platinum Complexes - Correlations with Nuclear-Quadrupole Resonance Studies.* Journal of the Chemical Society-Dalton Transactions, 1973(2): p. 169-172.

45. Booth, C.H., *R-space X-ray Absorption Package.* See: http://lise.lbl.gov/RSAXP/. 2010.

46. Horsley, J.A., *Relationship between the area of L 2, 3 x-ray absorption edge resonances and the d orbital occupancy in compounds of platinum and iridium.* The Journal of Chemical Physics, 1982. **76**(3): p. 1451-1458.

47. Mansour, A.N., J.W. Cook Jr, and D.E. Sayers, *Quantitative technique for the determination of the number of unoccupied d-electron states in a platinum catalyst using the L2, 3 X-ray absorption edge spectra.* The Journal of Physical Chemistry, 1984. **88**(11): p. 2330-2334.

48. Friebel, D., et al., *In situ X-ray probing reveals fingerprints of surface platinum oxide.* Physical Chemistry Chemical Physics, 2011. **13**(1): p. 262-266.

49. Yoshida, H., et al., *Quantitative determination of platinum oxidation state by XANES analysis.* Physica Scripta, 2005. **2005**(T115): p. 813.

50. Zeng, M. and Y. Li, *Recent advances in heterogeneous electrocatalysts for the hydrogen evolution reaction.* Journal of Materials Chemistry A, 2015. **3**(29): p. 14942-14962.

51. Abd El-kader, F.H., et al., *Influence of the nitrogen content on the optical properties of CNx films.* Spectrochimica Acta Part A: Molecular and Biomolecular Spectroscopy, 2012. **97**: p. 1115-1119.

52. Benedetti, M., et al., *New method for the synthesis of PtCl{eta(1)-CH2C(O)R}(N-N) ketonyl derivatives starting from the Zeise's salt.* Inorganica Chimica Acta, 2014. **413**: p. 109-114.

## Chapter 4 Electrocatalytic Generation of Reactive Species and Implications in Microbial Inactivation

## 4.1 Abstract

Controlling microbial proliferation in water systems, including wastewater, recreational water, and drinking water, is essential to societal health. Microbial inactivation through electrochemically generated reactive species (RS) mediated pathways provides an effective route toward this microbial control. Herein we provide an overview of recent progress toward electrocatalytic generation of RS and their application in water disinfection, with a focus on the selective production of RS, the microorganism interactions with RS (including both RS mechanisms of action and innate microorganism responses to RS), and practical implementation of electrochemically generated RS for microbial inactivation. The article is concluded with a perspective where the challenges and opportunities of RS-based electrochemical disinfection of water are highlighted, along with possible future research directions.

## 4.2 Introduction

Assurance of safe and healthy water is critical for progress of life on earth. Many methods for water disinfection have been implemented, including physical, biological, and chemical pathways [1]. A chemical route toward water disinfection typically involves the use of advanced processes to remove contaminants through oxidation. Several advanced oxidative processes (AOP) have already been implemented into water treatment, including ozonation and UV light [2]. The field of electrochemistry provides another viable pathway toward efficient water disinfection, which also poses a sustainable pathway as electricity supply becomes increasingly renewable [3]. Water treatment by AOP primarily focusses on production of highly oxidizing substances, such as hydroxyl radicals (HO$^{\bullet}$); however, significant research has been dedicated in recent literature to the electrochemical generation of many other reactive species (RS), including reactive oxygen species (ROS) like superoxide ($O_2^{\bullet-}$) and hydrogen peroxide ($H_2O_2$),

reactive chlorine species (RCS), reactive nitrogen species (RNS), as well as reactive sulfur species (RSS), which can also be used in the water treatment process [4-7].

Numerous microorganisms have been found to transmit diseases through water systems, including bacteria, viruses, protozoa, and helminths [8]. It is essential for humans to treat these threats during the water disinfection process. Bacteria are particularly susceptible to the presence of RS with damage to proteins, DNA, and lipid membranes leading to cell death [4-7]. This makes electrochemical generation of RS an attractive pathway toward microbial inactivation during water treatment (Fig. 1).

There are several distinct advantages of electrochemical RS generation over other methods such as photocatalysis. One major advantage is the ability for an electrochemical device to disinfect a wide variety of contaminated water including particularly cloudy or murky water that would otherwise prevent the transmittance of light through the water medium necessary for photocatalytic treatment. Another distinct advantage is the ability to have fine control over the input energy source, electricity, during the decontamination process. Other advantages and disadvantages of electrochemical RS generation will be discussed below throughout the review.

We begin this review outlining the primary RS studied in recent electrocatalysis research, with a focus on the electrochemical conditions and RS reactivity, and provide a context into recent reports of the deliberate design and engineering of relevant electrocatalysts. We then outline how these RS interact with microbial organisms leading to microbial inactivation. We conclude the review by summarizing recent work involving the generation of specific RS toward microbial inactivation with a prospective of the field and what is needed to progress the current technologies.

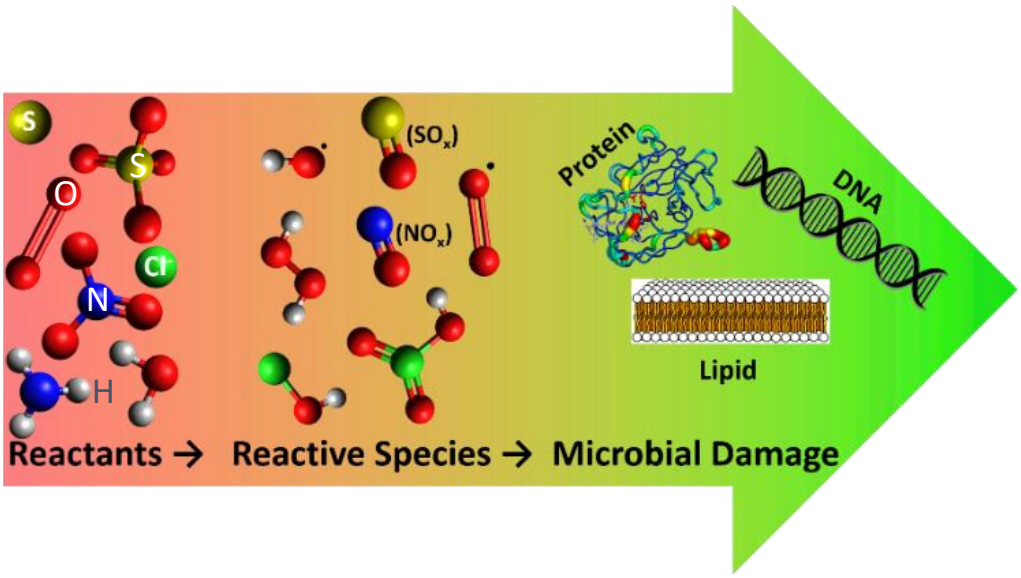


Fig. 1. Schematic representation of the electrosynthesis of RS and corresponding targets for microbial damage. Spheres represent oxygen (red), hydrogen (grey), chlorine (green), sulfur (yellow), and nitrogen (blue) atoms.

### 4.3 Electrocatalytic generation of reactive species

#### 4.3.1 Reactive oxygen species

Organisms that rely on aerobic respiration as a means of energy production are required to interact with molecular oxygen, as it is the final electron acceptor in the electron transport chain. At the end of aerobic respiration, the fourth and final enzyme in the electron transport chain, cytochrome C oxidase, catalyzes the reduction of molecular oxygen to water [9-19]. Like the oxygen reduction reaction (ORR) in fuel cell electrocatalysis, the conversion of molecular oxygen to water in a biological cell is not without error and can lead to toxic oxygen byproducts, such as superoxide ($O_2^{\bullet-}$) and hydrogen peroxide ($H_2O_2$) [16-24]. Production of these species during electrocatalysis is often categorized as an undesirable effect; however, production of such ROS can be advantageous under controlled conditions. From the electrochemistry perspective,

researchers are beginning to design electrocatalysts capable of efficiently producing ROS for many applications, including industrial hydrogen peroxide production, organic molecule synthesis, microbial inactivation, water disinfection, electrocoagulation, and other contaminant disinfection (e.g., organic dye degradation) [4-7, 25-32].

Electrochemical ROS generation can occur on the cathode by reduction of molecules, including molecular oxygen, or at the anode through oxidation of adsorbates, such as water. A proposed stepwise mechanism for generating such ROS is depicted in reaction (1), flowing from left to right for the reduction processes and right to left for the oxidation processes [33].

$$O_2 \leftrightarrows O_2^{\bullet -} \leftrightarrows H_2O_2 \leftrightarrows HO^{\bullet} \leftrightarrows H_2O \quad (1)$$

From reaction (1), we can see that there are three primary ROS products, superoxide, hydrogen peroxide, and hydroxyl radical. In the following sections, we will explore in further detail the relationship between these species, their chemical reactivity, and relevant electrocatalysts reported recently for the synthesis of these species.

**Superoxide ($O_2^{\bullet -}$)**

Generation of $O_2^{\bullet -}$ in electrochemical systems can occur by one-electron reduction of adsorbed oxygen at the cathode surface, as shown by reaction (2), with a formal potential (E°) of +0.330 V vs reversible hydrogen electrode (RHE). $O_2^{\bullet -}$ can also be produced by the oxidation of $H_2O_2$ following reaction (3). $O_2^{\bullet -}$ generation has been studied primarily in aprotic solvents, such as dimethyl sulfoxide (DMSO), as $O_2^{\bullet -}$ quickly reacts in protic solvents forming $O_2$ and hydroperoxide anion ($HO_2^-$), the conjugate base of $H_2O_2$, as shown in reaction (4), with a short half-life of only 5 s at physiological pH, which renders it difficult to harvest for actual bacterial control applications [34-36].

$$O_2 + e^- \rightarrow O_2^{\bullet -} \quad (2)$$

$$H_2O_2 \rightarrow O_2^{\bullet -} + 2H^+ + e^- \quad (3)$$

$$O_2^{\bullet -} + H_2O \rightarrow O_2 + HO_2^- + HO^{\bullet} \quad (4)$$

**Hydrogen peroxide ($H_2O_2$)**

Relative to $O_2^{\bullet -}$, $H_2O_2$ has a long half-life of ca. 1 h in protic solvents and at physiological pH with spontaneous disproportionation occurring by reaction (5) [37]. Thus, $H_2O_2$ can be collected and used for an array of applications. Electrochemical generation of $H_2O_2$ has been extensively studied alongside fuel cell research [33, 38-43], where $H_2O_2$ is produced through a two-electron process either by the reduction of $O_2$ ($E° = 1.230$ V vs RHE) or oxidation of $H_2O$ ($E° = 1.760$ V vs RHE), shown by reactions (6) and (7), respectively.

$$H_2O_2 \rightarrow H_2O + ½O_2 \quad (5)$$

$$O_2 + 2H^+ + 2e^- \rightarrow H_2O_2 \quad (6)$$

$$2H_2O \rightarrow H_2O_2 + 2H^+ + 2e^- \quad (7)$$

$$O_2 + 4H^+ + 4e^- \rightarrow 2H_2O \quad (8)$$

In fact, hydrogen peroxide generation at the cathode during ORR has been rather extensively studied as a side reaction occurring in fuel cell electrocatalysis [44-49]. Classical fuel cell research aims to design an electrocatalysts which facilitate the complete reduction of oxygen to water via the four-electron pathway shown in reaction (8) and avoid possible peroxide generation, to maximize the electrocatalytic performance and minimize corrosion of the fuel cell device.

However, for water disinfection purposes, generation of hydrogen peroxide can be advantageous, as manifested in a series of earlier studies [50-52]. $H_2O_2$ is sometimes used as a precursor to produce homogeneous $HO^{\bullet}$ via the electro-Fenton process.

Heterogeneous HO• can also be produced directly at the electrode surface and will be discussed further in the next section of this review. It should be noted that homogeneous and heterogeneous HO• may be produced in tandem for improved decontamination efficiency. For instance, Brillas and co-workers [53] successfully demonstrated this application in their study of the degradation of monoazo, diazo, and triazo dyes using an electrochemical setup consisting of a carbon-ploytetrafluoroethylene (PTFE) air-diffusion cathode and a boron doped diamond anode (BDD). Carbon-PTFE has been used widely as a cathode for the two-electron reduction of water forming $H_2O_2$ [54-56], while BDD has been extensively studied as an inactive anode for the direct production of heterogeneous HO• [57-61]. It was found that dye degradation occurred to both heterogeneous HO• created at the BDD anode and homogeneous HO• produced by the electro-Fenton process, where $H_2O_2$, produced at the carbon-PTFE cathode, reacted with added $Fe^{2+}$.

Recently, researchers have also studied electrocatalysts specifically designed to allow ORR via the two-electron pathway shown in reaction (6), and single atom catalysts (SACs) have emerged as a unique, powerful platform that can selectively catalyze the two-electron reduction of oxygen to hydrogen peroxide [62], due to the possibility of tailoring the catalytic activity through deliberate modifications to the single atom coordination environment [62]. For instance, Tang and co-workers recently reported on a Mo SAC with unique O and S coordination towards two-electron ORR [63]. The material was synthesized through a two-step process involving hydrothermal synthesis of MgO nanosheets from bulk MgO followed by calcination and a final carbonization step incorporating S from benzyl disulfide precursor. The SAC structure was confirmed by high-angle annular dark-field scanning transmission electron microscopy (HAADF-STEM), X-ray photoelectron spectroscopy (XPS), extended X-ray absorption fine

structure (EXAFS), and Wavelet transform-EXAFS (WT-EXAFS) analysis. Fig. 2a depicts a pseudo-color surface plot produced from the high-angle annular dark field-scanning transmission electron microscopy (HAADF-STEM) images for the obtained $Mo_1$/OSG-H sample, where single Mo atoms (blue) were deposited on a carbon matrix (green) with significant defect sites (yellow). Fig. 2b shows the real-space EXAFS spectra for $Mo_1$/OSG-H, bulk $MoS_2$, bulk molybdenum oxide ($Na_2MoO_4$), and bulk molybdenum foil. $Mo_1$/OSG-H exhibited a primary peak near 1.2 Å, which was assigned to Mo-O coordination, and the lack of spectral features at longer distance suggested virtually no Mo-Mo interactions, in agreement with HAADF-STEM findings. Electrochemical tests with a rotating ring-disk electrode (RRDE) in a three-electrode electrochemical setup were carried out to assess the material's ability to catalyze $H_2O_2$ formation from molecular oxygen, revealing 95% selectivity under these conditions. First principles density functional theory (DFT) calculations were then employed to better understand the significance of the Mo-O/Mo-S coordination environments (Fig. 2c), and the results revealed preferential OOH* adsorption on C adjacent to Mo (Mo-$O_4$-C), with electron transfer occurring from Mo to adsorbed OOH*, as evidenced in Bader charge calculations (the asterisk denotes a species adsorbed onto the catalyst surface). Notably, the adsorption was significantly improved upon S incorporation (Mo-$O_3$S-C), and a further increase of S loading resulted in improved OOH* binding strength and reduced free energy of adsorbed OOH* intermediate (Mo-$S_4$-C).

Jung and co-workers also highlighted the ability to optimize the electrocatalytic performance through engineering SAC coordination environment in their recent report of a $CoN_4$ catalyst toward two-electron reduction of molecular oxygen to $H_2O_2$ [64]. They began their work by understanding the relationship between M-$N_4$/graphene moieties and ORR selectivity through DFT calculations forming adjacent volcano plots that

corresponded to catalyst selectivity toward the two- or four-electron reduction of oxygen (Fig. 2d). It was demonstrated through first principles DFT calculations that the OOH* free energy ($\Delta G_{OOH*}$) on the $CoN_4$/graphene moiety can be tailored by the addition of electron-rich oxygen functional groups around the $CoN_4$ centers, due to a slight increase of the Co charge state and thus $\Delta G_{OOH*}$. These findings were indeed confirmed experimentally. Three samples were prepared by controlled pyrolysis, one containing only graphene oxide (GO) (NG(O)), another with cobalt single atoms embedded in GO ($Co_1$-NG(O)), and a third one with cobalt single atoms embedded in reduced graphene oxide ($Co_1$-NG(R)). $Co_1$-NG(O) was found to contain 6.6 at.% oxygen, while only 2.1 at.% for $Co_1$-NG(R). ORR tests were then carried out with a three-electrode setup and an RRDE as the working electrode, and the results (Fig. 2e) from collection experiments revealed a substantial current response at the ring electrode with the $Co_1$-NG(O) sample (red curve), in comparison to the metal-free NG(O) (black curve) and oxygen-deficient ($Co_1$-NG(R) (blue curve). The corresponding $H_2O_2$ selectivity (Fig. 2f) was estimated to be 80% for $Co_1$-NG(O), markedly higher than that (<50%) for $Co_1$-NG(R). Results from this study provided a unique method for tailoring the electrocatalyst selectivity toward $H_2O_2$ generation through controlled oxygen functionality within the GO support.

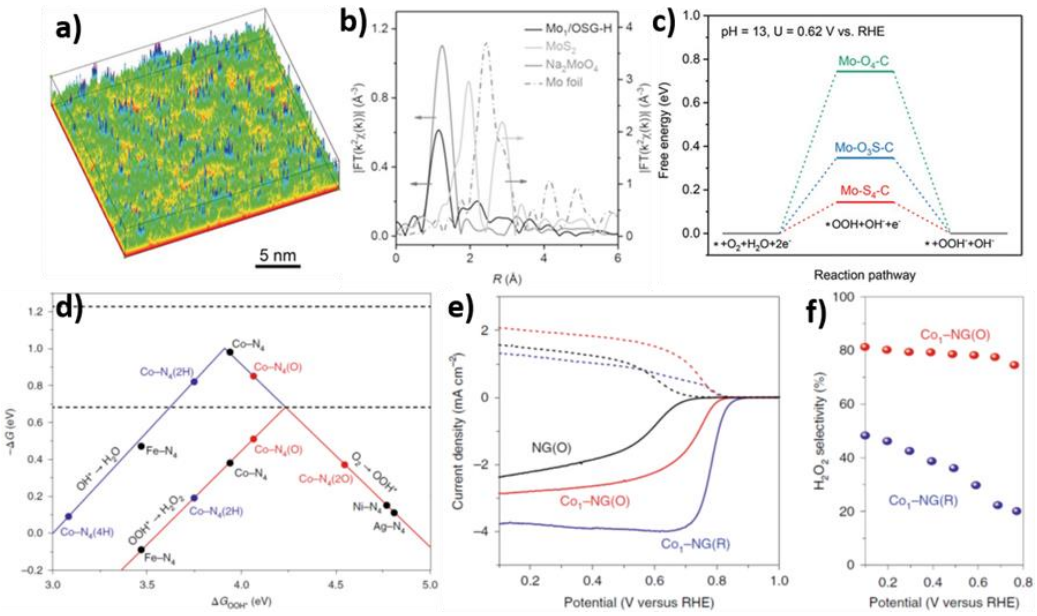


Fig. 2. (a) Pseudo-color surface plot created from HAADF-STEM image of $Mo_1$/OSG-H. (b) FT-EXAFS curves at Mo K edge. (c) Free energy diagram of $2e^-$ ORR on three substrates at equilibrium potential. Panels (a-c) reproduced with permission from ref. [63], copyright 2020, Wiley-VCH. (d) Volcano plots for ORR producing water (blue) and $H_2O_2$ (red). Solid lines are created from the calculations of various M-$N_4$ species (M = Co, Ni, Fe, and Ag). (e) Polarization curves for NG(O) (black), $Co_1$-NG(O) (red), and $Co_1$-NG(R) (blue) with currents from the disk (solid) and ring (dashed) electrodes. (f) $H_2O_2$ selectivity % measured for $Co_1$-NG(O) (red) and $Co_1$-NG(R) (blue) over the potential range of 0.1 V – 0.8 V vs RHE. Measurements performed at 1600 rpm rotation rate in 0.1M KOH. Panels (d-f) reproduced with permission from ref. [64], copyright 2020, Springer Nature.

In these previous studies, theoretical calculations were employed to assist the rational design of effective electrocatalysts for two-electron reduction of $O_2$ to $H_2O_2$. Another side of the same coin can be found in the work toward $H_2O_2$ production through the two-electron water oxidation reaction ($2e^-$ WOR, reaction (7)). As mentioned previously, the

oxidizing conditions typically require large overpotentials, due to the thermodynamic constraints in the water oxidation processes. Thus, materials selected for this electrocatalytic process are often metal oxides capable of handling large overpotentials applied over an extended period of time. For example, Shi and co-workers prepared various metal oxide electrocatalysts toward $H_2O_2$ via $2e^-$ WOR [65]. DFT calculations were carried out to evaluate the limiting potentials as a function of OH* adsorption energy for the $2e^-$ and $4e^-$ WOR processes, as shown by the black and blue curves in Fig. 3a, respectively. Important WOR intermediates include OH*, O*, and OOH*. These intermediates arise from the $1e^-$, $2e^-$, and $4e^-$ oxidations of water, respectively. OH* is the first intermediate produced in WOR and its adsorption energy often dictates reaction products, where strong OH* binding typically follows the $4e^-$ WOR, while weak OH* binding leads to $2e^-$ WOR and $H_2O_2$ generation [66]. Therefore, OH* binding was chosen as the descriptor in identifying possible candidates for $2e^-$ WOR electrocatalysts. Of the four metal oxides, $WO_3$(100) (black triangle), $SnO_2$(110) (blue square), $TiO_2$ (110) (pink diamond), and $BiVO_4$(111) (red circle), where the facet was selected based on stability for each material (Fig. 3a), the calculated onset potentials were found to be consistent with the experimental results, increasing in the order of $WO_3 < BiVO_4 < SnO_2 < TiO_2$ (Fig. 3b). However, $BiWO_4$ was observed to have the greatest selectivity among the series of materials at 70%, resulting in the highest $H_2O_2$ production rate of ca. 6 mole $min^{-1}$ $cm^{-2}$.

In a more recent report [67], Kelly and colleagues demonstrated improved activity and selectivity of a unique ZnO($10\bar{1}0$) material toward $2e^-$ WOR. To better understand the WOR pathways, a free energy diagram was constructed beginning with water, including intermediate steps, and possible reaction products such as $OH^{\bullet}$, $H_2O_2$, and $O_2$, as shown in Fig. 3c. To facilitate $2e^-$ WOR on ZnO, the ideal adsorption energy of the OH*

intermediate ($\Delta G_{OH*}$) was determined to be in the range of 1.6 to 2.4 eV, shown by the green shaded region in Fig. 3d, such that the binding of OH* is not too strong, leading to $4e^-$ WOR, or too weak, leading to OH* desorption and $OH^{\bullet}$ generation. All ZnO facets studied in this report were determined to have $DG_{OH*}$ within this idealized range. The limiting potentials for these various ZnO facets were then calculated, and the ZnO($10\bar{1}0$) facet was found to possess the lowest limiting potential and thus the highest predicted $2e^-$ WOR rate. Motivated by these theoretical results, ZnO with predominant ($10\bar{1}0$) facets was synthesized on fluorine-doped tin oxide (FTO) glass and characterized by scanning electron microscopy (SEM) (Fig. 3e), transmission electron microscopy (TEM), and X-ray diffraction (XRD) measurements. Electrochemical measurements revealed outstanding $2e^-$ WOR selectivity and reaction rate with ZnO($10\bar{1}0$), as compared to that with Zn(0001) and results reported previously in the literature with relevant metal oxides (Fig. 3f). In fact, ZnO($10\bar{1}0$) exhibited a faradaic efficiency (FE) over 80% and a current density of 0.1 mA $cm^{-2}$ at a low overpotential of 40 mV, much better than various other oxide materials reported under similar reaction conditions (Fig. 3g).

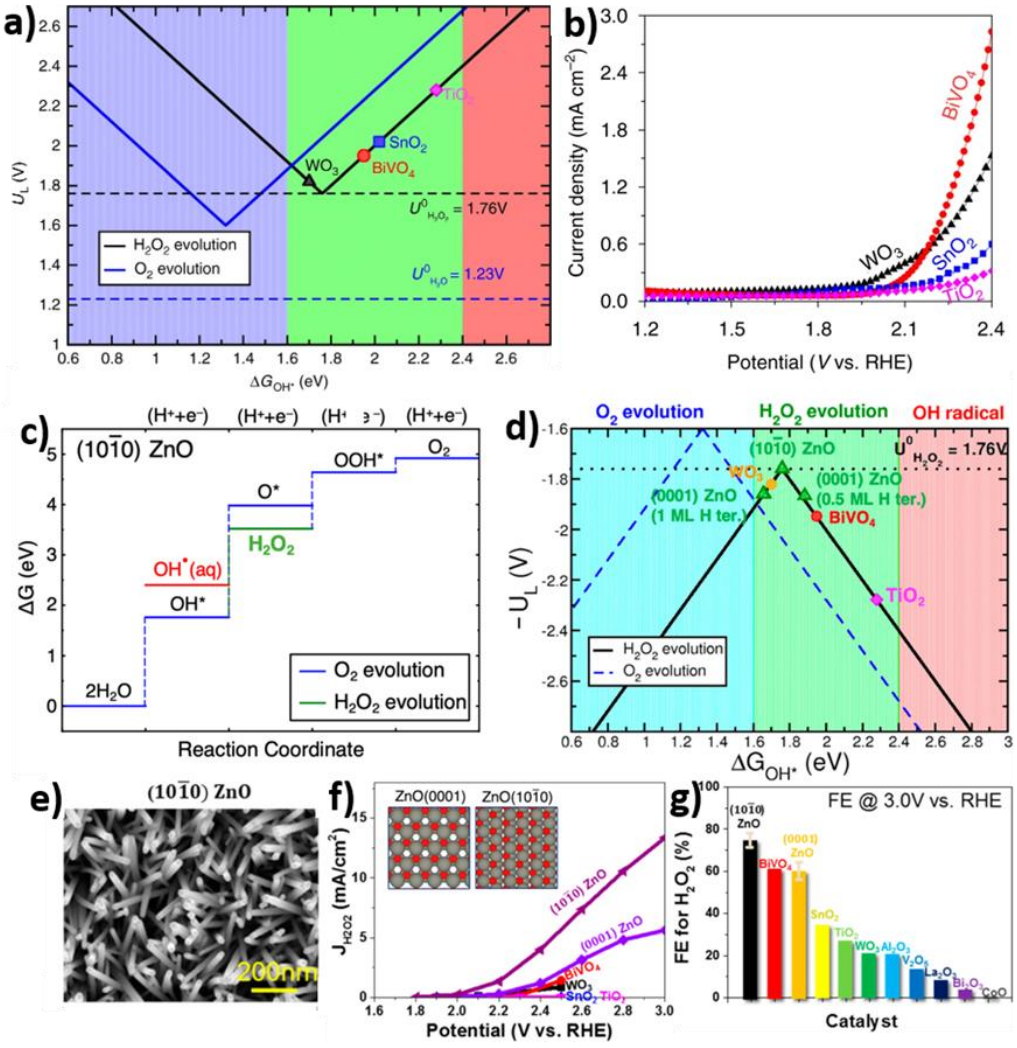


Fig. 3. (a) Volcano plot of electrocatalytic activity corresponding to limiting potential vs $OH^*$ adsorption energy for $2e^-$ (black) and $4e^-$ (blue) WOR. Equilibrium potentials are shown in dashed lines. (b) Polarization curves for four select metal oxides toward $2e^-$ WOR. Panels (a,b) reproduced with permission from ref. [66], Springer Nature. (c) Free energy diagram for the stepwise $O_2$ evolution reaction (blue) and $H_2O_2$ evolution reaction (green) with 4 intermediate steps. (d) Volcano plots produced from calculated limiting potential ($U_L$) as a function of OH* binding free energy ($\Delta G_{OH^*}$) for the four-electron water oxidation (blue dashed line) and two electron water oxidation to $H_2O_2$ (black line). Three favorable reaction pathways are highlighted by shading $O_2$ evolution (blue), $H_2O_2$

evolution (green), and $OH^{\bullet}$ production (red). (e) SEM images of ZnO($10\bar{1}0$) nanorods. (f) Catalytic activity of $2e^-$ WOR in 2M potassium bicarbonate of ZnO($10\bar{1}0$), Zn(0001) and other metal oxides. Inset depicts model representations of the ZnO(0001) and ZnO($10\bar{1}0$) crystal structures. (g) Faraday Efficiency (FE) at 3.0 V vs RHE for ZnO($10\bar{1}0$), as compared to various other metal oxide materials with error bars taken from 5 independent measurements. Panels (c-g) reproduced with permission from ref. [67], copyright 2019, American Chemical Society.

In summary, with a sufficiently long half-life for the inactivation of bacteria, $H_2O_2$ can be produced through the partial reduction of oxygen or partial oxidation of water, where the design and engineering of relevant electrocatalysts plays a critical role. Towards this end, SACs have emerged as high-performance electrocatalysts for the selective production of $H_2O_2$. The key advantage of SACs over conventional catalysts lies in the maximal atom efficiency and mass activity, a unique feature to optimize the use of precious metals added and minimize the catalyst cost. Table S1 lists additional electrocatalysts for $H_2O_2$ generation in recent studies. In the following section we will examine the relationship between $H_2O_2$ and $HO^{\bullet}$.

**Hydroxyl radical ($HO^{\bullet}$)**

$H_2O_2$ can undergo homolytic fission to produce two hydroxyl radicals with substantial oxidizing capability, as depicted in reaction (9), due to the high standard reduction potential ($E° = 2.330$ V vs RHE) of reaction (10) [68].

$$H_2O_2 \rightarrow 2HO^{\bullet} \quad (9)$$

$$HO^{\bullet} + H^+ + e^- \rightarrow H_2O \quad (10)$$

Note that reaction (9) is readily facilitated by the addition of ferrous ($Fe^{2+}$) ions via the Fenton reaction, which was first reported in 1894 [69, 70]. Utilizing this premise, one

may facilitate the formation of HO• through the addition of ferrous ions into the electrolyte medium containing an $H_2O_2$ electrocatalyst. This is commonly referred to as the electro-Fenton process and has been studied with success in recent literature reports [71-74]. For instance, Li and co-workers employed nitrogen-doped graphene to catalyze the production of $H_2O_2$ and subsequent HO• upon the addition of ferrous ion via the electro-Fenton process [75]. Experimentally, N-doped graphene was synthesized by using a modified Hummer's method followed by a carbonization step with the addition of dopamine hydrochloride as the nitrogen source. The resulting N-doped graphene was combined with graphite felt (GF) through a secondary annealing process to create the N-doped graphene/GF catalyst. RRDE tests were then carried out to examine the electrocatalytic activity for the $2e^-$ reduction of oxygen to $H_2O_2$, which was confirmed by analysis of the Koutecky-Levich (KL) plots, and further supported by results from hydroxyl radical scavenger probes and electron spin resonance (ESR) measurements with the addition of 0.5 mM $Fe^{2+}$ to the electrolyte solution (0.05 M $Na_2SO_4$). Notably, the composite catalyst was found to be active in the degradation of phenacetin for wastewater treatment purposes, achieving a 98% degradation rate after 2 h of electrocatalysis at the applied current density of 7 mA $cm^{-2}$.

In a more recent study [74], Sheng and co-workers studied the electro-Fenton chemistry of cobalt selenide with samples prepared by hydrothermal selenization of cobalt hydroxide carbonate hydrate followed by thermal annealing, which removed excess selenium and was used to control the $CoSe_2$ polymorphism. Low-temperature annealing was found to produce orthorhombic marcasite-$CoSe_2$ (o-$CoSe_2$), while annealing above 300 °C resulted in complete transition to cubic pyrite-$CoSe_2$ (c-$CoSe_2$). Cubic cobalt sulfide (c-$CoS_2$) was also produced for comparison. Based on spin polarized electronic structure calculations with the Vienna *ab initio* simulation package (VASP), the obtained

surface Pourbaix diagrams revealed OH* surface coverage at the cobalt sites for both o-$CoSe_2$ and c-$CoSe_2$ polymorphs at low overpotentials. Note that $4e^-$ reduction of molecular oxygen requires sufficient $O_2$ binding and cleaving of the O-O bond, whereas a high Co-OH* surface coverage prevents $O_2$ binding to Co and subsequent O-O bond cleavage. Thus, the high surface coverage of OH* on the cobalt site was determined to be beneficial for selective $2e^-$ ORR, as shown in Fig. 4a. In fact, electrochemical measurements showed that the $H_2O_2$ selectivity decreased in the order of o-$CoSe_2$ > c-$CoSe_2$ > c-$CoS_2$, due to the increased Co-OH* surface coverage at low to moderate overpotentials on o-$CoSe_2$. Fig. 4b shows the corresponding kinetic current density for $H_2O_2$ generation. One can see that within the potential range of 0.5 to 0.7 V, the current density decreases in the order of c-$CoSe_2$ (green) > o-$CoSe_2$ (red) > c-$CoS_2$ (blue), and they are all markedly greater than results reported previously for other $2e^-$ ORR catalysts. o-$CoSe_2$ was then used in the degradation of rhodamine B (RhB) dye via the electro-Fenton process in a $Na_2SO_4$ (0.5 M) electrolyte containing 0.5 mM $Fe^{2+}$ at 0.5 V vs RHE. Complete degradation of rhodamine B (RhB, 20 $mgL^{-1}$) occurred within 20 min. As current generation was not correlated to RhB degradation during the chronoamperometric measurements, RhB removal was most likely due to the produced hydroxyl radicals rather than direct degradation of RhB in contact with the electrode surface.

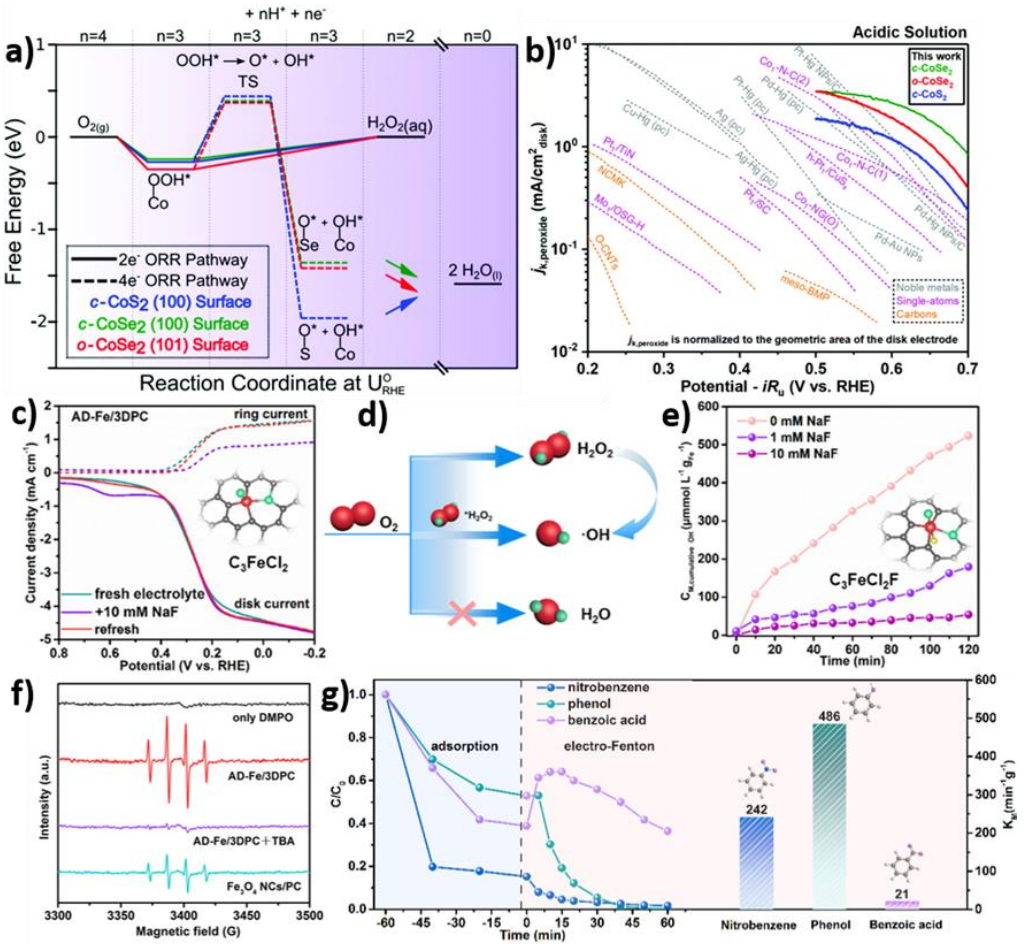


**Fig. 4.** (a) Calculated free energy diagrams of $2e^-$ and $4e^-$ ORR for c-$CoS_2$ (100) (blue), c-$CoSe_2$ (100) (green), and o-$CoSe_2$ (101) (red). (b) Kinetic current density for $H_2O_2$ normalized to geometric surface area and compared to previously reported $2e^-$ ORR catalysts. Panels (a,b) reproduced with permission from ref. [74], copyright 2020, Royal Chemistry Society. (c) Linear sweep voltammetry (LSV) with 1200 rpm rotation and 10 mV $s^{-1}$ scan rate in 0.05 M $Na_2SO_4$ (pH = 6) for fresh electrolyte (green), 10 mM NaF poisoning agent (purple), and repeated with fresh electrolyte after poisoning measurements (red). (d) Schematic representation of $O_2$ stepwise reduction to $H_2O_2$ and $OH^{\bullet}$. (e) $OH^{\bullet}$ yield with increased levels of poisoning agent, NaF. (f) Spin trapping ESR spectra with DMPO (3mM). (g) degradation of nitrobenzene (blue), phenol (green), and

benzoic acid (purple) with calculated kinetic constants normalized to Fe mass ($K_M$). Panels (c-g) reproduced with permission from ref. [76] copyright 2020, Springer Science.

The electro-Fenton process is a useful technique, but it would be desirable in many applications to remove the requirement for added ferrous ions and catalyze $HO^{\bullet}$ formation directly using an electrocatalyst. Heterogeneous SACs are an ideal candidate for this process, since a series of studies have shown that homolytic fission of $H_2O_2$ can occur on select SACs. For example, Wu and co-workers recently developed a SAC containing isolated copper atoms through a two-part synthesis process [76]. Experimentally, copper nitrate was mixed into solutions of melamine and cyanuric acid, where a small amount of solution-phase copper was trapped within the strong hydrogen bonding network of melamine and cyanuric acid before dropping out of the solution as a precipitate. GO was then added into the solution to form a composite. The precipitate was freeze-dried and carbonized to produce high-loading copper single atoms in nitrogen-doped graphene (Cu-SA/NGO). The atomic dispersion of Cu was visualized in HAADF-STEM measurements, and EXAFS studies showed a Cu-N coordination number of 4.0, signifying the formation of $CuN_4$ moieties. The electro-Fenton activity of the obtained samples was then tested towards the degradation of various organic contaminants, such as acetaminophen (APAP), in the presence of $H_2O_2$ at controlled concentrations. Complete electro-Fenton degradation of APAP (10 mg $L^{-1}$) was achieved within 1 h at a catalyst loading of 25 mg $L^{-1}$. First principles DFT calculations suggested that the mechanism involved a two-electron transfer step to form $H_2O_2$ followed by a third electron transfer and homolytic fission of $H_2O_2$ to produce $HO^{\bullet}$, which was confirmed in ESR measurements in the presence of a spin-trapping agent, 5,5-dimethyl-1-pyrroline N-oxide (DMPO), and methanol as a hydroxyl radical quenching agent.

One step beyond the progress by Wu et al. [76] would be to develop a bifunctional catalyst that can facilitate both the electrochemical production of $H_2O_2$ and homolytic cleavage of $H_2O_2$ to HO•. This is demonstrated recently by Cao and co-workers [77], where they synthesized single iron atoms on porous carbon with Fe-C/Fe-Cl in an unsaturated coordination configuration through a three-step synthesis route. Experimentally, $FeCl_3$, p-phthalic acid (PTA), and NaOH were mixed and subject to a hydrothermal treatment to produce a hydrogel mixture, which was washed and dried before carbonization and finally acid treatment to remove undesired metal particles. The unique Fe-C/Fe-Cl coordination environment was confirmed by EXAFS measurements. Electrochemical studies (Fig. 4c) confirmed a $3e^-$ ORR pathway with $H_2O_2$ formed as an intermediate and an additional electron transfer to the produced $H_2O_2$ generating HO•. A schematic representation of this reaction pathway is depicted in Fig. 4d, and results from DFT calculations suggest that the unique Fe coordination configuration was responsible for the $3e^-$ ORR pathway. Notably, in RRDE collection experiments (Fig. 4c), a clear increase in ring current was observed upon the removal of the poisoning agent NaF, as $F^-$ was known to attach to the Fe single atom sites within the material, blocking $O_2$ adsorption and preventing oxygen reduction from occurring (Fig. 4e). The formation of HO• was, again, confirmed by ESR measurements using DMPO as the spin trapping agent and *tert*-butyl alcohol (TBA) as the HO• quenching probe (Fig. 4f). The electrocatalyst was further applied to the degradation of small molecules (Fig. 4g), where complete degradation of phenol and nitrobenzene (at an initial contaminant concentration of 0.12 mM) was achieved in 45 min at an applied potential of 0.15 V vs RHE. The degradation rate for benzoic acid was markedly lower, which was correlated to the difference in aromatic ring electron density and the consequent catalyst-adsorbate interactions.

In summary, HO• can be generated from the partial reduction of oxygen or the partial oxidation of water as seen with $H_2O_2$. HO• can also be formed by the homolytic fission of $H_2O_2$ and possesses the highest oxidizing power of the three ROS discussed. Rational design and engineering of the electrocatalysts is critical in dictating the specific reaction pathways, efficiency and selectivity. Table S2 summarizes the performance of additional electrocatalysts for HO• generation in recent literature.

### 4.3.2 Reactive chlorine species

Another category of RS is the RCS, which are particularly important to keep in mind when chloride-containing electrolytes are utilized, especially under oxidizing conditions [78-82]. Chlorine evolution reaction (CER, E° = 1.358 V vs RHE), shown in reaction (11), is energetically more favorable than WOR in aqueous electrolytes.

$$2Cl^- \rightarrow Cl_2 + 2e^- \quad (11)$$

$$½Cl_2 + H_2O \rightarrow HClO + H^+ + e^- \quad (12)$$

$$Cl^- + H_2O \rightarrow HClO + H^+ + 2e^- \quad (13)$$

$$6ClO^- + 3H_2O \rightarrow 2ClO_3^- + 6H^+ + 4Cl^- + 3/2O_2 + 6e^- \quad (14)$$

Note that chlorine produced in aqueous media can undergo hydrolysis forming hypochlorous acid (HClO, reaction (12–13)), which partially dissociates to hypochlorite ion ($ClO^-$), a species that can be further oxidized to chlorate ($ClO_3^-$, reaction (14)). Further oxidation of $ClO_3^-$ can lead to the formation of perchlorate ($ClO_4^-$). $ClO_3^-$ and $ClO_4^-$ are toxic, stable byproducts that should be considered [83]. This activity has been exploited for the design of chlorine-generating electrocatalysts [21, 84-92]. For instance, Cho and colleagues [93] developed an unique composite material containing $Ir_{0.7}Ta_{0.3}O_y/Bi_xTi_{1-x}O_z$ heterojunctions as an anode catalyst for electrochemical chlorine

generation, where the outer layer of $Bi_xTi_{1-x}O_z$ served to improve $OH^*$ adsorption, while the inner $Ir_{0.7}Ta_{0.3}O_y$ layer improved electrical conductivity and electron shuttling. Similar mixed metal oxide materials have also been implemented in previous studies as some of the most efficient RCS generating electrocatalysts [94, 95]. The sample was synthesized by following a thermal decomposition approach in which $H_2IrCl_6$ and $TaCl_5$ were coated on Ti metal sheets and annealed at 525 °C. The heterojunctions were created through the deposition of bismuth citrate and titanium butoxide solutions followed by a secondary annealing step at 425 °C. Linear sweep voltammetry (LSV) of the resulting material was performed in NaCl (50 mM), and the RCS current efficiency ($\eta_{RCS}$) was calculated by equation (15),

$$\eta_{RCS} = (2VF/I)(d[Cl_{DPD}/dt] \quad (15)$$

with V being the electrolyte volume (L), F the Faraday's constant (96480 C $mol^{-1}$), $[Cl_{DPD}]$ the RCS concentration (M), I the current (A), and t the electrolysis time (s). The $Ir_{0.7}Ta_{0.3}O_y$ catalyst layer proved essential for sufficient electrical conductivity, while a decreasing Bi:Ti molar ratio resulted in improved RCS generation. Note that the electrochemical oxidation of chloride can follow two reaction pathways on a metal oxide surface, as shown in reactions (16–17).

$$MO_x(HO^{\bullet}) + Cl^- \rightarrow MO_x + ½Cl_2 + OH^- \quad (16)$$

$$MO_{x+1} + Cl^- \rightarrow MO_x + ClO^- \quad (17)$$

Reaction (16) depicts the formation of hydroxyl radicals on metal oxide surfaces ($MO_x$) followed by a fast direct electron transfer from $Cl^-$ to produce $Cl_2$, which then undergoes hydrolysis forming hypochlorous acid through reaction (17), depicting the direct transfer and consumption of oxygen within the metal oxide lattice forming the conjugate base of hypochlorous acid ($ClO^-$). Reaction (16) occurs much faster than displacement of the

lattice oxygen, which makes this reaction pathway more desirable for electrochemical chlorine generation [96]. In the study of the degradation kinetics of formate ions, it was determined that high Bi mole fractions (> 0.3) accelerated RCS generation through the undesirable pathway of reaction (17); however, a low mole fraction of Bi (≤ 0.3) resulted in improved chlorine generation with $\eta_{RSC}$ >85%. Recently, Hong and colleagues [86] prepared a similar composite anode material for RCS generation and also determined that Bi incorporation had limited to adverse contributions toward catalysis.

Other researchers came to similar conclusions that $TiO_2$ may serve as a sole framework for RCS generation. For instance, Heo and co-workers recently used $RuO_2$ deposited on black $TiO_2$ (b-$TiO_2$) for CER electrocatalysis [85]. b-$TiO_2$ was synthesized through electrochemical anodization of a Ti foil followed by an annealing step at 450 °C in an argon atmosphere, which resulted in the formation of significant oxygen vacancies within the $TiO_2$ lattice, enhanced visible light absorption and hence a blackened coloration. A crystalline $TiO_2$ sample was created for comparison in air and denoted (c-$TiO_2$). $RuO_2$ nanoparticles were deposited on the resulting titania through a pulsed electrodeposition method using solution-phase $Ru^{3+}$. HAADF-STEM and XPS measurements confirmed the homogeneous deposition of $RuO_2$ nanoparticles on the titania scaffolds. Dramatic differences were seen in the CER polarization curves in which $RuO_2$/b-$TiO_2$ displayed excellent CER activity with an $\eta_{RSC}$ of 95.25% in 5.0 M NaCl, in comparison to almost 0% with $RuO_2$/c-$TiO_2$. Mott-Schottky analysis showed that $RuO_2$/b-$TiO_2$ exhibited a charge carrier density 5 orders of magnitude higher than that of $RuO_2$/c-$TiO_2$. Furthermore, cyclic voltammetry measurements in the presence of ferrocene revealed that $RuO_2$/c-$TiO_2$ was electrochemically inactive under anodic polarization. Therefore, the remarkable CER performance of $RuO_2$/b-$TiO_2$ was attributed to the improved conductivity of the b-$TiO_2$ scaffold under anodic conditions.

In another study [84], Ha and co-workers prepared metal oxide catalysts for highly selective chlorine generation by using a hot injection method to synthesize $Co_3O_4$ nanoparticles ($Co_3O_4$ NPs) with cobalt(II) acetate and myristic acid as the precursors in 1-octadecene at 315 °C. Amorphous $CoO_x$ (Co-Pi), bulk CoO, and bulk $C_3O_4$ were also prepared by electrodeposition, along with commercially available dimensionally stable anode (DSA) composed of $RuO_2$-based mixed-metal oxides used for comparison. The structure of the $Co_3O_4$ NPs was carefully examined by XRD, TEM, and XPS measurements, and spin-coated on FTO for electrochemical assessments. From Fig. 5a, one can see that the $Co_3O_4$ NPs exhibited a more positive onset potential towards CER than bulk CoO and $Co_3O_4$ in 0.6 M NaCl. In situ X-ray absorption near-edge structure (XANES) measurements were carried out under CER and OER conditions to discern possible competition between the two pathways. From Fig. 5b, one can see that under OER conditions, the XANES profile exhibited an apparent positive energy shift, as compared to that under CER, signifying a higher Co oxidation state in the former. This suggests that under CER conditions $O_2$ did not compete with $Cl^-$ for Co binding. It was therefore determined that the reaction mechanism did not follow the classical metal oxide pathway, as described in reactions (16) and (17), but the one proposed by Krishtalik [97]. In the Krishtalik pathway, the chlorine adsorbate binds to the metal of the metal oxide (e.g., Co in the present study) followed by two electron-transfer steps from Cl to the metal center, such that a cationic chlorine intermediate is produced and then combined with $Cl^-$ to form the final $Cl_2$ product (Fig. 5e), where the rate determining step is the second electron-transfer process. This is supported by results from in situ Raman spectroscopy measurements, where the Co-Cl vibration (ca. 502 $cm^{-1}$) became intensified with an anodic shift of the applied potential (Fig. 5c), whereas the Raman shift remained virtually invariant in $H_2O$, $D_2O$, and $H_2{}^{18}O$ (Fig. 5d), ruling out any possible contribution of H or O to the interaction.

RCS can also be produced using nonactive electrode materials including DSA. For example, Araujo and co-workers [98] compared the use of two DSA materials ($IrO_2$ and $RuO_2$) and BDD toward inactivation of *Pseudomonas aeruginosa*, a gram-negative bacterium commonly found in water and soil. With a stainless-steel cathode and a 7 mM $Na_2SO_4$ electrolyte, complete inactivation of 100 mL of $10^6$ CFU $mL^{-1}$ bacteria was achieved at a current density of 33.3 mA $cm^{-2}$ within 30 min for both DSAs, in comparison to 60 min for BDD. Most interestingly, complete activation using the DSAs was achieved in just 5 min under the same experimental conditions and the addition of 1 mM NaCl. BDD inactivation time also improved with the addition of NaCl to 30 min. *N*,*N*-diethyl-*p*-phenylenediamine (DPD) was used as a colorimetric method to quantify RCS produced during electrocatalysis. These measurements suggested $RuO_2$ to be the most active of the three materials toward RCS generation producing more than 5 mg $L^{-1}$ of active chlorine within 15 min of electrolysis. These results highlight the ability for nonactive electrodes such as BDD and other DSAs to produce RCS under electrochemical conditions.

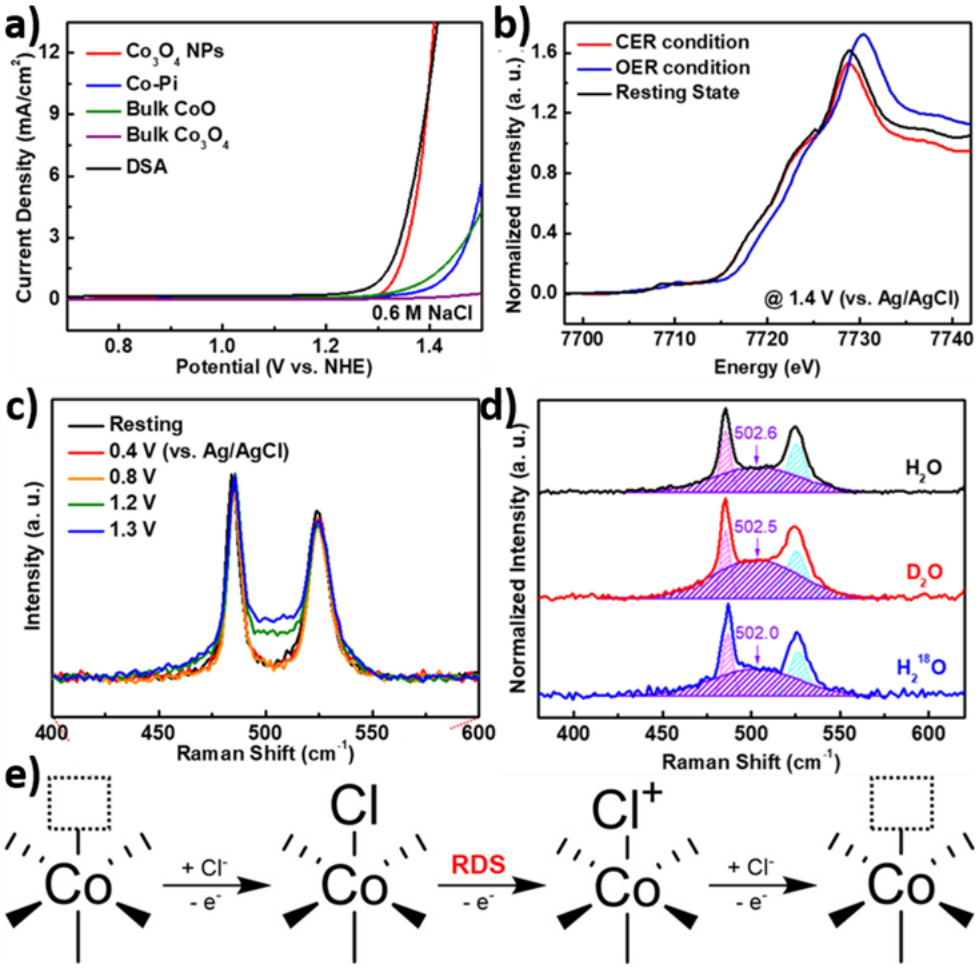


**Fig. 5.** (a) Polarization curves for chlorine evolution reaction (CER) for various cobalt containing materials. (b) In situ XANES at Co K edge for $Co_3O_4$ nanoparticles under CER and OER conditions in 0.6 M NaCl and 0.5 M phosphate buffered species (Pi), respectively. (c) In situ Raman measurements under increasing oxidative potentials from 0.4 V to 1.3 V in 4M NaCl. Broad peak occurs near 500 $cm^{-1}$ ascribed to Co-Cl, with deconvolution (d) in $H_2O$, $D_2O$, and $H_2{}^{18}O$. Reproduced with permission from ref. [84], copyright 2019, American Chemical Society.

In summary, the generation of RCS is important when the electrolyte or water used for disinfection contains a significant concentration of chloride ions. Chlorine can be produced from the oxidation of chloride ions, and further oxidation can produce

various RCS including hypochlorous acid, chlorate, and perchlorate. If the disinfected water is to be consumed by humans, it would be important to prevent the formation of toxic stable species such as chlorate and perchlorate. Table S3 summarizes the performance of additional electrocatalysts for the generation of RCS reported in recent studies. Beyond chloride, the presence of other species in the disinfection medium gives rise to the possibility of forming other RS discussed in the following section, such as reactive nitrogen and sulfur species.

### 4.3.3 Other reactive species

Under typical electrochemical conditions, ROS and RCS are the pertinent RS that are produced. However, depending on the specific experimental conditions, the production of less common RS, such as RNS [99-101] and RSS [102-105], need to be investigated as well. A series of possible reaction pathways toward RNS is provided in equation (18).

$$NO_3^- \leftrightarrows NO_2^{\bullet} \leftrightarrows NO_2^- \leftrightarrows NO^{\bullet} \leftrightarrows HNO \leftrightarrows NR_{3-x}H_x \quad (18)$$

RNS can be produced through nitrate ($NO_3^-$) reduction (from left to right in reaction (18)), or by amine ($NR_{3-x}H_x$) oxidation (from right to left in reaction (18)). A variety of amine species may be present in the experimental systems, including ammonia ($NH_3$) and biologically derived amines, such as nitrogen within the amino acid L-arginine [106]. Through these reduction or oxidation reactions, a range of RNS can be produced, including nitrogen dioxide ($N_2O^{\bullet}$), nitrite ($NO_2^-$), nitric oxide ($NO^{\bullet}$), and nitroxyl (HNO) [107]. Many more species can be formed between HNO and ammonia, including nitroxyl radical ($H_2NO$) and hydroxyl amine ($H_2NOH$) [108]. These various RNS are often grouped together and referred to as $NO_x$ in the literature [109-112]. It is also important to note that formation of these RNS require either molecular oxygen or water for successful

species formation. Therefore, these species should be kept in mind during electrocatalysis when nitrogen-containing compounds are present within the system of interest.

Like RNS, RSS can be found in many oxidation states and are often grouped together as $SO_x$ species [102]. Non-oxygen containing RSS can be formed by the reduction of elemental sulfur ($S_2$) or oxidation of sulfide-type species, like hydrogen sulfide ($H_2S$), as seen in reaction (19).

$$H_2S \leftrightarrows HS^{\bullet} \leftrightarrows H_2S_2 \leftrightarrows S_2^{\bullet} \leftrightarrows S_2 \quad (19)$$

Such non-oxygen containing RSS include thiyl radical ($HS^{\bullet}$), hydrogen persulfide ($H_2S_2$), and persulfide radical ($S_2^{\bullet-}$) [103]. The importance of RSS, as compared to RNS and ROS, has been a growing topic in biology, and it has been concluded that biologically derived RSS play a more important role in oxidative stress than once believed nearly two decades prior [103-105]. For these reasons, RSS should be taken into account in electrochemical systems containing elemental sulfur, hydrogen sulfide, or sulfate species.

Other peroxo species may be formed under electrochemical conditions beyond hydrogen peroxide, such as persulfate, percarbonate, and perphosphate [113-117]. Specifically, persulfate ($SO_5^{2-}$ or $S_2O_8^{2-}$) can be produced from sulfate, percarbonate ($H_3CO_6$) from carbonate, and perphosphate ($PO_5^{3-}$ or $P_2O_8^{2-}$) from phosphate.

Recently, there has also been significant advancement in the electrochemical production of ozone as a viable oxidant source [118-122]. This is a desirable strategy since the production and use of ozone involves only oxygen, preventing the further formation of undesirable byproducts and toxins.

In summary, there are numerous other possible reactive species, such as RNS and RSS, that can be formed during the electrocatalytic generation of ROS and RCS depending on

the disinfection media and precursors. Thus, contributions from these various RS to the electrodisinfection activity cannot be ignored, and careful analysis is called for.

### 4.3.4 Homogeneous electrocatalysis for RS generation

In the above sections, the electrogeneration of RS is primarily achieved by heterogeneous catalysis. However, it should be noted that homogeneous electrocatalysis has also been exploited for RS production [123-128]. For example, Siu et al. [123] recently reviewed their work on redox-active molecular catalysts, and discussed in detail the electrocatalytic mechanisms of radical formation and the activity in the heterodifunctionalization of alkenes. One can imagine the application of a similar homogeneous catalyst for the purposes of microbial control, as these materials produce high-energy radical species which can be used for the deterioration of microorganism components, such as lipids, proteins, and DNA, as described in the sections below.

## 4.4 Interactions of Reactive Species with Microorganisms

Now that we have established a foundation to produce RS, it is critical to investigate how these RS interact with microorganisms. RS can cause severe damage within a microorganism at high enough levels and in the absence of remediation pathways [28, 129-132]. For instance, RS can oxidize amino acids within proteins and nucleic acids within DNA, leading to protein and DNA inactivation [133-137]. Oxidation of polyunsaturated lipids within the microorganism's lipid membrane can cause structural damage with apoptosis and cell death after prolonged lipid membrane degradation [138-142]. Outer lipid membrane degradation is of particular importance since RS does not need to penetrate the cell to cause microorganism inactivation, considering the limited lifespan of the generated RS and difficulties penetrating microbial membranes [143, 144]. If the RS can contact the surface lipid layer of the microorganism, microbial inactivation

can occur [145, 146]. Notably, microorganisms produce small levels of RS on their own, which has led to the development of specific enzymes used to break down RS, as shown in Fig. 6. The following section will explore the regulation of these RS within the cell.

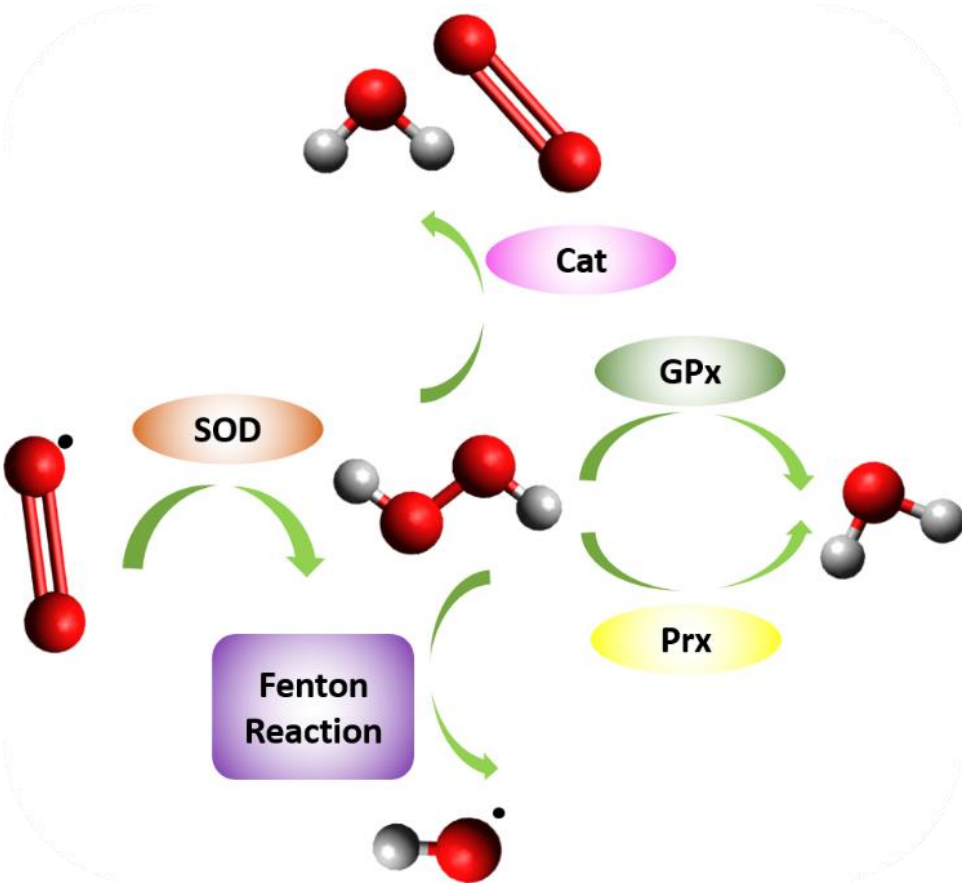


**Fig. 6.** Regulation of reactive oxygen species within the cell by enzymes superoxidase dismutase (SOD), Catalase (Cat), and other peroxidase enzymes (GPx, and Prx). Red spheres represent oxygen and grey spheres denote hydrogen.

### 4.4.1 Oxidative homeostasis regulated within microorganisms

It is also important to note that microorganisms encounter some level of RS regularly with response pathways designed to circumvent the damaging effects of RS [147, 148]. Toxic RS can be removed by antioxidant enzymes within a microorganism. These enzymes include superoxidase dismutase (SOD), catalase (Cat) and glutathione

peroxidase (GPx) (Fig. 6) [149]. SOD was first discovered by Fridovich and McCord in 1969 [150]. The most common RS found natively within the cell is $O_2^{\bullet-}$ produced within the electron transport chain of mitochondria [9, 12]. SOD has been found to catalyze the conversion of $O_2^{\bullet-}$ to $H_2O_2$. Working alone, the conversion of one RS to another is not ideal; however, Loew identified an antioxidant enzyme, Cat, in 1900 which catalyzed the conversion of $H_2O_2$ to $H_2O$ and $O_2$ [151]. In 1957, Mills discovered another enzyme, GPx, that was responsible for breaking down hydroperoxides, including lipid hydroperoxides, which were formed during radical reactions with lipid membranes found in microorganisms [152]. There have been several other peroxidase (Prx)-like enzymes discovered thereafter [4, 153-156]. A schematic summary of RS conversion within the cell is shown in Fig. 6. It is important to note the familiarity that microorganisms have with RS, such as $O_2^{\bullet-}$ and $H_2O_2$, due to their production within mitochondria and their evolved methods for controlling damage from these species. RS including $HO^{\bullet}$ and HClO are not directly produced within the cell, providing less pathways for damage prevention by the microorganism's stress response. Under increased levels of oxidative stress, microorganisms are unable to prevent damage caused by their interaction with RS. In these cases, there are some measures that the microorganism can take to repair damage to the cell. In-depth studies of these pathways can be found in the literature [156-159].

Microorganisms exist under a spectrum of RS exposure (Fig. 7a). This is because microorganisms naturally produce some level of RS, most often within mitochondria, through aerobic respiration processes. Normal levels of RS are handled by various cellular processes and minor damage caused by RS can be repaired. When a certain RS threshold is surpassed, cellular processes cannot keep up with RS removal and the microorganism enters a state of oxidative stress. Under these conditions, microbes increase the production of glutathione (GSH), which is limited by the availability of the

precursor amino acid, cysteine, and the expression of the gene *gshA* [160]. GSH will become oxidized to glutathione disulfide (GSSG) upon contact with RS (Fig. 7b). Oxidation of GSH prevents oxidation of other nearby species that may result in long-lasting damage to the microbial organism. Many research reports have used this as a method of determining effective antimicrobial catalysts through quantifying GSH interactions [161, 162]. Electrocatalysts must produce enough RS to overcome the presence of glutathione before moving on to degrade the microorganism's cellular components. One frequently used method for quantifying GSH and thiol oxidation is known as the Ellman's assay [163, 164]. In this process the Ellman reagent, 5,5′-dithio-bis(2-nitrobenzoic acid) (DTNB), is added and light absorption near 430 nm is measured over time (Fig. 7c). As shown in Fig. 7a, there is a point at which the microorganism cannot properly function in the presence of RS, and experience damaging effects, as detailed below.

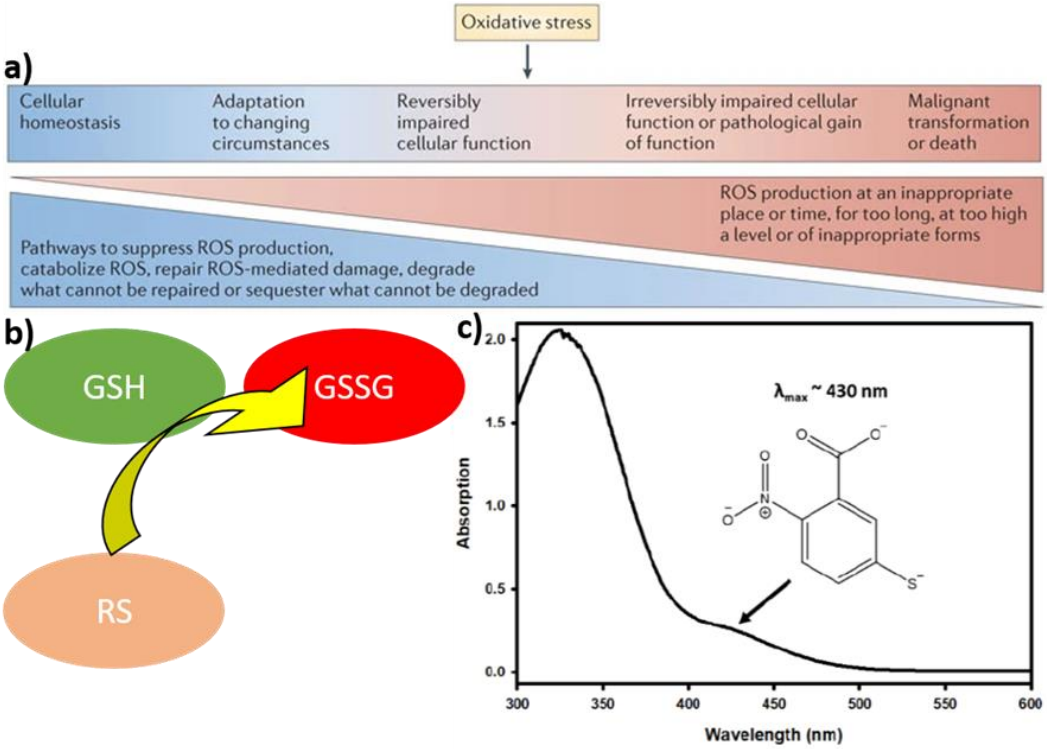

**Fig. 7.** (a) spectrum of cellular response to RS ranging from cellular homeostasis, left, to cell death, right. (b) Schematic representation of glutathione (GSH) oxidation to glutathione disulphide (GSSG) by reactive species (RS). (c) UV-vis absorption spectrum for the Ellman's reagent. Panels (a) reproduced with permission from ref. [147] copyright 2013, Springer Nature. Panel (c) reproduced with permission from ref. [163] copyright 2020, Royal chemistry society.

### 4.4.2 Damaging effects caused by reactive species

#### Lipids

Exogenous RS first encounter the lipid membrane of the cell, and this must be breached to further interact with organelle and other cell components, such as proteins and DNA. In eukaryotes, this lipid membrane is composed of glycerophospholipids with >50% of these phospholipids comprised of phosphatidylcholine [165]. These lipids self-organize to form a bilayer exposing polar groups toward the surface of the membrane. Nonpolar groups within the membrane are comprised of saturated and cis-unsaturated fatty acyl chains. Both the polar groups at the surface of the membrane and the unsaturated acyl chains are vulnerable to RS oxidation. The oxidation of the unsaturated nonpolar fatty acyl chains by RS is known as lipid peroxidation and results in the oxidative degradation [145, 146, 166-168]. Fig. 8a depicts the lipid peroxidation of linoleate resulting in structural changes to the lipid and addition of polar oxygen-containing functional groups. This reaction follows a free radical chain reaction mechanism resulting in proliferation of membrane damage and incorporation of oxygen functional groups within the nonpolar chains. The oxygen functional groups at this site are polar in nature and leads to increased hydrophilicity and ultimately decomposition of the membrane barrier and exposure of endogenous cellular components.

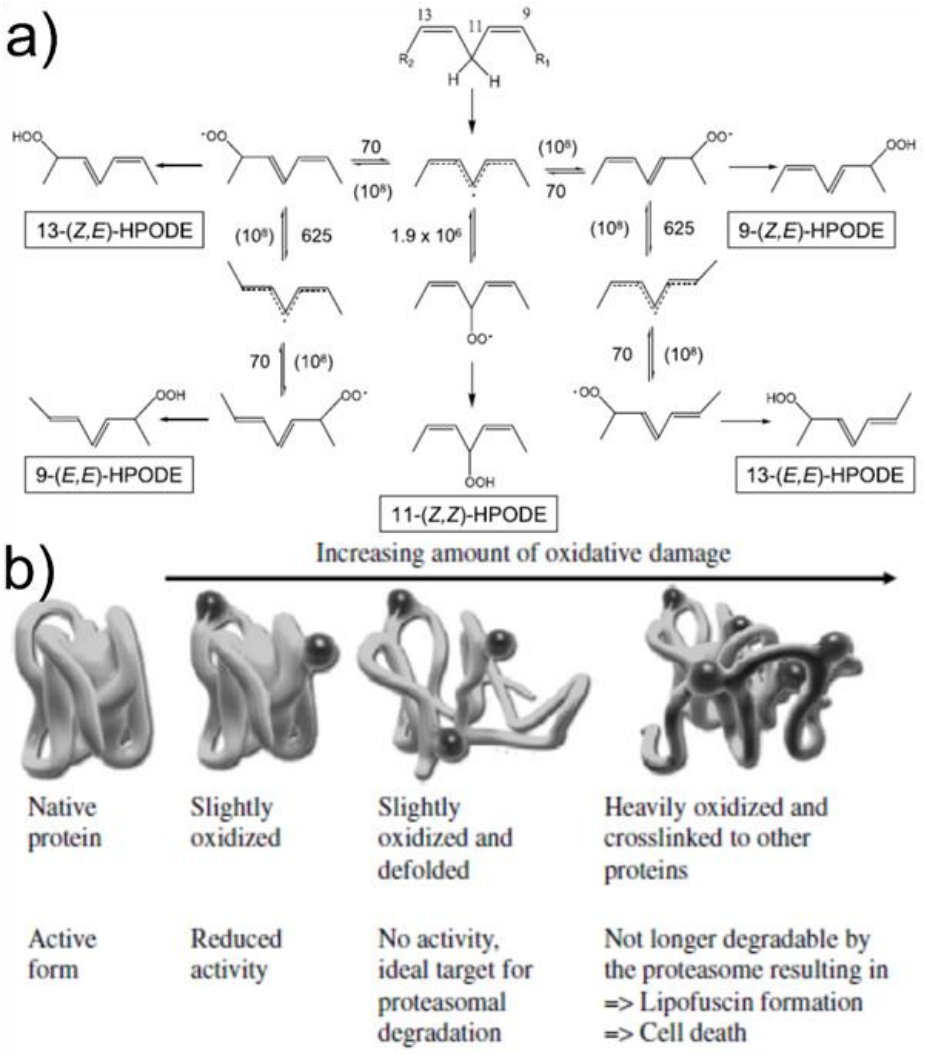


**Fig. 8.** (a) An example of lipid peroxidation using linoleate as the starting substrate. Reproduced with permission from ref. [167] copyright 2005, Elsevier. (b) Results of protein damage caused by increased levels of oxidation. Reproduced with permission from ref. [170] copyright 2003, Elsevier.

**Proteins**

Once the lipid membrane of the organism is compromised, further RS damage may be accrued to inner cellular components, including proteins and DNA. Exposure of RS to a protein leads to modifications of amino acid side chains by protein oxidation. These

changes can prevent protein function or make the protein increasingly susceptible to proteolytic degradation by the proteosome, a catalytic ATP-independent enzyme complex designed to degrade proteins tagged by ubiquitin [169]. This is part of the cell's evolved methods for self-preservation by removing damaged cellular components.

The ability for the proteosome to track and remove damaged protein has been shown to correlate with oxidant concentration [170]. At mild oxidant concentrations the proteosome can keep up with proper removal of damaged proteins. Under conditions of high oxidant concentrations, damaged proteins are less likely to be captured and removed from the cell matrix resulting in an increased opportunity for these proteins to become further damaged or interact with undamaged cell components. These protein-protein interactions can lead to protein cross-linkage where two proteins become attached to one another either by hydrophobic, electrostatic, or covalent interactions. Left unchecked, the cross-linking can continue and create a protein aggregate. Such aggregates can overwhelm the proteolytic system making basic cell function increasingly difficult. Fig. 8b depicts the progression of protein damage with increased oxidation from left to right. Heavily oxidized and crosslinked proteins cannot be degraded by the proteosome and establish cell signals related to programmed cell death. For antimicrobial purposes, this creates a circumstance in which increased RS production only improves bacterial inactivation efficiency.

**DNA**

A third vital component susceptible to RS interactions is DNA. The central dogma of biology states that DNA holds the code necessary for producing cellular components critical for survival. DNA is converted to RNA through transcription within the nucleus and RNA produces the final product including proteins and enzymes through translation [171]. Thus, cell function relies on the preservation of DNA and any deletions, mutations,

or other structural damage can lead to devastating effects during the transcription or translation processes.

Structurally DNA is comprised of a sugar phosphate backbone connected in a double helix through hydrogen bonding between 4 unique nucleotide bases, adenine, thymine, guanine, and cytosine. Damage to the DNA can occur in many ways including deletion of one or more nucleotide base pair, mutation of one or more base pairs replaced by another, or by breaks in the DNA chain either through single (SSB) or double strand breaks (DSB) [172, 173]. This type of damage to DNA is so frequent that multiple recovery pathways have evolved within the cell to correct such damage and prevent mutant RNA or protein from being produced. With this reasoning, DNA damage does not directly result in cell death, but prolonged exposure to RS and further DNA damage can result in irreversible DNA damage and contribute to cell inactivation.

$OH^{\bullet}$ has been shown to interact with DNA nucleotide base pairs through addition to the pyrimidine region of thymine and cytosine and to the purine region of adenine and guanine [174]. This interaction can lead to separation of the double stranded structure and prevent transcription from occurring. HClO has also been shown to cause nucleotide chlorination leading to similar damaging effects [175]. With sufficient RS concentration the microorganism exhibits an increase in devastating effects including lipid peroxidation, protein degradation, and irreversible DNA damage culminating to prevent necessary cell functions and ultimately results in cell inactivation.

## 4.5 Electrogenerated Reactive Species for Microbial Inactivation

Now that we have established a foundation for different types of RS and their interactions with microorganisms, it is of particular interest to summarize where the field of electrogenerated RS for microbial inactivation currently resides. Electrogenerated RS for

microorganism inactivation is a new and growing field. In the studies of electrodisinfection throughout the last decade [31, 176-194], the electrochemical activity is primarily attributed to electric field (EF), microbial cohesion, and electrocoagulation, with less focus on quantifying RS generation and the impacts on microbial inactivation. RCS are the leading RS quantified and discussed in these accounts [177, 179-181, 189, 192, 193, 195]. For instance, Cotallis and colleagues recently reported on a water electrodisinfection device created with a stainless-steel cathode and a BDD anode attached by a filter pressed stack with 40 mm separation between the cathode and anode compartments [195]. Three of these filter stacks were used in series during experimental operation. Chloride (82.19 mg $dm^{-3}$), nitrate (14.8 mg $L^{-1}$), sulfate (152.10 mg $L^{-1}$), ammonia (18.89 mg $L^{-1}$), and *E. coli* (1100 – 2200 CFU $mL^{-1}$) were the most likely species within the untreated water to interact with the electrode surface during water electrodisinfection. An optimized current density in the range of 5 – 10 mA $m^{-2}$ and applied electrical charge of 0.1 kAh $L^{-1}$ resulted in complete disinfection of the contaminated water. Successful removal of *E. coli* was quantified through changes in water turbidity and cell cultures of the resulting water. Free and combined chlorine species were considered as the primary disinfectants, and ion chromatography measurements showed a level close to 0.5 mM at the applied current density of 10 mA $m^{-2}$ and electrical charge of 0.1 kAh $L^{-1}$. It was noted that some leaching of Fe occurred at the stainless-steel anode and these dissolved species might have assisted, to some degree, in the coagulation process and improved water turbidity.

Other research groups have also had success studying simulated wastewater, created under controlled laboratory conditions. This allows for close studies into the possible reactants involved and possible products generated during the electrodisinfection process. Ding and colleagues used a commercially available DSA electrode composed of Ru-Ir-Ti

oxides with graphite felt as a cathode material, and studied how changing water conditions would influence wastewater treatment. Simulated wastewater was created using deionized water, NaCl, and $NH_4Cl$ (as a source of ammonia), and electrodisinfection rates were measured at varying contents of ammonia (0, 10 mg $L^{-1}$) and chloride (50 – 500 mg $L^{-1}$), as well as constant *E. coli* concentration (1000 CFU $mL^{-1}$). It was determined that bacterial inactivation was optimized at 250 mg $L^{-1}$ chloride ions, and addition of more chloride ions did not improve bacterial inactivation under the same reaction conditions. Also, a minimum applied charge of 0.07 Ah $L^{-1}$ was required for complete water disinfection over a 24 h period. Free chlorine generation was found to vary with the applied electrical charge and peaked at 0.4 Ah $L^{-1}$. Beyond this applied charge, chloramines and chlorate ions were the leading chlorine species produced. Complete *E. coli* removal was obtained at 0.07 Ah $L^{-1}$, 250 mg $L^{-1}$ chloride, in 4 h.

As Ghernaout pointed out in their most recent review [177], future work must also look to determine contributions from oxygen containing RS including the hydroxyl radical. In fact, ROS have been identified under similar electrochemical conditions without the presence of chloride in the electrolyte solution. For example, Qi and co-workers [196] observed synergistic effects between rGO and BDD toward electrochemical inactivation of *E. coli*. Experimentally, GO was first synthesized by a modified Hummer's method and chemically reduced by hydrazine to produce rGO. The electrodisinfection tests were carried out with an electrochemical cell comprised of a 400 mL beaker, commercially purchased BDD anode (4 $cm^2$), and a stainless-steel cathode (4 $cm^2$) separated 1 cm away from the anode. Multiple electrochemical measurements were conducted with rGO alone, BDD alone, and with both BDD and rGO. It should be noted that rGO was dispersed in the electrolyte during these studies. It was found that increasing the applied current density led to improved antimicrobial activity. rGO loading, degree of reduction, and

electrolyte concentration were then optimized to further improve the antimicrobial activity. The HO• concentration was quantified by a colorimetric method involving reaction with *N,N*-dimethy-*p*-nitrosoaniline. It was observed that the OH• concentration increased over electrolysis time and was markedly higher in the presence of both BDD and rGO, as compared to that with BDD or rGO alone. The antimicrobial activity was also significantly better in the presence of BDD and rGO, suggesting that the electrochemically generated HO• was responsible for the antibacterial performance, where rGO was postulated to increase the electric field within the electrolyte and improve charge carrier migration, leading to improved antimicrobial inactivation by direct charge transfer. However, when the power was turned off after 5 min's electrolysis, the *E. coli* count continued to decline over time. This implies that in addition to RS, other contributors need to be identified and considered for the continued bacterial inactivation, and more systematic research is desired. A similar electrochemical setup was also utilized in other reports in the investigation of pristine $TiO_2$ and bismuth-doped $TiO_2$ nanotubes [197, 198].

A significant amount of research has also been dedicated to the study of BDD toward water disinfection over the previous two decades [51, 57, 183, 193, 195, 196, 199-205]. BDD is typically produced through chemical vapor deposition at low temperatures often with methane as a carbon source and gaseous boron in the form of $B_2H_6$ or $B(OCH_3)_3$ [206]. Pristine BDD contains only $sp^3$ carbon similar to diamond; however, $sp^2$ type surface carbon defects are widely accepted as active sites for much of the catalytic properties associated with the BDD electrodes [204, 207]. With this reasoning, significant research has been developed toward the preparation of nanocrystalline diamond (NCD), containing crystal grain sizes under 100 nm, and ultra-nanocrystalline diamond (UNCD),

containing grain sizes of 3-5 nm [208, 209]. Reducing the BDD grain size introduces surface defects and $sp^2$ carbon content thereby improving electrochemical performance.

For example, Glass and co-workers recently studied the production of $H_2O_2$ using an UNCD BDD electrode [205]. Commercially available boron-doped UNCD was deposited onto a silicon wafer by a thin copper wire and silver paste. The copper wire and paste were isolated from the electrolyte by glass tubing and nonconductive epoxy. XPS was used to identify functional groups on the surface of the UNCD electrode both before and after electrochemical cycling. It was found that prolonged use of the electrode under cathodic conditions resulted in removal of oxygen functional groups at the electrode surface and decreased $H_2O_2$ production. In addition, $H_2O_2$ generation could be improved by a pre-anodization step in which the UNCD electrode was first oxidized prior to cathodic $H_2O_2$ generation. Furthermore, the use of a repeated oxidation-reduction cycling process was found to improve $H_2O_2$ generation under catholic conditions and prolong the electrode lifetime. Incorporation of an oxidation step allowed reincorporation of oxygen functional groups on the surface of the electrode necessary for $H_2O_2$ generation.

In a later study [210], Glass and co-workers demonstrated the effectiveness of the potential cycling process toward blackwater disinfection using an oxidized BDD electrode. The potential cycling approach improved the disinfection energy efficiency by as much as 124%. Furthermore, the production of RCS was quantitatively assessed using black water samples containing 0.154 M NaCl. Potential cycling (between –2 and +2 V) was shown to dramatically improve the production of free $Cl_2$ to 30 μg $cm^{-2}$, as compared to less than 15 μg $cm^{-2}$ produced by constant applied potentials of +2 and –2 V. Mechanistically, $Cl^-$ adsorption and oxidation was facilitated by anodic polarization due to the generated $HO^{\bullet}$ species, and cathodic polarization led to desorption of RCS into the bulk solution. Similarly, $O_2$ rather than $Cl^-$ was adsorbed during the anodic cycles to

produce $H_2O_2$. This demonstrates how multiple RS were produced under working conditions, each contributing to the disinfection of blackwater.

In another study [211], Jiang et al. incorporated a membrane to separate the cathode and anode compartments in their study of transition-metal (TM) SACs toward oxygen reduction for hydrogen peroxide generation and their applications in bacterial inactivation. They used a cathode material for hydrogen peroxide production and a commercial $IrO_2$ catalyst as the anode, and the anode and cathode compartments were separated by a Fumasep FAA-3-PK-130 anion exchange membrane in an H cell. Various TMs (i.e., Fe, Pd, Co, and Mn) were atomically deposited on carbon nanotubes (CNT) synthesized by a freeze drying and thermal annealing process under an Ar atmosphere at 600 °C. Fig. 9a shows the HAADF-STEM image of Fe-CNT where Fe single atoms can be readily identified. Consistent results were obtained in the corresponding FT-EXAFS spectrum (Fig. 9b), where no evident Fe-Fe neighbors can be found; for bulk $Fe_3O_4$ (blue) and Fe foil (black), the Fe spectra exhibited a small peak characteristic of Fe-O linkage. Electrochemical tests revealed a $H_2O_2$ yield over 80% for the Fe-CNT sample within a wide range of applied potentials, which decreased in the order of Fe-CNT > Pd-CNT > Co-CNT > Mn-CNT (Fig. 9c). Two additional Fe containing samples were prepared for comparison, one with nitrogen doping (Fe-N-CNT) and the other by a gas-phase reduction step of the as-prepared Fe-CNT, denoted as Red. Fe-CNT. From Fig. 9d one can see a significant loss of $H_2O_2$ production with the addition of N (red) or reduction (blue), likely due to Fe-N propensity toward $4e^-$ ORR and removal of oxygen during the reduction process losing the Fe-C-O character. DFT analysis further supported the proposed F-C-O moiety as the active site for selective $H_2O_2$ generation with initial $O_2$ adsorption occurring on the C site. The materials were then tested for electrochemical disinfection of water by quantifying the inactivation of *E. coli* at neutral pH and in a

phosphate buffered saline solution (PBS, 0.1 M) at the catalyst loading of 0.5 mg $cm^{-2}$ and applied current density of 20 mA $cm^{-2}$. Colorimetric analysis showed an $H_2O_2$ concentration of 1613 ppm after 210 min's electrolysis, with a calculated FE of 90.8%. Apparent inactivation of *E. coli* was observed with the population decreased by 43% in 5 min and 99.9999% in 120 min (Fig. 9e).

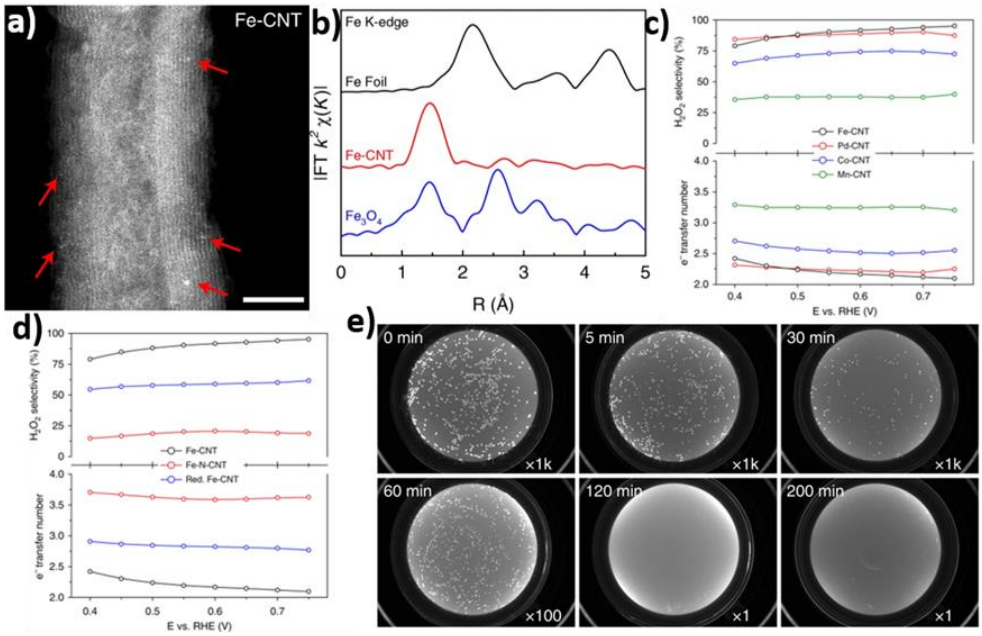


**Fig. 9.** (a) HAADF-STEM image of Fe-CNT composites. (b) FT-EXAFS R real-space plot of Fe foil (black), Fe-CNT (red), and $Fe_3O_4$ (blue). (c) Calculated $H_2O_2$ selectivity and electron transfer number for Fe-CNT (black), Pd-CNT (red), Co-CNT (blue), and Mn-CNT (green). (d) Calculated $H_2O_2$ selectivity and electron transfer number for Fe-CNT (black), nitrogen doped Fe-N-CNT (red), and gas reduced Red. Fe-CNT (blue). (e) CCD Photos of overnight cultured *E. coli* plates taken from different electrolysis timepoints. Reproduced with permission from ref. [211] copyright 2019, Springer Nature.

### 4.6 Conclusions and perspectives

In summary, substantial progress has been made toward a fundamental understanding of the electrochemical generation of various RS and their implication in bacterial inactivation. RRDE measurements have proven to be a most popular and trusted route toward the characterization of RS generation, particularly for the two-electron reduction of oxygen producing $H_2O_2$. Anodic and cathodic pathways are both feasible routes toward electrocatalytic generation of RS with a slight edge given to the cathodic pathways, primarily dure to favorable thermodynamics. Among the significant breakthroughs in the field over recent years is the work demonstrating the feasibility of $H_2O_2$ homolytic fission under electrochemical conditions yielding highly reactive $HO^{\bullet}$ [77]. Furthermore, there have been a number of studies into the practical applications of RS-generating electrocatalysts toward microbial disinfection. These studies have provided the groundwork of research to further understand the conditions required for effective disinfection, in particular, in light of the recent emergence of SACs.

Toward future progress into the field, significant breakthroughs are needed on various fronts. Rational design and engineering of effective electrocatalysts is a critical first step toward electrochemical microbial inactivation. For instance, the breakthrough in the research of monometallic and bimetallic single atom electrocatalysts can be capitalized for the effective and selective production of RS [62, 212, 213], laying the groundwork to scale up the technology for industrial water disinfection applications. Towards this end, it is important to entail rigorous characterization of a material's electrocatalytic capacity toward the generation of RS outlined above, in particular, under *operando* condition. In many cases, more than one RS may provide contributions toward microbial disinfection. It is therefore critical to identify and quantify all possible RS produced within a given system, such that a correlation can be established with the bactericidal activity to advance mechanistic understanding of the inner working of the system of interest.

Furthermore, from the microorganism perspective, current research has focused mostly on a narrow range of possibilities. It is of both fundamental and technological significance to develop electrochemical technologies towards the disinfection of a wide range of microorganisms, including gram-positive/-negative bacteria, viruses, fungi, and helminths, within the context of electrochemical RS generation. For instance, there are three major groups of microorganisms found in wastewater, with the most common being bacteria followed by viruses and helminths [214-219]. It is therefore imperative to quantify a material's ability to inactivate a range of microorganisms to accurately develop an ideal wastewater electrocatalyst. Previous reports have focused primarily on the antibacterial activity toward *E. coli,* the most common gram-negative strain of bacteria, likely due to the accessibility of various *E. coli* strains in most biology laboratories. However, bacterial interactions with electrocatalysts are likely influenced, most likely to a varying degree, by electrostatic interactions with *E. coli*. Future studies should aim to examine and compare the activity to at least one bacterium from each strain, ideally an additional one with gram-positive nature. Furthermore, viruses may pose a higher risk in wastewater than bacteria due to increased difficulty in detection and lower doses required for infection to occur [220, 221]. Therefore, future work should also look to quantify disinfection activity toward common virus strains as well. In these studies, it is also critical to carry out relevant assays to unravel the biochemical origin of the disinfection, as various mechanisms of action may be involved, such as oxidative stress induction, protein dysfunction, membrane damage, and transcriptional arrest [222]. Of these, study in conjunction with metabolomic and proteomic analysis [223-225] represents an attractive route and is a focal area of ongoing research.

## 4.7 References

1. Miklos, D.B., et al., *Evaluation of advanced oxidation processes for water and wastewater treatment–A critical review.* Water Res., 2018. **139**: p. 118-131.
2. Vallejo, M., et al., *Overview of the PCDD/Fs degradation potential and formation risk in the application of advanced oxidation processes (AOPs) to wastewater treatment.* Chemosphere, 2015. **118**: p. 44-56.
3. Hand, M.M. and S.D. Baldwin, E.; Reilly, J.M.; Mai, T.; Arent, D.; Porro, G.; Meshek, M.; Sandor, D. eds, *Renewable Electricity Futures Study.* NREL, 2012. **1-4**.
4. Imlay, J.A., *Pathways of oxidative damage.* Annu. Rev. Microbiol., 2003. **57**(1): p. 395-418.
5. Nosaka, Y. and A.Y. Nosaka, *Generation and Detection of Reactive Oxygen Species in Photocatalysis.* Chem. Rev., 2017. **117**(17): p. 11302-11336.
6. Krumova, K. and G. Cosa, *Chapter 1 Overview of Reactive Oxygen Species*, in *Singlet Oxygen: Applications in Biosciences and Nanosciences, Volume 1*. 2016, The Royal Society of Chemistry. p. 1-21.
7. Gerschman, R., *Oxygen poisoning and x-irradiation: a mechanism in common*, in *Glutathione*. 1954, Elsevier. p. 288-291.
8. Lugo, J.L., E.R. Lugo, and M. Puente, *A systematic review of microorganisms as indicators of recreational water quality in natural and drinking water systems.* J. Water Health, 2020. **19**(1): p. 20-28.
9. Zhao, R.Z., et al., *Mitochondrial electron transport chain, ROS generation and uncoupling (Review).* Int. J. Mol. Med., 2019. **44**(1): p. 3-15.
10. Sharma, A., et al., *Photosynthetic Response of Plants Under Different Abiotic Stresses: A Review.* J. Plant Growth Regul., 2020. **39**(2): p. 509-531.

11. Lee, J., et al., *Boosting the Ambipolar Performance of Solution-Processable Polymer Semiconductors via Hybrid Side-Chain Engineering.* J. Am. Chem. Soc., 2013. **135**(25): p. 9540-9547.

12. Lambert, A.J. and M.D. Brand, *Reactive oxygen species production by mitochondria.* Methods Mol. Biol., 2009. **554**: p. 165-81.

13. Guo, R.Y., et al., *Architecture of Human Mitochondrial Respiratory Megacomplex I2III2IV2.* Cell, 2017. **170**(6): p. 1247-1257.

14. Dröge, W., *Free radicals in the physiological control of cell function.* Physiol. Rev., 2002. **82**(1): p. 47-95.

15. Carstensen, A., et al., *The Impacts of Phosphorus Deficiency on the Photosynthetic Electron Transport Chain.* Plant Physiol., 2018. **177**(1): p. 271-284.

16. Mercado, R., et al., *Nitrogen-Doped Porous Carbon Cages for Electrocatalytic Reduction of Oxygen: Enhanced Performance with Iron and Cobalt Dual Metal Centers.* ChemCatChem, 2020. **12**(12): p. 3230-3239.

17. Lu, B., et al., *Oxygen Reduction Reaction Catalyzed by Carbon-Supported Platinum Few-Atom Clusters: Significant Enhancement by Doping of Atomic Cobalt.* Research, 2020. **2020**: p. 9167829.

18. Jiang, H., et al., *Defect-rich and ultrathin N doped carbon nanosheets as advanced trifunctional metal-free electrocatalysts for the ORR, OER and HER.* Energy Environ. Sci., 2019. **12**(1): p. 322-333.

19. Li, J.Z., et al., *Atomically dispersed manganese catalysts for oxygen reduction in proton-exchange membrane fuel cells.* Nat. Catal., 2018. **1**(12): p. 935-945.

20. Jiang, K., J. Zhao, and H. Wang, *Catalyst design for electrochemical oxygen reduction toward hydrogen peroxide.* Adv. Funct. Mater., 2020. **30**(35): p. 2003321.

21. Tian, X., et al., *Understanding the Promotion Effect of Mn on CuO/Al2O3 for Catalyzed HCl Oxidation to Cl2.* ChemCatChem, 2020. **12**(12): p. 3240-3248.

22. He, D., et al., *Hydrogen peroxide electrosynthesis via regulating the oxygen reduction reaction pathway on Pt noble metal with ion poisoning.* Electrochim. Acta, 2021. **371**: p. 137721.

23. Dong, K., et al., *Noble-metal-free electrocatalysts toward H 2 O 2 production.* J. Mater. Chem. A, 2020. **8**(44): p. 23123-23141.

24. Jung, E., et al., *Recent Advances on Electrochemical Oxygen Reduction to H2O2: Catalyst and Cell Design.* ACS Energy Lett., 2020. **5**(6): p. 1881-1892.

25. Pelaez, M., et al., *A review on the visible light active titanium dioxide photocatalysts for environmental applications.* Appl. Catal. B . 2012. **125**: p. 331-349.

26. Fu, P.P., et al., *Mechanisms of nanotoxicity: Generation of reactive oxygen species.* J. Food Drug Anal., 2014. **22**(1): p. 64-75.

27. Graves, D.B., *The emerging role of reactive oxygen and nitrogen species in redox biology and some implications for plasma applications to medicine and biology.* J. Phys. D Appl. Phys., 2012. **45**(26): p. 263001.

28. Sirelkhatim, A., et al., *Review on Zinc Oxide Nanoparticles: Antibacterial Activity and Toxicity Mechanism.* Nanomicro Lett., 2015. **7**(3): p. 219-242.

29. Li, Q.L., et al., *Antimicrobial nanomaterials for water disinfection and microbial control: Potential applications and implications.* Water Res., 2008. **42**(18): p. 4591-4602.

30. Barrera-Díaz, C., et al., *Electrochemical advanced oxidation processes: an overview of the current applications to actual industrial effluents.* J. Mex. Chem., 2014. **58**(3): p. 256-275.

31. Gonzalez-Rivas, N., H. Reyes-Perez, and C.E. Barrera-Diaz, *Recent Advances in Water and Wastewater Electrodisinfection.* Chemelectrochem, 2019. **6**(7): p. 1978-1983.

32. Linares-Hernández, I., et al., *A combined electrocoagulation–electrooxidation treatment for industrial wastewater.* J. Hazard. Mater., 2010. **175**(1-3): p. 688-694.

33. Song, C. and J. Zhang, *Electrocatalytic oxygen reduction reaction*, in *PEM Fuel Cell Electrocatalysts and Catalyst Layers*. 2008, Springer. p. 89-134.

34. Hayyan, M., M.A. Hashim, and I.M. AlNashef, *Superoxide Ion: Generation and Chemical Implications.* Chem. Rev., 2016. **116**(5): p. 3029-3085.

35. Sawyer, D.T. and J.L. Roberts, *Electrochemistry of oxygen and superoxide ion in dimethylsulfoxide at platinum, gold and mercury electrodes.* J. Electroanal. Chem., 1966. **12**(2): p. 90-101.

36. Marklund, S., *Spectrophotometric study of spontaneous disproportionation of superoxide anion radical and sensitive direct assay for superoxide dismutase.* J. Biol. Chem., 1976. **251**(23): p. 7504-7507.

37. Abdollahi, M. and A. Hosseini, *Hydrogen Peroxide*, in *Encyclopedia of Toxicology (Third Edition)*, P. Wexler, Editor. 2014, Academic Press: Oxford. p. 967-970.

38. Wang, H., et al., *Direct and continuous strain control of catalysts with tunable battery electrode materials.* Science, 2016. **354**(6315): p. 1031-1036.

39. Peng, Y., et al., *Impacts of interfacial charge transfer on nanoparticle electrocatalytic activity towards oxygen reduction.* Phys. Chem. Chem. Phys., 2017. **19**(14): p. 9336-9348.

40. Liu, Q., Q. Li, and S. Chen, *Metal-Nitrogen Coordination Moieties in Carbon for Effective Electrocatalytic Reduction of Oxygen.* Curr. Opin. Electrochem., 2020. **21**: p. 46-54.

41. Li, M., et al., *Ultrafine jagged platinum nanowires enable ultrahigh mass activity for the oxygen reduction reaction.* Science, 2016. **354**(6318): p. 1414-1419.

42. Jiang, Y.Y., et al., *Selective Electrochemical H2O2 Production through Two-Electron Oxygen Electrochemistry.* Adv. Energy Mater., 2018. **8**(31): p. 1801909.

43. Bu, L., et al., *Biaxially strained PtPb/Pt core/shell nanoplate boosts oxygen reduction catalysis.* Science, 2016. **354**(6318): p. 1410-1414.

44. Chong, L., et al., *Ultralow-loading platinum-cobalt fuel cell catalysts derived from imidazolate frameworks.* Science, 2018. **362**(6420): p. 1276-+.

45. Xie, P., et al., *Highly efficient decomposition of ammonia using high-entropy alloy catalysts.* Nat. Commun., 2019. **10**(1): p. 4011.

46. Tian, X., et al., *Engineering bunched Pt-Ni alloy nanocages for efficient oxygen reduction in practical fuel cells.* Science, 2019. **366**(6467): p. 850-856.

47. Yang, L.J., et al., *Carbon-Based Metal-Free ORR Electrocatalysts for Fuel Cells: Past, Present, and Future.* J. Adv. Mater., 2019. **31**(13): p. 1804799.

48. Chen, Y.J., et al., *Enhanced oxygen reduction with single-atomic-site iron catalysts for a zinc-air battery and hydrogen-air fuel cell.* Nat. Commun., 2018. **9**: p. 5422.

49. Tian, X.L., et al., *Engineering bunched Pt-Ni alloy nanocages for efficient oxygen reduction in practical fuel cells.* Science, 2019. **366**(6467): p. 850-+.

50. Brillas, E. and C.A. Martinez-Huitle, *Decontamination of wastewaters containing synthetic organic dyes by electrochemical methods. An updated review.* Appl. Catal. B . 2015. **166**: p. 603-643.

51. Martinez-Huitle, C.A. and E. Brillas, *Decontamination of wastewaters containing synthetic organic dyes by electrochemical methods: A general review.* Appl. Catal. B . 2009. **87**(3-4): p. 105-145.

52. Sires, I., et al., *Electrochemical advanced oxidation processes: today and tomorrow. A review.* Environ. Sci. Pollut. Res., 2014. **21**(14): p. 8336-8367.

53. Garcia-Segura, S., et al., *Comparative decolorization of monoazo, diazo and triazo dyes by electro-Fenton process.* Electrochim. Acta, 2011. **58**: p. 303-311.

54. Brillas, E., et al., *ELECTROCHEMICAL DESTRUCTION OF ANILINE AND 4-CHLOROANILINE FOR WASTE-WATER TREATMENT USING A CARBON-PTFE O-2-FED CATHODE.* J. Electrochem. Soc., 1995. **142**(6): p. 1733-1741.

55. Zhou, M.H., et al., *Electro-Fenton method for the removal of methyl red in an efficient electrochemical system.* Sep. Purif. Technol., 2007. **57**(2): p. 380-387.

56. Brillas, E., J.C. Calpe, and J. Casado, *Mineralization of 2,4-D by advanced electrochemical oxidation processes.* Water Res., 2000. **34**(8): p. 2253-2262.

57. Armijos-Alcocer, K.G., et al., *Electrochemical degradation of nonylphenol ethoxylate-7 (NP 7 EO) using a DiaClean® cell equipped with boron-doped diamond electrodes (BDD).* Water Air Soil Pollut., 2017. **228**(8): p. 1-8.

58. Barrera, H., et al., *Catalytic effect of hydrogen peroxide in the electrochemical treatment of phenolic pollutants using a BDD anode.* ChemElectroChem, 2019. **6**(8): p. 2264-2272.

59. Rodríguez-Peña, M., et al., *Nonylphenol degradation by simultaneous electrooxidation on BDD anode and oxidation by H2O2 in a continuous flow electrochemical reactor.* Int. J. Electrochem. Sci., 2019. **14**: p. 4409-4419.

60. Duan, X.G., H.Q. Sun, and S.B. Wang, *Metal-Free Carbocatalysis in Advanced Oxidation Reactions.* Acc. Chem. Res., 2018. **51**(3): p. 678-687.

61. Trellu, C., et al., *Removal of hydrophobic organic pollutants from soil washing/flushing solutions: A critical review.* J. Hazard. Mater., 2016. **306**: p. 149-174.

62. Zhu, W.Y. and S.W. Chen, *Recent Progress of Single-Atom Catalysts in the Electrocatalytic Reduction of Oxygen to Hydrogen Peroxide.* Electroanalysis, 2020. **32**(12): p. 2591-2602.

63. Tang, C., et al., *Coordination Tunes Selectivity: Two-Electron Oxygen Reduction on High-Loading Molybdenum Single-Atom Catalysts.* Angew. Chem. Int. Ed., 2020. **132**(23): p. 9256-9261.

64. Jung, E., et al., *Atomic-level tuning of Co–N–C catalyst for high-performance electrochemical H2O2 production.* Nat. Mater., 2020. **19**(4): p. 436-442.

65. Shi, X., et al., *Understanding activity trends in electrochemical water oxidation to form hydrogen peroxide.* Nat. Commun., 2017. **8**(1): p. 701.

66. Viswanathan, V., H.A. Hansen, and J.K. Nørskov, *Selective Electrochemical Generation of Hydrogen Peroxide from Water Oxidation.* J. Phys. Chem. Lett., 2015. **6**(21): p. 4224-4228.

67. Kelly, S.R., et al., *ZnO As an Active and Selective Catalyst for Electrochemical Water Oxidation to Hydrogen Peroxide.* ACS Catal, 2019. **9**(5): p. 4593-4599.

68. Perry, S.C., et al., *Electrochemical synthesis of hydrogen peroxide from water and oxygen.* Nat. Rev. Chem., 2019. **3**(7): p. 442-458.

69. Fenton, H.J.H., *LXXIII.—Oxidation of tartaric acid in presence of iron.* J. Chem. Soc. Faraday Trans., 1894. **65**(0): p. 899-910.

70. Vasquez-Medrano, R., D. Prato-Garcia, and M. Vedrenne, *Chapter 4 - Ferrioxalate-Mediated Processes*, in *Advanced Oxidation Processes for Waste Water Treatment*, S.C. Ameta and R. Ameta, Editors. 2018, Academic Press. p. 89-113.

71. Ganiyu, S.O., M. Zhou, and C.A. Martínez-Huitle, *Heterogeneous electro-Fenton and photoelectro-Fenton processes: A critical review of fundamental principles and application for water/wastewater treatment.* Appl. Catal. B., 2018. **235**: p. 103-129.

72. Divyapriya, G. and P.V. Nidheesh, *Importance of Graphene in the Electro-Fenton Process.* ACS Omega, 2020. **5**(10): p. 4725-4732.

73. Yu, T. and C.B. Breslin, *Graphene-Modified Composites and Electrodes and Their Potential Applications in the Electro-Fenton Process.* Materials, 2020. **13**(10): p. 2254.

74. Sheng, H., et al., *Stable and selective electrosynthesis of hydrogen peroxide and the electro-Fenton process on CoSe 2 polymorph catalysts.* Energy & Environmental Science, 2020. **13**(11): p. 4189-4203.

75. Li, G. and Y. Zhang, *Highly selective two-electron oxygen reduction to generate hydrogen peroxide using graphite felt modified with N-doped graphene in an electro-Fenton system.* New J. Chem., 2019. **43**(32): p. 12657-12667.

76. Wu, Q., et al., *High-loaded single Cu atoms decorated on N-doped graphene for boosting Fenton-like catalysis under neutral pH.* J. Mater. Chem. A, 2020. **8**(27): p. 13685-13693.

77. Cao, P., et al., *High-Efficiency Electrocatalysis of Molecular Oxygen toward Hydroxyl Radicals Enabled by an Atomically Dispersed Iron Catalyst.* Environ. Sci. Technol., 2020. **54**(19): p. 12662-12672.

78. Karlsson, R.K.B. and A. Cornell, *Selectivity between Oxygen and Chlorine Evolution in the Chlor-Alkali and Chlorate Processes.* Chem. Rev., 2016. **116**(5): p. 2982-3028.

79. Fang, J.Y., Y. Fu, and C. Shang, *The Roles of Reactive Species in Micropollutant Degradation in the UV/Free Chlorine System.* Environ. Sci. Technol., 2014. **48**(3): p. 1859-1868.

80. Yuan, R.X., et al., *Effects of chloride ion on degradation of Acid Orange 7 by sulfate radical-based advanced oxidation process: Implications for formation of chlorinated aromatic compounds.* J. Hazard. Mater., 2011. **196**: p. 173-179.

81. Shields, B.J. and A.G. Doyle, *Direct C(sp(3))-H Cross Coupling Enabled by Catalytic Generation of Chlorine Radicals.* J. Am. Chem. Soc., 2016. **138**(39): p. 12719-12722.

82. Wu, Z.H., et al., *Roles of reactive chlorine species in trimethoprim degradation in the UV/chlorine process: Kinetics and transformation pathways.* Water Res., 2016. **104**: p. 272-282.

83. Jasper, J.T., Y. Yang, and M.R. Hoffmann, *Toxic byproduct formation during electrochemical treatment of latrine wastewater.* Environ. Sci. Technol., 2017. **51**(12): p. 7111-7119.

84. Ha, H., et al., *Highly Selective Active Chlorine Generation Electrocatalyzed by Co3O4 Nanoparticles: Mechanistic Investigation through in Situ Electrokinetic and Spectroscopic Analyses.* J. Phys. Chem. Lett., 2019. **10**(6): p. 1226-1233.

85. Heo, S.E., et al., *Anomalous potential dependence of conducting property in black titania nanotube arrays for electrocatalytic chlorine evolution.* J. Catal., 2020. **381**: p. 462-467.

86. Hong, S., et al., *Enhanced chlorine evolution from dimensionally stable anode by heterojunction with Ti and Bi based mixed metal oxide layers prepared from nanoparticle slurry.* J. Catal., 2020. **389**: p. 1-8.

87. Gedam, N., et al., *Novel Lead dioxide-Graphite-Polymer composite anode for electrochemical chlorine generation.* Electrochim. Acta, 2015. **169**: p. 109-116.

88. Kim, J., et al., *RuO2 coated blue TiO2 nanotube array (blue TNA-RuO2) as an effective anode material in electrochemical chlorine generation.* J. Ind. Eng. Chem., 2018. **66**: p. 478-483.

89. Luu, T.L., et al., *The Effect of Preparation Parameters in Thermal Decomposition of Ruthenium Dioxide Electrodes on Chlorine Electro-Catalytic Activity.* B. KOREAN CHEM. SOC., 2015. **36**(5): p. 1411-1417.

90. Palma-Goyes, R.E., et al., *The Effects of ZrO2 on the Electrocatalysis to Yield Active Chlorine Species on Sb2O5-Doped Ti/RuO2 Anodes.* J. Electrochem. Soc., 2016. **163**(9): p. H818-H825.

91. Shi, Z.Q., et al., *Pt nanostructure from electrodeposition: Electrocatalyst to generate chlorine for marine biofouling inhibition.* Colloids Surf., A Physicochem Eng. Asp., 2017. **520**: p. 522-531.

92. Mondelli, C., et al., *Shaped RuO2/SnO2–Al2O3 Catalyst for Large-Scale Stable Cl2 Production by HCl Oxidation.* ChemCatChem, 2011. **3**(4): p. 657-660.

93. Cho, K. and M.R. Hoffmann, *BixTi1–xOz Functionalized Heterojunction Anode with an Enhanced Reactive Chlorine Generation Efficiency in Dilute Aqueous Solutions.* Chem. Mater., 2015. **27**(6): p. 2224-2233.

94. Comninellis, C. and G. Vercesi, *Characterization of DSA®-type oxygen evolving electrodes: choice of a coating.* J. Appl. Electrochem., 1991. **21**(4): p. 335-345.

95. Menzel, N., et al., *Dimensionally stable Ru/Ir/TiO2-anodes with tailored mesoporosity for efficient electrochemical chlorine evolution.* ACS Catal, 2013. **3**(6): p. 1324-1333.

96. Trasatti, S., *Progress in the understanding of the mechanism of chlorine evolution at oxide electrodes.* Electrochim. Acta, 1987. **32**(3): p. 369-382.

97. Ehrenburg, R., L. Krishtalik, and I. Yaroshevskaya, *On mechanism of chlorine evolution at ruthenium-titanium oxide electrode.* Ehlektrokhimiya, 1975. **11**(7): p. 1068-1072.

98. Bruguera-Casamada, C., et al., *Effect of electrogenerated hydroxyl radicals, active chlorine and organic matter on the electrochemical inactivation of*

*Pseudomonas aeruginosa using BDD and dimensionally stable anodes.* Sep. Purif. Technol., 2017. **178**: p. 224-231.

99. Dedon, P.C. and S.R. Tannenbaum, *Reactive nitrogen species in the chemical biology of inflammation.* Arch. Biochem. Biophys., 2004. **423**(1): p. 12-22.

100. Bruskov, V.I., et al., *Formation of the Reactive Species of Oxygen, Nitrogen, and Carbon Dioxide in Aqueous Solutions under Physical Impacts.* Phys. Wave Phenom, 2020. **28**(2): p. 103-106.

101. Borgmann, S., *Electrochemical quantification of reactive oxygen and nitrogen: challenges and opportunities.* Anal. Bioanal. Chem., 2009. **394**(1): p. 95-105.

102. Werne, J.P., et al., *Organic sulfur biogeochemistry: recent advances and future research directions.* Geol. Soc. Am. Spec., 2004. **379**: p. 135-150.

103. DeLeon, E.R., et al., *A case of mistaken identity: are reactive oxygen species actually reactive sulfide species?* Am. J. Physiol. Regul. Integr. Comp. Physiol., 2016. **310**(7): p. R549-R560.

104. Giles, G.I., K.M. Tasker, and C. Jacob, *Hypothesis: the role of reactive sulfur species in oxidative stress.* Free Radic. Biol. Med., 2001. **31**(10): p. 1279-1283.

105. Giles, G.I., et al., *The reactive sulfur species concept: 15 years on.* Antioxidants, 2017. **6**(2): p. 38.

106. Nathan, C. and M.U. Shiloh, *Reactive oxygen and nitrogen intermediates in the relationship between mammalian hosts and microbial pathogens.* PNAS, 2000. **97**(16): p. 8841-8848.

107. Kapil, V., et al., *The noncanonical pathway for in vivo nitric oxide generation: the nitrate-nitrite-nitric oxide pathway.* Pharmacol. Rev., 2020. **72**(3): p. 692-766.

108. Lifshitz, C., et al., *NH2O· and NHOH·: Generation and characterization of their neutral species and cations in the gas phase.* Rapid Commun. Mass Spectrom., 1987. **1**(4): p. 61-63.

109. Zhu, N., et al., *A superior Fe-V-Ti catalyst with high activity and SO2 resistance for the selective catalytic reduction of NOx with NH3.* J. Hazard. Mater., 2020. **382**: p. 120970.

110. Zha, K.W., et al., *Promotional effects of Fe on manganese oxide octahedral molecular sieves for alkali-resistant catalytic reduction of NOx: XAFS and in situ DRIFTs study.* Chem. Eng. J., 2020. **381**: p. 122764.

111. Han, L.P., et al., *Fe2O3-CeO2@Al2O3 Nanoarrays on Al-Mesh as SO2-Tolerant Monolith Catalysts for NO, Reduction by NH3.* Environ. Sci. Technol., 2019. **53**(10): p. 5946-5956.

112. Bhattacharya, P., et al., *Catalytic Ammonia Oxidation to Dinitrogen by Hydrogen Atom Abstraction.* Angew. Chem. Int. Ed., 2019. **58**(34): p. 11618-11624.

113. Liu, T.C., et al., *Degradation of thiacloprid via unactivated peroxymonosulfate: The overlooked singlet oxygen oxidation.* Chemical Engineering Journal, 2020. **388**: p. 124264.

114. Luo, H.W., et al., *Rapid removal of organic micropollutants by heterogeneous peroxymonosulfate catalysis over a wide pH range: Performance, mechanism and economic analysis.* Separation and Purification Technology, 2020. **248**: p. 117023.

115. Alikarami, M., R.D.C. Soltani, and A. Khataee, *An innovative combination of electrochemical and photocatalytic processes for decontamination of bisphenol A endocrine disruptor form aquatic phase: Insight into mechanism, enhancers*

*and bio-toxicity assay.* Separation and Purification Technology, 2019. **220**: p. 42-51.

116. Jojoa-Sierra, S.D., et al., *Elimination of the antibiotic norfloxacin in municipal wastewater, urine and seawater by electrochemical oxidation on IrO2 anodes.* Science of the Total Environment, 2017. **575**: p. 1228-1238.

117. Martikyan, S.O., V.A. Shepelin, and E.V. Kasatkin, *Ellipsometric and Electrochemical Examination of Perphosphate Formation at Platinum Anodes - Chemisorption of Fluorine-Containing Species.* Soviet Electrochemistry, 1978. **14**(7): p. 943-946.

118. Montero-Guadarrama, I., et al., *Phenol Red Degradation Using a Synergetic Method (Electrochemical Oxidation with Ozone) in Batch and Continuous System.* Int. J. Electrochem. Sci, 2020. **15**: p. 7883-7895.

119. Rodríguez-Peña, M., et al., *New insights about the electrochemical production of ozone.* Curr. Opin. Electrochem, 2021. **27**: p. 100697.

120. Barrera-Diaz, C.E. and N. González-Rivas, *Electrooxidation-Ozonation: A Synergistic Sustainable Wastewater Treatment Process*, in *Physico-Chemical Wastewater Treatment and Resource Recovery*. 2017, IntechOpen.

121. Torres-Blancas, T., et al., *Ozonation enhancement by Fe–Cu biometallic particles.* J. Taiwan Inst. Chem. Eng., 2017. **74**: p. 225-232.

122. Lara-Ramos, J.A., et al., *Electro-ozonizers: A new approach for an old problem.* Sep. Purif. Technol., 2020. **241**: p. 116701.

123. Siu, J.C., N. Fu, and S. Lin, *Catalyzing electrosynthesis: a homogeneous electrocatalytic approach to reaction discovery.* Acc. Chem. Res., 2020. **53**(3): p. 547-560.

124. Morris, A.J., G.J. Meyer, and E. Fujita, *Molecular Approaches to the Photocatalytic Reduction of Carbon Dioxide for Solar Fuels.* Acc. Chem. Res., 2009. **42**(12): p. 1983-1994.

125. Das, A., et al., *Nickel Complexes for Robust Light-Driven and Electrocatalytic Hydrogen Production from Water.* ACS Catal., 2015. **5**(3): p. 1397-1406.

126. Sheldon, R.A. and I. Arends, *Organocatalytic oxidations mediated by nitroxyl radicals.* Adv. Synth. Catal., 2004. **346**(9-10): p. 1051-1071.

127. Shaw, W.J., M.L. Helm, and D.L. DuBois, *A modular, energy-based approach to the development of nickel containing molecular electrocatalysts for hydrogen production and oxidation.* Biochim Biophys Acta Bioenerg BBA-BIOENERGETICS, 2013. **1827**(8-9): p. 1123-1139.

128. Lee, C. and D.L. Sedlak, *A novel homogeneous Fenton-like system with Fe(III)-phosphotungstate for oxidation of organic compounds at neutral pH values.* J. Mol. Catal. A Chem., 2009. **311**(1-2): p. 1-6.

129. Chen, G.Y. and G. Nunez, *Sterile inflammation: sensing and reacting to damage.* Nat. Rev. Immunol., 2010. **10**(12): p. 826-837.

130. Holmstrom, K.M. and T. Finkel, *Cellular mechanisms and physiological consequences of redox-dependent signalling.* Nat. Rev. Mol., 2014. **15**(6): p. 411-421.

131. Hou, J., et al., *Toxicity and mechanisms of action of titanium dioxide nanoparticles in living organisms.* J. Environ. Sci., 2019. **75**: p. 40-53.

132. Liao, X.W., et al., *Enhanced Electrocatalysis via Boosted Separation of Hot Charge Carriers of Plasmonic Gold Nanoparticles Deposited on Reduced Graphene Oxide.* Chemelectrochem, 2019. **6**(5): p. 1419-1426.

133. Singh, A., et al., *Oxidative Stress: A Key Modulator in Neurodegenerative Diseases.* Molecules, 2019. **24**(8): p. 1583.

134. Kryston, T.B., et al., *Role of oxidative stress and DNA damage in human carcinogenesis.* Mutat. Res. Fund. Mol. M., 2011. **711**(1-2): p. 193-201.

135. Dizdaroglu, M. and P. Jaruga, *Mechanisms of free radical-induced damage to DNA.* Free Radic. Res., 2012. **46**(4): p. 382-419.

136. Cadet, J., T. Douki, and J.L. Ravanat, *Oxidatively generated base damage to cellular DNA.* Free Radic. Biol. Med., 2010. **49**(1): p. 9-21.

137. Cadet, J. and K.J.A. Davies, *Oxidative DNA damage & repair: An introduction.* Free Radic. Biol. Med., 2017. **107**: p. 2-12.

138. Prochazkova, D., I. Bousova, and N. Wilhelmova, *Antioxidant and prooxidant properties of flavonoids.* Fitoterapia, 2011. **82**(4): p. 513-523.

139. Mateen, S., et al., *Increased Reactive Oxygen Species Formation and Oxidative Stress in Rheumatoid Arthritis.* PloS One, 2016. **11**(4): p. 0152925.

140. Garcia, J.J., et al., *Protective effects of melatonin in reducing oxidative stress and in preserving the fluidity of biological membranes: a review.* J. Pineal Res., 2014. **56**(3): p. 225-237.

141. Bains, M. and E.D. Hall, *Antioxidant therapies in traumatic brain and spinal cord injury.* Biochim. Biophys. Acta. Mol. Basis Dis., 2012. **1822**(5): p. 675-684.

142. Skouta, R., et al., *Ferrostatins Inhibit Oxidative Lipid Damage and Cell Death in Diverse Disease Models.* J. Am. Chem. Soc., 2014. **136**(12): p. 4551-4556.

143. Shi, X.L., N.S. Dalal, and K.S. Kasprzak, *GENERATION OF FREE-RADICALS FROM HYDROGEN-PEROXIDE AND LIPID HYDROPEROXIDES IN THE PRESENCE OF CR(III).* Arch. Biochem. Biophys., 1993. **302**(1): p. 294-299.

144. Torreggiani, A., M. Tamba, and C. Ferreri, *Radical damage involving sulfur-containing enzymes and membrane lipids.* Protein Pept. Lett., 2007. **14**(7): p. 716-722.

145. Pre, J., *FREE-RADICALS AND LIPID-PEROXIDATION .1. GENERAL BIOLOGICAL ASPECTS.* Sem. Hop. Inf., 1992. **68**(41): p. 1430-1437.

146. Cheeseman, K.H., *MECHANISMS AND EFFECTS OF LIPID-PEROXIDATION.* Mol. Asp. Med., 1993. **14**(3): p. 191-197.

147. Nathan, C. and A. Cunningham-Bussel, *Beyond oxidative stress: an immunologist's guide to reactive oxygen species.* Nat. Rev. Immunol., 2013. **13**(5): p. 349-361.

148. Staerck, C., et al., *Microbial antioxidant defense enzymes.* Microb. Pathog., 2017. **110**: p. 56-65.

149. Marín-García, J., *Post-genomic cardiology*. 2011: Academic Press.

150. McCord, J.M. and I. Fridovich, *Superoxide Dismutase: AN ENZYMIC FUNCTION FOR ERYTHROCUPREIN (HEMOCUPREIN).* J. Biol. Chem., 1969. **244**(22): p. 6049-6055.

151. Loew, O., *A new enzyme of general occurrence in organismis.* Science, 1900. **11**(279): p. 701-702.

152. Mills, G.C., *Hemoglobin catabolism: I. Glutathione peroxidase, an erythrocyte enzyme which protects hemoglobin from oxidative breakdown.* J. Biol. Chem., 1957. **229**(1): p. 189-197.

153. Sies, H., *Oxidative stress: Oxidants and antioxidants.* Exp. Physiol., 1997. **82**(2): p. 291-295.

154. Rodriguez, C., et al., *Regulation of antioxidant enzymes: a significant role for melatonin.* J. Pineal Res., 2004. **36**(1): p. 1-9.

155. Blokhina, O., E. Virolainen, and K.V. Fagerstedt, *Antioxidants, oxidative damage and oxygen deprivation stress: a review.* Ann. Bot., 2003. **91**(2): p. 179-194.

156. Imlay, J.A., *Cellular defenses against superoxide and hydrogen peroxide.* Annu. Rev. Biochem., 2008. **77**: p. 755-776.

157. Marnett, L.J., *Oxyradicals and DNA damage.* Carcinogenesis, 2000. **21**(3): p. 361-370.

158. Chapman, J.R., M.R.G. Taylor, and S.J. Boulton, *Playing the End Game: DNA Double-Strand Break Repair Pathway Choice.* Mol. Cell, 2012. **47**(4): p. 497-510.

159. Ciccia, A. and S.J. Elledge, *The DNA Damage Response: Making It Safe to Play with Knives.* Mol. Cell, 2010. **40**(2): p. 179-204.

160. Masip, L., K. Veeravalli, and G. Georgiou, *The many faces of glutathione in bacteria.* Antioxidants, 2006. **8**(5-6): p. 753-762.

161. Gong, N., et al., *Carbon-dot-supported atomically dispersed gold as a mitochondrial oxidative stress amplifier for cancer treatment.* Nat. Nanotechnol., 2019. **14**(4): p. 379.

162. Chaudhary, R.G., et al., *Graphene-based Materials and their Nanocomposites with Metal Oxides: Biosynthesis, Electrochemical, Photocatalytic and Antimicrobial Applications*. Magnetic Oxides and Composites II. Vol. 83. 2020. 79-116.

163. Rojas-Andrade, M.D., et al., *Antimicrobial activity of graphene oxide quantum dots: impacts of chemical reduction.* Nanoscale Adv., 2020. **2**(3): p. 1074-1083.

164. Riener, C.K., G. Kada, and H.J. Gruber, *Quick measurement of protein sulfhydryls with Ellman's reagent and with 4, 4'-dithiodipyridine.* Anal. Bioanal. Chem., 2002. **373**(4): p. 266-276.

165. Van Meer, G., D.R. Voelker, and G.W. Feigenson, *Membrane lipids: where they are and how they behave.* Nat. Rev. Mol. Cell Biol., 2008. **9**(2): p. 112-124.

166. El-Beltagi, H.S. and H.I. Mohamed, *Reactive Oxygen Species, Lipid Peroxidation and Antioxidative Defense Mechanism.* Not. Bot. Horti. Agrobo., 2013. **41**(1): p. 44-57.

167. Niki, E., et al., *Lipid peroxidation: Mechanisms, inhibition, and biological effects.* Biochem Bioph Res Co, 2005. **338**(1): p. 668-676.

168. Svingen, B.A., et al., *MECHANISM OF NADPH-DEPENDENT LIPID PEROXIDATION - PROPAGATION OF LIPID PEROXIDATION.* J. Biol. Chem., 1979. **254**(13): p. 5892-5899.

169. Cabiscol Català, E., J. Tamarit Sumalla, and J. Ros Salvador, *Oxidative stress in bacteria and protein damage by reactive oxygen species.* Int. J. Microbiol., 2000. **3**(1): p. 3-8.

170. Grune, T., et al., *Selective degradation of oxidatively modified protein substrates by the proteasome.* Biochem Bioph Res Co, 2003. **305**(3): p. 709-718.

171. Tansey, J.T., *Biochemistry*. 2020, John Wiley & Sons,: Hoboken, NJ. p. 1 online resource.

172. Yamaza, T., et al., *Oxidative stress-induced DNA damage in the synovial cells of the temporomandibular joint in the rat.* Journal of Dental Research, 2004. **83**(8): p. 619-624.

173. Limoli, C.L., et al., *Attenuation of radiation-induced genomic instability by free radical scavengers and cellular proliferation.* Free Radical Biology and Medicine, 2001. **31**(1): p. 10-19.

174. Cadet, J. and J.R. Wagner, *DNA base damage by reactive oxygen species, oxidizing agents, and UV radiation.* Cold Spring Harb. Perspect. Biol., 2013. **5**(2): p. a012559.

175. Badouard, C., et al., *Detection of chlorinated DNA and RNA nucleosides by HPLC coupled to tandem mass spectrometry as potential biomarkers of inflammation.* J. Chromatogr. B. J. Chromatogr. B., 2005. **827**(1): p. 26-31.

176. Cotillas, S., et al., *Use of carbon felt cathodes for the electrochemical reclamation of urban treated wastewaters.* Appl. Catal. B., 2015. **162**: p. 252-259.

177. Ghernaout, D., M. Aichouni, and M. Touahmia, *Mechanistic insight into disinfection by electrocoagulation-A review.* Desalin. Water Treat., 2019. **141**: p. 68-81.

178. Ghernaout, D., et al., *Application of electrocoagulation in Escherichia coli culture and two surface waters.* Desalination, 2008. **219**(1-3): p. 118-125.

179. Ghernaout, D. and B. Ghernaout, *From chemical disinfection to electrodisinfection: The obligatory itinerary?* Desalin. Water Treat., 2010. **16**(1-3): p. 156-175.

180. Hakizimana, J.N., et al., *Hybrid electrocoagulation/electroflotation/electrodisinfection process as a pretreatment for seawater desalination.* Chem. Eng. Sci., 2017. **170**: p. 530-541.

181. La Motta, E.J., et al., *Field Testing of a Small-Scale Continuous-Flow Wastewater Electrodisinfection Unit Using Direct Current.* J. Environ. Eng., 2018. **144**(1): p. 04017090.

182. Llanos, J., et al., *Conductive diamond sono-electrochemical disinfection (CDSED) for municipal wastewater reclamation.* Ultrason. Sonochem., 2015. **22**: p. 493-498.

183. Llanos, J., et al., *Effect of bipolar electrode material on the reclamation of urban wastewater by an integrated electrodisinfection/electrocoagulation process.* Water Res., 2014. **53**: p. 329-338.

184. Mook, W.T., M.K. Aroua, and G. Issabayeva, *Prospective applications of renewable energy based electrochemical systems in wastewater treatment: A review.* Renew. Sustain. Energy Rev., 2014. **38**: p. 36-46.

185. Rahmani, A.R., et al., *Electrodisinfection of bacteria-laden in surface water using modified Ti electrode by antimony-and nickel-doped tin oxide composite.* Chemosphere, 2021. **263**: p. 127761.

186. Sanchez, L. and M.A.L. Lit, *Ultrasound-Assisted Electrodisinfection Process for the Inactivation of Escherichia coli Biotech 1640 in Selected Crops.* Philipp. J. Crop Sci., 2018. **43**(2): p. 20-26.

187. Simas, A., et al., *Electrodisinfection of real swine wastewater for water reuse.* Environ. Chem. Lett., 2019. **17**(1): p. 495-499.

188. Chen, L., et al., *Removal of Intracellular and Extracellular Antibiotic Resistance Genes in Municipal Wastewater Effluent by Electrocoagulation.* Environ. Eng. Sci., 2020. **37**(12): p. 783-789.

189. Cotillas, S., et al., *Electrocoagulation-UV Irradiation Process for Urban Wastewater Reuse*, in *10th Esee: European Symposium on Electrochemical Engineering*, S. Palmas, M. Mascia, and A. Vacca, Editors. 2014. p. 133-138.

190. Cotillas, S., et al., *Coupling UV irradiation and electrocoagulation for reclamation of urban wastewater.* Electrochim. Acta, 2014. **140**: p. 396-403.

191. Ding, J., et al., *Electrochemical treatment of bio-treated landfill leachate: Influence of electrode arrangement, potential, and characteristics.* Chem. Eng. J., 2018. **344**: p. 34-41.

192. Ding, J., et al., *Electrochemical disinfection and removal of ammonia nitrogen for the reclamation of wastewater treatment plant effluent.* Environ. Sci. Pollut. Res., 2017. **24**(6): p. 5152-5158.

193. Ghernaout, D., M.W. Naceur, and A. Aouabed, *On the dependence of chlorine by-products generated species formation of the electrode material and applied charge during electrochemical water treatment.* Desalination, 2011. **270**(1-3): p. 9-22.

194. Isidro, J., et al., *Operating the CabECO (R) membrane electrolytic technology in continuous mode for the direct disinfection of highly fecal-polluted water.* Sep. Purif. Technol., 2019. **208**: p. 110-115.

195. Cotillas, S., et al., *Scaling-up an integrated electrodisinfection-electrocoagulation process for wastewater reclamation.* Chem. Eng. J., 2020. **380**: p. 122415.

196. Qi, X., et al., *Synergetic antibacterial activity of reduced graphene oxide and boron doped diamond anode in three dimensional electrochemical oxidation system.* Sci. Rep., 2015. **5**(1): p. 10388.

197. Huang, X., et al., *Electrochemical disinfection of toilet wastewater using wastewater electrolysis cell.* Water Res., 2016. **92**: p. 164-172.

198. Ahmadi, A. and T. Wu, *Inactivation of E. coli using a novel TiO 2 nanotube electrode.* Environ. Sci. Water Res. Technol., 2017. **3**(3): p. 534-545.

199. Brillas, E., et al., *Electrochemical destruction of chlorophenoxy herbicides by anodic oxidation and electro-Fenton using a boron-doped diamond electrode.* Electrochimica Acta, 2004. **49**(25): p. 4487-4496.

200. Canizares, P., et al., *Electrochemical treatment of 4-nitrophenol-containing aqueous wastes using boron-doped diamond anodes.* Ind. Eng. Chem. Res., 2004. **43**(9): p. 1944-1951.

201. Ekimov, E.A., et al., *Superconductivity in diamond.* Nature, 2004. **428**(6982): p. 542-545.

202. Suffredini, H.B., et al., *Enhanced electrochemical response of boron-doped diamond electrodes brought on by a cathodic surface pre-treatment.* Electrochimica Acta, 2004. **49**(22-23): p. 4021-4026.

203. Cotillas, S., et al., *Optimization of an integrated electrodisinfection/electrocoagulation process with Al bipolar electrodes for urban wastewater reclamation.* Water Res., 2013. **47**(5): p. 1741-1750.

204. Macpherson, J.V., *A practical guide to using boron doped diamond in electrochemical research.* Phys. Chem. Chem. Phys., 2015. **17**(5): p. 2935-2949.

205. Thostenson, J.O., et al., *Enhanced H2O2 production at reductive potentials from oxidized boron-doped ultrananocrystalline diamond electrodes.* ACS Appl. Mater. Interfaces, 2017. **9**(19): p. 16610-16619.

206. Sato, Y. and M. Kamo, *Synthesis of diamond from the vapour phase*. 1992: Academic Press: London, UK.

207. de Araújo, D.M., et al., *Electrochemical conversion/combustion of a model organic pollutant on BDD anode: Role of sp3/sp2 ratio.* Electrochem. commun., 2014. **47**: p. 37-40.

208. Williams, O.A., *Nanocrystalline diamond.* Diam. Relat. Mater., 2011. **20**(5-6): p. 621-640.

209. Wang, J., et al., *Surface functionalization of ultrananocrystalline diamond films by electrochemical reduction of aryldiazonium salts.* Langmuir, 2004. **20**(26): p. 11450-11456.

210. Thostenson, J.O., et al., *Improved blackwater disinfection using potentiodynamic methods with oxidized boron-doped diamond electrodes.* Water Res., 2018. **140**: p. 191-199.

211. Jiang, K., et al., *Highly selective oxygen reduction to hydrogen peroxide on transition metal single atom coordination.* Nat. Commun., 2019. **10**(1): p. 3997.

212. Wang, Y.X., et al., *Advanced Electrocatalysts with Single-Metal-Atom Active Sites.* Chem. Rev., 2020. **120**(21): p. 12217-12314.

213. Peng, Y., B.Z. Lu, and S.W. Chen, *Carbon-Supported Single Atom Catalysts for Electrochemical Energy Conversion and Storage.* J. Adv. Mater., 2018. **30**(48): p. 1801995.

214. Toze, S., *PCR and the detection of microbial pathogens in water and wastewater.* Water Res., 1999. **33**(17): p. 3545-3556.

215. Steele, M. and J. Odumeru, *Irrigation water as source of foodborne pathogens on fruit and vegetables.* J. Food Prot., 2004. **67**(12): p. 2839-2849.

216. Johnson, P.T.J. and S.H. Paull, *The ecology and emergence of diseases in fresh waters.* Freshw. Biol., 2011. **56**(4): p. 638-657.

217. Guzman, C., et al., *Occurrence and levels of indicators and selected pathogens in different sludges and biosolids.* J. Appl. Microbiol., 2007. **103**(6): p. 2420-2429.

218. Armon, R., et al., *Surface and subsurface irrigation with effluents of different qualities and presence of Cryptosporidium oocysts in soil and on crops.* Water Sci. Technol., 2002. **46**(3): p. 115-122.

219. Abreu-Acosta, N. and L. Vera, *Occurrence and removal of parasites, enteric bacteria and faecal contamination indicators in wastewater natural reclamation systems in Tenerife-Canary Islands, Spain.* Ecol. Eng, 2011. **37**(3): p. 496-503.

220. Fong, T.T. and E.K. Lipp, *Enteric viruses of humans and animals in aquatic environments: Health risks, detection, and potential water quality assessment tools.* Microbiol. Mol. Biol. Rev., 2005. **69**(2): p. 357-+.

221. Hijnen, W.A.M., E.F. Beerendonk, and G.J. Medema, *Inactivation credit of UV radiation for viruses, bacteria and protozoan (oo)cysts in water: A review.* Water Res., 2006. **40**(1): p. 3-22.

222. Rojas-Andrade, M.D., et al., *Antibacterial mechanisms of graphene-based composite nanomaterials.* Nanoscale, 2017. **9**(3): p. 994-1006.

223. Planchon, M., et al., *Metabolomic and proteomic investigations of impacts of titanium dioxide nanoparticles on Escherichia coli.* PloS One, 2017. **12**(6): p. e0178437.

224. Ma, Q., et al., *Integrated Proteomic and Metabolomic Analysis of an Artificial Microbial Community for Two-Step Production of Vitamin C.* PloS One, 2011. **6**(10): p. e26108.

225. Chang, D.D., et al., *Proteomic and metabolomic analysis of the cellular biomarkers related to inhibitors tolerance in Zymomonas mobilis ZM4.* Biotechnol. Biofuels, 2018. **11**: p. 283.

## Chapter 5 Graphene Oxide Quantum Dot-Based Functional Nanomaterials for Effective Antimicrobial Applications

## 5.1 Abstract

Conventional β-lactam antibiotics are resisted by bacteria at an increasing rate, prompting studies into the development of alternate antibiotic agents. In this personal account, we summarize recent progress in the design and engineering of graphene oxide quantum dot-based nanomaterials as potent antimicrobial agents. Specifically, we examine the impacts of chemical reduction on the antimicrobial activity of graphene oxide quantum dots, and enhancement of the bactericidal performance by the formation of nanocomposites with metal oxide nanoparticles, within the context of photodynamic generation of reactive oxygen species. A perspective is also included where the promises and challenges are highlighted in the development of high-performance antimicrobial agents based on graphene derivatives.

## 5.2 Introduction

Antibiotic resistance is becoming increasingly common around the world and threatening the well-being of humanity.[1-4] In particular, β-lactam antibiotics are the most frequently prescribed antibiotic in hospital settings; however, bacteria are able to produce enzymes known as β-lactamases that result in bacterial resistance.[5] Significant research has therefore been dedicated to developing alternate antibiotic agents that can overcome the bacteria's resistance through unique bactericidal pathways. One such alternate route includes the use of graphene-based nanomaterials capable of inhibiting bacterial growth through mechanisms such as physical adsorption and confinement, disruption of cellular processes, and membrane damage through physical and chemical interactions. Furthermore, some forms of functionalized graphene have been shown to have semiconductor properties making these materials light sensitive and capable of photocatalyzing the formation of reactive oxygen species (ROS), such as superoxide ($O_2^-$), singlet oxygen ($O_2^{\bullet}$), hydroxyl radical ($^{\bullet}OH$), and hydrogen peroxide ($H_2O_2$),[6-8]

that are known to be potent antimicrobial reagents involving various destructive pathways, such as degradation of bacterial DNA and cell wall.[9] It is inherently difficult for bacteria to overcome such destructive mechanisms of attack and therefore less likely for the bacteria to resist ROS-generating nanomaterials.

Graphene-based nanomaterials represent a diverse class of carbon functional materials, including an exfoliated version of graphite called graphene, oxidized graphene called graphene oxide (GO), and a partially reduced form of GO called reduced graphene oxide (rGO).[10-17] These materials have been shown to be effective antimicrobial agents on their own, and the antimicrobial activity can be further enhanced when combined with other materials to form a composite, notably with metal nanoparticles, metal oxide nanoparticles, and more recently with atomically dispersed metal atoms.[18] By tailoring the synthesis methods of the graphene-based materials, one can control the size, shape, and degree of oxidation to enhance water solubility, bacterial membrane contact, semiconductor properties, and other important properties for maximal antimicrobial performance.[19, 20]

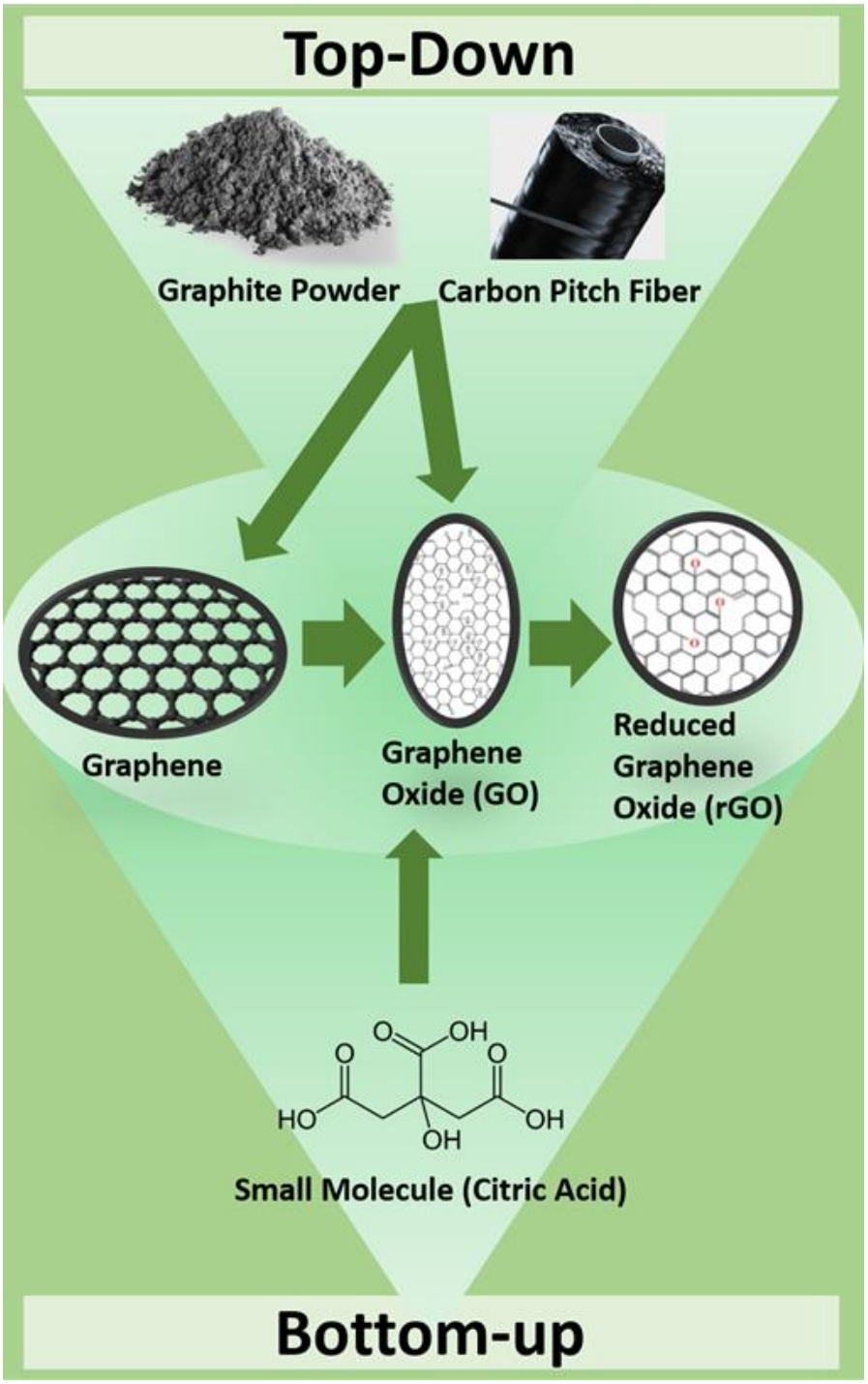


Figure 1. Schematic representation of graphene-based material preparation by top-down and bottom-up approaches.

Graphene-based nanomaterials can be prepared through numerous methods, which mostly fall into two categories, namely, top-down and bottom-up routes, as depicted in Figure 1. In the top-down synthesis of graphene-based nanomaterials, the starting material is usually some form of bulk graphite and then broken down through physical or chemical processes, where exfoliation ultimately results in the production of small graphitic carbon consisting of a varied number of graphene layers. One such top-down method is known as the Hummers' method,[21, 22] in which graphite flakes or pitch carbon fiber can be broken down through chemical oxidation by concentrated acids, resulting in the formation of GO. Depending on the degree of oxidation, controlled through reaction temperature, time, and acid concentration, one can obtain GO with sizes varied from several hundred nanometers down to the quantum dot regime of only a few nanometers in diameter.[14, 23-26] In the bottom-up route, the starting materials involve a small-molecule carbon source (along with any desired heteroatom dopant materials, such as nitrogen and sulfur), which can be polymerized through various methods involving reduction and condensation reactions. For instance, thermal treatment of citric acid or trisodium citrate at high temperatures in a closed autoclave can be used to produce GO. Under these reaction conditions, citric acid goes through multiple dehydration reactions, resulting in the formation of graphitic carbon nanomaterials with the size regulated by the reaction conditions.[13, 17, 27, 28]

Graphene-based composite materials have shown significant promise for antimicrobial applications. Previous reports include incorporation of graphene derivatives with metals, metal oxides, simple complexes, and other semiconducting photocatalysts.[19, 29, 30] One of the intriguing aspects of this approach is taking advantage of the semiconductor properties of small graphene derivatives through the creation of semiconductor heterojunctions. For example, we have recently reported on a graphene oxide quantum

dot (GOQD)/ZnO composite photocatalyst for bacterial control.[28] The formation of composite materials was shown to improve the dispersibility of ZnO in aqueous media and significantly increase the efficiency of ROS production, likely due to improved contact with the bacterial membrane and enhanced charge separation of the photoexcited electron-hole pairs.

In this personal account, we summarize recent progress in the use of GOQD-based functional nanomaterials for effective antimicrobial applications within the context of photodynamic manipulation. Synthesis of these materials is realized through a top-down or bottom-up approach (Figure 1). The structural characteristics of these materials are unraveled by a range of microscopic and spectroscopic measurements and correlated to the antimicrobial activity towards both Gram-positive and Gram-negative bacteria. Mechanistic insights are obtained by a careful comparison of the bactericidal performance in the dark and under photoirradiation.

### 5.3 Graphene Oxide Quantum Dots

Graphene-based materials have been under study for microbial control for more than a decade. In an early study,[31] the antimicrobial properties of graphene and GO were examined and compared toward both Gram-positive and Gram-negative strains of bacteria. Experimentally, GO was synthesized through a (top-down) modified Hummers' method using graphite powders as the starting materials. A graphene nanowall array was then grown onto a stainless-steel substrate by electrophoretic deposition. It was observed that membrane damage caused by the sharp edges of the GO nanosheets was the primary mechanism of bacterial control. This notion was further supported by the resistance of *Escherichia coli* (*E. coli*), a Gram-negative bacterial strain with a developed outer membrane, as compared to the Gram-positive strain of *Staphylococcus aureus* (*S. aureus*), which lacks the protective outer membrane.

This proposed mechanism was further built upon through the study of the antimicrobial activity of graphite, graphite oxide, GO, and rGO.[32] The interactions of these carbon materials with *E. coli* cells were investigated by scanning electron microscopic (SEM) studies and the material's ability to oxidize glutathione was quantitatively assessed — note that glutathione is a common redox mediator in bacterial cells. The conclusions from the previous report[31] were validated, as SEM images clearly showed cell membrane damage caused by the sharp edges of the GO nanosheets.

Oxidative stress may also play an important role, as GO can induce substantial glutathione oxidation, in comparison to other graphene derivatives, and glutathione deficiencies have been known to impact cell growth, due to unregulated potassium channels and sensitivity to methylglyoxal, a toxic byproduct of bacteria metabolism.[33] Notably, results from earlier studies have shown that a decreasing lateral size of GO prepared through a modified Hummers' method resulted in an increase of the antibacterial activity,[34, 35] as evidenced in a range of characterizations based on fluorescence microscopy, glutathione oxidation, and cell viability assays, where smaller GO was found to exhibit more oxidative stress toward *E. coli*. Results from these studies further solidify the importance of oxidative stress in the bactericidal action of graphene-based nanomaterials.

Such oxidative stress most likely arises from the rich oxygenated functional moieties on the GO surface, which can be readily manipulated by chemical reduction. In a recent study,[26] ultrasmall GO nanosheets, also known as GOQD,[23, 24, 36-38] were prepared by the modified Hummers' method using pitch carbon fibers as the starting materials, and the antimicrobial activity was examined and compared before and after chemical reduction by $NaBH_4$. Figure 2a depicts a representative transmission electron microscopic (TEM) image of the as-produced GOQD, which exhibited a diameter of 10

to 20 nm and clear lattice fringes, with an interplanar spacing of 0.263 nm that is consistent with that of the graphene (002) lattice. Topographic study based on atomic force microscopy (AFM) shows good dispersion of the GOQD without apparent agglomeration, most likely due to the abundant oxygenated moieties on the GOQD surface that rendered the GOQDs dispersible in water, and from the line scan, the height of the GOQDs was found to range from 0.5 to 2 nm, corresponding to 1 to 4 graphene layers. The morphology of the reduced form (rGOQD) was largely unchanged.[26]

Yet the optical and photoluminescence characteristics varied rather markedly after $NaBH_4$ reduction. From the UV-vis absorption spectra in Figure 2b, one can see that GOQD exhibited a major absorption peak at 230 nm, and three broad shoulders at 290, 360, and 460 nm (marked by asterisks) on an exponential decay profile. Note that the 230 nm peak is generally ascribed to the $\pi \rightarrow \pi^*$ transitions of $sp^2$ carbon, and the 460 nm one to the $n \rightarrow \pi^*$ transitions of C=O moieties.[39, 40] After $NaBH_4$ reduction, the 230 nm peak red-shifted and the 460 nm one disappeared, suggesting enlarged $sp^2$ carbon domains in rGOQD, most likely due to effective removal of oxygenated species. In fact, based on the Tauc plots derived from the UV-vis absorption profiles, the optical band gap can be found to decrease somewhat from 3.50 eV for GOQD to 3.15 eV for rGOQD. Consistent results were obtained in $^1H$ NMR measurements where signals of aromatic protons were found to intensify with rGOQD, as compared to that of GOQD.[26]

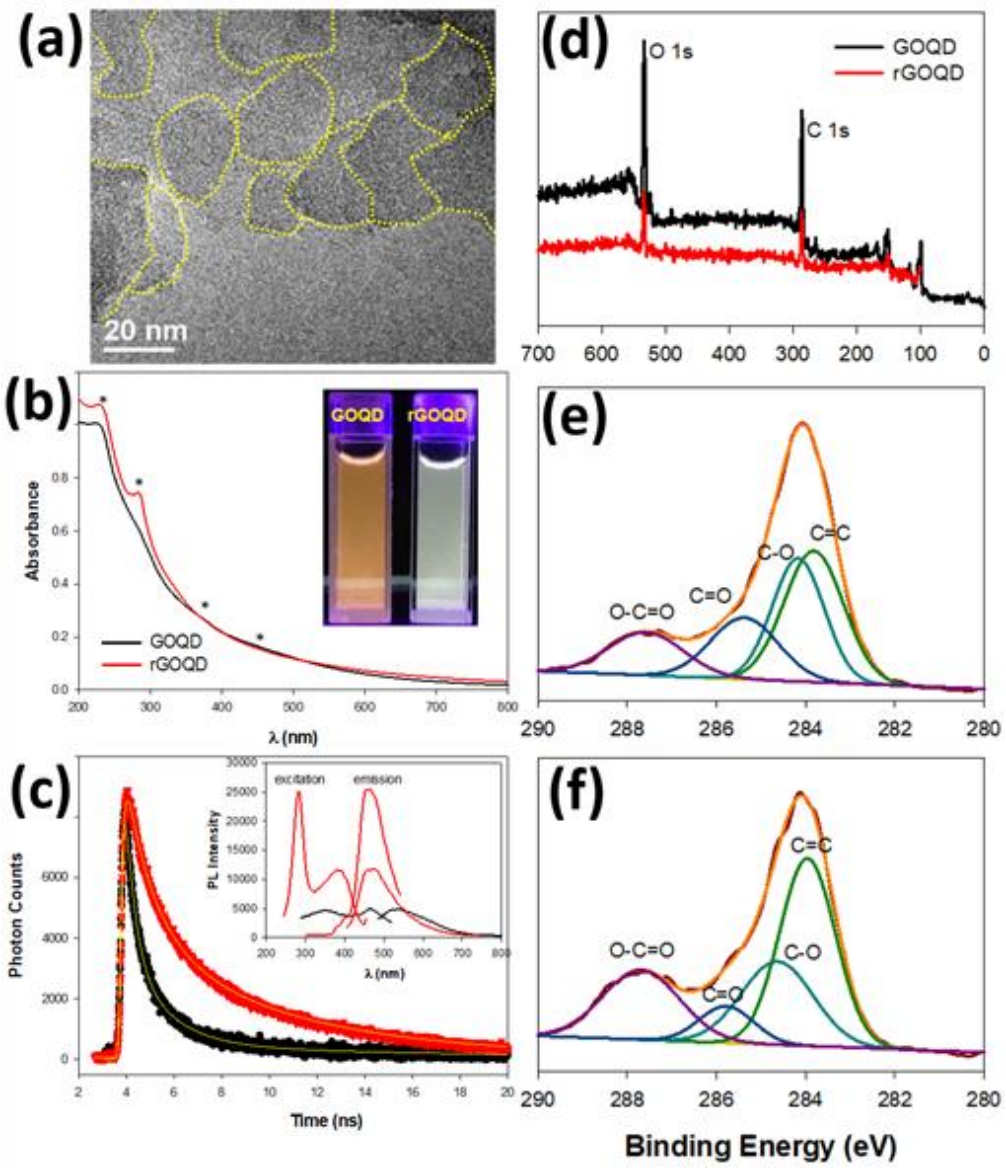


**Figure 2.** (a) TEM image of GOQD. Scale bar 20 nm. (b) UV-Vis spectra of GOQD (black) and rGOQD (red). Inset are the photographs of the two solutions upon irradiation at 365 nm. (c) Time-resolved photoluminescence (TRPL) emission spectra for GOQD (black) and rGOQD (red) with an excitation wavelength of 400 nm. Inset depicts the steady-state fluorescence spectra. Yellow lines depict exponential decay fittings to TRPL spectra. (d) X-ray Photoelectron Spectroscopy (XPS) survey spectra for GOQD (black)

and rGOQD (red). High resolution XPS spectra of the carbon 1s orbitals for (e) GOQD and (f) rGOQD. Reproduced with permission from ref. 27, copyright 2020, the authors.

The photoluminescence properties varied accordingly, as manifested in the photographs of the sample solutions under 365 nm photoirradiation, yellow-green for GOQD and blue-green for rGOQD (Figure 2b inset). In steady-state photoluminescence measurements (Figure 2c inset), GOQDs exhibited two excitation peaks ($\lambda_{ex}$) centered at 350 and 465 nm, very close to the absorption peak positions observed in UV-vis measurements (Figure 2b), and a corresponding emission peak ($\lambda_{em}$) at 535 nm. However, upon $NaBH_4$ chemical reduction, the excitation peak at 465 nm vanished, a new excitation peak appeared at 280 nm, and the emission band blue-shifted to 460 nm, with the (normalized) emission intensity more than doubled. Consistent behaviors were observed in time-resolved photoluminescence measurements (Figure 2c), where the emission lifetime of the rGOQD was estimated to be 1.73 ns, somewhat longer than that (1.05 ns) for GOQDs, in good accord with the removal of structural defects (trap states) upon $NaBH_4$ reduction.[26]

Such a structural evolution is indeed confirmed by X-ray photoelectron spectroscopy (XPS) measurements. From the survey spectra in Figure 2d, one can see that both the GOQD and rGOQD samples exhibited two main peaks at 284 eV for C 1s and 530 eV for O 1s electrons, and based on the integrated peak areas, the oxygen content of rGOQD diminished by more than 10%, as compared to that of GOQD, suggesting effective removal of oxygen species by $NaBH_4$ reduction. Deconvolution of the high-resolution C 1s spectra for GOQD (Figure 2e) and rGOQD (Figure 2f) further reveals the difference in oxygen functional groups within the carbon framework. Whereas four components can be resolved in both samples at 282.8, 284.2, 285.4, and 287.6 eV, corresponding to C=C, C-O, C=O, and O-C=O, respectively, the contents of the oxygenated species decrease rather

markedly, carbonyl species from 19.2% in GOQD to 8.3% in rGOQD, and C-O from 29.7% to 25.1%, and concurrently the fraction of $sp^2$ carbon increases from 36.2 for GOQD % to 44.1% for rGOQD.

The clear difference in the contents of oxygen functional groups between GOQD and rGOQD provided an excellent platform to examine how these oxygen moieties play a role in microbial inactivation. To quantify the antimicrobial properties of these materials a photodynamic experiment involving plate streaking was implemented. A typical procedure for this type of experiment is as follows: briefly, the material of interest is dissolved in a desired solvent, typically water or phosphate buffered saline (PBS), into which an amount of cultured bacteria is added and shaken to form a homogeneous solution. Use of a buffer solution is particularly critical when the material of interest has the ability to significantly alter the experimental pH conditions, as seen previously when GO containing acidic impurities was used.[41] The resulting solution is then irradiated at the desired photon energy for a specific time interval. At each timepoint a small aliquot is taken from the solution, serially diluted, and streaked onto an agar plate. The plates are then incubated typically at 37 °C for 16-24 h, depending on the microbe under study. The incubated plate is then taken, and individual colonies are counted and compared. Control plates are typically made to efficiently compare difference in colony formation. For example, the bar chart in Figure 3a demonstrates a clear difference in photoinactivation between GOQD and rGOQD, as compared to a control group with water alone.

The photodynamic experiment described above is useful to quantify antibacterial properties as a function of photoirradiation. Experimentally, each sample was exposed to light irradiation (400 nm) for 3 min and changes in cell viability were measured through colony counts. From the top panel of Figure 3a, one can see a ca. 60% loss of cell viability of *Staphylococcus epidermitis* (*S. epidermitis*) in the presence of GOQD upon

photoirradiation, in comparison to ca. 35% in the control, while 95% of the bacterial cells survive with rGOQD. Such a difference of the cell viability can also be readily visualized in the corresponding photographs of bacterial colonies in the bottom panel. It is likely that the rGOQD possesses surface functional groups with antioxidant nature resulting in improved cell viability under 400 nm light irradiation. The source of this antioxidant behavior is likely due to the increased $sp^2$ carbons in rGOQD, which can undergo hydroxyl addition in the presence of radical species.

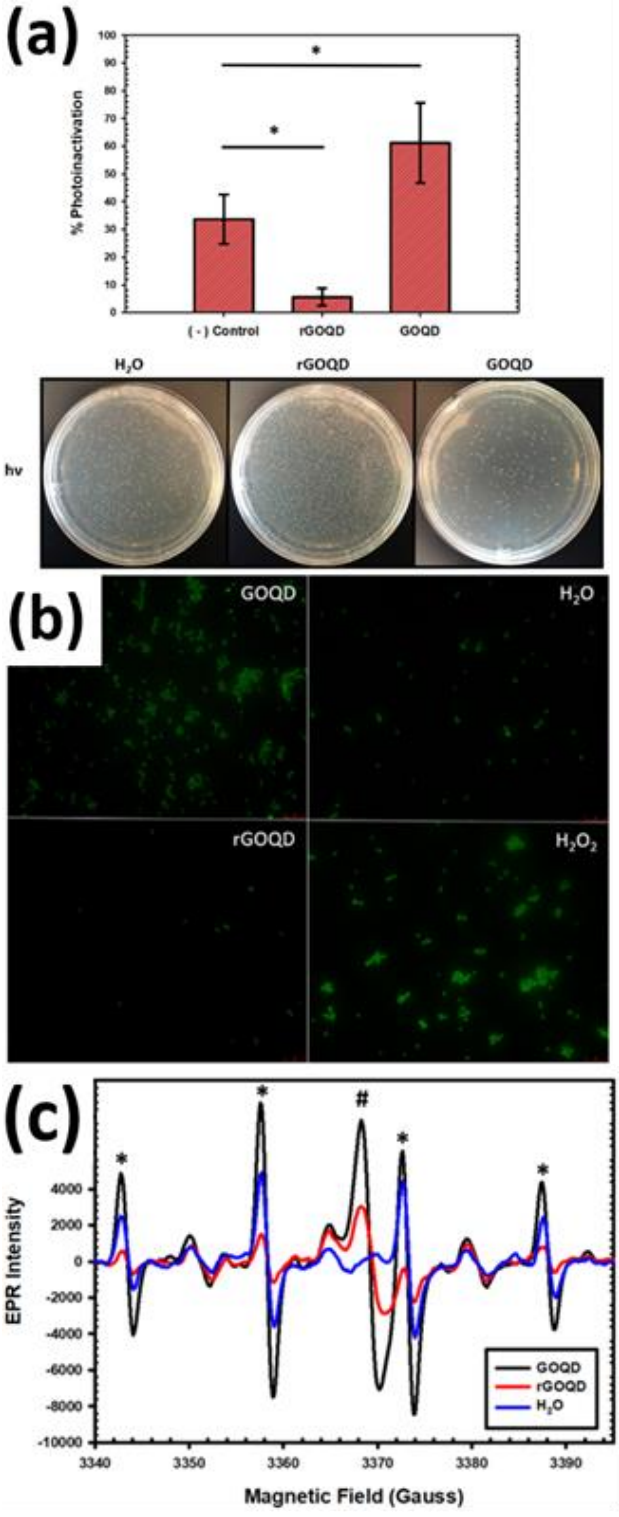


**Figure 3**. (a) Photodynamic experiment results depicting the photoinactivation % for GOQD and rGOQD toward *Staphylococcus Epidermitis*. (b) Fluorescence microscopy

micrographs imaging fluorescence of CellROX green. (c) EPR spectra of GOQD (black) and rGOQD (red) upon light irradiation (400 nm) for 1 minute in the presence of the spin-trapping reagent, DMPO. Reproduced with permission from ref. 27, copyright 2020, the authors.

Fluorescence microscopy studies, in conjunction with electron paramagnetic resonance (EPR) spectroscopy, indeed provide an adequate foundation to understand the mechanisms for ROS formation upon light irradiation. Figure 3b depicts fluorescence micrographs of CellROX green-stained *S. epidermitis* bacterial cells in the presence of GOQD (top-left panel), rGOQD (bottom-left panel), a hydrogen peroxide positive control (bottom-right panel), and water alone as a negative control (top-right panel). CellROX green is a dye molecule that binds to nucleic acids with a primary binding to DNA after oxidation. Upon oxidation and dye accumulation within the cell, CellROX green emissions can be observed at 525 nm with an excitation wavelength of 470 nm. The resulting fluorescence intensity can be normalized and compared between samples to quantify the degree of ROS production where an increased fluorescence intensity is correlated to an increased amount of ROS produced. From Figure 3b, one can see a 2-fold increase in CellROX green intensity for GOQD, as compared to that for rGOQD — the former is actually comparable to that with $H_2O_2$ whereas the latter is similar to that of $H_2O$. Such a clear increase in ROS production by GOQD can be correlated to the rich oxygenated species, as evidenced in XPS measurements (Figure 2d-f).

Consistent results were obtained in EPR measurements.[42] The studies described herein utilize a spin-trapping method where 5,5-dimethyl-1-pyrroline N-oxide (DMPO) is oxidized at the nitrone functional group by free radicals to form a radical adduct with a half-life ($\tau_{1/2}$) on the order of several minutes. This allows for reliable detection of free radicals formed by the photocatalyst of interest. Figure 3c depicts such spin-trapping

assays in which DMPO reacts with radicals formed by GOQD and rGOQD upon photoirradiation for 1 min, along with a control group containing water alone. The EPR spectra show a peak (marked by #) at 3369 G for GOQD and rGOQD, as compared to the water control, and the scaling factor (g) was estimated to be 2.0034 ± 0.0005 for GOQD and rGOQD, which lies between the literature values of 2.0023 for carbon-centered radicals and 2.004 for oxygen-centered radicals.[43, 44] From Figure 3c, one can see that GOQD is producing significantly more of these radicals than rGOQD with a peak height nearly double that of rGOQD. This can be ascribed to chemical reduction of GOQD to rGOQD that removes the oxygenated moieties necessary for such radical formation. Furthermore, formation of a quartet (depicted by asterisks) is seen with an intensity ratio of 1:2:2:1 and hyperfine couplings of $a_N = a_H = 14.9$ G, characteristic of hydroxyl radical adducts to DMPO. From the peak intensity of these quartets, one can see a 7-fold increase for GOQD, as compared to that of rGOQD, further confirming that radical formation was hindered after $NaBH_4$ reduction, likely due to the removal of oxygen moieties necessary for radical formation from the GOQD surface.

These results suggest that the antimicrobial activity of graphene derivatives may arise from multiple contributions. In addition to physical damage of the cell membranes, graphene-based nanomaterials can effectively inhibit bacterial cell growth by ROS production, which is closely related to the oxygen functional moieties. Further enhancement of the bactericidal performance can be achieved by the formation of nanocomposites with select metal oxide nanoparticles, as detailed below.

### 5.4 Graphene Oxide Quantum Dots/Metal Oxide Nanocomposites

Incorporation of graphene-based materials with metal or metal oxide nanostructures to produce nanocomposites has been rather extensively studied toward efficient antimicrobial activity.[16] The key to a successful composite material largely relies on (i)

a sufficient contact between the graphene-based material and metal (oxide) nanostructures and (ii) biocompatibility of the latter. Silver has been a common metal of choice. For instance, silver nanoparticles have been deposited on rGO and the resulting Ag/rGO nanocomposite was found to display improved antibacterial activity, as compared to silver alone; and the activity is even comparable to that of ampicillin, a penicillin antibiotic.[45] Efficient control of the growth of Gram-positive and Gram-negative bacterial strains has also been observed with Ag/GO nanocomposites.[46]

For metal oxide/graphene nanocomposites, the antimicrobial performance can be further enhanced by taking advantage of the photochemical activity of the semiconducting metal oxides. This is because upon photoirradiation of a semiconductor with photons of an appropriate energy, electrons may be excited from the valence band to the conduction band, and the ensuing separation of the photogenerated electron-hole pairs can be exploited for a range of reduction/oxidation reactions, in particular, ROS production for antimicrobial applications.[47-49] In addition, the incorporation of graphene derivatives helps improve the dispersibility, charge transfer, and other aspects pertinent to ROS production.[16] Zinc oxide (ZnO) is a commonly used photocatalyst with a direct bulk band gap of 3.3 eV at room temperature.[50] Beyond its unique band structure, ZnO is highly desirable for antimicrobial applications due to its low cost, high stability, and biocompatibility.[51] For example, ZnO nanoparticles have been deposited on rGO for water disinfection via the ROS mediated pathway.[52] Experimentally, two samples were prepared, one with ZnO nanoparticles in the range of 20 nm to 100 nm and the other from 50 nm to 500 nm. Through photodegradation of methylene blue and photoreduction of Cr(VI) to Cr(III), it was clear that a reduced ZnO nanoparticle size resulted in an improved photocatalytic performance, which was ascribed to improved ZnO/rGO interfacial contact and thus enhanced photodegradation efficiency.

As previously mentioned, use of GO over rGO may substantially improve the material's ability to form ROS under photoirradiation. To this end, we have recently constructed ZnO/GOQD nanocomposites utilizing a bottom-up procedure, where GOQDs were thermally derived from citric acid followed by the deposition of ZnO nanoparticles.[17] The ZnO nanoparticles, with the particle size ranging from 5 to 12 nm in diameter and an average diameter of 8.37 nm ± 2.72 nm (markedly smaller than those in the literature[52]), were successfully deposited onto the as-prepared GOQD surface. Figure 4a depicts the UV-vis absorption and photoluminescence emission spectra of the ZnO/GOQD nanocomposite, ZnO nanoparticles, and GOQDs alone.[17] One can see that despite similar UV-vis absorption profiles, the photoluminescence emission intensity varied markedly among the samples. Specifically, significant quenching can be observed with the ZnO/GOQD composite, as compared to the as-prepared GOQD alone. This suggests a reduced recombination of photogenerated electron-hole pairs upon ZnO deposition, likely due to charge transfer occurring from the GOQD to the ZnO at the ZnO/GOQD interface.

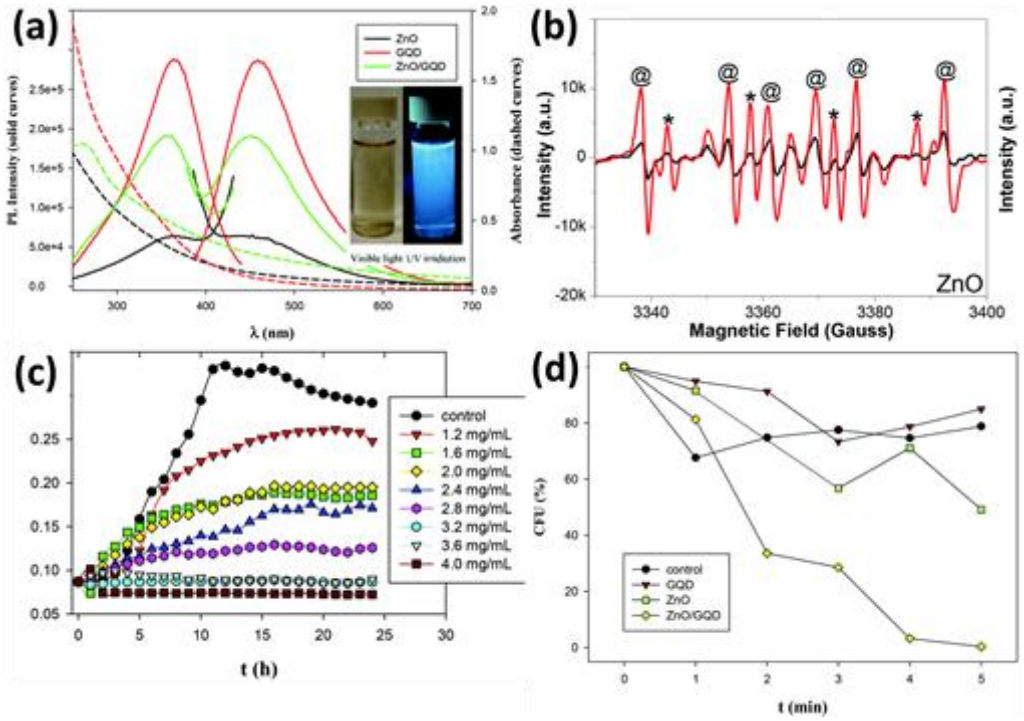


**Figure 4.** (a) UV-vis and steady state photoluminescence spectra for ZnO (black), GOQD (red), and ZnO/GOQD composite (green). Inset depicts the color of the ZnO/GOQD solution under UV (365 nm) and visible light photoirradiation. (b) EPR spectra for water control (black) and ZnO/GOQD nanocomposite (red) upon photoexcitation for 1 min. (c) Bacterial growth at varying concentrations of ZnO/GOQD composite from 0 mg/mL (black) to 4.0 mg/mL (red square) performed in the dark for 24 h. Measurements are taken from light absorption at 600 nm for each timepoint. (d) Results from photodynamic experiments plotting colony forming units (CFU) versus irradiation time (min). Reproduced with permission from ref. 17, copyright 2018, the Royal Society of Chemistry.

Indeed, the ZnO/GOQD composite possessed markedly enhanced ROS production. EPR measurements in Figure 4b show a typical quartet (marked by asterisks) that is indicative of the formation of hydroxyl radicals, as well as three doublets with hyperfine splitting of $a_H$ = 15.6 G and $a_N$ = 22.9 G, corresponding to $H^{\bullet}$ formation likely produced by ZnO

photoreduction of water. These EPR results help explain the significantly improved antibacterial properties of ZnO/GOQD shown in Figure 4d, which depicts results from a photodynamic assay of the colony forming units (CFU) under UV light irradiation. The ZnO/GOQD composite (yellow diamonds) displays complete bacterial inactivation after a photoirradiation period of only 5 min. This is a significant improvement from the control sample containing only *E. coli* and water (black circles), GOQD (red triangles), and ZnO (green squares). This clearly demonstrates the improved antibacterial properties of the composite made by the GOQD and ZnO. Note that the activity is also markedly better than those observed with similar composites but consisting of larger ZnO nanoparticles,[52] likely due to the combined contributions of enhanced dispersion and interfacial charge transfer. In contrast, microbial growth in the dark requires significantly more material to sufficiently stop bacterial growth (Figure 4c), suggesting photocatalyzed production of OH• to be the primary mechanism responsible for the antibacterial properties of the ZnO/GOQD composite.

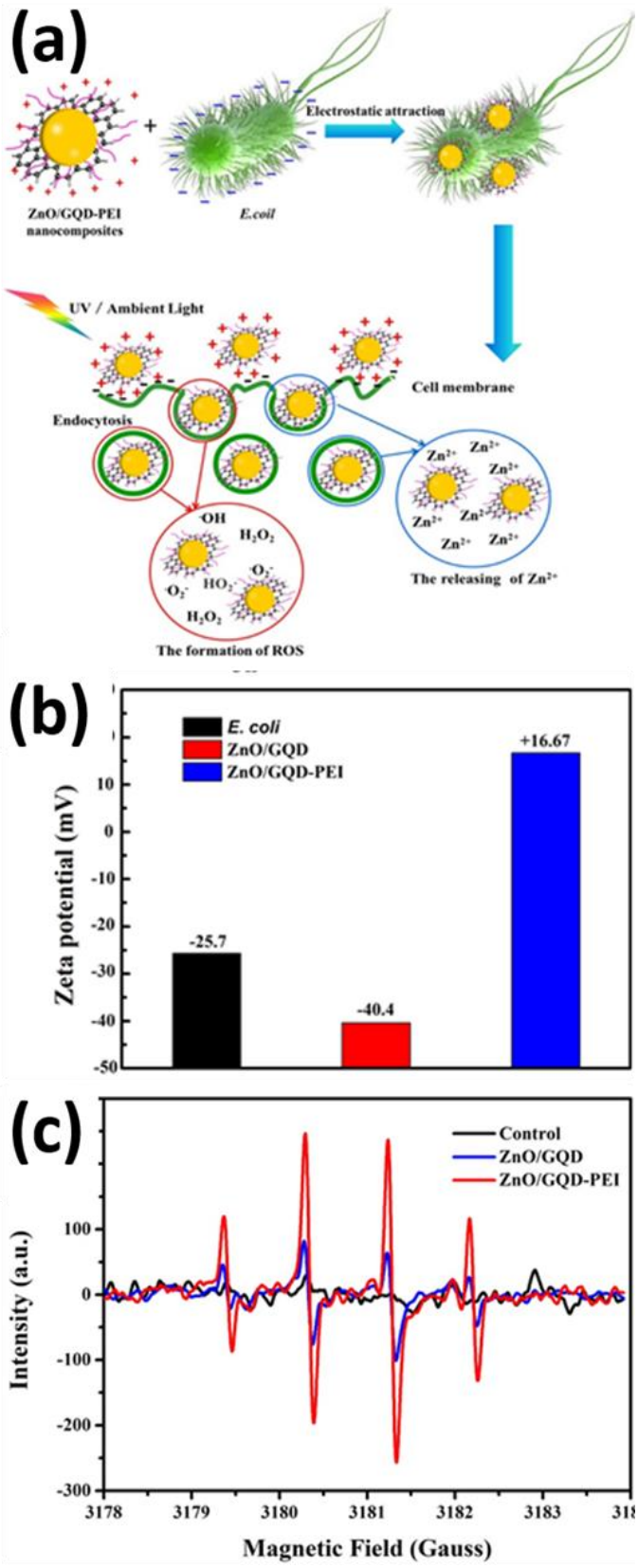
(a)
ZnO/GQD-PEI
nanocomposites
E.coil
Electrostatic attraction
UV / Ambient Light
Cell membrane
Endocytosis
The releasing of Zn2+
The formation of ROS
(b)
E. coli
ZnO/GQD
ZnO/GQD-PEI
Zeta potential (mV)
+16.67
-25.7
-40.4
(c)
Control
ZnO/GQD
ZnO/GQD-PEI
Intensity (a.u.)
Magnetic Field (Gauss)

**Figure 5.** Schematic representation of ZnO/GOQD-PEI antibacterial mechanism (a). (b) Measured ζ-potentials for E. coli (black), ZnO/GOQD (red), and ZnO/GOQD-PEI (blue). (c) EPR results in water with addition of DMPO spin-trapping reagent after light irradiation for 1 min. Reproduced with permission from re. 28, copyright 2019, the American Chemical Society.

It has long been argued that sufficient contact with the bacterial membrane is critical for efficient antibacterial performance.[19, 53, 54] Indeed, the importance of membrane contact with GO basal planes has been highlighted.[55] For example, bacterial membrane contact was enhanced with a ZnO/GO composite, leading to improved bactericidal activity, as compared to ZnO particles alone.[56] It was hypothesized that GO incorporation facilitated the dispersion of ZnO nanoparticles, slowed the dissolution of ZnO, and enabled intimate contact with *E. coli* cell membranes. This was evidenced by SEM imaging and solubilization measurements in which the prepared nanocomposites were dispersed in culture media for 24 h with periodic quantification of released Zn. This highlights the importance of nanocomposite dispersibility and bacterial membrane contact in the bactericidal efficiency.

One route toward increased dispersion, and hence improved antibacterial activity, involves the incorporation of hydrophilic polymers into the antimicrobial agents. In an early study,[57] GO was synthesized from graphite powders through a modified Hummers' method, and functionalized with a guanidine polymer (GP) by mixing GO, polyethylene glycol (PEG), and GP at elevated temperatures. The resulting GO-PEG-GP nanocomposite displayed structural characteristics similar to those of GO, as evidenced in FTIR, SEM, TGA (thermogravimetric analysis), and XRD (X-ray diffraction) measurements, but with significantly improved water dispersibility even in prolonged periods of time. The antimicrobial activity towards *E. coli* and *S. aureus* bacteria was

then evaluated by counting the CFUs after an incubation period. It was found that after 60 min the GO-PEG-GP composite led to complete bacterial inactivation for both the Gram-positive and Gram-negative strains, because the improved GO dispersion resulted in improved microbe contact. In another study,[58] $Cu_2O$/rGO nanocomposites were prepared in the presence of PEG, which exhibited enhanced dispersibility and stability in water and facilitated ROS production, leading to excellent antibacterial activity towrds *E. coli* and *S. aureus*, in comparison to $Cu_2O$ nanoparticles alone.

Bridging previous reports on nanoparticle dispersion and an understanding of bacteria surface charge, we demonstrated that the bacteria surface charge can indeed be exploited for further improvement of membrane contact and bacterial inactivation.[28] Experimentally, cationic polyethylenimine (PEI) was used as the capping polymer to further functionalize the ZnO/GOQD nanocomposites,[17] as schematically depicted in Figure 5a. The obtained ZnO/GOQD-PEI composite exhibited a positively charged surface, which was anticipated to possess electrostatic attraction toward the negatively charged surface of Gram-negative *E. coli* membranes. This was indeed evidenced in ζ-potential measurements (Figure 5b). One can see that incorporation of PEI shifted the ζ-potential from -40.4 mV for ZnO/GOQD to +16.67 mV for the ZnO/GOQD-PEI composite, and the ZnO/GOQD-PEI composites displayed significantly improved dispersibility for up to 48 h, as compared to ZnO/GOQD alone. This can be ascribed to increased hydrophilicity with the PEI coating.

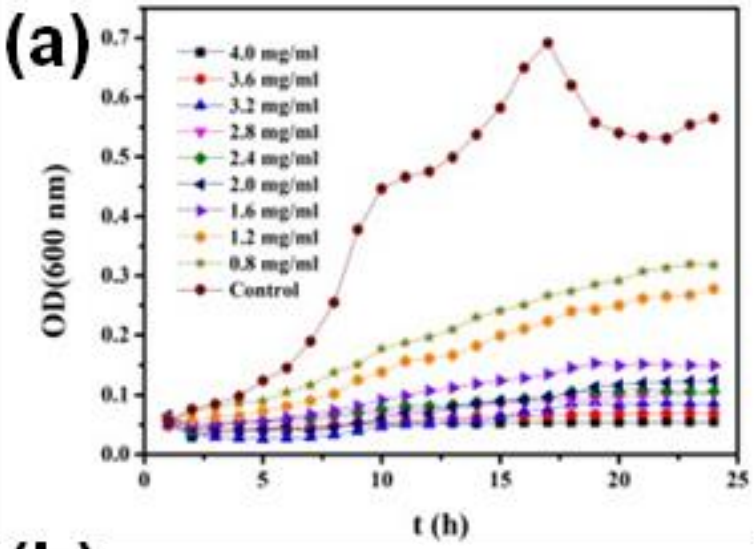
(a)
4.0 mg/ml
3.6 mg/ml
3.2 mg/ml
2.8 mg/ml
2.4 mg/ml
2.0 mg/ml
1.6 mg/ml
1.2 mg/ml
0.8 mg/ml
Control
OD(600 nm)
t (h)

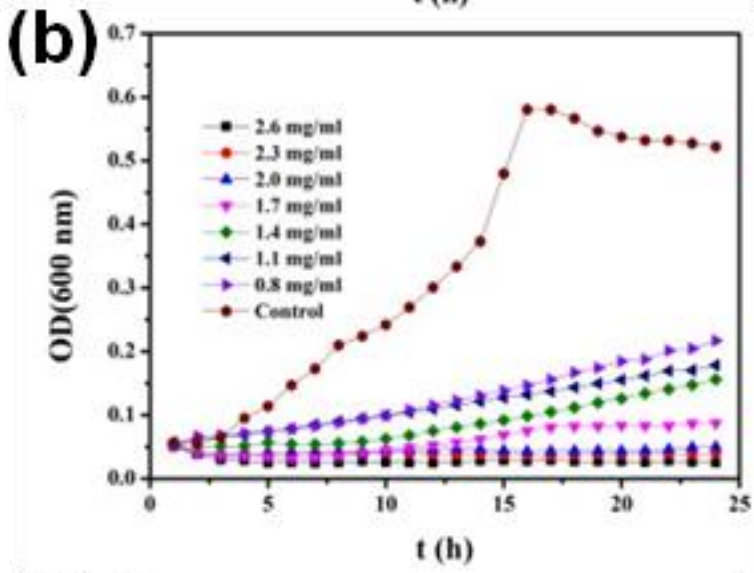
(b)
2.6 mg/ml
2.3 mg/ml
2.0 mg/ml
1.7 mg/ml
1.4 mg/ml
1.1 mg/ml
0.8 mg/ml
Control
OD(600 nm)
t (h)

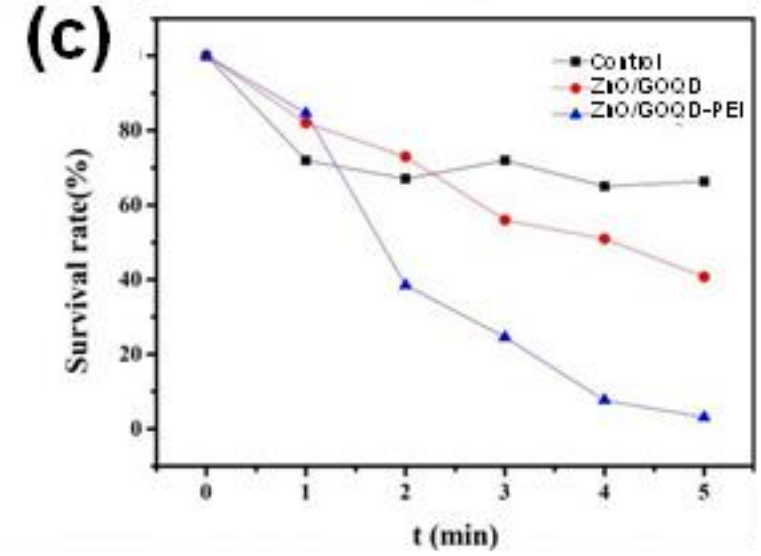
(c)
Control
ZnO/GOQD
ZnO/GOQD-PEI
Survival rate(%)
t (min)

**Figure 6**. *E. coli* growth assays performed under dark conditions for (a) ZnO/GOQD and (b) ZnO/GOQD-PEI over a 24 h period at varying nanoparticle concentrations ranging from 0.8 – 4.0 mg/mL. Photodynamic experiment performed under UV irradiation for ZnO/GOQD (red circles) and ZnO/GOQD-PEI (blue triangles) over a 5 min period. Reproduced with permission from ref. 28, copyright 2019, the American Chemical Society.

Similarity in morphology and atomic composition was further evidenced in XRD measurements, where both samples displayed closely similar patterns attributed to hexagonal wurtzite ZnO (JCPDS No. 36-1451) with six signature peaks occurring at $2\theta$ = 331.77°, 34.42°, 36.25°, 47.54°, 56.60°, and 62.86°. Furthermore, PEI incorporation improved the nanocomposite's ability to form ROS as manifested in EPR measurements. Figure 5c depicts the EPR data, again, utilizing DMPO as the spin trapping agent. One can see the formation of a quartet with the peak intensity ratio of 1:2:2:1 in the range of 3179 to 3183 G for both ZnO/GOQD and ZnO/GOQD-PEI samples, as compared to the control group containing water and DMPO alone. This is the clear signature of hydroxyl radical formation upon light irradiation. Further comparing the quartet peak intensity between both samples, a 3-fold increase in ROS generation can be observed for ZnO/GOQD-PEI, as compared to ZnO/GOQD.

The antibacterial activity of the two samples was then carried out in both dark and light conditions. Figure 6 depicts the growth of *E. coli* cells in the dark in the presence of (a) ZnO/GOQD and (b) ZnO/GOQD-PEI. From these spectra, a minimum inhibitory concentration (MIC) can be estimated for each sample, 4.0 mg/mL for ZnO/GOQD, and 2.7 mg/mL for ZnO/GOQD-PEI. This suggests an improved antibacterial control with the incorporation of PEI, possibly due to the increased dispersion of particles as evidenced above. Next, the antibacterial activity under photoirradiation was characterized, with

results presented in Figure 6c. Based on the results from the dark conditions, the nanocomposite concentration was set at 2.0 mg/mL for all photodynamic experiments, below the MIC found for both samples. From Figure 6c, both ZnO/GOQD and ZnO/GOQD-PEI can be observed to exhibit apparent bactericidal activity, as compared to the control, and most notably, the performance was markedly enhanced with ZnO/GOQD-PEI, as compared to ZnO/GOQD. In fact, complete bacterial inactivation was achieved at an irradiation time of 5 min for ZnO/GOQD-PEI. The improved antibacterial activity under UV irradiation can be attributed to the electrostatically enhanced contact between the nanocomposite and bacterial cells which led to improved bacterial decomposition by $Zn^{2+}$ dissolution and ROS degradation.

### 5.5 Summaries and Perspectives

The antimicrobial activity of graphene derivatives can arise from multiple mechanisms of actions, such as membrane damage by the sharp edges of the graphene nanosheets, nutrient deprivation of the bacterial cells due to graphene encapsulation, as well as ROS production facilitated by the rich oxygen moieties within the graphene framework. Thus, one can envision that chemical reduction/oxidation can be exploited as a facile strategy to manipulate the surface functional groups and hence the bactericidal performance. Further enhancement of the antimicrobial activity can be achieved by the formation of nanocomposites with select metal oxide nanoparticles by taking advantage of the unique photocatalytic activity. Notably, incorporation of graphene derivatives to the composite system not only helps improve the dispersibility and stability of the nanocomposite in water, but also facilitate ROS generation through interfacial charge transfer. Additionally, the composite's surface charge can be exploited to increase electrostatic attraction between the nanocomposite and bacterial membrane resulting in improved interfacial contact and delivery of photocatalyzed ROS.

Despite substantial progress in recent research, several challenges remain. First, it remains challenging, and yet particularly important, to precisely control the GOQD size, surface morphologies, and oxygen functionalization, which has been known to affect ROS production and oxidative stress. To this end, new synthetic chemistry needs to be developed for the ready control of the GOQD dimensions and structures, as well as the specific oxygenated functional moieties. Second, there are many factors that can contribute to the overall antimicrobial activity of these materials. To parse the contributions from each of these factors and develop a holistic interpretation of the antibacterial mechanism of the material, analysis in real time (in vivo) will be needed to deconvolute the antimicrobial activity occurring on different time scales. For example, ROS related bacterial death occurs at a much shorter time scale (typically within min), as compared to bacterial growth dynamics that occur throughout several hours. Finally, a multidisciplinary approach must be taken to unravel the biological origin of bacterial cell death. There are numerous biological assays that have the potential to significantly improve our understanding of the bacteria-graphene interactions and the impacts on important biochemical processes within the bacterial cell. For example, metabolite screening may be used to quantify changes in microbial metabolism in the presence of ROS generating materials, which has the potential to provide substantial insights into the mechanism of action for graphene-based materials as well as many other prospective antimicrobial nanomaterials.[59, 60] Research along these lines is ongoing.

## 5.6 References


1. Zheng, K.Y., et al., *Antimicrobial silver nanomaterials.* Coordination Chemistry Reviews, 2018. **357**: p. 1-17.
2. Piddock, L.J.V., *The crisis of no new antibiotics—what is the way forward?* The Lancet Infectious Diseases, 2012. **12**(3): p. 249-253.

3. Klein, E.Y., et al., *Global increase and geographic convergence in antibiotic consumption between 2000 and 2015.* Proceedings of the National Academy of Sciences of the United States of America, 2018. **115**(15): p. E3463-E3470.

4. Partridge, S.R., et al., *Mobile Genetic Elements Associated with Antimicrobial Resistance.* Clinical Microbiology Reviews, 2018. **31**(4).

5. Bush, K. and P.A. Bradford, *Interplay between β-lactamases and new β-lactamase inhibitors.* Nature Reviews Microbiology, 2019: p. 1.

6. Kumar, R., et al., *Antimicrobial properties of ZnO nanomaterials: A review.* Ceramics International, 2017. **43**(5): p. 3940-3961.

7. Qi, K.Z., et al., *Review on the improvement of the photocatalytic and antibacterial activities of ZnO.* Journal of Alloys and Compounds, 2017. **727**: p. 792-820.

8. Nosaka, Y. and A.Y. Nosaka, *Generation and Detection of Reactive Oxygen Species in Photocatalysis.* Chemical Reviews, 2017. **117**(17): p. 11302-11336.

9. Dwyer, D.J., M.A. Kohanski, and J.J. Collins, *Role of reactive oxygen species in antibiotic action and resistance.* Current Opinion in Microbiology, 2009. **12**(5): p. 482-489.

10. He, T., et al., *Nanocomposites Based on Ruthenium Nanoparticles Supported on Cobalt and Nitrogen-Codoped Graphene Nanosheets as Bifunctional Catalysts for Electrochemical Water Splitting.* ACS applied materials & interfaces, 2019. **11**(50): p. 46912-46919.

11. Yang, W., et al., *Graphene oxide-supported zinc cobalt oxides as effective cathode catalysts for microbial fuel cell: High catalytic activity and inhibition of biofilm formation.* Nano Energy, 2019. **57**: p. 811-819.

12. Wang, N., et al., *Cage Breaking of C60 Into Photoluminescent Graphene Oxide Quantum Dots: An Efficient Peroxidase Mimic.* physica status solidi (b), 2018. **255**(4): p. 1700535.

13. Chen, L., et al., *Platinum nanoparticles encapsulated in nitrogen-doped graphene quantum dots: Enhanced electrocatalytic reduction of oxygen by nitrogen dopants.* International Journal of Hydrogen Energy, 2017. **42**(49): p. 29192-29200.

14. Deming, C.P., et al., *Oxygen electroreduction catalyzed by palladium nanoparticles supported on nitrogen-doped graphene quantum dots: impacts of nitrogen dopants.* ACS Sustainable Chemistry & Engineering, 2016. **4**(12): p. 6580-6589.

15. Lu, B., et al., *Ruthenium atomically dispersed in carbon outperforms platinum toward hydrogen evolution in alkaline media.* Nature Communications, 2019. **10**(1): p. 631.

16. Rojas-Andrade, M.D., et al., *Antibacterial mechanisms of graphene-based composite nanomaterials.* Nanoscale, 2017. **9**(3): p. 994-1006.

17. Liu, J., et al., *Photo-enhanced antibacterial activity of ZnO/graphene quantum dot nanocomposites.* Nanoscale, 2018. **10**(1): p. 158-166.

18. Szunerits, S. and R. Boukherroub, *Antibacterial activity of graphene-based materials.* Journal of Materials Chemistry B, 2016. **4**(43): p. 6892-6912.

19. Wang, H., et al., *Direct and continuous strain control of catalysts with tunable battery electrode materials.* Science, 2016. **354**(6315): p. 1031-1036.

20. Zuo, P.L., et al., *A review on syntheses, properties, characterization and bioanalytical applications of fluorescent carbon dots.* Microchimica Acta, 2016. **183**(2): p. 519-542.

21. Hummers, W.S. and R.E. Offeman, *Preparation of Graphitic Oxide.* Journal of the American Chemical Society, 1958. **80**(6): p. 1339-1339.

22. Rajapaksha, P., et al., *Antibacterial Properties of Graphene Oxide–Copper Oxide Nanoparticle Nanocomposites.* ACS Applied Bio Materials, 2019. **2**(12): p. 5687-5696.

23. Fan, X., et al., *Chemical functionalization of graphene quantum dots.* Science of Advanced Materials, 2015. **7**(10): p. 1990-2010.

24. Deming, C.P., et al., *Graphene quantum dots-supported palladium nanoparticles for efficient electrocatalytic reduction of oxygen in alkaline media.* ACS Sustainable Chemistry & Engineering, 2015. **3**(12): p. 3315-3323.

25. Liu, K., Y. Song, and S. Chen, *Oxygen reduction catalyzed by nanocomposites based on graphene quantum dots-supported copper nanoparticles.* international journal of hydrogen energy, 2016. **41**(3): p. 1559-1567.

26. Rojas-Andrade, M.D., et al., *Antimicrobial activity of graphene oxide quantum dots: impacts of chemical reduction.* Nanoscale Advances, 2020.

27. Chen, L., et al., *Intervalence Charge Transfer of Ruthenium–Nitrogen Moieties Embedded within Nitrogen-Doped Graphene Quantum Dots.* The Journal of Physical Chemistry C, 2016. **120**(24): p. 13303-13309.

28. Liu, J., et al., *Antimicrobial Activity of Zinc Oxide–Graphene Quantum Dot Nanocomposites: Enhanced Adsorption on Bacterial Cells by Cationic Capping*

*Polymers.* ACS Sustainable Chemistry & Engineering, 2019. **7**(19): p. 16264-16273.

29. Perreault, F., A.F. de Faria, and M. Elimelech, *Environmental applications of graphene-based nanomaterials.* Chemical Society Reviews, 2015. **44**(16): p. 5861-5896.

30. Seabra, A.B., et al., *Nanotoxicity of Graphene and Graphene Oxide.* Chemical Research in Toxicology, 2014. **27**(2): p. 159-168.

31. Akhavan, O. and E. Ghaderi, *Toxicity of Graphene and Graphene Oxide Nanowalls Against Bacteria.* ACS Nano, 2010. **4**(10): p. 5731-5736.

32. Liu, S.B., et al., *Antibacterial Activity of Graphite, Graphite Oxide, Graphene Oxide, and Reduced Graphene Oxide: Membrane and Oxidative Stress.* Acs Nano, 2011. **5**(9): p. 6971-6980.

33. Masip, L., K. Veeravalli, and G. Georgiou, *The many faces of glutathione in bacteria.* Antioxidants & redox signaling, 2006. **8**(5-6): p. 753-762.

34. Liu, S., et al., *Lateral Dimension-Dependent Antibacterial Activity of Graphene Oxide Sheets.* Langmuir, 2012. **28**(33): p. 12364-12372.

35. Perreault, F., et al., *Antimicrobial Properties of Graphene Oxide Nanosheets: Why Size Matters.* ACS Nano, 2015. **9**(7): p. 7226-7236.

36. He, G., et al., *Oxygen Reduction Catalyzed by Platinum Nanoparticles Supported on Graphene Quantum Dots.* ACS Catalysis, 2013. **3**(5): p. 831-838.

37. Song, Y. and S. Chen, *Graphene Quantum-Dot-Supported Platinum Nanoparticles: Defect-Mediated Electrocatalytic Activity in Oxygen Reduction.* ACS Applied Materials & Interfaces, 2014. **6**(16): p. 14050-14060.

38. Hu, W.B., et al., *Graphene-Based Antibacterial Paper.* Acs Nano, 2010. **4**(7): p. 4317-4323.

39. Loh, K.P., et al., *Graphene oxide as a chemically tunable platform for optical applications.* Nature chemistry, 2010. **2**(12): p. 1015.

40. Shang, J., et al., *The origin of fluorescence from graphene oxide.* Scientific reports, 2012. **2**: p. 792.

41. Barbolina, I., et al., *Purity of graphene oxide determines its antibacterial activity.* 2D Materials, 2016. **3**(2): p. 025025.

42. Suzen, S., H. Gurer-Orhan, and L. Saso, *Detection of reactive oxygen and nitrogen species by electron paramagnetic resonance (EPR) technique.* Molecules, 2017. **22**(1): p. 181.

43. Green, U., et al., *Exploring the radical nature of a carbon surface by electron paramagnetic resonance and a calibrated gas flow.* JoVE (Journal of Visualized Experiments), 2014(86): p. e51548.

44. Tampieri, F., et al., *A comparative electron paramagnetic resonance study of expanded graphites and graphene.* Journal of Materials Chemistry C, 2014. **2**(38): p. 8105-8112.

45. Xu, W.-P., et al., *Facile synthesis of silver@ graphene oxide nanocomposites and their enhanced antibacterial properties.* Journal of Materials Chemistry, 2011. **21**(12): p. 4593-4597.

46. Tang, J., et al., *Graphene Oxide–Silver Nanocomposite As a Highly Effective Antibacterial Agent with Species-Specific Mechanisms.* ACS Applied Materials & Interfaces, 2013. **5**(9): p. 3867-3874.

47. Morrison, S. and T. Freund, *Chemical role of holes and electrons in ZnO photocatalysis.* The Journal of chemical physics, 1967. **47**(4): p. 1543-1551.

48. Sakthivel, S., et al., *Solar photocatalytic degradation of azo dye: comparison of photocatalytic efficiency of ZnO and TiO2.* Solar energy materials and solar cells, 2003. **77**(1): p. 65-82.

49. Chakrabarti, S. and B.K. Dutta, *Photocatalytic degradation of model textile dyes in wastewater using ZnO as semiconductor catalyst.* Journal of hazardous materials, 2004. **112**(3): p. 269-278.

50. Youn, C.J., et al., *Optical properties of Zn-terminated ZnO bulk.* Journal of Crystal Growth, 2004. **261**(4): p. 526-532.

51. Zhou, J., N.S. Xu, and Z.L. Wang, *Dissolving behavior and stability of ZnO wires in biofluids: a study on biodegradability and biocompatibility of ZnO nanostructures.* Advanced Materials, 2006. **18**(18): p. 2432-2435.

52. Zhang, Y., et al., *Size effect induced activity enhancement and anti-photocorrosion of reduced graphene oxide/ZnO composites for degradation of organic dyes and reduction of Cr(VI) in water.* Applied Catalysis B: Environmental, 2013. **140-141**: p. 598-607.

53. Foster, H.A., et al., *Photocatalytic disinfection using titanium dioxide: spectrum and mechanism of antimicrobial activity.* Applied Microbiology and Biotechnology, 2011. **90**(6): p. 1847-1868.

54. Sirelkhatim, A., et al., *Review on Zinc Oxide Nanoparticles: Antibacterial Activity and Toxicity Mechanism.* Nano-Micro Letters, 2015. **7**(3): p. 219-242.

55. Hui, L., et al., *Availability of the Basal Planes of Graphene Oxide Determines Whether It Is Antibacterial.* ACS Applied Materials & Interfaces, 2014. **6**(15): p. 13183-13190.

56. Wang, Y.-W., et al., *Superior Antibacterial Activity of Zinc Oxide/Graphene Oxide Composites Originating from High Zinc Concentration Localized around Bacteria.* ACS Applied Materials & Interfaces, 2014. **6**(4): p. 2791-2798.

57. Li, P., et al., *Developing of a novel antibacterial agent by functionalization of graphene oxide with guanidine polymer with enhanced antibacterial activity.* Applied Surface Science, 2015. **355**: p. 446-452.

58. Yang, Z., et al., *Long-term antibacterial stable reduced graphene oxide nanocomposites loaded with cuprous oxide nanoparticles.* Journal of Colloid and Interface Science, 2019. **533**: p. 13-23.

59. Lopatkin, A.J., et al., *Bacterial metabolic state more accurately predicts antibiotic lethality than growth rate.* Nature microbiology, 2019. **4**(12): p. 2109-2117.

60. Tao, Y., et al., *Metabolic-activity-based assessment of antimicrobial effects by D2O-labeled single-cell Raman microspectroscopy.* Analytical chemistry, 2017. **89**(7): p. 4108-4115.

## Chapter 6 Antibacterial Activity of Nitrogen-Doped Carbon Dots Enhanced by Atomic Dispersion of Copper

## 6.1 Abstract

Antibiotic resistance is an imminent threat to human health, requiring development of effective alternate antibacterial agents. One such alternative includes nanoparticle (photo)catalysts that are good at producing reactive oxygen species (ROS). Herein, we report the design and preparation of nitrogen-doped carbon dots functionalized with atomically dispersed copper centers by Cu-N coordination (Cu/NCD) that exhibit apparent antibacterial activity towards Gram-negative *Escherichia coli* (*E. coli*) under photoirradiation. The growth of *E. coli* cells is found to be markedly inhibited by Cu/NCD under 365 nm photoirradiation, whereas no apparent inhibition is observed in the dark or with the copper-free carbon dots alone. This is ascribed to the prolonged photoluminescence lifetime of Cu/NCD that facilitates the separation of photogenerated electron-hole pairs and the ROS formation. Addition of *tert*-butyl alcohol is found to completely diminish the antimicrobial activity, suggesting that hydroxyl radicals are responsible for the microbial death. Consistent results are obtained in fluorescence microscopic studies using CellROX$^{TM}$ green as the probe. Similar bactericidal behaviors were observed with Gram-positive *Staphylococcus epidermidis (S. epidermidis)*. The copper content within the carbon material is optimized at a low loading of 1.09 wt%, reducing the possibility of toxic copper ion leaching. Results from this study highlight the significance of carbon-based nanocomposites with isolated metal species as potent antimicrobial reagents.

## 6.2 Introduction

Antibiotic resistance is on the rise and considered one of the greatest health threats facing humanity.[1-4] β-lactam antibiotics are the most frequently prescribed antibiotics in hospital settings; however, this type of antibiotics is shown to become easily resisted by bacteria through bacterial enzymes known as β-lactamases.[5] Although researchers have

provided short-term mechanisms to overcome this type of antibacterial resistance, the use of such antibiotics is proving to be an uphill and losing battle.[5] Significant research has therefore been dedicated to developing alternate antibiotic agents that can overcome the bacteria's resistance through unique bactericidal pathways. One such alternate route includes the use of light-sensitive nanomaterials capable of producing destructive reactive oxygen species (ROS), such as superoxide ($O_2^-$), singlet oxygen ($O_2^{\bullet}$), hydroxyl radical ($^{\bullet}OH$), and hydrogen peroxide ($H_2O_2$).[6-8] The mechanism of attack involves various destructive pathways, such as degradation of bacterial DNA and bacterial cell wall.[9] It is inherently difficult for bacteria to overcome such destructive mechanisms of attack and therefore less likely for the bacteria to resist ROS-generating nanomaterials. Towards this end, graphene derivatives represent a unique functional nanomaterial.[10-17] In a recent study,[18] we examined and compared the bactericidal activity of graphene oxide quantum dots before and after chemical reduction, and found that the oxidized forms were preferred for improved antibacterial activity under UV photoirradiation. This was attributed to oxygenated structural defects within the graphene oxide quantum dots that led to the ready production of ROS under photo excitation.

Copper-based photocatalysts have also been rather extensively studied for their ability to produce ROS upon photoirradiation.[19-30] However, the materials used in these studies typically contain high levels of copper, which can cause leaching of copper ions and devastating biological effects including copper toxicity.[31] To facilitate ROS production and concurrently prevent uncontrolled ion leaching, metal loading should be minimized and stabilized but without compromising the antibacterial efficiency. One route to this end involves metal species atomically dispersed within a carbon-based support material. For example, Gong et al.[32] observed ROS production by atomically dispersed gold-carbon dots, and found that an optimal Au loading of 15.3 wt% resulted in nearly

complete glutathione degradation, owing to high Au atomic dispersion. When the Au loading was increased to 45.7 wt% and large Au nanoparticles were formed instead, glutathione degradation was found to actually decrease. The increased activity by the material containing single Au atoms was attributed to mitochondrial targeting, glutathione depletion, and ROS production within bacterial membranes. Such atomic dispersion of metals can be readily realized with nitrogen-doped carbon dots by, for instance, a facile wet impregnation procedure with the formation of metal-nitrogen coordination linkages.[33, 34] The surface enrichment of the active metal centers can lead to the effective production of ROS due to enhanced separation and migration of the photogenerated electron-hole pairs.[35-37] This unique feature may be exploited for the development of high-performance antimicrobial reagents, in comparison to the conventional homogeneous organometallic complexes. This is the primary motivation of the present work.

Herein, nitrogen-doped carbon dots with atomically dispersed copper (Cu/NCD) were prepared by a solid-state thermal route. The copper content was found to be around 1 wt% among all samples. Transmission electron microscopic (TEM) measurements suggest atomic dispersion of copper within the carbon matrix by the formation of Cu-N bonds, as manifested in X-ray photoelectron spectroscopic (XPS) measurements. Steady-state photoluminescence (SSPL) measurements showed that the emission was markedly quenched with the incorporation of copper into the carbon dots, consistent with the increased lifetime as observed in time-resolved photoluminescence (TRPL) measurements. The bactericidal activity of the obtained composites was then tested using Gram-negative *E. coli* as the initial illustrating example. It was found that the bacterial growth was apparently inhibited under 365 nm photoirradiation, whereas no inhibition was observed in the dark; and the inhibition activity increased with increasing $sp^2$ carbon

content in the sample, possibly due to improvement in electron-hole migration. Consistent results were obtained in scanning electron microscopic (SEM) measurements of the bacterial cell morphologies. In addition, the bactericidal activity was found to diminish markedly upon the addition of *tert*-butyl alcohol, suggesting that hydroxy radicals were responsible for the antimicrobial activity, which was further confirmed in fluorescence microscopic measurements using CellROX$^{TM}$ green as the probe. Similar bactericidal performance was observed with Gram-positive *S. epidermidis.*

## 6.3 Results and Discussion

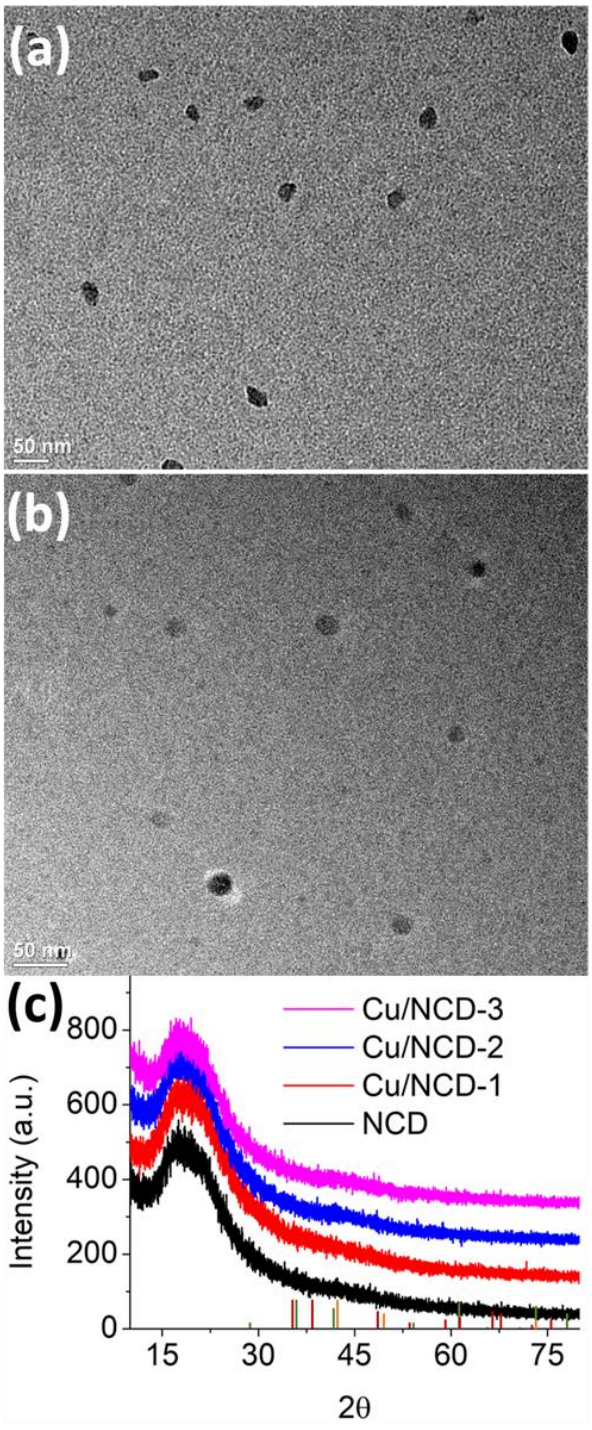


**Figure 1.** Representative TEM images of (a) NCD and (b) Cu/NCD-3. Scale bars are both 50 nm. (c) XRD patterns of (black) NCD, (red) Cu/NCD-1, (blue) Cu/NCD-2, and (magenta) Cu/NCD-3. Reference XRD patterns are provided along the X-axis for copper (orange, 00-001-1241), CuO (dark red, 00-002-1040), and $Cu_2O$ (green, 00-003-0892).

The successful production of carbon dots was first confirmed by TEM measurements. From Figure 1a, one can see that for the copper-free sample (NCD), carbon dots are very well dispersed without apparent agglomeration, with a roughly spherical shape, most likely due to the abundant oxygenated functional moieties on the carbon dot surface that rendered them soluble in water, as observed previously.[35, 36] Statistical analysis based on ca. 100 nanoparticles shows that the particle size falls mostly in the range of 12 to 37 nm, with an average of 22.8 ± 7.2 nm, as manifested in the core size histogram in Figure 2. For the copper-containing carbon dots, the morphologies remained virtually invariant, as evidenced with Cu/NCD-3 in Figure 1b, which shows a somewhat smaller average core size of 15.8 ± 3.0 nm. Notably, high-resolution TEM measurements of both samples show no well-defined lattice fringes (Figure 3) that can be ascribed to either carbon or copper (oxide), suggesting only short-range ordering of the carbon skeletons into which copper was most likely atomically dispersed. Consistent results are obtained in elemental mapping measurements (Figure 4).

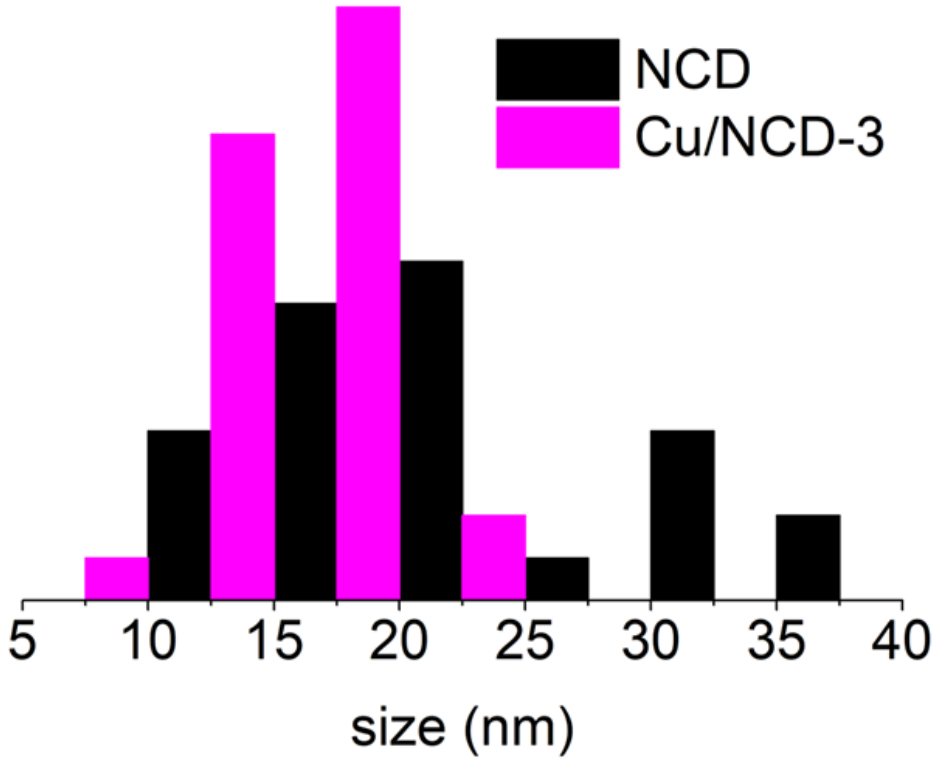


**Figure 2.** Core size histogram of the NCD (black) and Cu/NCD-3 (magenta) samples.

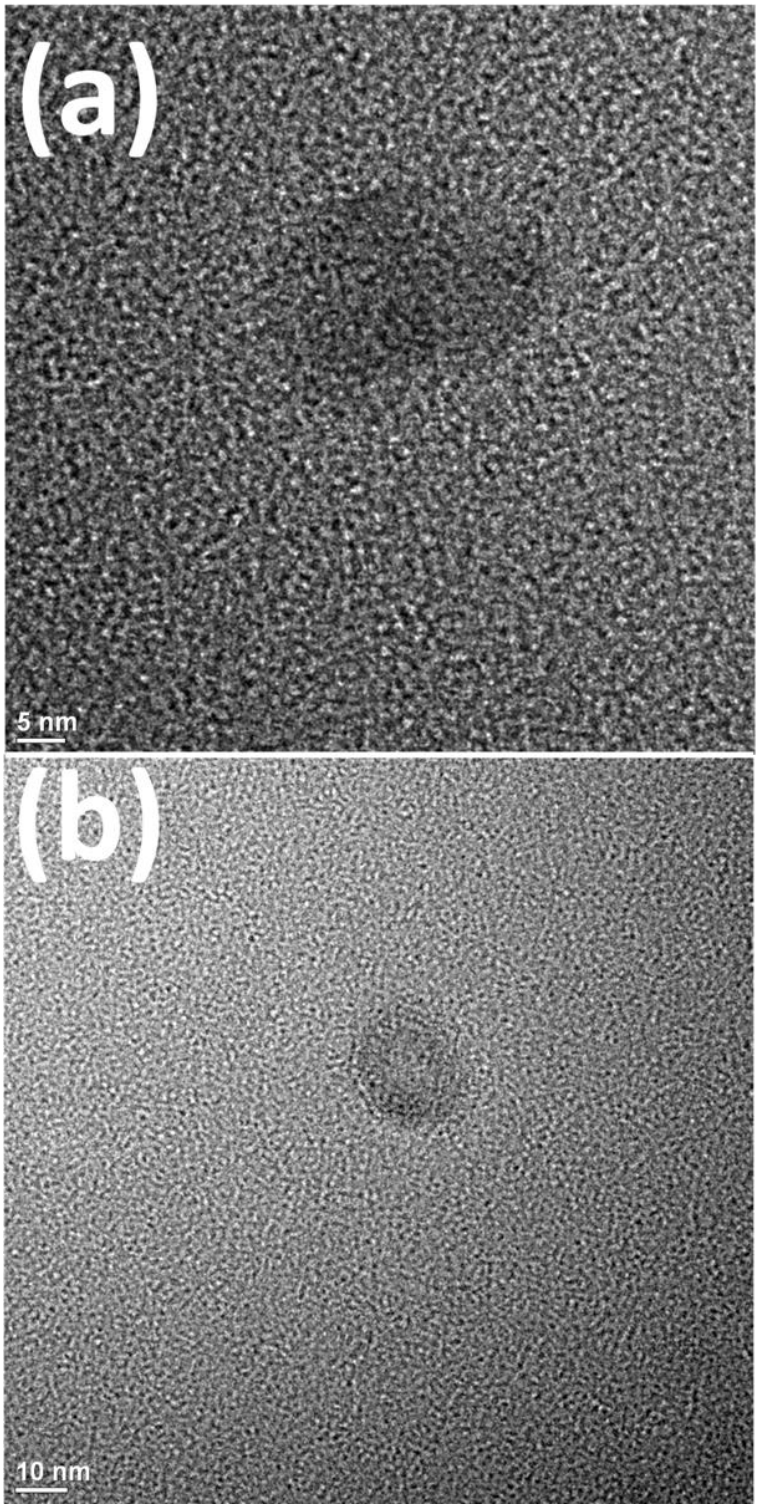


**Figure 3.** High-resolution TEM images of (a) NCD and (b) Cu/NCD-3. Scale bars are (a) 5 nm and (b) 10 nm.

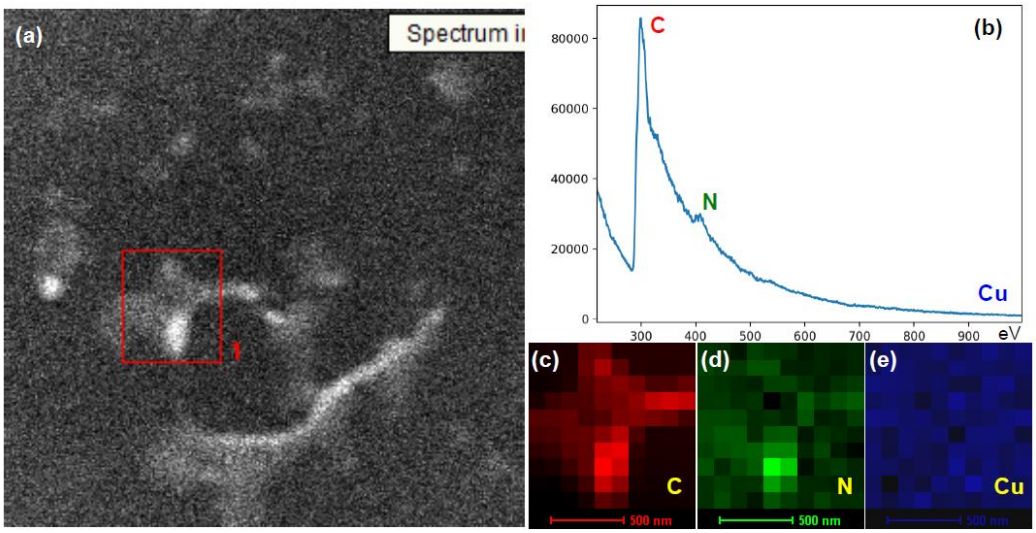


**Figure 4.** (a) STEM image of the Cu/NCD-3 sample, where the red box marks the region for elemental mapping analysis. (b) EELS spectrum acquired from the red box region in panel (a) with signals originating primarily from carbon and nitrogen and virtually no detectable copper signal (ca. 930 eV), as the Cu content (Table S2) is below the sensitivity limitation of STEM (ca. 1 at%). The fact that no particulate forms of Cu are detected is also consistent with the atomic dispersion of Cu in the carbon dots. The corresponding elemental maps are shown in (c) C, (d) N and (e) Cu.

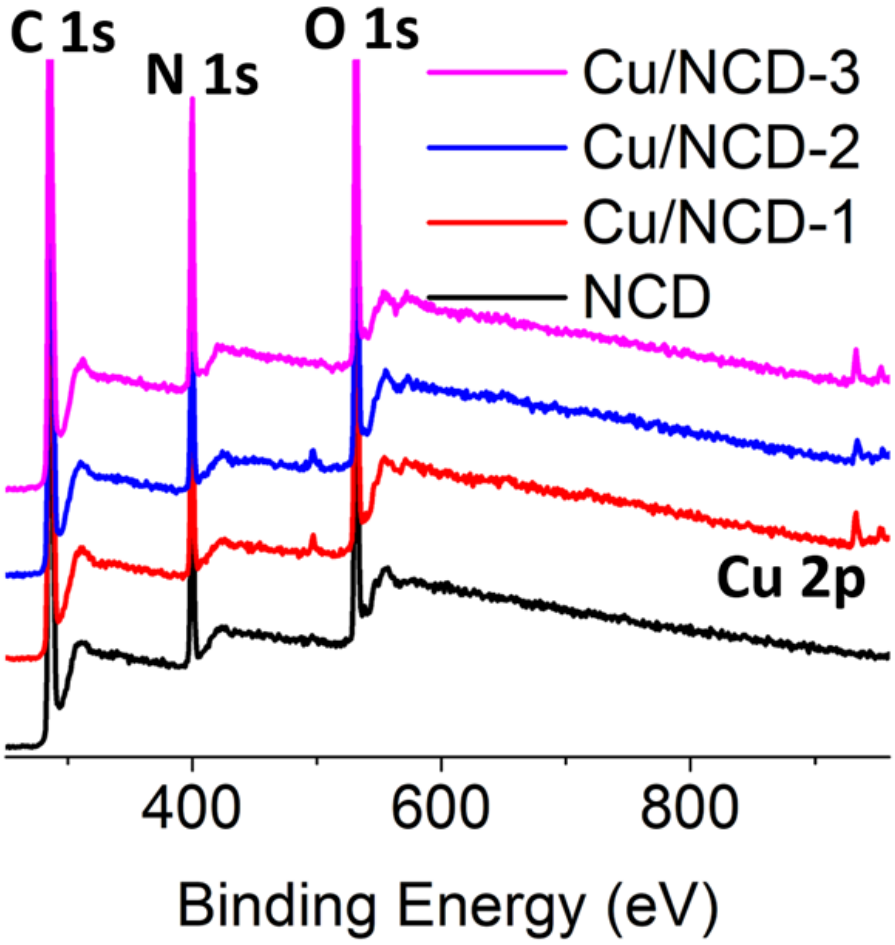


**Figure 5.** XPS survey scans of NCD (black), Cu/NC-1 (red), Cu/NC-2 (blue), and Cu/NC-3 (magenta).

Consistent results were obtained in XRD measurements. From the XRD patterns in Figure 1c, one can see that within the 2θ range of 10° to 80°, all samples display only a single broad peak centered at 2θ = 18°, which is characteristic of amorphous carbon including the combination of $sp^2$ and $sp^3$ carbons.[38] The lack of any other diffraction features in the XRD patterns suggests the absence of crystalline particles containing copper metal or copper oxide within the produced materials. This is consistent with the absence of lattice fringes observed in TEM measurements (Figure 3).

The elemental compositions and valence states of the samples were then examined by XPS measurements. In the survey scans (Figure 5), the elements of C, O and N can be readily identified in all samples, with Cu also in Cu/NCD-1, Cu/NCD-2 and Cu/NCD-3. The absence of other elements suggests high purity of the samples. Figure 6a depicts the corresponding high-resolution XPS spectra of the C 1s electrons. Deconvolution yields three components for all samples, (green) $sp^2$ carbon at ca. 284.5 eV, (orange) $sp^3$ carbon at 285.6 eV, and (purple) oxidized carbon (i.e., COOH, C=O) at 287.5 eV (Table S1). Notably, the $sp^2$ carbon content is found to increase with increasing $Cu(acac)_2$ feed from 36.31 at% for NCD to 39.18 at% for Cu/NC-1, 40.32 at% for Cu/NC-2, and 46.94 at% for Cu/NC-3; and the $Csp^2$:$Csp^3$ ratio increases accordingly, at 2.4, 3.3, 3.4, and 7.3, respectively, whereas the amount of oxidized carbon remains relatively constant among the samples (Table 2). This implies enhanced graphitization of citric acid and melamine by $Cu(acac)_2$ under the thermal conditions.

Figure 6b depicts the high-resolution XPS spectra of the N 1s electrons. For the NCD sample, deconvolution yields a primary peak (shaded in green) at 399.3 eV, and two minor ones at 398.0 and 400.5 eV, which can be assigned to pyrrolic, pyridinic and graphitic N, respectively (Table 1).[39, 40] This suggests successful doping of N into the carbon skeleton. With the addition of $Cu(acac)_2$ in sample preparation, the binding energies of these peaks remain virtually unchanged, likely because of the low contents of the Cu dopants (Table 2). In addition, the N dopant concentrations were found to be rather consistent among the samples, at 15.24 at% for NCD, 13.44 at% for Cu/NCD-1, 13.00 at% for Cu/NCD-2, and 15.61 at% for Cu/NCD-3 (Table 2).

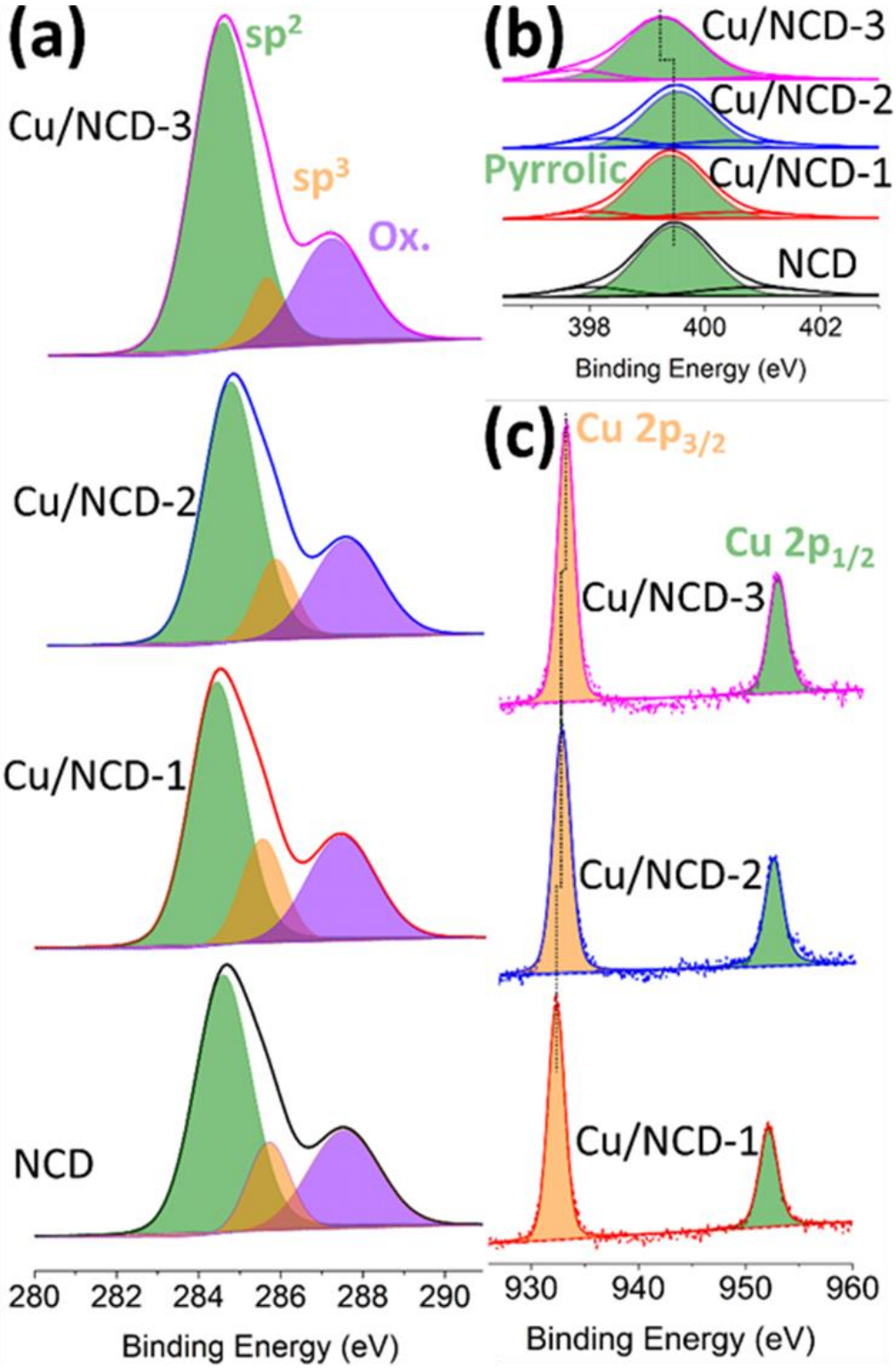
(a)
Cu/NCD-3
sp²
sp³
Ox.
Cu/NCD-2
Cu/NCD-1
NCD
280
282
284
286
288
290
Binding Energy (eV)
(b)
Cu/NCD-3
Cu/NCD-2
Pyrrolic
Cu/NCD-1
NCD
398
400
402
Binding Energy (eV)
(c)
Cu 2p3/2
Cu 2p1/2
Cu/NCD-3
Cu/NCD-2
Cu/NCD-1
930
940
950
960
Binding Energy (eV)

**Figure 6.** High-resolution XPS spectra of the (a) C 1s, (b) N 1s and (c) Cu 2p electrons of the NCD and Cu/NCD samples Solid curves are experimental data and shaded peaks are deconvolution fits.

The high-resolution XPS scans of the Cu 2p electrons are shown in Figure 6c. One can see that for the Cu/NCD samples, two well-defined peaks can be resolved, at 932.2 and 952.0 eV for Cu/NCD-1, 932.3 and 952.1 eV for Cu/NCD-2, and 932.4 and 952.2 eV for Cu/NCD-3, with a spin-orbit coupling of $\Delta = 19.8$ eV (Table S1).[41] These can be assigned to the $2p_{3/2}$ (orange) and $2p_{1/2}$ (green) electrons of Cu(I) (further confirmed in UV-vis absorption measurements, *vide infra*), as the lack of well-defined satellite peaks rules out the formation of Cu(II) species.[42] This suggests (partial) reduction of $Cu^{2+}$ in the thermal synthesis of the samples; yet the degree of reduction became lesser with increasing $Cu(acac)_2$ feed, as manifested by the slight increase of the Cu $2p_{3/2}$ binding energy from Cu/NCD-1 to Cu/NCD-3 (Table 1).[43] Furthermore, the copper content within the samples was found to be very low, only 1.57 wt% (0.32 at%) for Cu/CND-1, 1.07 wt% (0.22 at%) for Cu/CND-2, and 1.09 wt% (0.22 at%) for Cu/CND-3 (Table S2). Consistent results were obtained in ICP-OES measurements, where the copper loading was estimated to be 1.55 wt% for Cu/NCD-1, 1.06 wt%, for Cu/NCD-2 and 1.12 wt%, for Cu/NCD-3. Comparison between the XPS and ICP-OES results can be seen in Figure 7.

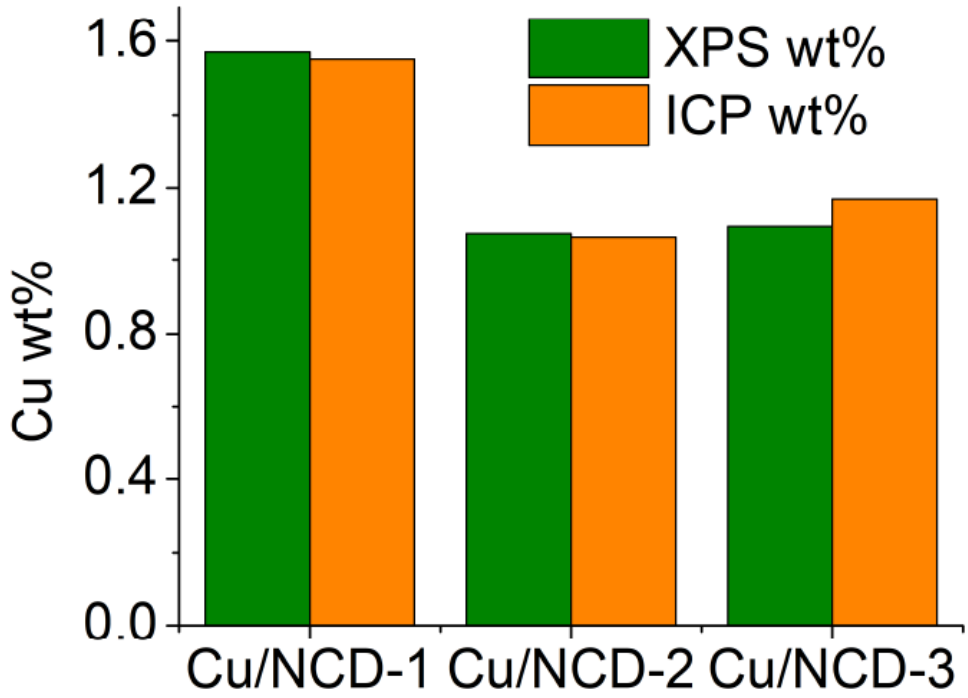


**Figure 7.** Comparison of copper wt% from the XPS (green) and ICP-OES (orange) measurements.

**Table 1.** XPS Binding energy (BE, eV) of the various elements in the series of samples

| Sample | $sp^2$ C | $sp^3$ C | Oxidized C | Pyridinic N | Pyrrolic N | Graphitic N | Cu $2p_{3/2}$ | Cu $2p_{5/2}$ |
|---|---|---|---|---|---|---|---|---|
| NCD | 284.5 | 285.6 | 287.6 | 398.0 | 399.5 | 400.8 | - | - |
| Cu/NCD-1 | 284.5 | 285.6 | 287.5 | 398.0 | 399.4 | 400.5 | 932.2 | 952.0 |
| Cu/NCD-2 | 284.6 | 285.7 | 287.5 | 398.3 | 399.5 | 400.5 | 932.3 | 952.1 |
| Cu/NCD-3 | 284.4 | 285.5 | 287.2 | 397.8 | 399.3 | 401.0 | 932.4 | 952.2 |

**Table 2.** Atomic percentage (at%) of the various elements in the series of samples

| Sample | $sp^2$ C | $sp^3$ C | Oxidized C | Pyridinic N | Pyrrolic N | Graphitic N | Cu | O |
|---|---|---|---|---|---|---|---|---|
| NCD | 36.31 | 15.19 | 17.24 | 1.8 | 11.48 | 1.96 | - | 16.02 |
| Cu/NCD-1 | 39.18 | 11.78 | 17.72 | 1.47 | 10.25 | 1.72 | 0.32 | 17.56 |
| Cu/NCD-2 | 40.32 | 11.72 | 17.78 | 1.86 | 9.01 | 2.13 | 0.22 | 16.96 |
| Cu/NCD-3 | 46.94 | 6.44 | 17.09 | 2.1 | 13.05 | 0.47 | 0.22 | 13.69 |

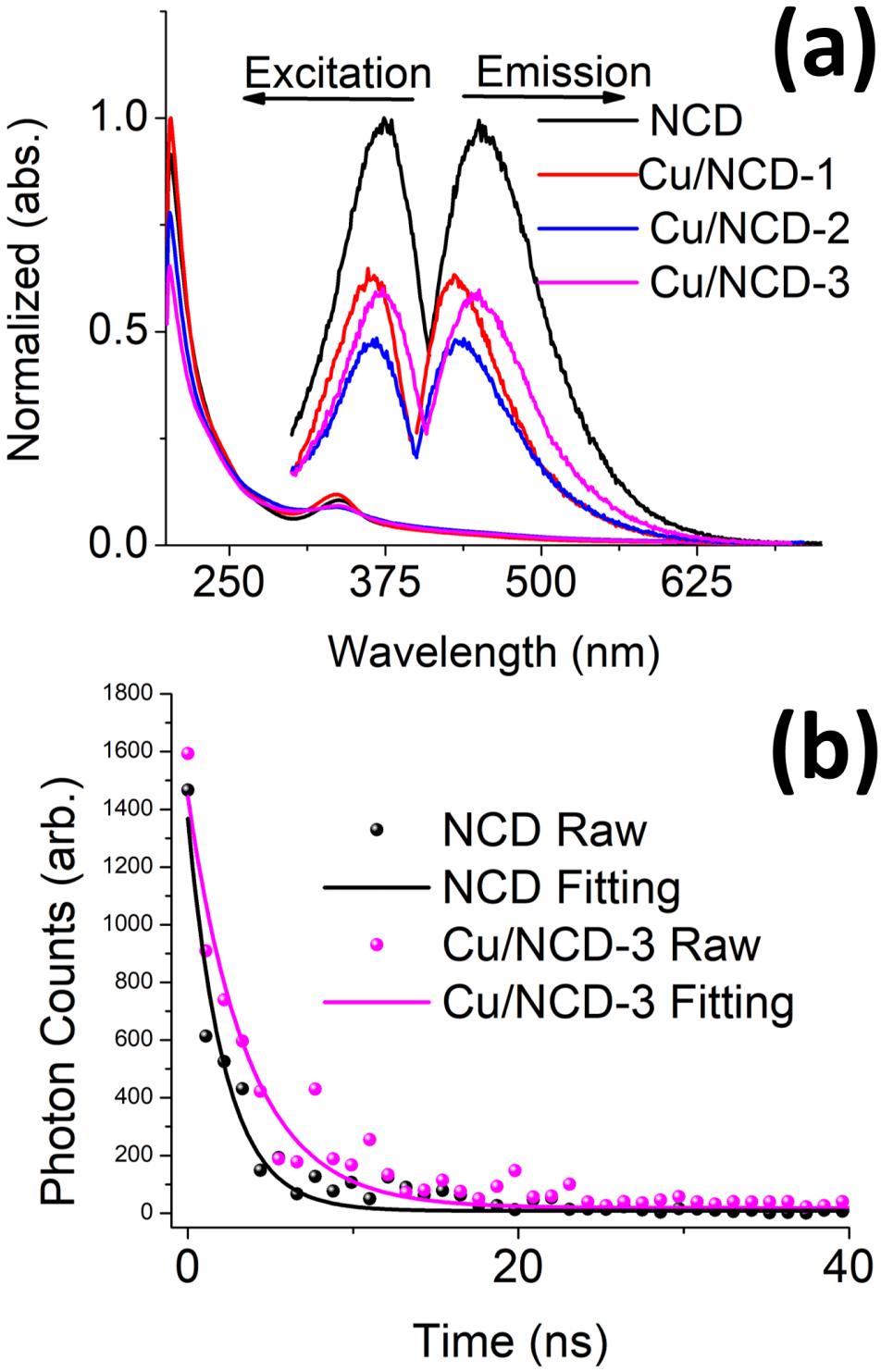


**Figure 8.** (a) UV-vis and SSPL spectra of (black) NCD, (red) Cu/CND-1, (blue) Cu/CND-2, and (magenta) Cu/CND-3. The UV-vis spectra are normalized to the respective absorbance at 203 nm and the fluorescence spectra are normalized to the

corresponding optical absorbance at the excitation wavelength and then normalized to the emission intensity of the NCD sample. All measurements are performed in PBS 1×. (b) TRPL emission spectra at the excitation of 365 nm for the NCD and Cu/NCD-3 samples. Symbols are experimental data and solid curves are exponential fits.

The optical properties of the samples were then examined by UV-vis and photoluminescence spectroscopy measurements. Figure 8a depicts the normalized UV-vis and SSPL spectra for the series of samples. In the UV-vis absorption measurements, all samples exhibit a primary absorption peak centered at ca. 335 nm, which can be attributed to the n → π* transitions of the C=O, C=C, and C=N moieties in the carbon dots that have been identified in XPS measurements (Figure 6).[44] In SSPL measurements, all samples display a pair of well-defined excitation and emission peaks, at $\lambda_{ex}$ = 372 nm and $\lambda_{em}$ = 451 nm for NCD, 364 nm and 430 nm for Cu/NCD-1, 366 nm and 435 nm for Cu/NCD-2, and 372 nm and 450 nm for Cu/NCD-3. One can see that the normalized photoluminescence intensity is apparently quenched with the incorporation of copper into the carbon scaffold, by 37% for Cu/NCD-1, 53% for Cu/NCD-2 and 42% for Cu/NCD-3.[45] Note that in the copper-free carbon dots, the photoluminescence most likely arose from the C=O and C=N functional moieties;[35, 36] whereas in the Cu/NCD samples, it is probably the Cu-N coordination structure that was responsible for the emission.[33] In fact, by subtracting the UV-vis absorption spectrum of NCD from those of the Cu/NCD samples, the resulting difference spectra exhibited multiple peaks within the range of 400 to 650 nm (Figure 9), which are characteristic of the Cu-N moieties in conventional copper(I)-pyrrole/pyridine complexes.[46-48] The fact that the NCD sample exhibited a markedly higher quantum yield than the Cu/NCD series suggests a more facile recombination of photogenerated electron-hole pairs in the former.

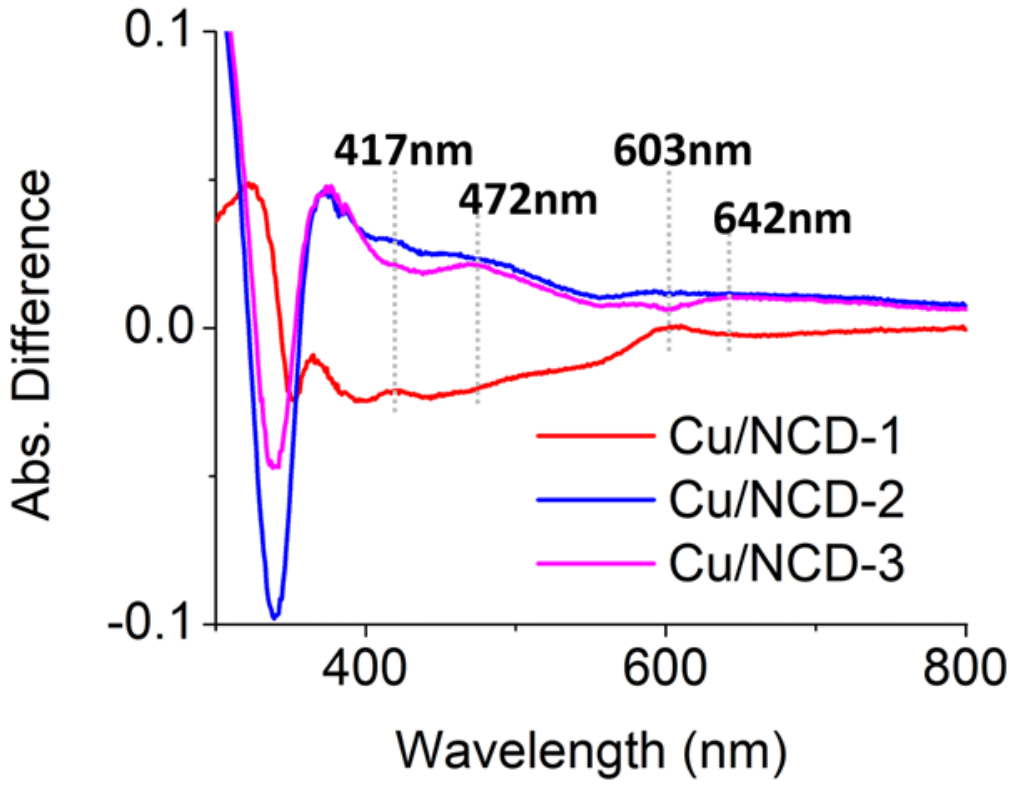


**Figure 9.** UV-vis difference spectra by normalizing the spectra to the absorbance at 250 nm and then subtracting the absorbance from the NCD spectrum.

Consistent behaviors were observed in TRPL measurements. Figure 8b depicts the TRPL profiles of NCD (black) and Cu/NCD-3 (magenta) after pulsed laser excitation at 365 nm, which were fitted to single-exponential decay kinetics, $I(t) = Ae^{-t/\tau}$. The calculated decay time constant ($\tau$) was estimated to be 2.2 ns for NCD and 3.6 ns for Cu/NCD-3. The extended lifetime from 2.2 to 3.6 ns with the addition of copper is in good agreement with diminished emission observed above in SSPL measurements and results reported in previous studies.[49, 50] This prolonged lifetime is conducive to the separation of the photogenerated electron-hole pairs, leading to enhanced performance in ROS production (vide infra).

To quantify the antibacterial properties of the produced materials, a series of photodynamic experiments were performed under photoirradiation with the peak wavelength at 365 nm, as shown in Figure 10a. Two control experiments were also included for comparison, one with *E. coli* alone (light green), and the other with $CuCl_2$ (orange) at an equivalent copper concentration to that of Cu/NCD-3. The corresponding photographs of the colonies grown on LB agar plates are shown in Figure 10b and 11. There are three aspects that warrant special attention. (i) In the two control experiments, no appreciable loss in CFUs was observed after 7 min of photoirradiation. (ii) NCD led to only a minimal loss of bacterial growth. (iii) Apparent photoinduced antibacterial activity can be seen with the Cu/NCD series, and the activity increased in the order of NCD < Cu/NCD-1 < Cu/NCD-2 < Cu/NCD-3, highlighting the importance of copper dispersion into the carbon dots in the bactericidal action. For instance, among the series of samples, a complete loss of all CFUs can be seen after 6 min of photoirradiation with Cu/NCD-2 and only 2 min with Cu/NCD-3, whereas appreciable growth of bacteria can still be seen with NCD and Cu/NCD-1. This suggests that Cu/NCD-3 possesses the greatest photoinduced antibacterial activity among all samples. This coincides with the longest lifetime of photogenerated electron-hole pairs of the sample, as demonstrated in TRPL measurements, suggesting that the Cu-N moieties likely facilitated the separation of the electron-hole pairs and the subsequent formation of ROS. Additional contributions may arise from the high $Csp^2$:$Csp^3$ ratio in Cu/NCD-3 that facilitated charge migration within the carbon dots. These results also suggest that copper leaching, if any, does not make any meaningful contribution to the antimicrobial activity.

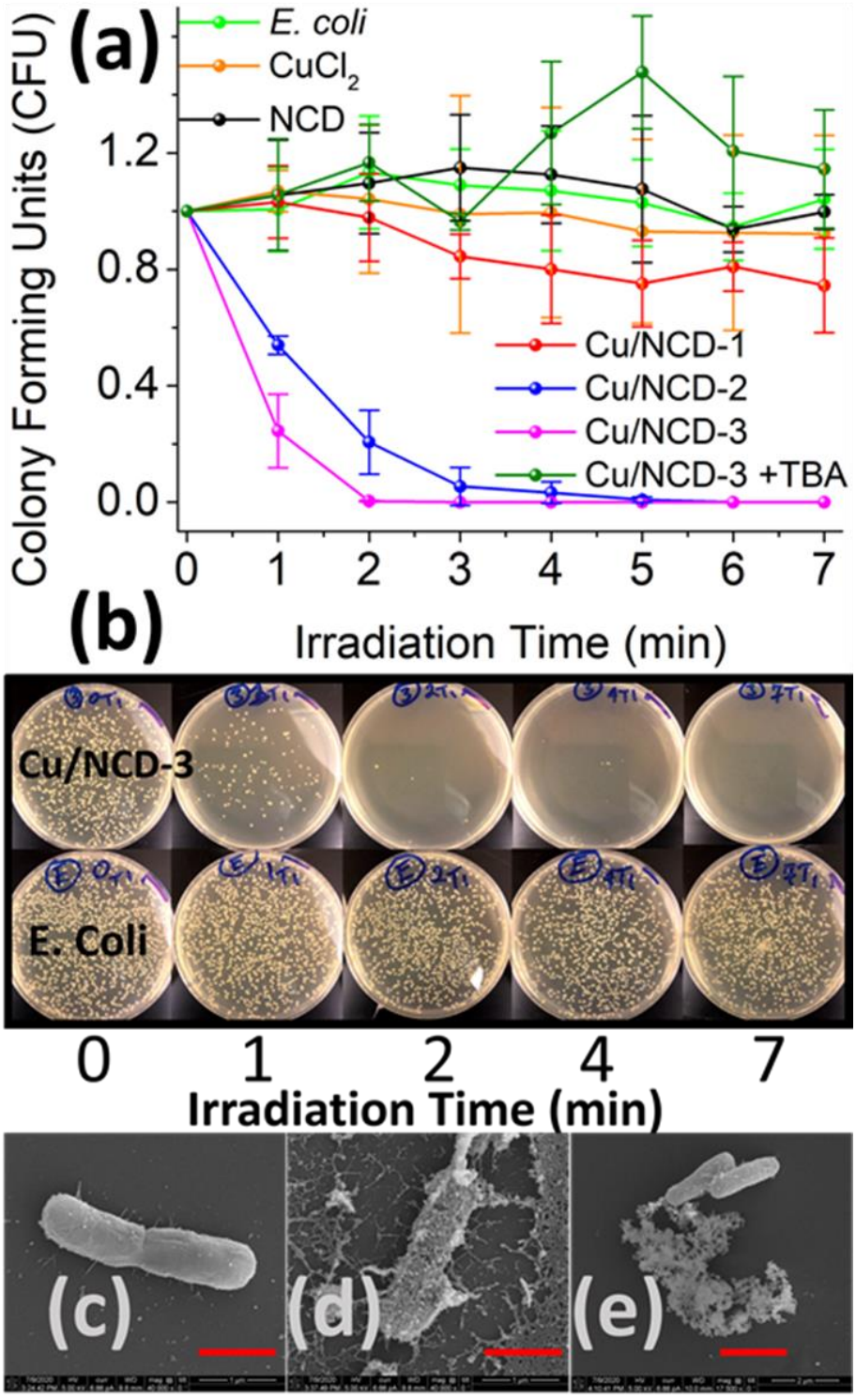


**Figure 10.** (a) Antibacterial studies under photoirradiation at the peak wavelength at 365 nm. Two control samples are included: (light green) *E. coli* alone in PBS 1×, and

(orange) $CuCl_2$ in PBS 1× at a concentration equivalent to that of Cu/NCD-3 (12.8 ppm). A second sample of Cu/NCD-3 is tested in the presence of a hydroxyl radical quencher, TBA at 10 mg $L^{-1}$ (dark green). All samples have been tested in triplicate and the data points display the corresponding average and standard deviation. (b) Photographs depicting *E. coli* grown on LB agar plates at different photoirradiation time points (0, 1, 2, 4, and 7 min) in the (bottom) absence and (top) presence of Cu/NCD-3. SEM images of (c) the *E. coli* control, (d) *E. coli* with Cu/NCD-3 after photo irradiation, for 7 min, and (e) *E. coli* with Cu/NCD-3 in the dark. The scale bars, indicated in red are 1 μm, 1μm, and 2μm, respectively.

The difference of the bactericidal activity can also be readily visualized in SEM measurements of the bacterial cell morphologies. From Figure 10c-e, one can see that the *E. coli* cells sustained significant membrane damages in the presence of Cu/NCD-3 under photoirradiation for 7 min (panel d), whereas in the dark, the cell morphology remained largely intact (panel e), in comparison to the control (panel c).

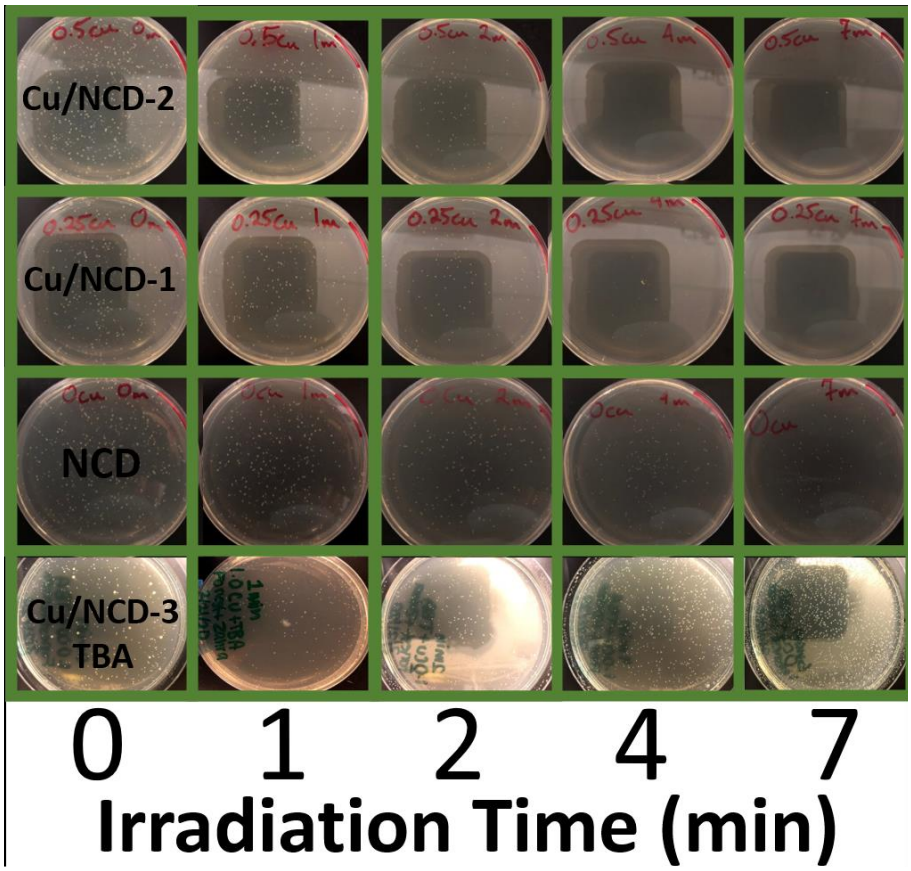


**Figure 11.** Digital photographs of incubated LB agar plates: from top to bottom for the samples of Cu/NCD-2, Cu/NCD-1, NCD, and Cu/NCD-3 + TBA. The columns from left to right are images acquired at the 0, 2, 4, and 7 min time points of photo irradiation at 356 nm.

Notably, Cu/NCD-3 lost all bactericidal activity in the presence of a common hydroxyl radical scavenger, TBA (Figure 10a and 11), suggesting that hydroxyl radicals were responsible for the antimicrobial activity of Cu/NCD-3, which are generally produced by photoreduction of oxygen and/or photo dissociation of water.[8, 51, 52] A similar trend was observed when a common Gram-positive strain of bacteria, *S. epidermidis*, was used in place of *E. coli* under otherwise identical experimental conditions. Results from this gram-positive test are shown in Figure 12.

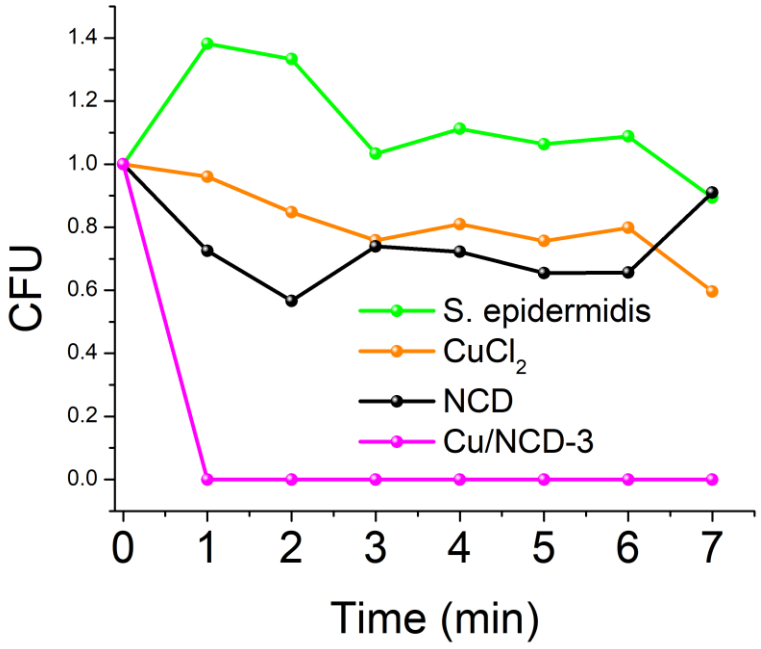


**Figure 12.** Gram positive antibacterial studies under photoirradiation with the peak wavelength at 365 nm. Two control samples are included: (light green) S. epidermidis alone in PBS 1×, and (orange) CuCl2 in PBS 1× at a concentration equivalent to that of Cu/NCD-3 (12.8 ppm). Data for Cu/NCD-3 is shown in magenta.

It is interesting to note that no apparent antimicrobial activity was observed with NCD or Cu/NCD in the dark. Figure 5 depicts the corresponding *E. coli* growth curves acquired in the dark. The growth rates during the log phase growth, between 3 and 6 h of incubation, in essence show little to no change between the samples and between trials. This suggests that bacterial growth in the absence of photoirradiation is unaffected by the presence of the NCD or Cu/NCD samples. These findings are consistent with the notion that photoirradiation plays a critical role in the antibacterial activity of the carbon dots.

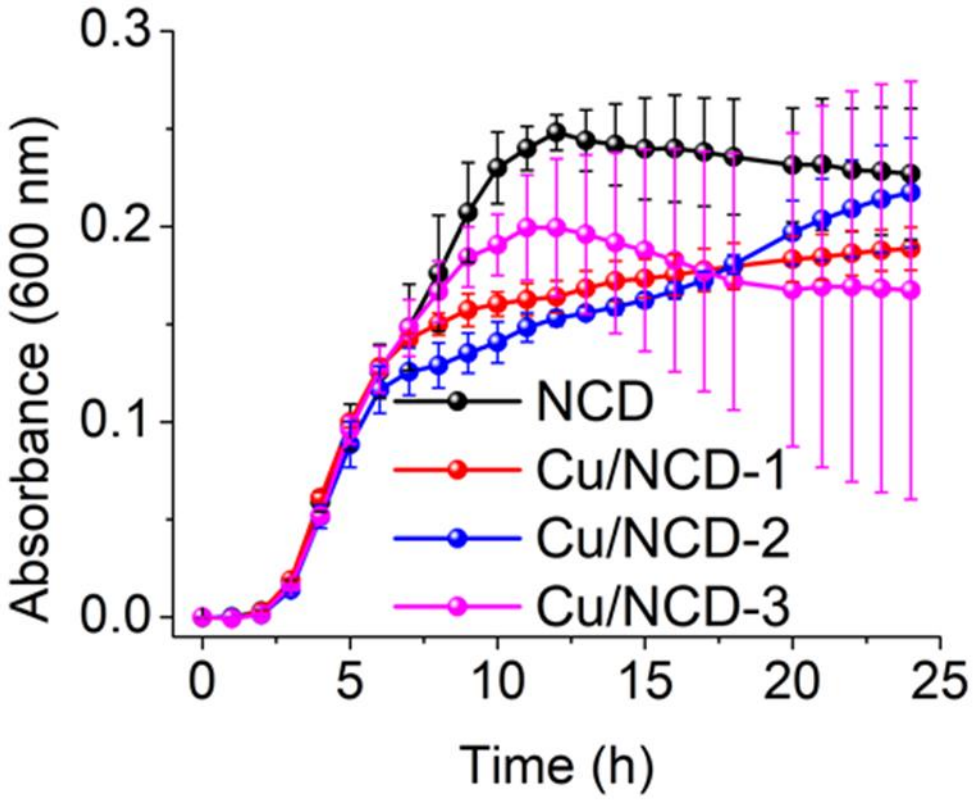


**Figure 13.** Bacterial growth curves in the dark. Each measurement is repeated in triplicate, with PBS 1× as the solvent. Sample concentrations are all 600 μg $mL^{-1}$, identical to those in photodynamic experiments in Figure 10.

Fluorescence microscopy studies were then carried out to quantify the intracellular ROS generation, using CellROX™ green as the fluorescence probe. Note that CellROX™ green is commonly utilized to measure oxidative stress of living cells. It is non-fluorescent in the reduced state but may bind to DNA and emit green fluorescence upon oxidation by, for instance, ROS. Thus, it may be used to visualize ROS production during the bactericidal actions. Figure 14 shows the representative fluorescence micrographs of the *E. coli* cells stained with CellROX™ green after 1 min of photoirradiation (395-400 nm) in (a) PBS only (as a control), (b) NCD, and (c) Cu/NCD-3. One can see that the green dots are far more abundant and intense in panel (c) than in panels (a) and (b).

Figure 14d is the graphical representation of the fluorescence intensity for each sample averaged over 3 ROIs for PBS alone (green), NCD (black), and Cu/NCD-3 (magenta). One can see that there is no significant statistical difference in the fluorescence intensity between the PBS control and NCD, suggesting minimal contribution from the carbon dots alone to the photo generation of ROS. By contrast, Cu/NCD-3 exhibited a fluorescence intensity that was almost 4-fold greater than those of the other two samples. This confirms the notion that ROS production was greatly facilitated by the atomic dispersion of Cu into the NCD skeleton, and such enhanced photocatalytic activity led to marked improvement of the antibacterial activity of Cu/NCD-3, which was likely aided by the enrichment of bacterial cells around the carbon dots (Figure 15).

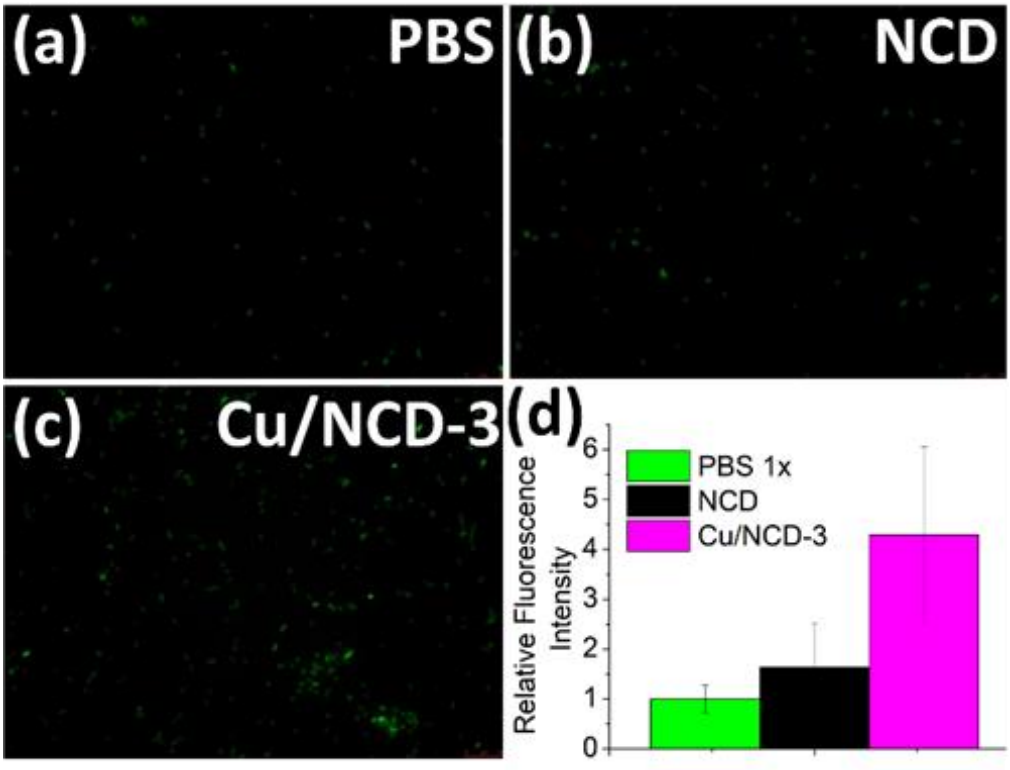


**Figure 14.** Representative fluorescence micrographs of *E. coli* cells stained with CellROX™ green after 1 min of photoirradiation at a peak wavelength between 395-400 nm in the presence of (a) PBS only, (b) NCD (600 μg/mL in PBS), and Cu/NCD-3 (600

µg/mL in PBS). (d) Bar charts of the average fluorescence intensity of the bacterial cells after photoirradiation.

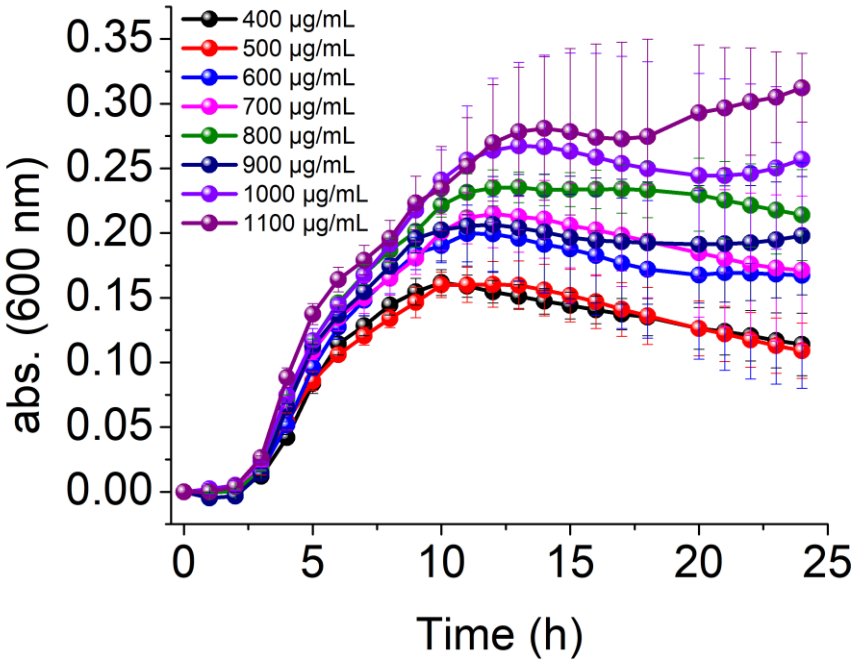


**Figure 15.** *E. coli* growth curves in the dark in the presence of Cu/NCD-3 at varying concentrations from 400 to 1100 µg/mL.

## 6.4 Experimental

### Chemicals

Melamine (99%, Acros Organics), citric acid anhydrous (Certified ACS, Fisher Chemicals), copper(II) acetylacetonate ($Cu(acac)_2$, 98%, Acros Organics), phosphate buffered saline tablets (PBS, Acros Organics), sodium chloride (NaCl, Fisher Chemicals), yeast extract (Fisher BioReagents), agar (Fisher BioReagents), *tert*-butyl alcohol (TBA, ≥99.5%, Sigma Aldrich), tryptone (Fisher BioReagents), and CellROX™ green (ThermoFisher) were used as received. All solvents were obtained through typical

commercial sources and used as received, too. Water was supplied with a Barnstead Nanopure water system (18.3 MΩ cm).

**Characterization**

Transmission electron microscopy (TEM) measurements were carried out on a JOEL JEM 2100F microscope. UV-Vis measurements were taken on a Perkin Elmer Lambda 35 UV-vis spectrometer with a scan rate of 240 nm $min^{-1}$ and a slit width of 1 nm. SSPL measurements were performed on a PTI fluorospectrometer. TRPL spectra were acquired using a Horiba QM-3304 instrument at the pulsed laser excitation of 337 nm in the time-correlated single-photon counting (TCSPC) mode. XPS measurements were performed with a Phi 5400/XPS instrument equipped with an Al $K_\alpha$ source operated at 350 W and $10^{-9}$ Torr. X-ray diffraction (XRD) measurements were conducted on a Rigaku Smartlab Powder & Thin Film Diffractometer with Cu $K_\alpha$ ($\lambda$ = 1.54 Å) radiation. Inductively coupled plasma-optical emission spectrometry (ICP-OES) measurements were carried out with a Perkin Elmer Optima instrument.

Synthesis of nitrogen-doped carbon dots with atomically dispersed copper

The samples were prepared by adopting a solid-state method reported previously.[53] Briefly, citric acid (0.8 g), melamine (1.6 g), and $Cu(acac)_2$ (0, 0.25, 0.5, or 1.0 mmole) were mixed into a homogeneous powder by mortar and pestle. The solid was then added into a Teflon-lined autoclave and heated to 180 °C for 5 h. Under these reaction conditions, citric acid and melamine underwent dehydration reactions to produce nitrogen-doped carbon dots.[53] $Cu(acac)_2$ was chosen for its thermal stability. Once cooled to room temperature, the Teflon liner was opened, and the product was dispersed in water by sonication. The dispersion was centrifuged at 6000 rpm for 10 min to remove insoluble aggregates. The resulting brown supernatant was purified with a dialysis

membrane (3.5K MWCO) for 72 h, condensed through rotary evaporation, and dried in a vacuum oven at 60 °C overnight. For the sample prepared in the absence of $Cu(acac)_2$, it was referred to as NCD, whereas those with the addition of $Cu(acac)_2$, as Cu/NCD-1, Cu/NCD-2, and Cu/NCD-3, respectively.

**Preparation of bacterial suspension**

*E. coli* (ATCC 25922) and *S. epidermidis* (ATCC 12228) streaked on sterile Luria-Bertani (LB) agar were incubated overnight at 37 °C. A single colony was selected and inoculated in sterile LB (3 mL) at 37 °C for 18 h with shaking. The resulting liquid culture was centrifuged at 8000 rpm for 1 min, followed by washing with sterile PBS 1× three times. The resulting bacterial suspension was diluted to an optical density (OD) of 0.1 at 600 nm and used in the following antibacterial experiments.

**Bacterial growth in the dark**

Bacterial growth in the dark was monitored using a sterile 96-well plate with a final volume of 200 µL in each well. NCD or Cu/NCD (120 µg) was loaded into each well through serial dilution of a 1 mg $mL^{-1}$ stock solution in PBS 1× to obtain a final concentration of 600 µg $mL^{-1}$. 40 µL of the previously prepared bacterial suspension (0.1 OD) was added to each well to obtain identical starting bacterial concentrations as those in the photocatalytic studies (below). 20 µL LB was added to each well and the wells were incubated at 37 ° for 24 h, with data collection acquired at 600 nm in 2-min intervals.

**Photocatalytic antibacterial studies**

Photocatalytic antimicrobial measurements were performed by using a modified method adopted from previous reports.[17, 54] Briefly, NCD and Cu/NCD solutions (1 mg $mL^{-1}$)

were prepared by dissolving the purified samples in PBS 1×. 600 µL of this solution was added to a 1.5 mL centrifuge tube. 200 µL of a bacterial suspension (0.1 OD) of either *E. coli* or *S. epidermidis* was added to each sample tube and the final volume was brought to 1 mL using PBS 1× to obtain a final NCD or Cu/NCD concentration of 600 µg $mL^{-1}$. After photoirradiation (100 W, 1000-1500 lumen with a peak emission of 365 nm, Dongguan Hongke Lighting Co, China) for a varied period of time (up to 7 min), 100 µL of the resulting solution was taken and diluted by a factor of $10^{-2}$. 10 µL of the diluted solution was dropped onto an LB agar plate and dispersed using sterile glass beads. The resulting LB agar plates were grown for 18 h at 37 °C in a dark incubator. The colony forming units (CFUs) on each plate were counted and recorded as a function of time.

To test the formation of hydroxyl radicals, TBA (10 µL, 1 g $L^{-1}$) was added to the suspension before dilution to a final volume of 1 mL with PBS 1×. This gave a TBA concentration of 10 mg $L^{-1}$ during the photodynamic experiments.

**Scanning electron microscopy studies**

SEM images of the bacterial cell morphologies were acquired with an FEI Quanta 3D field-emission scanning electron microscope. For the control experiment, 100 µL of the *E. coli* suspension (0.1 OD in PBS 1×) was dropcast onto a sterile glass slide in the dark. The droplet was set to dry just at the edges for approximately 15 min before serial washing in solutions of 10%, 25%, 50%, 75%, 90%, and 100% ethanol to dehydrate the sample. Once in 100% ethanol, the sample was placed in a critical point dryer (CPD) where ethanol was exchanged with $CO_2$. The fully dried sample was then sputtered with gold to improve contrast and resolution during SEM imaging. Two more samples were prepared in the same manner but in the presence of Cu/NCD-3, one in the dark and the other under photoirradiation at 365 nm for 7 min.

**Fluorescence microscopy**

300 µL of the bacterial suspensions, prepared as previously described, was added to centrifuge tubes and diluted to 1 mL using either PBS alone, NCD in PBS, or Cu/NCD-3 in PBS to obtain a final nanoparticle concentration of 600 µg $mL^{-1}$. These centrifuge tubes were irradiated with light (395-400 nm) positioned 10 cm above the light base for 1 min. CellROX™ green (1.8 µL, 2.5 mM in DMSO) was added to each of the resulting irradiated centrifuge tubes to obtain a final concentration of 25 µM and incubated for 10 min at 37 °C. 1 µL of CellROX™ green-stained cell suspension was added to an agar pad (1 $cm^2$, 1% $H_2O$). Fluorescence images were collected using 470 ± 40 nm excitation and 525 ± 50 nm emission filters, 63× water immersion lens, and 3 regions of interest (ROIs) per sample. Integrated fluorescence intensity after background subtraction was averaged across the 3 ROIs.

## 6.5 Conclusions

Carbon dots doped with Cu-N coordination moieties were readily prepared by a solid-state thermal process, with the particle size ranging from 12 to 37 nm in diameter. Copper was found to be in the Cu(I) oxidation state with no apparent copper crystallinity, and the loadings ranged from 1.07 to 1.57 wt%. Photoluminescence studies showed that the atomic dispersion of copper centers into the carbon dots markedly quenched the emissions and prolonged the photoluminescence lifetime. The photoinduced antibacterial activity was found to increase in the order NCD < Cu/NCD-1 < Cu/NCD-2 < Cu/NCD-3, coincident with the increase of the $sp^2$ carbon content. This may be due to improved photoinduced electron-hole pair migration and separation leading to hydroxyl radical formation, as evidenced in fluorescence microscopic studies with CellROX™ green as the probe and control experiments using TBA as the hydroxyl radical scavenger. The

produced materials were found to have little to no effect on bacterial growth in the absence of photoirradiation. These functional nanocomposites may see important application in wound care devices and may help alleviate the current role of β-lactam based antibiotics.

## 6.6 References


1. Zheng, K.Y., et al., *Antimicrobial silver nanomaterials.* Coordination Chemistry Reviews, 2018. **357**: p. 1-17.
2. Piddock, L.J.V., *The crisis of no new antibiotics—what is the way forward?* The Lancet Infectious Diseases, 2012. **12**(3): p. 249-253.
3. Klein, E.Y., et al., *Global increase and geographic convergence in antibiotic consumption between 2000 and 2015.* Proceedings of the National Academy of Sciences of the United States of America, 2018. **115**(15): p. E3463-E3470.
4. Partridge, S.R., et al., *Mobile Genetic Elements Associated with Antimicrobial Resistance.* Clinical Microbiology Reviews, 2018. **31**(4).
5. Bush, K. and P.A. Bradford, *Interplay between β-lactamases and new β-lactamase inhibitors.* Nature Reviews Microbiology, 2019: p. 1.
6. Kumar, R., et al., *Antimicrobial properties of ZnO nanomaterials: A review.* Ceramics International, 2017. **43**(5): p. 3940-3961.
7. Qi, K.Z., et al., *Review on the improvement of the photocatalytic and antibacterial activities of ZnO.* Journal of Alloys and Compounds, 2017. **727**: p. 792-820.
8. Nosaka, Y. and A.Y. Nosaka, *Generation and Detection of Reactive Oxygen Species in Photocatalysis.* Chemical Reviews, 2017. **117**(17): p. 11302-11336.

9. Dwyer, D.J., M.A. Kohanski, and J.J. Collins, *Role of reactive oxygen species in antibiotic action and resistance.* Current Opinion in Microbiology, 2009. **12**(5): p. 482-489.

10. He, T., et al., *Nanocomposites Based on Ruthenium Nanoparticles Supported on Cobalt and Nitrogen-Codoped Graphene Nanosheets as Bifunctional Catalysts for Electrochemical Water Splitting.* ACS applied materials & interfaces, 2019. **11**(50): p. 46912-46919.

11. Yang, W., et al., *Graphene oxide-supported zinc cobalt oxides as effective cathode catalysts for microbial fuel cell: High catalytic activity and inhibition of biofilm formation.* Nano Energy, 2019. **57**: p. 811-819.

12. Wang, N., et al., *Cage Breaking of C60 Into Photoluminescent Graphene Oxide Quantum Dots: An Efficient Peroxidase Mimic.* physica status solidi (b), 2018. **255**(4): p. 1700535.

13. Chen, L., et al., *Platinum nanoparticles encapsulated in nitrogen-doped graphene quantum dots: Enhanced electrocatalytic reduction of oxygen by nitrogen dopants.* International Journal of Hydrogen Energy, 2017. **42**(49): p. 29192-29200.

14. Deming, C.P., et al., *Oxygen electroreduction catalyzed by palladium nanoparticles supported on nitrogen-doped graphene quantum dots: impacts of nitrogen dopants.* ACS Sustainable Chemistry & Engineering, 2016. **4**(12): p. 6580-6589.

15. Lu, B., et al., *Ruthenium atomically dispersed in carbon outperforms platinum toward hydrogen evolution in alkaline media.* Nature Communications, 2019. **10**(1): p. 631.

16. Rojas-Andrade, M.D., et al., *Antibacterial mechanisms of graphene-based composite nanomaterials.* Nanoscale, 2017. **9**(3): p. 994-1006.

17. Liu, J., et al., *Photo-enhanced antibacterial activity of ZnO/graphene quantum dot nanocomposites.* Nanoscale, 2018. **10**(1): p. 158-166.

18. Rojas-Andrade, M.D., et al., *Antimicrobial activity of graphene oxide quantum dots: impacts of chemical reduction.* Nanoscale Advances, 2020.

19. Azimirad, R. and S. Safa, *Photocatalytic and Antifungal Activity of Flower-Like Copper Oxide Nanostructures.* Synthesis and Reactivity in Inorganic Metal-Organic and Nano-Metal Chemistry, 2014. **44**(6): p. 798-803.

20. Katwal, R., et al., *Electrochemical synthesized copper oxide nanoparticles for enhanced photocatalytic and antimicrobial activity.* Journal of Industrial and Engineering Chemistry, 2015. **31**: p. 173-184.

21. Leyland, N.S., et al., *Highly Efficient F, Cu doped TiO2 anti-bacterial visible light active photocatalytic coatings to combat hospital-acquired infections.* Scientific Reports, 2016. **6**.

22. Ray, S.K., et al., *Cu-alpha-NiMoO4 photocatalyst for degradation of Methylene blue with pathways and antibacterial performance.* Journal of Photochemistry and Photobiology a-Chemistry, 2017. **348**: p. 18-32.

23. Rtimi, S., et al., *Advances in catalytic/photocatalytic bacterial inactivation by nano Ag and Cu coated surfaces and medical devices.* Applied Catalysis B-Environmental, 2019. **240**: p. 291-318.

24. Xiong, L.B., et al., *Size-controlled synthesis of Cu2O nanoparticles: size effect on antibacterial activity and application as a photocatalyst for highly efficient H2O2 evolution.* Rsc Advances, 2017. **7**(82): p. 51822-51830.

25. Yadav, H.M., et al., *Preparation and characterization of copper-doped anatase TiO2 nanoparticles with visible light photocatalytic antibacterial activity.* Journal of Photochemistry and Photobiology a-Chemistry, 2014. **280**: p. 32-38.

26. Yordanova, S., et al., *Synthesis, characterization and in vitro antimicrobial activity of a new blue fluorescent Cu(II) metal complex of bis-1,8-naphthalimide.* Journal of Molecular Structure, 2015. **1101**: p. 50-56.

27. Bagihalli, G.B., et al., *Synthesis, spectral characterization, in vitro antibacterial, antifungal and cytotoxic activities of Co(II), Ni(II) and Cu(II) complexes with 1,2,4-triazole Schiff bases.* European Journal of Medicinal Chemistry, 2008. **43**(12): p. 2639-2649.

28. Qi, L.F., et al., *Preparation and antibacterial activity of chitosan nanoparticles.* Carbohydrate Research, 2004. **339**(16): p. 2693-2700.

29. Ruparelia, J.P., et al., *Strain specificity in antimicrobial activity of silver and copper nanoparticles.* Acta Biomaterialia, 2008. **4**(3): p. 707-716.

30. Stanic, V., et al., *Synthesis, characterization and antimicrobial activity of copper and zinc-doped hydroxyapatite nanopowders.* Applied Surface Science, 2010. **256**(20): p. 6083-6089.

31. Gaetke, L.M. and C.K. Chow, *Copper toxicity, oxidative stress, and antioxidant nutrients.* Toxicology, 2003. **189**(1-2): p. 147-163.

32. Gong, N., et al., *Carbon-dot-supported atomically dispersed gold as a mitochondrial oxidative stress amplifier for cancer treatment.* Nature nanotechnology, 2019. **14**(4): p. 379.

33. Peng, Y., et al., *Hydrogen evolution reaction catalyzed by ruthenium ion-complexed graphitic carbon nitride nanosheets.* Journal of Materials Chemistry A, 2017. **5**(34): p. 18261-18269.

34. Peng, Y., et al., *Ruthenium Ion-Complexed Graphitic Carbon Nitride Nanosheets Supported on Reduced Graphene Oxide as High-Performance Catalysts for Electrochemical Hydrogen Evolution.* Chemsuschem, 2018. **11**(1): p. 130-136.

35. Tian, L., et al., *Nanosized Carbon Particles From Natural Gas Soot.* Chemistry of Materials, 2009. **21**(13): p. 2803-2809.

36. Tian, L., et al., *Hydrothermally enhanced photoluminescence of carbon nanoparticles.* Scripta Materialia, 2010. **62**(11): p. 883-886.

37. Jiang, L., et al., *Doping of graphitic carbon nitride for photocatalysis: a reveiw.* Applied Catalysis B: Environmental, 2017. **217**: p. 388-406.

38. Lee, H.-M., et al., *Comparative studies of porous carbon nanofibers by various activation methods.* Carbon letters, 2013. **14**(3): p. 180-185.

39. Titantah, J.T. and D. Lamoen, *Carbon and nitrogen 1s energy levels in amorphous carbon nitride systems: XPS interpretation using first-principles.* Diamond and Related Materials, 2007. **16**(3): p. 581-588.

40. Akada, K., et al., *Control of work function of graphene by plasma assisted nitrogen doping.* Applied Physics Letters, 2014. **104**(13): p. 131602.

41. Xia, J., et al., *A rapid approach to urushiol–copper (I) coordination polymer under UV irradiation.* Progress in Organic Coatings, 2009. **65**(4): p. 510-513.

42. Brettholle, M., et al., *Plasma electrochemistry in ionic liquids: deposition of copper nanoparticles.* Physical Chemistry Chemical Physics, 2010. **12**(8): p. 1750-1755.

43. Peng, Y., et al., *Impacts of interfacial charge transfer on nanoparticle electrocatalytic activity towards oxygen reduction.* Physical Chemistry Chemical Physics, 2017. **19**(14): p. 9336-9348.

44. Chen, L., et al., *Intervalence Charge Transfer of Ruthenium–Nitrogen Moieties Embedded within Nitrogen-Doped Graphene Quantum Dots.* The Journal of Physical Chemistry C, 2016. **120**(24): p. 13303-13309.

45. Wang, F., et al., *Graphene quantum dots as a fluorescent sensing platform for highly efficient detection of copper(II) ions.* Sensors and Actuators B: Chemical, 2014. **190**: p. 516-522.

46. Tümer, F., et al., *Absorption, redox and aggregation properties of new α,α-diamino-porphyrin based ligands and their Cu(II) complexes.* Journal of Molecular Structure, 2019. **1190**: p. 148-159.

47. Kantekin, H., et al., *New peripherally tetra-[trans-3, 7-dimethyl-2, 6-octadien-1-ol] substituted metallophthalocyanines: synthesis, characterization and catalytic activity studies on the oxidation of phenolic compounds.* Journal of Coordination Chemistry, 2018. **71**(1): p. 164-182.

48. Kim, E., et al., *Superoxo, μ-peroxo, and μ-oxo complexes from heme/O2 and heme-Cu/O2 reactivity: Copper ligand influences in cytochrome c oxidase models.* Proceedings of the National Academy of Sciences, 2003. **100**(7): p. 3623-3628.

49. Kollmannsberger, M., et al., *Ultrafast Charge Transfer in Amino-Substituted Boron Dipyrromethene Dyes and Its Inhibition by Cation Complexation: A New Design Concept for Highly Sensitive Fluorescent Probes.* The Journal of Physical Chemistry A, 1998. **102**(50): p. 10211-10220.

50. Peng, Y., et al., *Point of Anchor: Impacts on Interfacial Charge Transfer of Metal Oxide Nanoparticles.* Journal of the American Chemical Society, 2018. **140**(45): p. 15290-15299.

51. Chen, C.-Y. and C.T. Jafvert, *Photoreactivity of Carboxylated Single-Walled Carbon Nanotubes in Sunlight: Reactive Oxygen Species Production in Water.* Environmental Science & Technology, 2010. **44**(17): p. 6674-6679.

52. Milligan, J.R. and J.F. Ward, *Yield of single-strand breaks due to attack on DNA by scavenger-derived radicals.* Radiation research, 1994. **137**(3): p. 295-299.

53. Iqbal, A., et al., *Heterogeneous synthesis of nitrogen-doped carbon dots prepared via anhydrous citric acid and melamine for selective and sensitive turn on-off-on detection of Hg (II), glutathione and its cellular imaging.* Sensors and Actuators B: Chemical, 2018. **255**: p. 1130-1138.

54. Liu, J., et al., *Antimicrobial Activity of Zinc Oxide–Graphene Quantum Dot Nanocomposites: Enhanced Adsorption on Bacterial Cells by Cationic Capping Polymers.* ACS Sustainable Chemistry & Engineering, 2019. **7**(19): p. 16264-16273.

## Chapter 7 Summary

Chapter 2 explored the use of platinum oxide nanoparticles deposited on a carbon nitride support material for hydrogen evolution. Platinum oxide in a +4-valence state was identified as the main contributor for efficient hydrogen generation. This concept was further demonstrated through two electrochemical cycling tests used to convert $Pt^{2+}$ to $Pt^{4+}$ through oxidative cycling to improve catalyst performance and recover performance after prolonged use.

Chapter 3 investigated the use of single atom chelated platinum on carbon nitride to improve HER mass activity. Phosphorous doping of the carbon nitride support was necessary to improve electrical conductivity and lead to a possible Pt-P synergistic interaction seen by Mott-Schottky analysis, XPS, and EXAFS fitting results. Single atom Pt loading and improved support conductivity lead to approximately 3-fold improvement in Pt mass activity compared to commercially available metallic Pt nanoparticles on carbon. This suggests the produced material can produce an equivalent amount of hydrogen gas with three times less Pt loading.

Chapter 4 summarized the current state of electrochemical generation of reactive species for microbial inactivation. This is a promising field with potential for improving human health. Adsorbate intermediate binding is found to be an optimal route toward improved reactive species selectivity. Chapter 5 summarized previous work in our group utilizing graphene based antimicrobial photocatalysts through ROS generation. Oxygen functional groups are found to be critical for ROS generation and strong photocatalyst-microorganism interactions are seen to be necessary for efficient microorganism inactivation likely due to short lived ROS lifetimes.

Chapter 6 introduced a novel copper single atom doped carbon quantum dot for photocatalytic microbial inactivation. Due to the low copper loading the material was found to have no antimicrobial capabilities without photoirradiation. Upon photoirradiation, the copper doped samples were seen to produce hydroxyl radicals through fluorescence microscopy of CellROX© treated bacteria and a common hydroxyl radical quenching agent, tertbutyl alcohol. The developed material showed complete cell death after only 2 minutes of photoirradiation. Such a material could be implemented into healthcare equipment such as bandages for wound care to assist in sterilization with minimal light exposure.